Conceptual Design and Analysis of a Large Antenna Utilizing Electrostatic Membrane Management

A. L. Brook, J. V. Coyner,
W. J. Gardner, and D. J. Mihora

NASA

NASA Contractor Report 3522

Conceptual Design and Analysis of a Large Antenna Utilizing Electrostatic Membrane Management

A. L. Brook, J. V. Coyner,
W. J. Gardner, and D. J. Mihora
Martin Marietta Denver Aerospace
Denver, Colorado

NASA

National Aeronautics
and Space Administration

Scientific and Technical
Information Branch

1982

Use of trade names or names of manufacturers in this report does not constitute an official endorsement of such products or manufacturers, either expressed or implied, by the National Aeronautics and Space Administration.

TABLE OF CONTENTS

CONCEPTUAL DESIGN AND ANALYSIS OF A LARGE ANTENNA
UTILIZING ELECTROSTATIC MEMBRANE MANAGEMENT

A. L. Brook[a], J. V. Coyner[b], W. J. Gardner[c], D. J. Mihora[d]

SUMMARY

Radiometer antennas of the 100-m diameter class can be placed into near-Earth orbit with one Shuttle flight. This study was performed under the title of "Advanced Space Systems Analysis (ASSA)", whose purpose was to develop certain conceptual designs and associated technologies for deployable antennas of this size. The study was divided into three tasks. This report is devoted to Task I.

Task I was dedicated to the design of an electrostatically suspended and controlled membrane mirror and to the performance of the necessary analysis to develop conceptual designs for the supporting structure. The scope included evaluating three leading structural concepts, selecting two, and proceeding with the design and analysis of the integrated spacecraft including STS cargo bay stowage and deployment. An antenna performance evaluation was performed as a measure of the quality of the membrane/spacecraft when used as a radiometer in the 1 GHz to 5 GHz region.

---

[a]Program Manager, Martin Marietta Corporation, Denver Colorado.
[b]Senior Staff Engineer, Martin Marietta Corporation, Denver, Colorado.
[c]Staff Engineer, Martin Marietta Corporation, Denver, Colorado.
[d]Program Manager, General Research Corporation, Santa Barbara, Calif.

1.0 INTRODUCTION

The electrostatically controlled membrane mirror (ECMM) spacecraft conceptual design was a joint effort between Martin Marietta Corporation and General Research Corporation. Together, Martin Marietta and General Research evaluated three structural concepts, which were candidates for maintaining the ECMM developed by General Research. Two concepts were selected for further study: Martin Marietta's columnless box truss hoop and Lockheed's wrapped radial rib (WRR), modified with a rim.

General Research then proceeded to design the ECMM to meet the mission model requirements for the box ring and the WRR. General Research also developed designs for the supportive subsystems, including the electrostatic support and control systems, power systems, control electrodes; performed stress and thermal analysis; investigated several surface figure sensing schemes; and developed a surface error model for rf analyses.

Martin Marietta developed designs for the stowed and deployed box truss hoop configuration, the feed support system, the cradle, the deployment system, the ECMM/structure interface; performed loads, thermal, dynamic and rf performance analysis; determined environmental disturbances and subsystem requirements; and configured the subsystems necessary for autonomous spacecraft operation.

Martin Marietta also developed a structural configuration for the WRR that is compatible with the radiometer mission requirements and ECMM integration (satisfying geometric and loads requirements); developed stowed and deployed designs, performed dynamic analyses, and configured subsystem layouts for autonomous operation.

Based on this study of 100-m radiometers using electrostatically controlled antenna membranes, the following conclusions can be made:

Higher surface loads caused by switching from a mesh to an ECMM can drive structural designs.

- Wrap radial rib requires added compression rim.
- Box truss ring member sizes are increased slightly.
- Contiguous truss not affected.

Box truss ring has significant advantages over contiguous truss and hybrid radial-rib/rim.

- Stiffer
- Not limited in diameter
- Best system integration with ECMM

ECMM provides surface control making low-cost aluminum box truss ring feasible.

- Shape control compensates for thermal and alignment errors of aluminum.

3

2.0 MISSION EVALUATION AND CONCEPT SELECTION

The conceptual design of the ECMM spacecraft began with selection of a typical radiometer mission. A functional analysis was performed on this mission to derive system and subsystem requirements. The three structural candidates were evaluated and ranked against these requirements.

2.1 RECOMMENDED MISSION

The ASSA program is a technology study, not a radiometer design. However, in an attempt to achieve realistic results, a mission was selected. The mission is a scaled-down version of the spherical dish radiometer, described on page 15 of "Focus Mission Scenario For Communications, Radiometer and Radio Astronomy ... LSST Technology Requirements Definition" by T. G. Campbell and J. DiBattista; NASA LaRC. The geometry was scaled to give a 100-m aperture using 50-m spots generated by beams on a linefeed of 23-m length, 100-m focal length. The 650-km circular orbit altitude was preserved although the 1-km resolution (at 1.08 GHz) could not be achieved. An efficient beam pattern was attained, however, by interlacing feed horn outputs. The mission characteristics are listed here:

(1) 100-m diameter spherical dish radiometer;

(2) Line feed; f/D = 2 per beam;

(3) 650 km circular orbit inclined 60 deg;

(4) 10-yr lifetime; 3-yr reservice;

(5) Single STS launch;

(6) 1-km resolution at 4.95 GHz;

(7) Rf payload frequencies 1.08, 2.03, 4.95 GHz;

(8) Antenna surface accuracy goal $\lambda/50$.

2.2 DERIVED ANTENNA AND SUBSYSTEM REQUIREMENTS

The basic mission requirements for the ASSA spacecraft are that it is a radiometer operating in the 1 to 5 GHz band and that it provides 1-km

resolution. Certain other design requirements can be derived readily using this information. First, atmospheric drag considerations (Section 4.8, 4.9) dictate that the system operate in an orbit at 650 km or higher. Knowing that higher altitudes dictate larger apertures, the 650-km figure was selected. Using the classical angular resolution equation for diffraction-limited optics (θ = 1.22 λ/D), we derived a second requirement, that is, the aperture diameter. Assuming that it is satisfactory to achieve the 1-km resolution at one frequency only, 5 GHz was selected as the frequency at which to achieve the 1-km resolution. Thus, the angular resolution must be θ = 1 km/650 km and, from θ = 1.22 λ/D , the 5 GHz apertures must be 50 m in diameter.

At this point, the goal turns to designing the largest aperture spacecraft (having adequate surface precision) that can be launched in, and deployed from, a single orbiter. By providing maximum aperture, the number of 50 m subapertures that can be implemented is maximized. This, in turn, provides the maximum swath width of approximately 160 km, assuming a fan of beams is aligned perpendicularly to the orbit plane.

Given that a certain number of feeds can be integrated for the various wavelengths, other derived requirements such as power and downlink data rates become available. These subsystem requirements are stated in Section 3.2.

2.3 FUNCTIONAL ANALYSIS

The top-down functions identified for the 100-m radiometer spacecraft are shown in Figure 2.3.1. For this study the sequence selected for functions 4.0 and 5.0 is for deployment followed by transfer. Each top level function has been similarly segmented into its set of subfunctions in order to identify the subsystems required for performance of each function and to derive subsystem and system requirements for performance of the mission described in Section 2.1. The major focus of this study is on functions 3.0, 4.0, 5.0, and 6.0. Analysis of these functions resulted in identification of major technological problems and provided early identification of design, development, test, and engineering (DDT&E) drivers likely to be encountered.
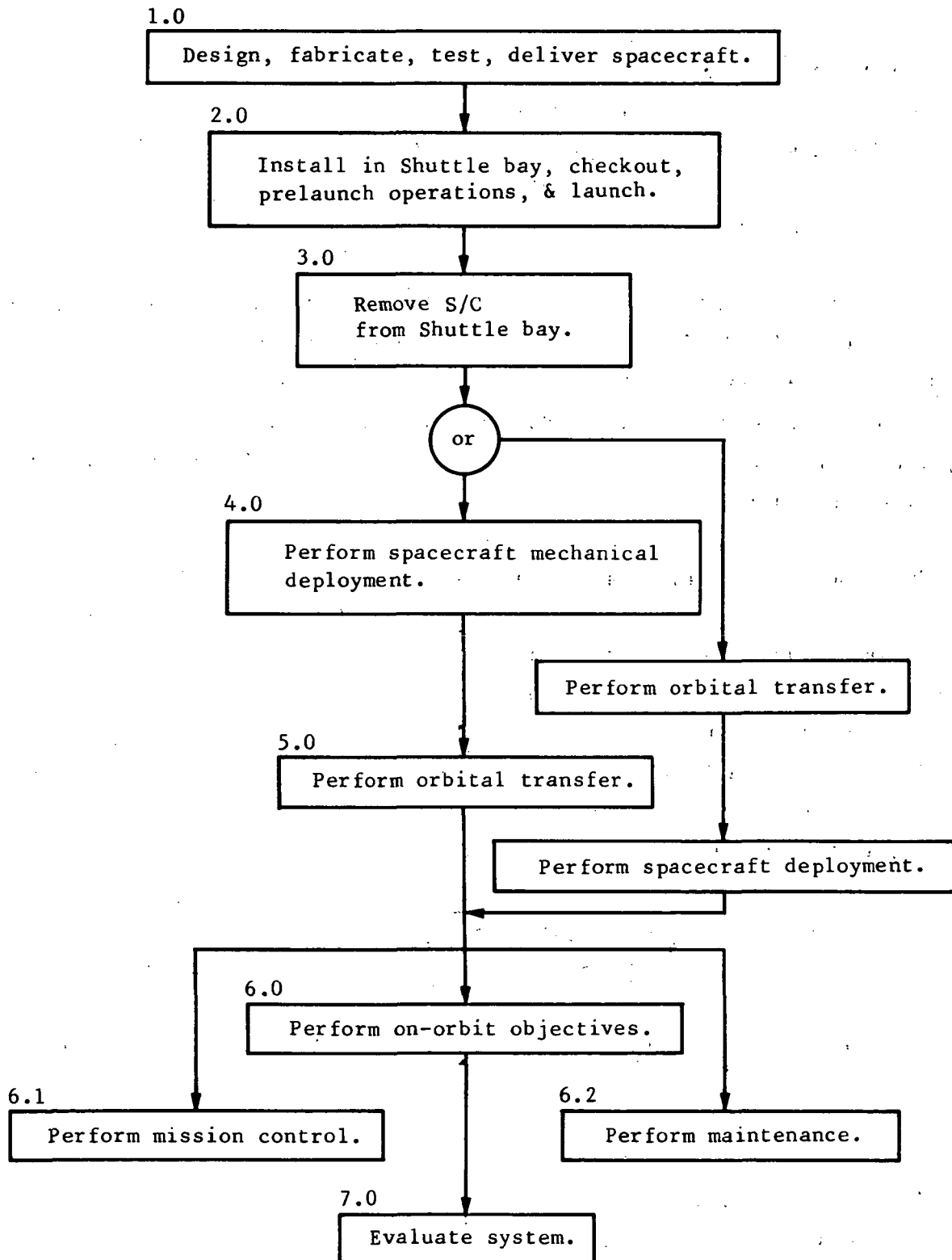
```
1.0
┌─────────────────────────────────────────┐
│  Design, fabricate, test, deliver spacecraft. │
└─────────────────────────────────────────┘
        │
2.0     ▼
┌─────────────────────────────────────────┐
│  Install in Shuttle bay, checkout,      │
│  prelaunch operations, & launch.        │
└─────────────────────────────────────────┘
        │
3.0     ▼
┌─────────────────────────┐
│  Remove S/C             │
│  from Shuttle bay.      │
└─────────────────────────┘
        │
        ▼
       (or)──────────────────────────┐
        │                            │
4.0     ▼                            │
┌─────────────────────────────┐      │
│  Perform spacecraft mechanical │    │
│  deployment.                 │      │
└─────────────────────────────┘      ▼
        │              ┌──────────────────────────┐
        │              │  Perform orbital transfer. │
        │              └──────────────────────────┘
5.0     ▼                            │
┌──────────────────────────┐         ▼
│  Perform orbital transfer. │  ┌──────────────────────────────┐
└──────────────────────────┘  │  Perform spacecraft deployment. │
        │                     └──────────────────────────────┘
        │◄──────────────────────────────┘
   ┌────┤
6.0│    ▼
   │  ┌──────────────────────────────┐
   │  │  Perform on-orbit objectives. │
   │  └──────────────────────────────┘
6.1│    │                            │6.2
┌──▼──────────────────────┐     ┌────▼───────────────────┐
│  Perform mission control. │     │  Perform maintenance.  │
└─────────────────────────┘     └────────────────────────┘
7.0     │
┌───────▼──────────┐
│  Evaluate system. │
└──────────────────┘
```

Figure 2.3.1. – Functional analysis of 100-m radiometer.

6

2.3.1 Remove Spacecraft from Shuttle Bay (Function 3.0)

The subfunctions required for this function are:

(1) Disconnect data and power buses;

(2) Release launch cradle tie downs;

(3) Physically remove spacecraft from STS cargo bay;

(4) Activate required spacecraft subsystems;

(5) Translate STS from spacecraft.

The requirements for this function must assess the change in mass properties of the STS/payload system resulting from spacecraft deployment, the time required for deployment, momentum and energy used in deployment, and orientation of the spacecraft and STS during and after separation. The options for deployment include use of the STS manipulator arm or inclusion of separate deployment mechanisms.

The spacecraft subsystems that are required for this function are:

(1) Power and power distribution;

(2) Restraint and cable disconnect;

(3) Communication;

(4) Data management and control;

(5) Spacecraft emplacement;

(6) Thermal control.

2.3.2 Perform Spacecraft Mechanical Deployment and Activation (Function 4.0)

The subfunctions required for deployment of a spacecraft after it has been removed from the STS cargo bay are:

(1) Deploy reflector surface structural elements;

(2) Deploy rf feed beam;

(3) Deploy feed beam structural support elements;

(4) Deploy feeds;

(5) Deploy solar arrays;

(6) Verify completion of deployment stages;

(7) Stabilize spacecraft rotation;

(8) Activate and check out subsystems.

Each of the first five subfunctions consists of a sequence of mechanically or electromechanically controlled operations. The functional requirements for these deployment stages are:

(1) Initiate a deployment stage only on successful completion of previous deployment stage;

(2) No single-point failure will prevent completion of a deployment stage.

Each structural deployment stage requires verification of successful completion. Automated closed-loop deployment control requires sensors to detect positive hinge latching or correct orientation of antenna feeds and solar arrays. This will permit spacecraft deployment at a safe distance from the STS. Indication of a deployment stage malfunction must be checked visually by flying near the spacecraft with the orbiter, with a crew member using a maneuvering unit, or with a robotic device. Deployment malfunctions should be correctable using either a manned or an unmanned unit.

The options considered for structural deployment should include the following:

(1) Can deployment be completely activated by potential energy?

(2) Is motor-driven deployment required for assistance?

(3) Is potential energy sufficient for reflector surface positioning?

(4) Is potential energy deployment sufficient for deployment of feed beam and feed masts?

8

Stabilization of initial rotation may be required on initial separation from the STS and during spacecraft deployment. To minimize induced rotations the deployment sequence should be performed in such a way as to maintain a constant center of mass location and minimal momentum exchange because the attitude control system may have limited restoring torque capability before structural deployment is completed.

The following subsystems have been identified as necessary for successful completion of this function:

  (1) Structural element deployment activation;

  (2) Feed beam deployment actuation;

  (3) Feed mast(s) deployment actuation;

  (4) Feeds deployment actuation;

  (5) Solar array deployment;

  (6) Power and power distribution;

  (7) Communication;

  (8) Data management and control;

  (9) Propulsion;

 (10) Attitude control;

 (11) Guidance and navigation;

 (12) Thermal control;

 (13) Reflective surface shape control.

2.3.3 Perform Orbital Transfer (Function 5.0)

Successful completion of mechanical deployment and activation permits the transfer of the spacecraft from low Earth orbit to its operational orbit. The subfunctions included in this operation are:

  (1) Perform attitude control;

  (2) Perform main thrusting;

  (3) Perform guidance and navigation;

  (4) Monitor spacecraft;

  (5) Separate spacecraft and booster.

2.3.3.1 Perform Attitude Control

During orbital transfer the spacecraft compares its sensed and actual flight orientation and performs appropriate rotational and translational correction. Sufficient control authority must be provided to overcome the expected disturbances due to atmospheric drag, solar pressure, gravity gradient torques, and onboard venting. This function includes final stabilization at the operational site before full activation. Because of the large inertias associated with this type of spacecraft and the low permissible acceleration loading, the attitude control system (ACS) should maintain a relatively tight limit cycle during transfer.

2.3.3.2 Perform Main Thrusting

The propulsion subsystem performs the main burns to change orbit. This would normally include several short thrusting periods separated by long coasting periods.

2.3.3.3 Perform Guidance and Navigation

The attitude control system provides proper orientation during transfer and the guidance and navigation system ensures that the spacecraft maintains the proper orbital transfer flight path. The current position of the spacecraft must be sensed, compared to the required position and the necessary translations performed. Drag resulting from atmosphere and solar pressure will decelerate the spacecraft requiring instantaneous monitoring of its position. The main propulsion system and ACS will operate in concert to provide the required orientation and position for successful transfer.

2.3.3.4 Monitor Spacecraft

During boost, the spacecraft will be monitored by the orbiter flight crew and/or ground controllers. The spacecraft transmits status updates, which are evaluated. Minor anomalies are diagnosed and the spacecraft is commanded to perform the appropriate corrective action.

10

2.3.3.5 Separate Spacecraft and Booster

This function is required if a reusable orbital tug is used as the booster, or if having the booster attached would interfere with spacecraft operation. After performing its function, the booster is separated and guided as required. This function is not applicable to spacecraft that have integral boost subsystems.

The spacecraft subsystems required for successful orbital transfer are:

(1) Attitude control system;

(2) Propulsion;

(3) Guidance and navigation;

(4) Communication;

(5) Data management and control;

(6) Power and power distribution;

(7) Thermal control.

2.3.4 Perform On-Orbit Objectives (Function 6.0)

The subfunctions required for this function have been broken down into:

(1) Perform radiometer function;

(2) Provide reflector surface/feed structural support;

(3) Perform surface shape control;

(4) Perform spacecraft attitude control;

(5) Perform guidance and navigation;

(6) Perform communications;

(7) Perform data management and executive control;

(8) Perform thermal control;

(9) Provide power and power distribution.

Each of these subfunctions requires a subsystem that may be identified from the subfunction. All these subsystems are required and must be interfaced and integrated for on-orbit operations. The following is a discussion of these subfunctions.

2.3.4.1 Perform Radiometer Function

The radiometer function consists of receiving microwave data, signal conditioning and storage, transmission to Earth, and evaluation. Microwave feed horns working with the reflector sense the microwave signature required for the mission defined in Section 2.1. The output of each feed horn is averaged for a short time. These data, along with the feed horn number and a time reference, are transferred to the ground through the communications subsystem. After arrival on the ground, the microwave data are stored and processed into a useable form.

2.3.4.2 Perform Reflector Surface/Feed Structural Support

The structure must provide low distortion of the reflector surface and maintain the feeds at the design focus point. The surface strongback should be insensitive to thermal gradients and should not be distorted by normal orbital operations such as attitude control.

2.3.4.3 Perform Surface Shape Control

The reflector surface shape control should be a closed-loop, automatic system. The basic subfunctions to be performed are shown in Figure 2.3.2.
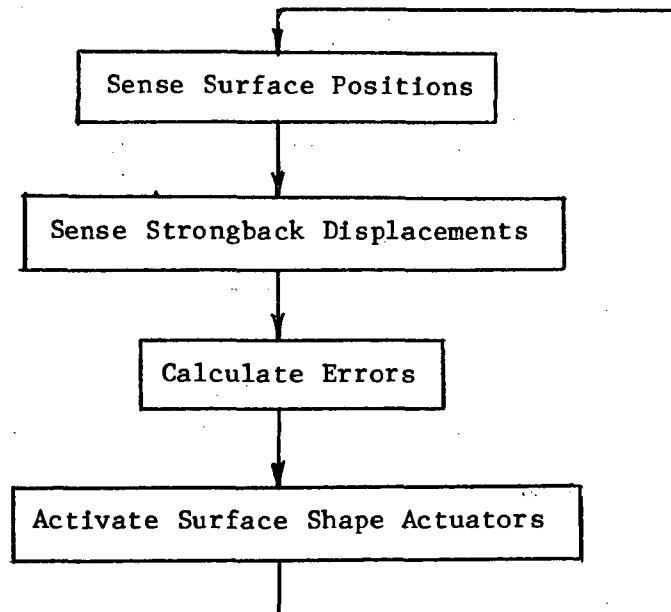

Figure 2.3.2. - Surface shape control functions.

There are two loops for surface control that may be required. The structural strongback can experience deflections of tie down points due to thermal gradients in the structure and due to modal displacements resulting from coupling effects between the structure and attitude or guidance control systems. Thermally induced displacements will have extremely large time constants and can sometimes be compensated for by electromechanical devices such as screw actuators. Smaller, higher frequency surface distortions must be compensated by active control. Specific subsystem components required for surface shape control can be identified as:

(1) Surface position sensors;

(2) Strongback position sensors;

(3) Surface position actuators;

(4) Strongback position actuators.

2.3.4.4 Perform Attitude Control

During operation, the attitude control system (ACS) must maintain the spacecraft in an orientation consistent with the mission requirements. All disturbing forces and torques must be counteracted. Options for ACS actuators include thrusters, reaction wheels, and magnetic torquers. ACS requirements were analyzed to determine the most effective combination of components that will produce satisfactory control.

2.3.4.5 Perform Guidance and Navigation

The spacecraft's present position must be sensed and compared with its desired position to maintain an orbit consistent with mission requirements. Atmospheric and solar drag forces on the spacecraft produce deceleration, which must be compensated for periodically during a mission. These degrading forces will vary on relative orbital and spatial spacecraft position. An automatic closed-loop guidance subsystem will be required to permit a successful radiometer function.

2.3.4.6 Perform Communication

The communication function requires transmission of microwave data and spacecraft status to the ground or STS and reception of commands from the ground or STS. Communications must be compatible between the satellite and the orbiter, the TDRSS relay network, and the ground relay network. Options include continuous versus occasional data transfer, data encryption, and operating frequencies.

2.3.4.7 Perform Data Management and Executive Control

The data management and control function provides control of the operation of the spacecraft under internal or external direction. Subsystem status is collected and evaluated internally. As an option, this status can be relayed to the ground through the communications subsystem. Based on preprogrammed algorithms and uplinked commands, appropriate commands are issued to the subsystems for normal operations sequencing, anomaly detection, and problem correction. Subsystems that will involve a large number of data signals include surface shape control and radiometer feed horns. The large size of the spacecraft requires study of techniques and components to provide an efficient onboard data transmission network. Wiring must provide redundancy and must maintain sizes consistent with structural packaging and deployment.

2.3.4.8 Perform Thermal Control

The thermal condition of all spacecraft components must be maintained within certain limits. The present thermal condition must be sensed, compared with a permissible range, and corrected. Control options included passive coatings, film heaters, louvers, and radiators. The control of thermally induced displacements in the reflector surface is discussed in Section 2.3.4.3.

2.3.4.9 Provide Power and Power Distribution

Spacecraft power must be generated, stored, regulated, and distributed. Generation options include solar arrays, fuel cells, auxiliary power units, and radioisotope generators. Normally, some storage capability is provided by batteries for redundancy and buffering. The power produced must be regulated

to the proper voltage, frequency, and current. A power switching and distribution network interfaces power producers and consumers and provides some protection and monitoring capability. The size of the spacecraft will result in significant amounts of cable for power distribution. The size, coupled with redundancy requirements for power distribution requires detailed analysis of cabling requirements and the interaction with packaging and deployment functions. Options that might be considered are high operating frequencies for power distribution to permit smaller cables, distributed versus centralized power units, and power distribution integral to structural elements.

2.4 STRUCTURAL CANDIDATE CONCEPTS

Three generic support structures (radial rib, truss ring, and truss) have been evaluated as a support structure for the electrostatic membrane.

The same mission requirements were prescribed to the three support structures. Loads and geometric requirements imposed on the support structure were defined by ECMM requirements. Membrane-generated loads imparted into the support structure were identical. Each structural candidate was configured to a rather specific three-membrane spacing requirement. The geometric layout of the support structure attempted to minimize the component parts and thus increase mechanical reliability. Common to all three support structures is the axisymmetric tensioned membrane. General Research Corporation has selected a baseline tensioned membrane exhibiting the properties shown in Table 2.4.1.

Figures 2.4.1 to 2.4.3 are conceptual layouts of the three ECMMs integrated with different support structures. Side views (A-A) show the integration of the three membranes. In all three layouts, the suspended membrane reflector (1) is attached only at the perimeter. Minimizing membrane reflector attachment points simplifies the thermal control problems. A design philosophy of minimizing part count complexity has led to the use of long gossamer elements. The compression ring and contiguous truss were sized to use nearly the entire Space Shuttle bay. In this arrangement, the number of hinges, springs, and deployment actuators were minimized.

TABLE 2.4.1. - MEMBRANE PROPERTIES.

Final tensioned radius of curvature, $\rho_f = 200$ m

Preformed untensioned radius of curvature, $\rho_0 = 208$ m

Centerline membrane deflection with electrostatics, $\Delta_z = 25$ cm

Centerline membrane to electrode gap, gap $= 10$ cm

Rim-membrane to electrode gap, gap $= 14.5$ cm

Centerline field strength, $E_E = 28\ 900$ v/cm

Rim-field strength, $E_E = 19\ 900$ v/cm

Centerline voltage, $V = 28\ 900$ volts

Rim voltage, $V = 28\ 900$ volts

Centerline stress/yield stress, $NR = 0.058$

Rim radial stress/yield stress, $NR = 0.043$

Rim azimuthal stress/yield stress, $NTH = 0.013$

2.4.1 Contiguous Truss

The 100-m space truss using long columns is shown in Figure 2.4.1. The Shuttle bay length is shown to scale. A more than adequate number of face elements provide hard points for attaching the control electrode surface. However, special mounting points are required for the perimeter attachment of the membrane reflector. The tetrahedral truss shown in Figure 2.4.1 is termed a "seven-ringer" because of seven concentric hexagons.

The contiguous space truss provides an optimum number of hard points for attaching the control electrodes. This structure provides the potential for significant improvement in surface quality beyond the 1.0 mm accuracy.

The control electrode surface (2) need not be attached at all points along the truss. The number and spacing of the electrodes will be discussed later in the report. Two locations are indicated for the Faraday membrane (3). The alternate (3) location is less acceptable because the structure is hidden during deployment.
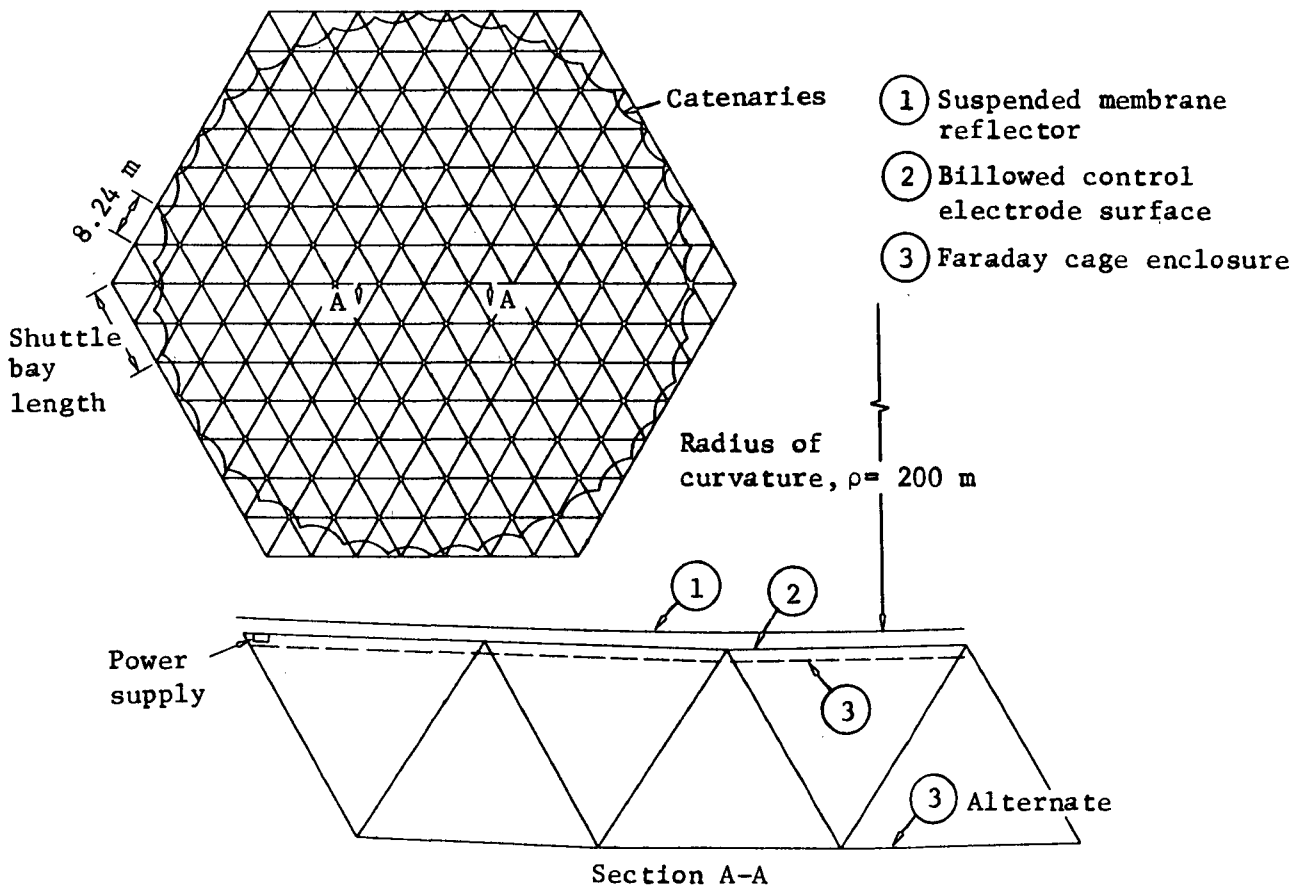

Figure 2.4.1. - 100-m diameter ECMM with minimum number of space truss elements.

2.4.2 Wrap Radial Rib

The wrap radial rib being developed by Lockheed Missiles and Space Company
is particularly attractive because of the low total part count. Hinges and
pins are replaced by strain-deformable members that can be spirally wrapped on
a ring. Lockheed provided design consulting on several rib members that could
be adapted to the ECMM. A hybrid wrap radial rib structure was forwarded. It
uses a significantly reduced number of radial ribs. These ribs are stabilized
by incorporating a rim that connects the ends of all ribs. Even with the rim,
the hybrid wrap radial rib design appears to be the most controllable during
the deployment phase. It also has the smallest structural packaging volume.
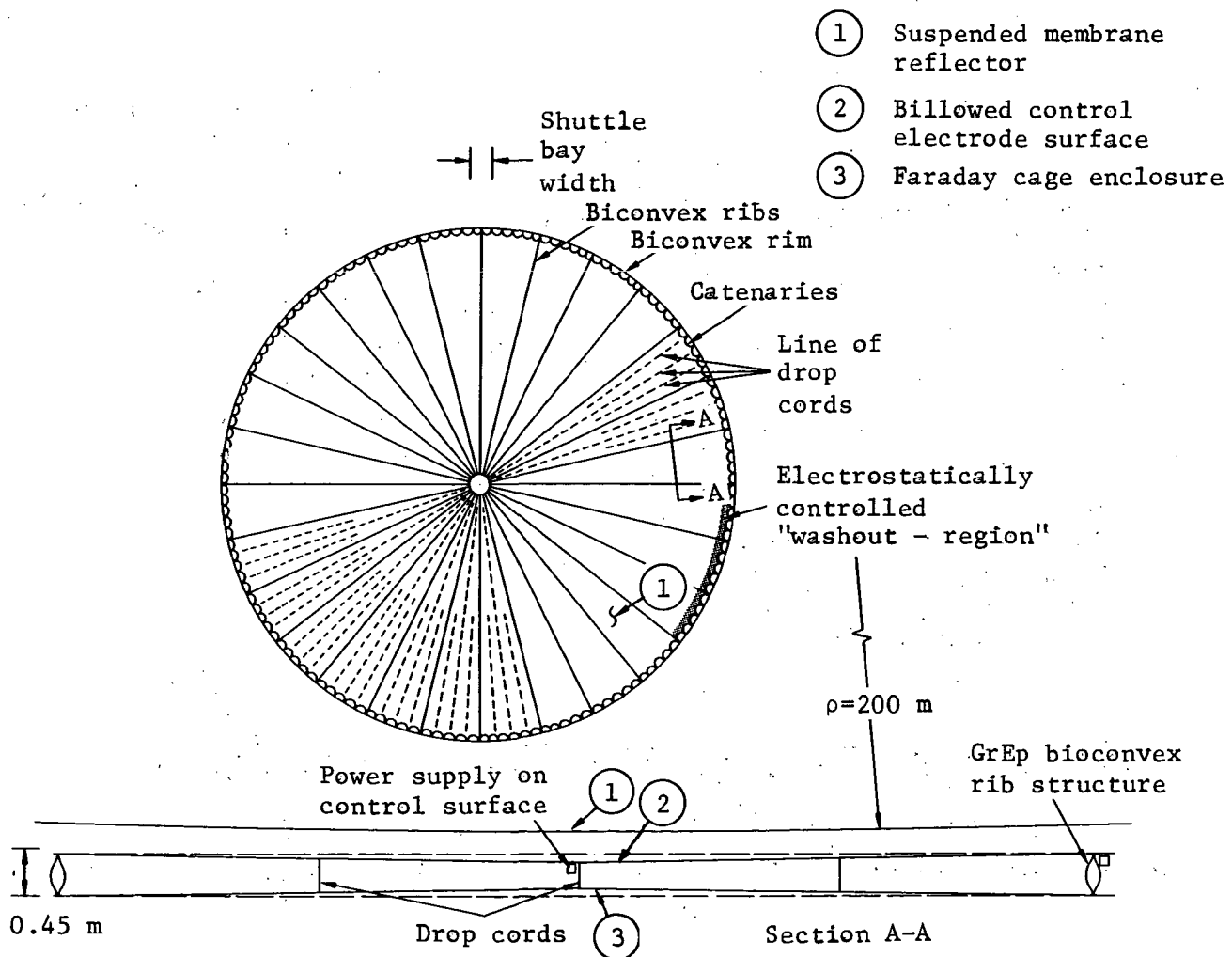
Figure 2.4.2. - 100-m diameter hybrid radial rib structure with ECMM.

A hybrid radial rib rim structure is shown in Figure 2.4.2. The graphite/ epoxy radial ribs are connected to a graphite/epoxy compression rim. Both the ribs and rim have a biconvex cross section. The rim-rib arrangement was proposed by Lockheed as a more efficient approach to handling ECMM loads than simply adding more ribs. The nominal perimeter loads are 17.5 N/m. The compression load applied to each of the 24 ribs from the ECMM is approximately 229 N. The rim structure stabilized the ribs and reduced deflections by an order of magnitude. The ribs are preshaped to compensate for this deflection. Note that the 24 ribs are significantly fewer than used on mesh-suspended concepts (About 80 ribs for a 5-GHz antenna).

Figure 2.4.3. - 100-m diameter, 28-bay compression hoop with ECMM.

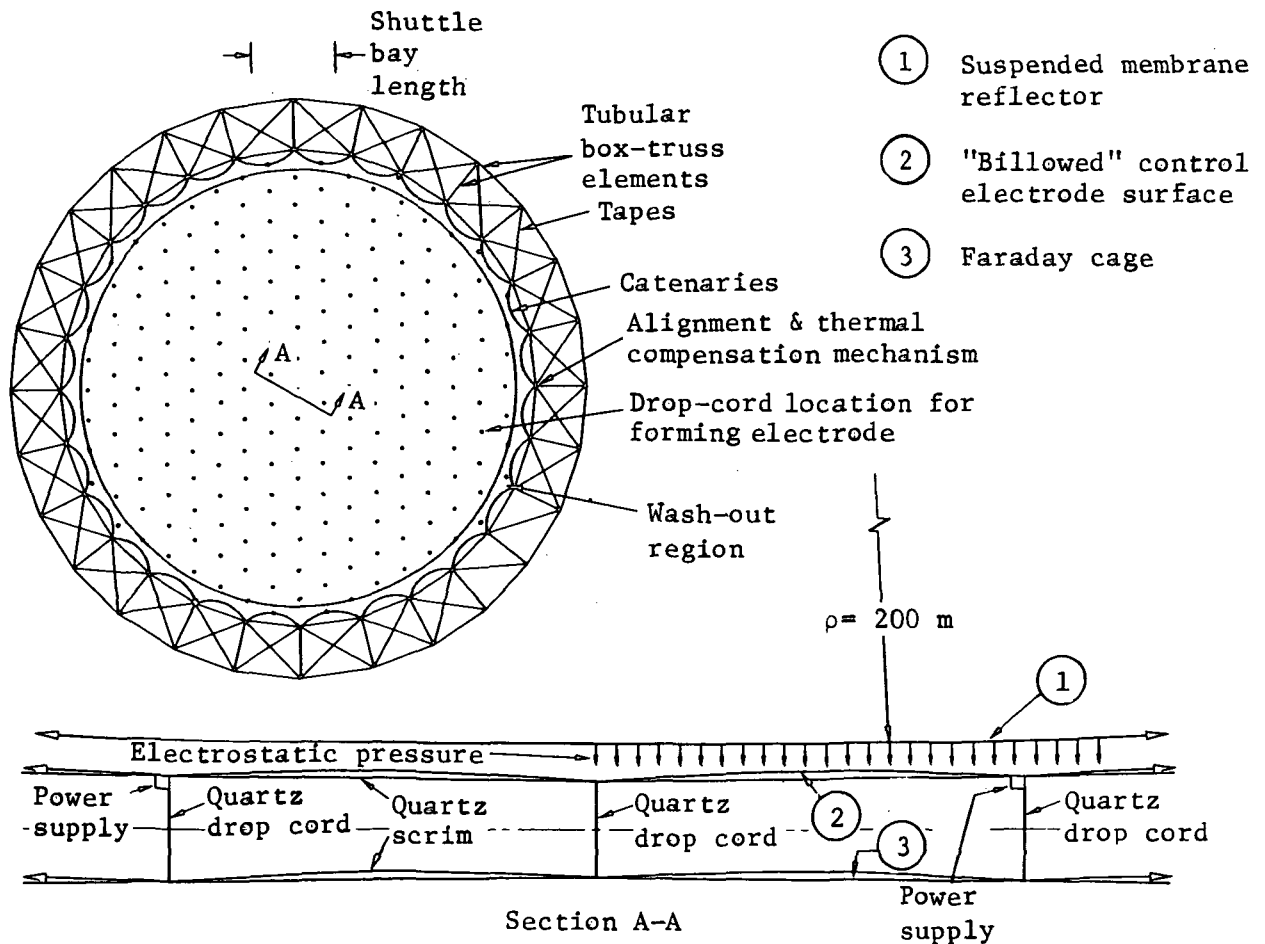The separation between the three membranes is shown in Figure 2.4.2 (Section A-A). The radial rib height of 0.45 m at the rim is required to provide adequate spacing between the control electrode surface and the Faraday cage membrane. The drop cords are employed to form the electrode control surface. The allowable irregularity of the electrode surface is ± 8 cm. The electrode power supplies are common to the control electrode surface.

2.4.3 Box Truss Ring

The third structural layout using the ECMM is shown in Figure 2.4.3. This layout is the Martin Marietta adaptation of the 3-longeron compression rim discussed in Reference 1. Unlike the prior ECMM designs, all three membranes are suspended along the perimeter, forming a tension structure. The membrane reflector (1) is tensioned and formed by electrostatic force. Membranes (2) and (3) are tensioned along the perimeter. Quartz drop cords and a grid scrim of quartz are imbedded in the layout of membranes (2) and (3) The quartz drop cords are approximately 4.5 m apart.

A compression ring structure potentially yields a very packageable ECMM layout. It is the only design in which the rigid support structure is totally outside the perimeter of the membranes. This layout allows many packaging arrangements of the ECMM.

2.5 STRUCTURAL CANDIDATES EVALUATION AND RANKING

This section evaluates the hybrid wrap radial rib/rim, the contiguous truss, the box truss ring, and compares and ranks each candidate.

---

1. D. J. Mihora, R. Chase, et al: Spaceborne Millimeter-Wave Antenna Technology, Vol. I: "Membrane Reflector Technology." General Research Corporation CR-786, August 1979.

2.5.1 Hybrid Wrap Radial Rib/Rim Candidate Evaluation

By applying the ECMM to the wrap radial rib concept, the design can be simplified by a reduction in the number of ribs, but must be complicated by the addition of the rim due to the higher membrane loads (17.5 N/m). In the standard wrap radial rib design, the surface accuracy is a function of the number of ribs. Typically 60 to 80 ribs would be required for a 100-m diameter antenna operating at 1 to 5 GHz. With the addition of the rim this can be reduced to 24 ribs. This reduces the required packaging diameter of the system and also the system weight.

To stabilize these ribs against deflections produced by the membrane loads, a rim must be added at the tip of the ribs. The rim is a lenticular boom that stows similarly to the ribs. The control electrode is supported between the ribs and the reflector surface is attached only at the periphery to the rim.

Table 2.5.1 presents the design options that were generated by Lockheed. Of the six configurations, four were eliminated due to packaging or deflection constraints. The two designs with no rim have excessive tip deflections. The two larger rib designs with rims have packaged diameters larger than the diameter of the orbiter cargo bay (427 cm). The design selected for study was the 43.7-cm deep rib tapering to 12.1-cm deep at the tip. Due to spacing requirements between the ECMM membranes, the baseline rib design was modified to have no depth taper as shown in Table 2.5.1.

TABLE 2.5.1. - WRAP RADIAL RIB CANDIDATE EVALUATION.

	Rib dimensions,[a] base		tip		Rib weight, kg[a]	Hub weight, kg[a]	Ring weight, kg[a]	Membrane Weight, kg[a]	Total weight, kg[b]	Package Dimensions, d x h, cm[c]	Deflections max./tip, cm[a]
	h	b	h	b							
24 ribs with ring	43.7	40.6	12.1	1.0	555	83	181	1220	2039	350x86	5.49/3.18
	55.9	52.8	19.3	2.5	738	110	181	1220	2249	435x112	3.96/2.24
	64.0	61.0	45.7	17.5	1060	159	181	1220	2620	498x127	2.13/1.24
Baseline	43.7	40.6	43.7	17.0	850	127	181	1220	2378	350x86	<5.0/3.0
24 ribs no ring	43.7	40.6	12.1	1.0	555	83		1220	1858	340x86	93.9/93.9
	50.8	47.7	12.7	1.0	675	101		1220	1996	390s102	71.1/71.1

[a]Data supplied by Art Woods, LMSC.

[b]Total weight does not include feed or feed support.

[c]Max. orbiter diameter = 427 cm

2.5.2 Contiguous Truss Candidate Evaluation

By applying the ECMM to the contiguous truss concept, the number of surface attachment points can be substantially reduced. Unfortunately truss spacing cannot be increased beyond the allowable packaged length. Thus the contiguous truss cannot take advantage of freedom offered by the ECMM for increased bay size and resulting parts count reduction. On the plus side, no modification of the truss is required to accommodate the ECMM loads. The truss is inherently stiff and strong enough to accommodate the FCMM. A technique for reduction of parts count was developed that led to the development of the truss ring concept. Because truss attachment points are not required in the center of the truss, the interior bays were removed to produce a truss ring. Table 2.5.2 summarizes the contiguous truss evaluation.

2.5.3 Box Truss Ring Candidate Evaluation

The box truss ring provides an efficient method for supporting the FCMM system. A factor of 3 to 10 reduction in parts count can be realized over a contiguous truss. The ring provides an efficient structure that is relatively stiff, light weight, and has excellent potential for integration of the required subsystems (feed, feed support, solar arrays, ACS, etc.). The open area in the center of the stowed ring can be used for packaging the feed, feed support, and ECMM system.

When comparing the contiguous truss and its required 294 bays to the box truss ring that requires only 28 boxes, a substantial weight and parts count reduction is realized. When comparing the box truss ring to the hybrid wrap radial rib/rim, a substantially stiffer structure is achieved from the truss ring. Table 2.5.3 summarizes the box truss ring evaluation.

2.5.4 Structural Comparison and Ranking

Table 2.5.4 presents a qualitative comparison of the three concepts. All three systems demonstrated that an FCMM can be integrated into the structural design. All three systems meet the stiffness, load, and attachment requirements. Therefore, additional performance parameters were evaluated. The chart shows that the box truss ring and hybrid radial rib/rim rank the highest.

TABLE 2.5.2. - CONTIGUOUS TRUSS CANDIDATE EVALUATION.

Contiguous truss requires a bay size of 8.24 m to allow 8 m for feed, feed support, subsystems, and surface; therefore, a 14 bay, 8.24 m per bay is required for a 100-m reflector (294 bays).

The ECMM does not require a hard point every 8.24 m.

The contiguous truss cannot take advantage of reduction of structure by making the bay larger.

Preliminary Design:

- Surface members: 5.0-cm diameter by 0.046-cm thick;
- Diagonal members: 4.0-cm diameter by 0.046-cm thick;
- ECMM weight = 0.15 kg/m^2;
- Total system weight[a] = 2950 kg.

TABLE 2.5.3. - BOX TRUSS RING CANDIDATE EVALUATION.

The box truss ring provides almost the stiffness of a contiguous truss without the intermediate structure, reducing the parts count by a factor of 3 to 10.

ECMM does not require the intermediate hard points of a contiguous truss, thus, the ring is a practical design.

A 28-bay box truss ring 14 x 11.3 m was selected. Surface and feed can be packaged inside stowed ring.

Preliminary Design

- Circumferential members: 10.2-cm and 8.9-cm diameter by 0.04-cm thick
- Radial members: 6.1-cm diameter by 0.046-cm thick
- Vertical members: 6.1 x 6.1 by 0.071-cm thick
- Diagonal members: Area = 0.23 cm^2
- ECMM weight = 0.15 kg/m^2
- Total system weight[a] = 2485 kg

[a]Total weight does not include feed or feed support.

TABLE 2.5.4. - STRUCTURAL COMPARISON AND RANKING

Constraints	Box truss ring	Hybrid radial rib/rim	Contiguous truss
Structural integrity	1	1	1
Structural stiffness	2	1	2
Three-membrane integration	1	1	1
Three-membrane deployment	1	1	1
Precision control at perimeter	2	1	2
Stability/rigidity of electrodes	1	1	2
Part-count complexity	1	2	0
Packaging volume	2	2	0
Reflector mass	2	2	1
Feed integration	2	0	2
Performance enhancememt	2	2	1
Total	17	14	13

0: Marginally satisfies requirements

1: Satisfies requirements

2: Exceeds requirements

2.6 SELECTION OF TWO PROMISING CANDIDATES

The structural comparison and ranking of the three concepts showed that no concept was clearly superior to the other concepts. The box truss ring and the hybrid radial rib/rim ranked slightly ahead of the contiguous truss, but all satisfied the requirements. Therefore, three constraints were identified as being of more importance than the others: packaging volume, parts count complexity, and rf performance enhancement. A comparison of these criteria showed a clear superiority for the box truss ring and the hybrid wrap radial

rib/rim. The truss ring and hybrid wrap radial rib/rim have over a 90 percent reduction in piece parts compared to the contiguous truss. The contiguous truss occupies almost the total orbiter bay; the truss ring has an 3.4-m diameter open area in the center for packaging of subsystems; and the hybrid wrap radial rib/rim system uses the total 4.3-m diameter but its stowed length is small. The performance enhancement of the hybrid wrap radial rib/rim allows for a reduction in ribs to 24. The box truss ring is essentially a contiguous truss without the unnecessary center boxes. Therefore, the two recommended concepts are box truss ring and the hybrid wrap radial rib/rim.

3.0 DETAILED DESIGNS

This section presents the system-level designs of the two candidate space-craft and subsystem characteristics.

3.1 SPACECRAFT DESIGNS

The following sections present the design details for a 100-m diameter box truss ring radiometer and a hybrid wrap radial rib/rim radiometer, including a definition of all subsystems that are required for an autonomous spacecraft. These designs were developed by Martin Marietta Corporation with exception of the ECMM design, which was developed by General Research Corporation, and are based on Lockheed concepts for the radial rib.

3.1.1 Box Truss Ring Spacecraft Design

The box truss ring radiometer design meets all mission requirements and allows for simple integration of all required subsystems. The ring provides the stiffness and strength to support the ECMM and has a large number of hard points for attachment of subsystems.

3.1.1.1 Stowage and Deployment

The satellite stows into a cylindrical form measuring 3.9 m in diameter by 14.2 m in length (fig. 3.1.1). A rigid shell is formed from the stowed vertical and surface tube members of the box truss ring. Symmetrically arranged about this shell exterior are hydrazine tanks with their thrusters, solar arrays, battery packs, and pulsed plasma thrusters. Attached to the interior surface of the shell is the electrostatic membrane. This membrane runs the full length of the shell, surrounding the feed support structure and Astromast canisters. The Astromast canisters are also attached to the box truss ring. During deployment, this attachment will act as a pivot. For maximum strength and stiffness all satellite subsystems attach to either the cube corner fittings or the vertical tubes of the box truss ring. The following paragraphs present a detailed description of deployment.
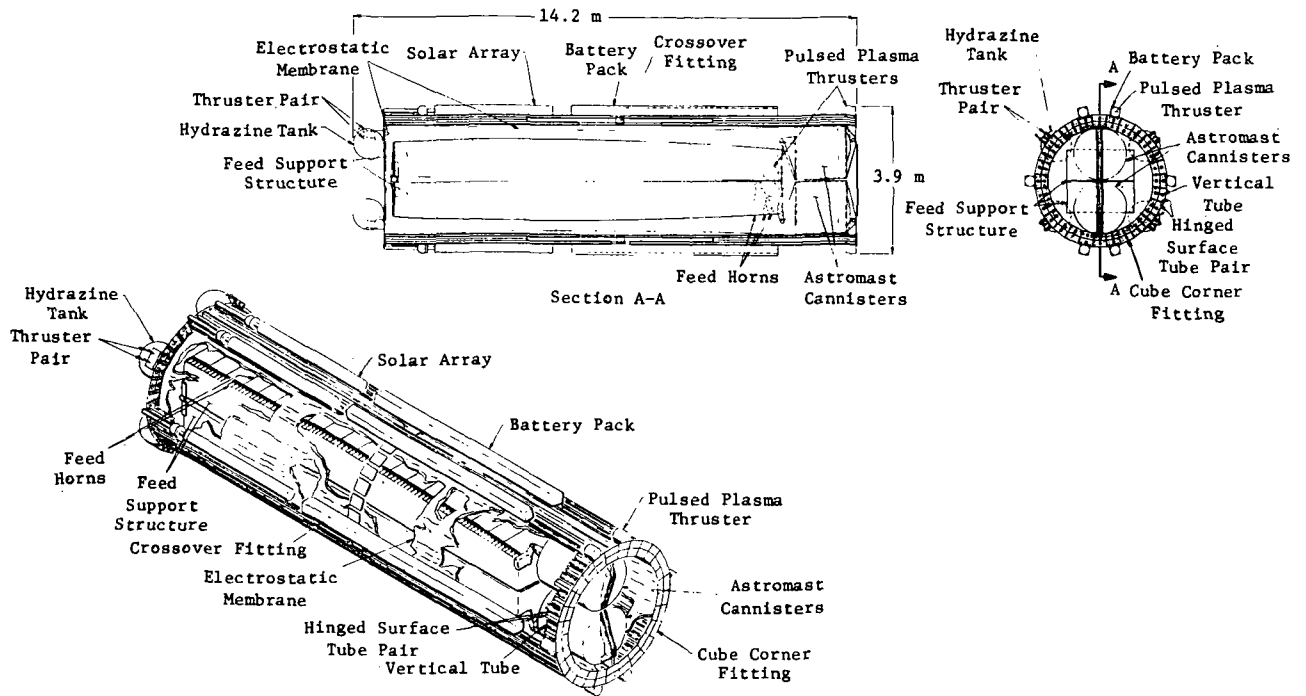
Figure 3.1.1 – Stowed configuration.
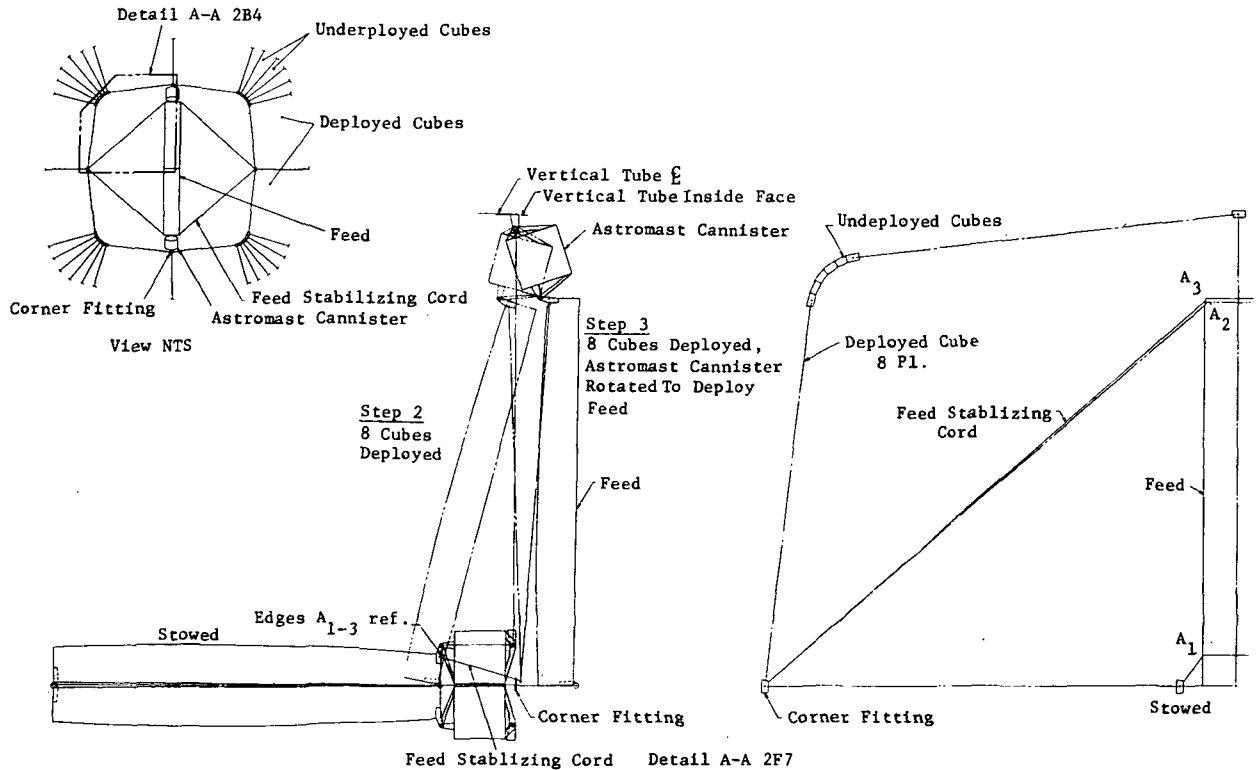
Figure 3.1.2. – Ring and feed deployment (steps 2 and 3).

27

The first step is the simultaneous deployment of the 56 surface tubes (28 front and 28 rear) that connect the inside and outside cube faces. This is done first so that a controlled deployment of the hoop can be accomplished. In other words, as the ring expands a fully deployed cube is dynamically more stable than a semideployed cube.

The second step is the simultaneous deployment of eight cubes shown in Figure 3.1.2. This arrangement expands the ring far enough to allow for the withdrawal of the feed from the stowed package.

The third step, withdrawal of the feed, is accomplished by rotating the
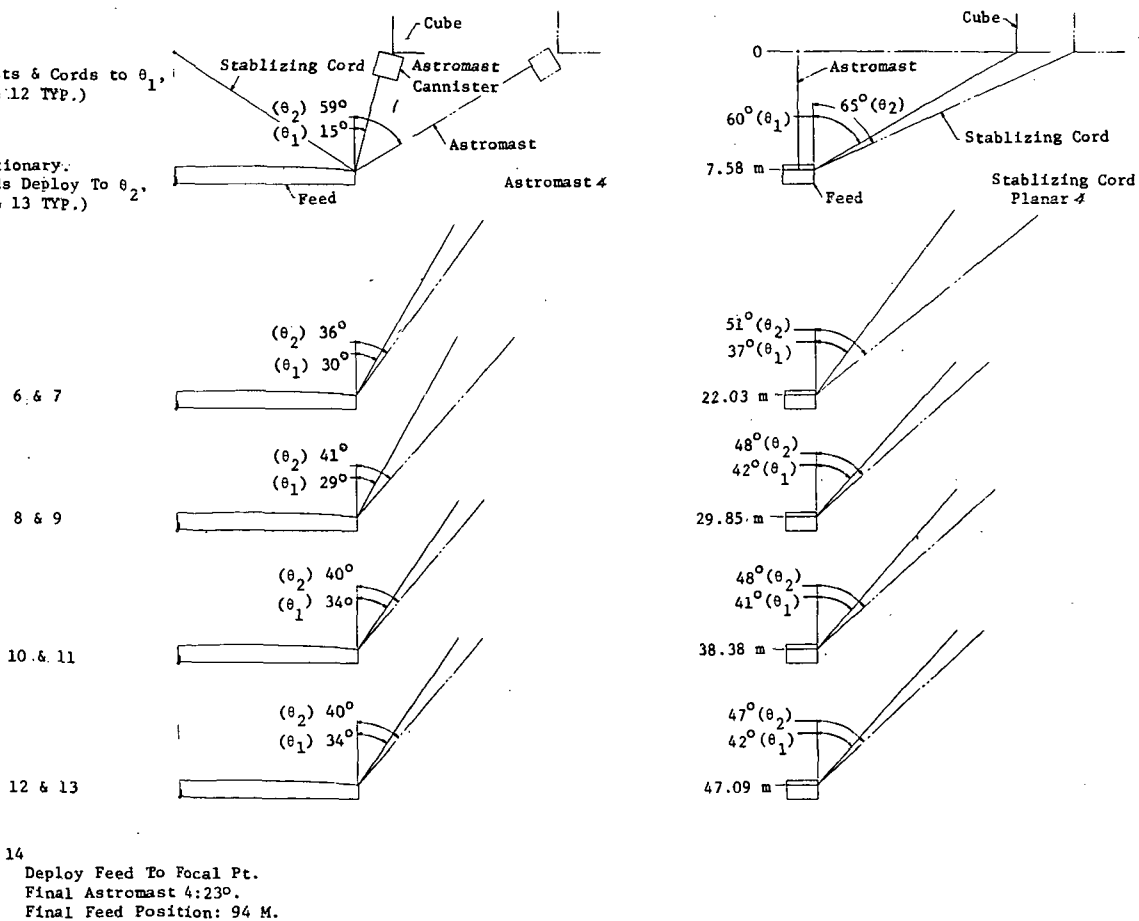
Figure 3.1.3. - Ring and feed deployment (steps 4,6,8,10, and 12).

Astromast canisters to allow the feed to move over center and lock into place (fig. 3.1.2).

In steps 4, 6, 8, 10, and 12, the feed is lowered to Angle θ_1 (fig. 3.1.3). The angles were selected to rely on the higher load carrying ability of the stabilizing cords.

The deployment of the feed can be controlled by synchronizing the motors controlling the Astromasts with the motors controlling the stabilizing cords.
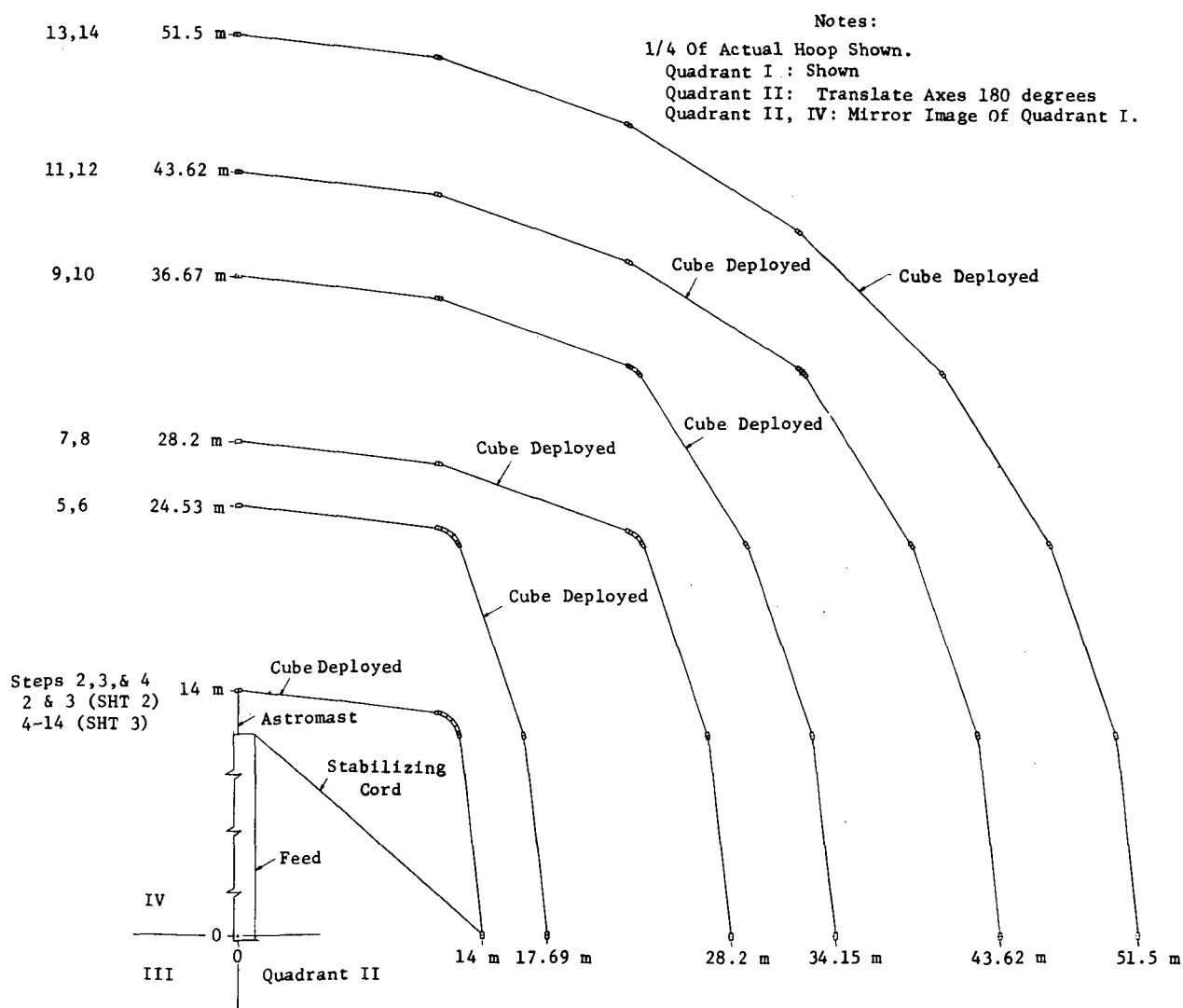
Figure 3.1.4. - Ring and feed deployment (steps 5,7,9,11, and 13).

In steps 5, 7, 9, 11, and 13, cubes arranged in sets of 4 are deployed (fig. 3.1.4). In steps 5 through 9 the cubes are symmetrical about an axis that lies perpendicular to the feed. In steps 7 and 11 this axis lies parallel to the feed. In step 13 the cube deployment is symmetrical about the feed. During these steps the distance between two parallel planes, one containing the feed and the other containing the ring, must be held constant. This implies that the length of the Astromasts and stabilizing cords must be variable (if the Astromasts and cords were held stationary and the distance between planes was variable the resulting bending load induced into the Astromasts would severely damage them). Also implied is that the spring force of the deploying tubes must be greater than the spring force required for the deployment of the Astromasts. The rate of cube deployment is controlled by the motors releasing the stabilizing cords. Once again, the motors controlling the Astromasts must be synchronized to the stabilizer cord motors. Step 13 completes deployment of the ring.

In steps 14 and 15 the feed is dropped to its final position and various equipment is deployed.

3.1.1.2 Deployed Spacecraft

The reflector support structure comprises 28 epoxy graphite box truss cubes joined together to form a structural ring (figs. 3.1.5 and 3.1.6). A typical box truss cube measures 11.56 m across the inside face, 13.46 m across the outside face, 8.5-m wide, and 14-m high. Lying in the plane of each cube face and extending from each corner is a telescoping tape (fig. 3.1.7). These tapes are secured to a flat plate called a crossover fitting. When a cube is deployed, the crossover fitting is located at the center of each cube face. The tapes lying in the top and bottom planes of the cube unwind from spools instead of telescoping and connecting to crossover fittings. All tapes are pretensioned and serve to stabilize the deployed cube. For ease of stowage, the eight horizontal members, called surface tubes, are hinged in the center. Each surface tube hinge employs an over center latch that locks it into position when deployed. The four 14-m long, nonfolding, vertical tubes are

attached to the corner fittings. At each corner where the surface tubes, the tapes, and a vertical intersect is a corner fitting. Member sizes are based on the ECMM loads and are summarized in Table 3.1.1.

TABLE 3.1.1. - ECMM SUPPORT STRUCTURE.

Surface tubes
Outer circumferential: 8.5-m x 6.1-cm diam x 0.046-cm wall, Pcr = 510 N, P applied = 62 N, factor of safety = 8.2   Inner circumferential: 11.56-m x 8.9-cm diam x 0.046-cm wall, Pcr = 856 N, P applied = 503 N, factor of safety = 1.7   Radial: 13.46-m x 10.2-cm diam x 0.046-cm wall, Pcr = 944 N, P applied = 479 N, factor of safety = 2.0
Vertical tube
14-m x 6.1-cm sq. x 0.071-cm wall, Pcr = 479 N, P applied = 102 N, factor of safety = 4.9

A honeycomb epoxy graphite structure houses the feed horns (fig. 3.1.8). A total of 302 individual horns are mounted inside the feed structure. To facilitate stowage the feed structure is hinged in the middle. An over center latch locks the feed into position once it is withdrawn from the stowed package. Two pulsed plasma thrusters are also stowed inside the feed along with a figure sensor, microprocessor, radiometer electronics, signal conditioning and control unit, attitude control system, and command and data handling.

The feed is suspended from the box truss ring by two Astromasts. Two sets of epoxy graphite cords serve to stabilize the feed (fig. 3.1.6).

Due to the manner in which the Astromasts are stowed, the canisters must be able to rotate during deployment. Therefore, the canisters are gimbal-mounted to an arm. Because the canisters are stored inside the box truss ring, they must travel through an arc of approximately 180 deg. Therefore, they are each hinge-mounted to a corner fitting on the box truss ring. It may be noted that in order to rotate the canisters through the 180 deg arc a drive motor will be required. The Astromasts attach to the feed. As the feed's position from stowage through deployment changes relative to the Astromast, a hinge fitting is required. The gimbal-mounted Astromast canisters offset the spiraling action of the deploying Astromast so that the Astromast remains stationary to the feed. These hinges and gimbals do not have to be locked since Astromast position is stabilized by guy lines.
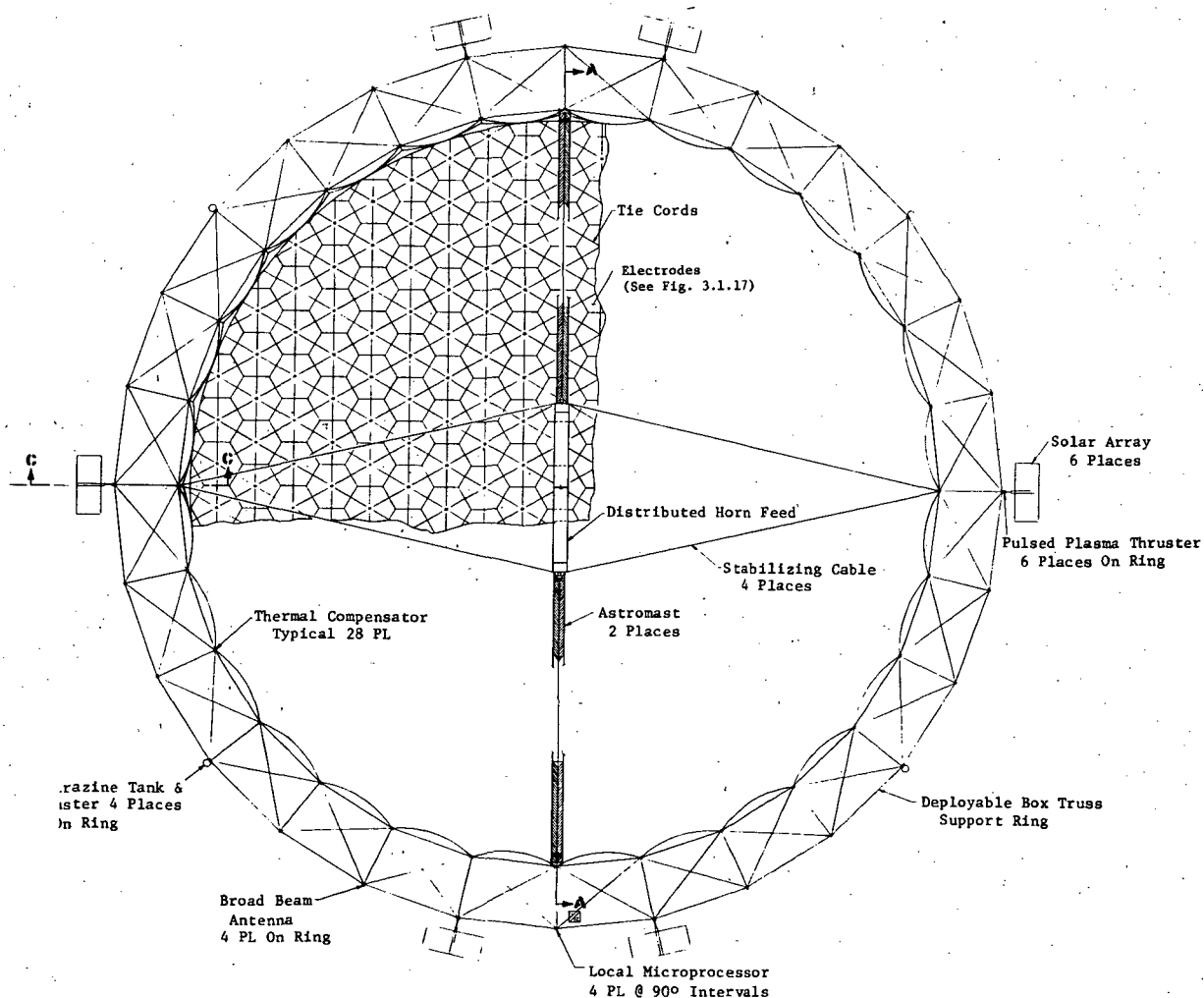
Figure 3.1.5. - Box truss ring (plan view).

A single box truss cube is stowed as follows. All four cube corner
fittings are butted against each other. Stowed between each folded surface
tube and a vertical tube is one of the telescoped diagonal tapes. The four
crossover fittings capture the eight exposed surface tube hinges and hold them
in place. The top and bottom diagonal tapes are rolled onto spools that in
turn are held in place by the cube corner fittings. The crossover fittings
are pinned to the verticals and the cube corner fittings are all pinned to one
another. See Figure 3.1.7 for clarification. To protect the membrane from
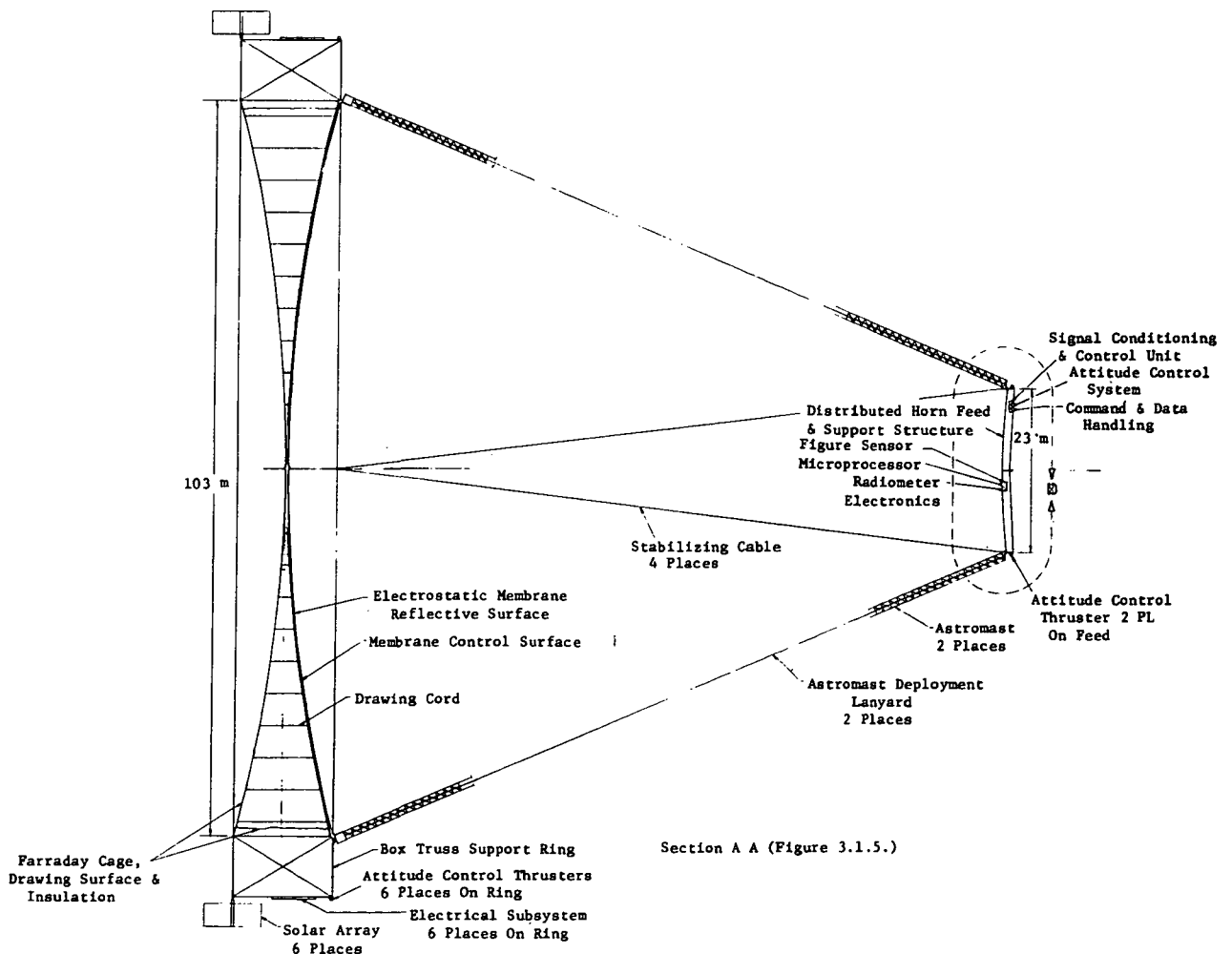
Figure   3.1.6. - Box truss ring (section A-A).

Exterior Diagonal—
Crossover Fitting
and Spool (4)

Cube Corner Fitting (8)

Surface Tube End Fitting (16)

Exterior Diagonal—
Brace Half (16)

Finned
Veritcal
Member (4)

Interior
Diagonal Brace
Half (18)

Surface Tube Half (16)

Midlink Hinge Latch (8)

Interior
Diagonal
Crossover
Fitting (2)
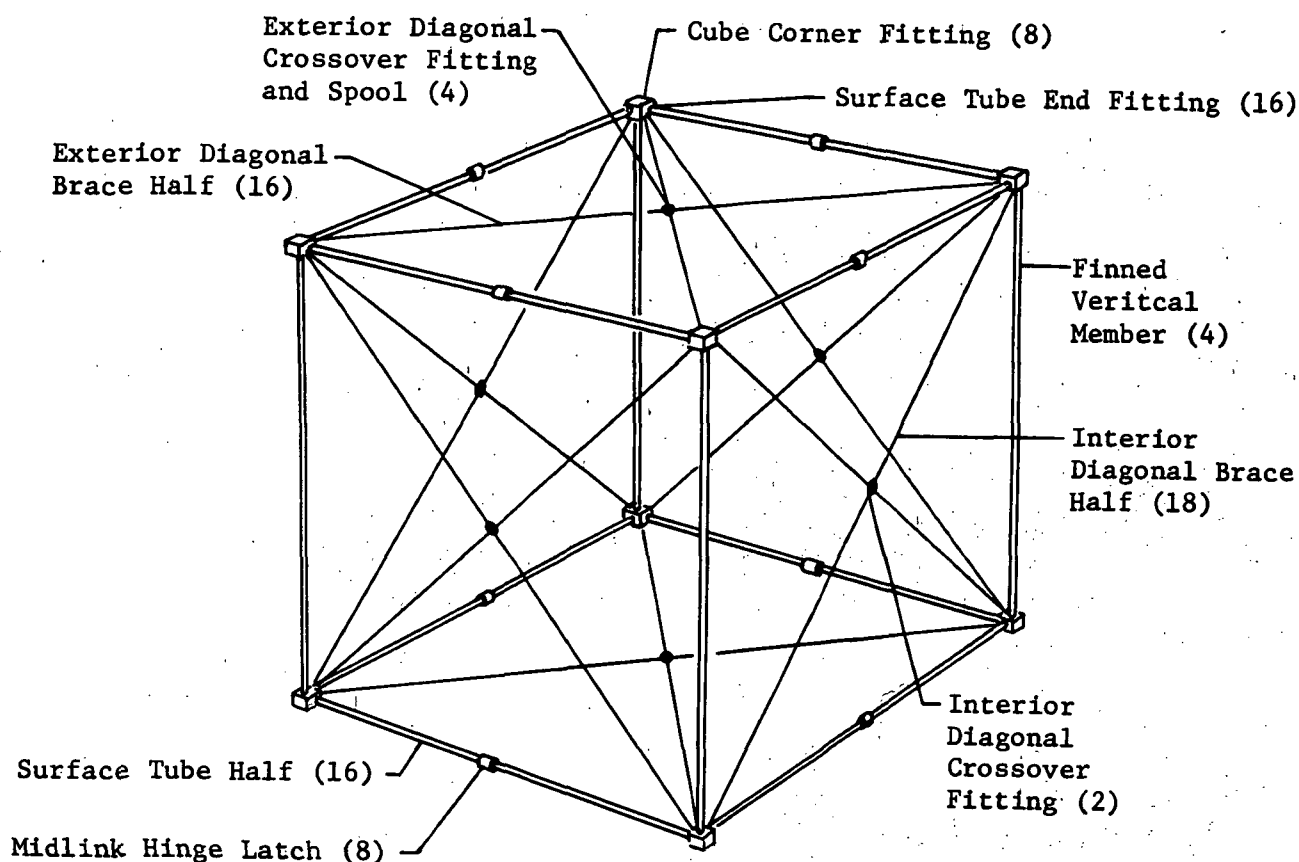
Figure 3.1.7. - Deployable box truss cube components.

the box truss ring all interior verticals have fins that interlock to give a
smooth, flat surface. The feed and Astromast canisters are covered with rf
transparent Mylar[1] to keep the electrostatic membrane free from snagging
(fig. 3.1.9).

The Astromasts, constructed from graphite epoxy, stow to a length that is
approximately 2 percent of their deployed length. The Astromasts use their
own stored strain energy for deployment. A lanyard connected to a motor
positioned at the back end of each canister controls the rate at which each
Astromast will deploy.

---

[1] Mylar: Registered trademark of Dupont Inc.

3.1.1.3 Electrical Generation and Power-Interface Designs

Two types of solar arrays supplying power to two types of battery and electronics modules are located in six different positions around the spacecraft ring structure (figs. 3.1.5 and 3.1.6). Figure 3.1.10 illustrates the solar arrays, and electrical subsystems and emphasizes the repackaging of existing systems.

Figure 3.1.8. — Feed assembly.

Deployment Lanyard

Astromast 1.523 m Diam.

100-m rad

Astromast Thruster

Pulsed Plasma Thruster

Interface Wire Bundle 3 Places

Signal Conditioning & Control Unit
Attitude Control System
Command & Data Handling

Support Structure (Honeycomb)

Latch 2 pl

Hinge

Mast Hinges

Figure Sensor
Microprocessor
Radiometer
Electronics

Support Structure (Honeycomb)

Stowed thrusters

Astromast cannister 2 req'd

Deployment Lanyard

Feed Horns
Type 3 40 Reqd
Type 2 76 Reqd
Type 1 188 Reqd
Pulsed Plasma Thruster
Interface Wire Bundle-3 Places
Astromast 1.523 M. Diam.

Thruster
Astromast

Feed shown as stowed

Detail 13 (Fig. 3.1.6.)
Feed Assy

Figure 3.1.8. — Feed assembly.

The Type I solar array is a modified roll-up (Frusa, type) with 19.5 m^2 of generating panel area supplying power to a modified Type I (Frusa type) battery pack with three 50-Ah Ni-Cad batteries. Four such systems are used to supply power to two quadrants of the spacecraft body and all subsystems located on the feed. These four systems will only see solar blockage during Earth eclipse.
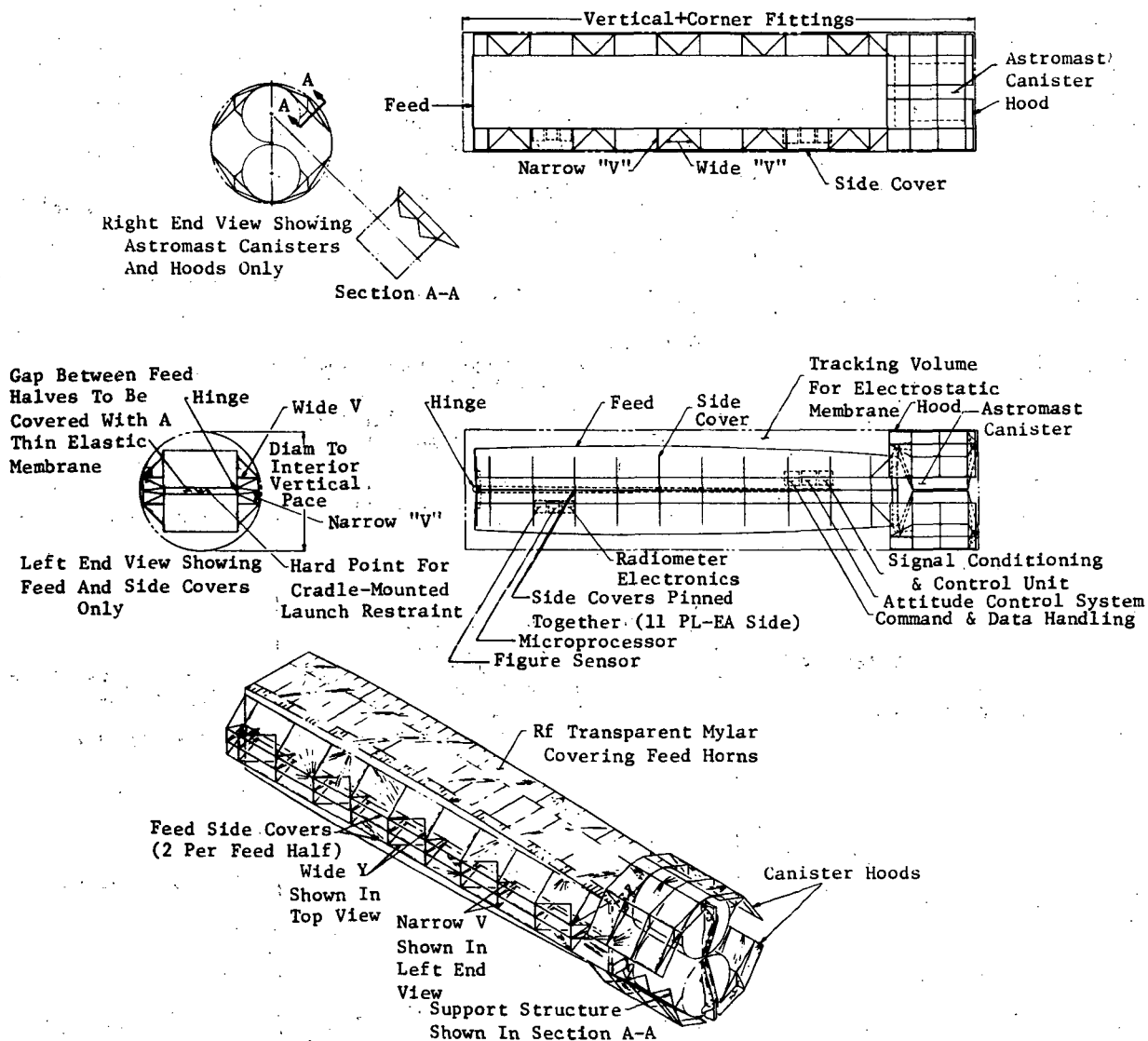
Figure 3.1.9. - Shielded feed and Astromast canisters.

The Type II solar array is the same as Type I except it is 31 percent larger (25.6 m^2) and supplies power to a modified (Frusa type) Type II battery pack with two 50-Ah Ni-Cad batteries. Two such systems are used to supply the remaining two quadrants of the spacecraft body. These two systems will see solar blockage during Earth eclipse and also by the spacecraft body during other orbital positions.

Surface Tube — 1.50 m

2-Degree Gimbal

Roll Up (Frusa Type)
Solar Array Deployed
Type I: 4 Reqd
64.01 m^2 (2.04 m x 9.75)
Type II: 2 Teqd
84.12 m^2 (2.04 m x 12.80)

Surface Tube

Diagonal Tape

2.04 m

Solar-Array Stowed

Stiffener Plate

.30 m Diam.

Local Microprocessor-4 Reqd
Location:
.24-m Cube
1 Ea. Mounted To Vertical Containing Type II Battery Pack.
.30 m^2
1 Ea. Mounted To Vertical In Between Type I Battery Packs.

14 m

Support Tube

Mounting Plate

Type I
6.10

Battery Pack & Electrical Subsystems (Frusa Type)
Type I: 4 Reqd
Uses 3 50 Ah In-Cad Batteries
Type II: 2 Reqd
Uses 2 5 Ah In-Cad Batteries

Toward Feed

Inboard

Outside Ring Vertical
Support Tube

Stiffener Plate

Battery Pack

Section D-D Full Size

Subsystem Mounting
Plate

Diagonal Tube

Type II
7.32 m

Surface Tube

Surface Tube

Pulsed Plasma Thruster
Microthruster
Fairchild Republic Co.

Surface Tube

View Looking Inboard
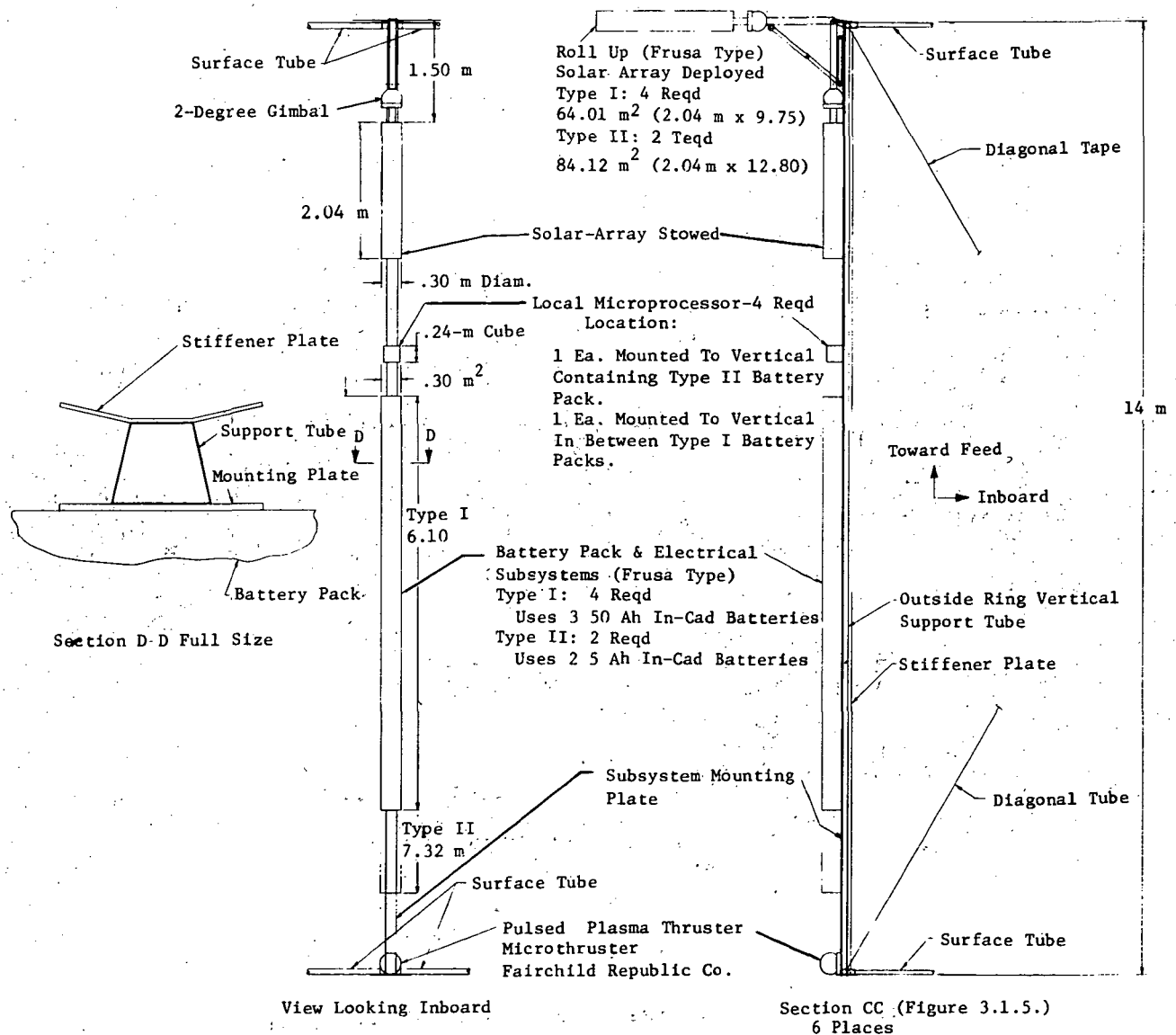
Section CC (Figure 3.1.5.)
6 Places

Figure 3.1.10. – Solar array, electrical subsystems, and pulsed plasma mounting.

Each articulated solar array and its associated battery pack and control electronics is permanently mounted to the same vertical members on the external ring of the spacecraft ring structure. The decision to mount the solar arrays to the rim structure rather than the feed was for the following reasons:

(1) The aperture blockage of 130 m^2 caused by mounting the arrays on the feed cannot be tolerated;

(2) Arrays mounted on the feed would be occulted by the radiometer during certain portions of certain orbits;

(3) Power-consuming subsystems are predominantly on the spacecraft ring structure (about 78 percent);

(4) Large concentrations of mass such as the battery packs should be located as close as possible to the spacecraft center of gravity, which is closer to the ring;

(5) Consideration was also given to spacecraft torqueing due to drag coefficients resulting from solar arrays mounted at the feed.

The solar arrays will require some redesign of the deployment actuators and gimbaling mechanism to accomodate stowage envelope and deployment constraints unique to the ASSA concept. The battery pack and associated electronics package will require extensive repackaging to meet envelope constraints unique to the ASSA concept. Preliminary studies show this to be feasible.

3.1.1.4 Attitude Control Thrusters

Four hydrazine thrusters used for orbit transfer are mounted at 45 deg to the spacecraft x- and y-axis around the back rim of the ring structure (fig. 3.1.11). Refer to paragraph 3.2.2 for thruster physical description and function. This section covers the mechanical integration of the thrusters.

Six pulsed plasma microthrusters used for station keeping and attitude control are mounted to the back rim of the ring structure. Each thruster will be mounted to the same structural member that is used to mount a solar array and its associated electronics and battery pack (fig. 3.1.10). The hydrazine thrusters may also be used to remove any spacecraft tumbling before step 1 of deployment.

Two more pulsed plasma microthrusters used for attitude control are located at the extreme ends of the feed structure. They are rotated and stowed inside the feed structure during launch. Following step 4 of the deployment sequence (paragraph 3.1.1.1), the thrusters are rotated out of the feed structure to their deployed position, and are then used for stabilization during the remainder of the spacecraft deployment sequence.
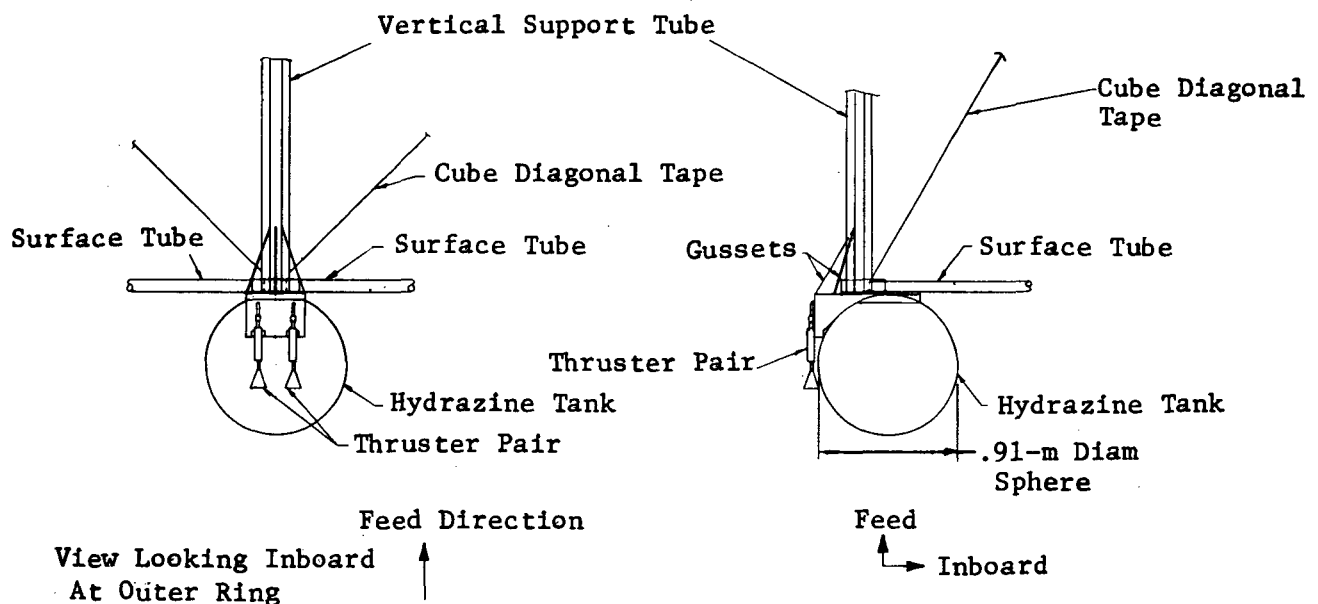
Figure 3.1.11. - Hydrazine thruster configuration and mounting.

Detail B
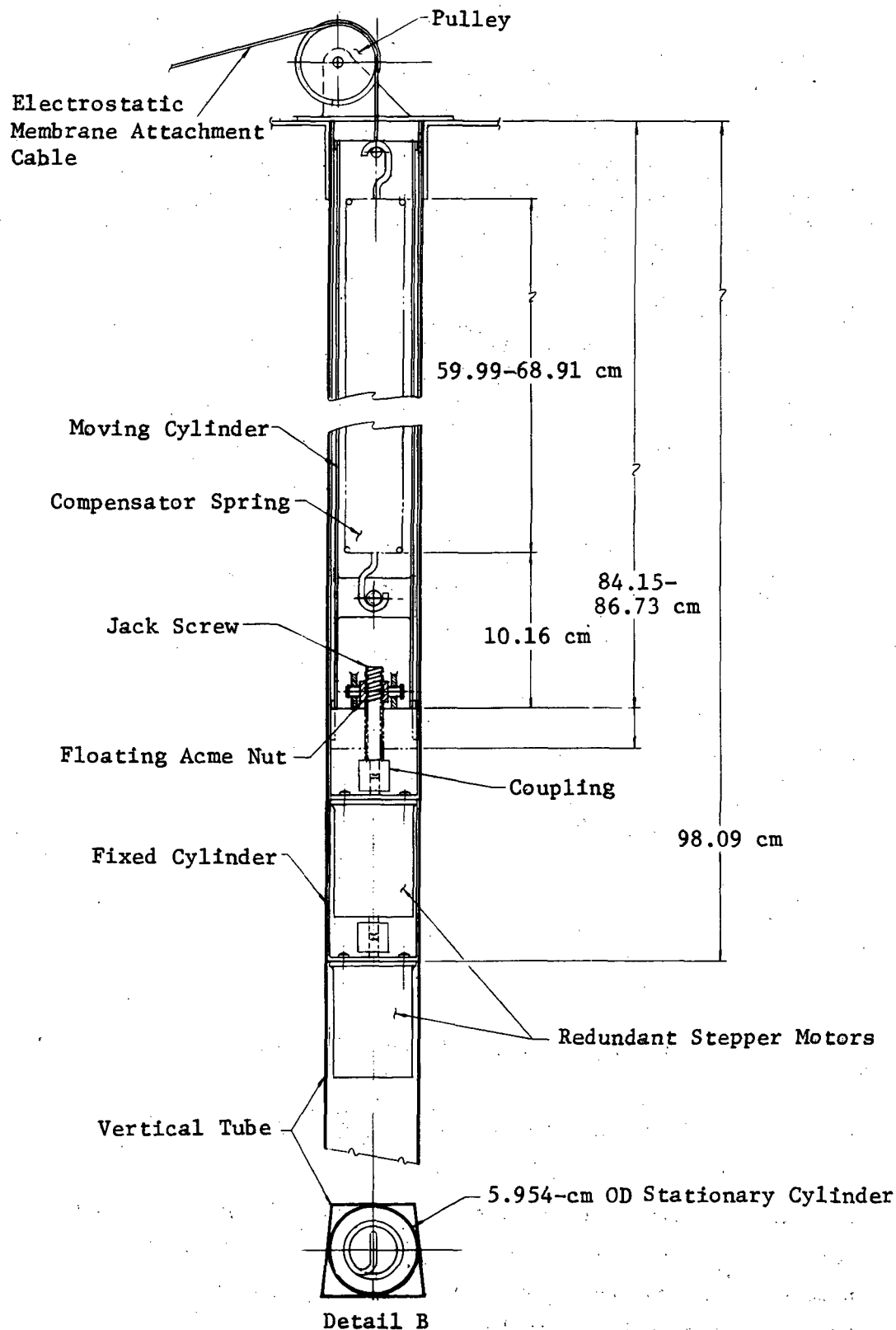
Figure 3.1.12. – Compensator spring and out-of-plane actuator.
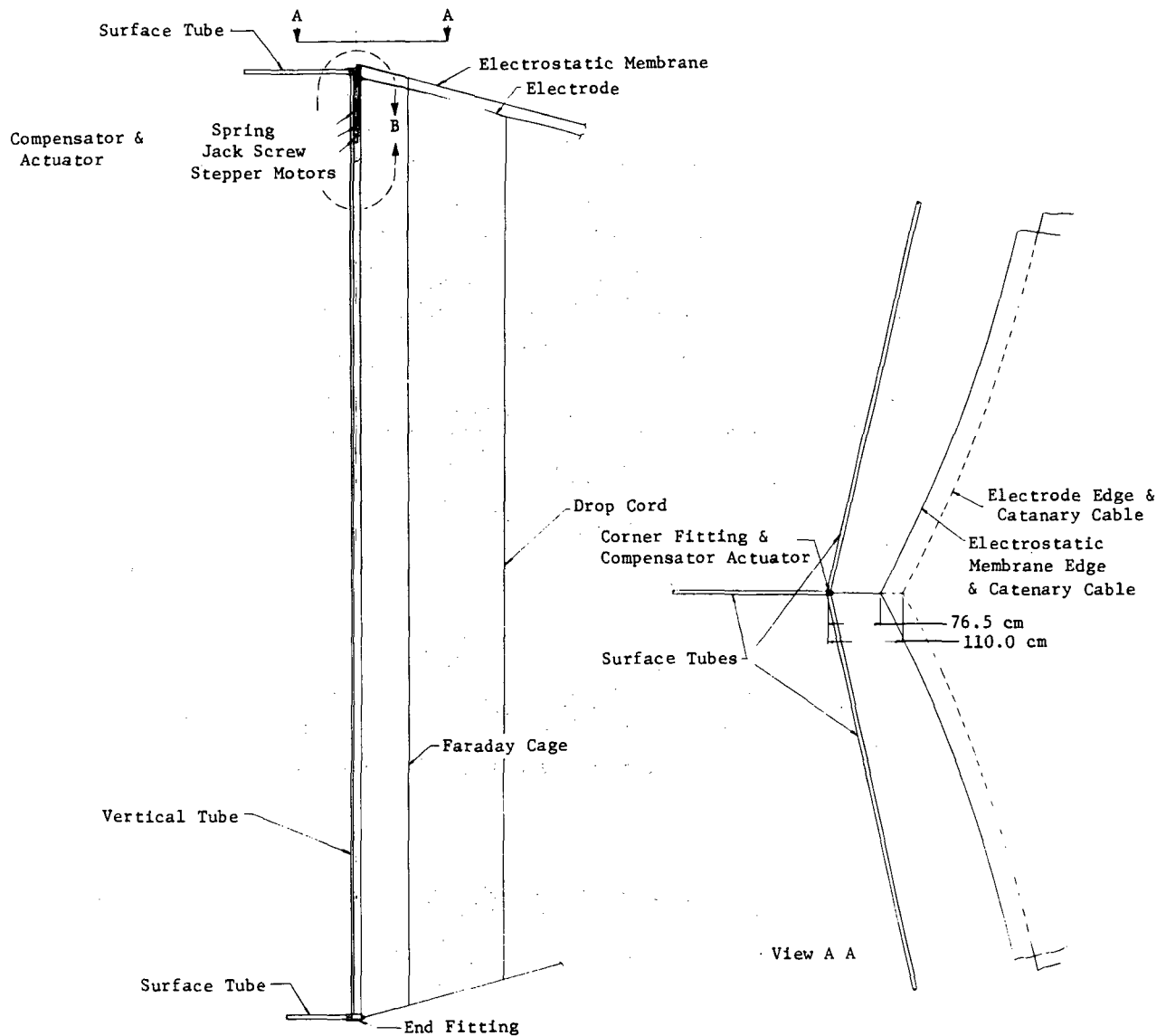
Figure 3.1.13. - Compensator spring and out-of-place actuator.

3.1.1.5 Thermal Interface Designs

Thermal analysis of the temperature excursions in orbit were performed. Membrane reflector temperature changes can be minimized by proper selection of α and ε of the six sides of the three membranes. Temperature changes of only 60 K are possible in the 650-km orbit. A 100 K temperature swing was assumed in determining voltage adjustments necessary to compensate for the thermal strains in the membrane reflector.

The changes in strain under orbital conditions are significant but manage-able. The thermal strain $\varepsilon_T = \alpha \Delta T$ where for $\alpha = 2 \times 10^{-5}/K$ (thermal expansion coefficient) and $\Delta T = 100$ K (temperature change), $\varepsilon_T = 0.002$. The membrane reflector's radius changes by about $\Delta r = r \varepsilon_T = 0.1$ m during each orbit. These strains are approximately 1.3 times larger than the electrostatically developed strain of the baseline. The addition of an innovative perimeter thermal compensation device prevents the development of large stresses from these introduced strains (figs. 3.1.12 and 3.1.13).

A one-degree-of-freedom spring device allows the membrane to expand and contract 5 cm without introducing significant thermally induced stress. Without the compensation, the membrane stresses would triple when the membrane cooled 100 K. A constant force spring would virtually eliminate thermal stresses, but would result in membrane instability. A spring constant, $K = 14$ N/cm was selected as a reasonable thermal compensation. Each compensator experiences a load variation from 294 N to 413 N as the temperature decreases 100 K.

This selection of a spring constant depends on several factors, one of which is the thermal compensation. The spring constant can have a significant effect on the thermal stress, voltages, eigenvalues, and control algorithms. Table 3.1.2 indicates several consequences of different spring constants. Some rationale for choosing $K = 14$ N/cm constant will be seen in Figures 3.1.14 through 3.1.16, which indicate the effects of varying compensation on pressure, field strength, and stress.

TABLE 3.1.2. - EFFECTS OF COMPENSATING SPRINGS.

Case	Spring constant, K, N/m	Force, 300 K N	Force, 200 K N	Motion, r cm	Compensating voltage V, volts
Constant force (Negator)	0	294	294	10.16	0
Soft linear compensation	630	294	353	9.2	14 000
Hard mount		294	1100	0.0	50 000

Figure 3.1.14 indicates the radial distribution of the pressure loading required to maintain the spherical surface with a radius of curvature ρ_f = 200 m. The baseline design at T = 300 K is shown by the thick dashed line. The solid lines denote operation at T = 200 K. Increments of thermal stress imparted to the membrane by varying the spring stiffness are presented for six cases. With a constant force or Negator-type spring, the increment in stress is $\Delta\sigma_r$ = 0 while the hard mount case is $\Delta\sigma_r = \sigma_T$. The pressure adjustments to maintain shape with the Negator spring are quite small. Without thermal compensation, the pressure changes are seen to be large -- central pressure must increase to 3.77 times the baseline value. The pressure converted to electric field strength is shown in Figure 3.1.15. The field strength must double if perimeter compensation is not introduced.

Stress changes in the membrane reflector due to the thermal environment are very important. Figure 3.1.16 summarizes the changes for ΔT = 100 K. The solid lines are the radial stresses and the dotted lines are the azimuthal stresses. For the baseline, the ratio of central stress to yield stress is 0.055 or 4.6×10^6 N/m^2. With no thermal compensation, the stress ratio is 0.19 or a stress of 1.57×10^7 N/m^2.

A Negator spring greatly improves operation in terms of voltages and stress, but has an adverse effect on low-frequency stability. The design process led to the selection of a soft spring, which introduces an incremental 20 percent thermal stress. The maximum stress ratio is 0.085.

The changing stress in the membrane reflector is not measured during operation. The surface is viewed by a figure sensor and the voltage is continually adjusted to keep the shape within specified tolerances. With quasi-static adjustments, shape control is straightforward. Control implementation becomes much more difficult when the deflection modes of the membrane reflector are excited, i.e., when the control periods are the same order as the natural structural periods. The membrane reflector is quite stiff, with a high natural frequency compared to the control periods, eliminating the need for modal control.
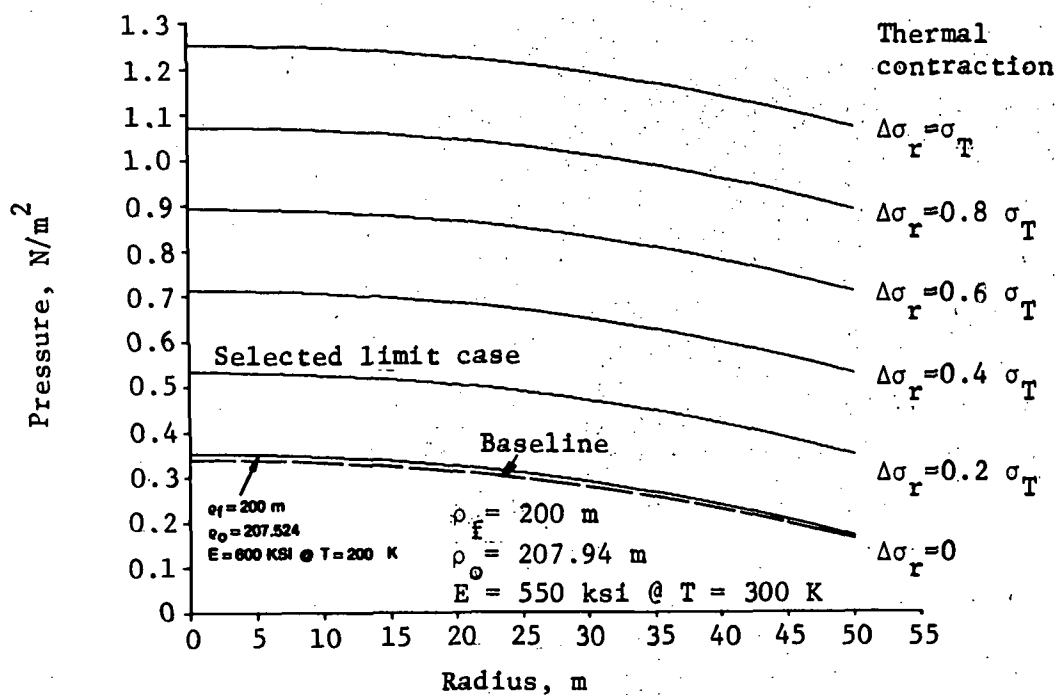
Figure 3.1.14. – Pressure loading required to compensate for thermal stress.
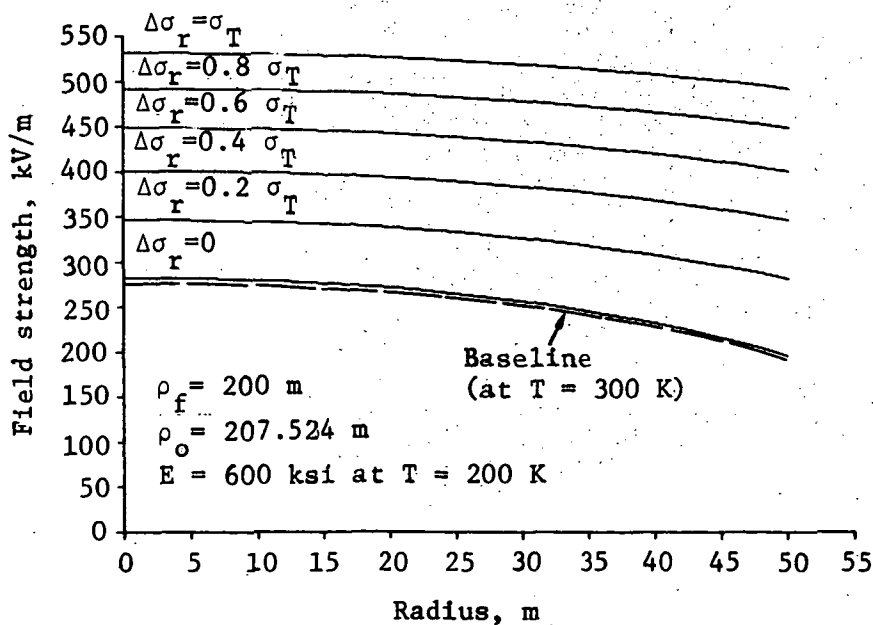
Figure 3.1.15. – Electric field strength required to compensate for thermal stress.

44

3.1.1.6 Shape Control Interface Designs

The shape control system is composed of the rf reflective membrane, the drawing cord network, the electrodes and the Faraday cage.

Located inside the vertical tubes, 28 out-of-plane actuators (fig. 3.1.12) are attached to cords that connect to the rf reflective membrane (fig. 3.1.13) producing a catenary-shaped membrane edge. These actuators control the general shape of the membrane. When deployed, the catenary acts as a shock absorber to protect the membrane. Directly behind the rf reflective membrane lies the front tie cords of the the drawing cord network (fig. 3.1.17). Pretensioned drawing cords connecting the front tie cords to the rear tie cords give the drawing cord network its convex shape. Two sets of catenaries, one at the front and one at the back, protect the drawing cord network. Cords attaching the catenaries to the verticals hold the drawing cord network in position. Positioned directly behind the front tie cords are the electrodes.

Figure 3.1.16. — Stress distribution in the presence of thermal stress.

They are hexagonally shaped and are used to control the shape of the reflector membrane to within ± 0.5 mm of true form. Attaching to the peripheral edge of the membrane and encasing both the electrodes and the drawing cord network is the Faraday cage (figs. 3.1.5 and 3.1.6).

The ECMM baseline relies heavily on prior design programs and test results from the 4.88-m model at NASA Langley. This ECMM baseline i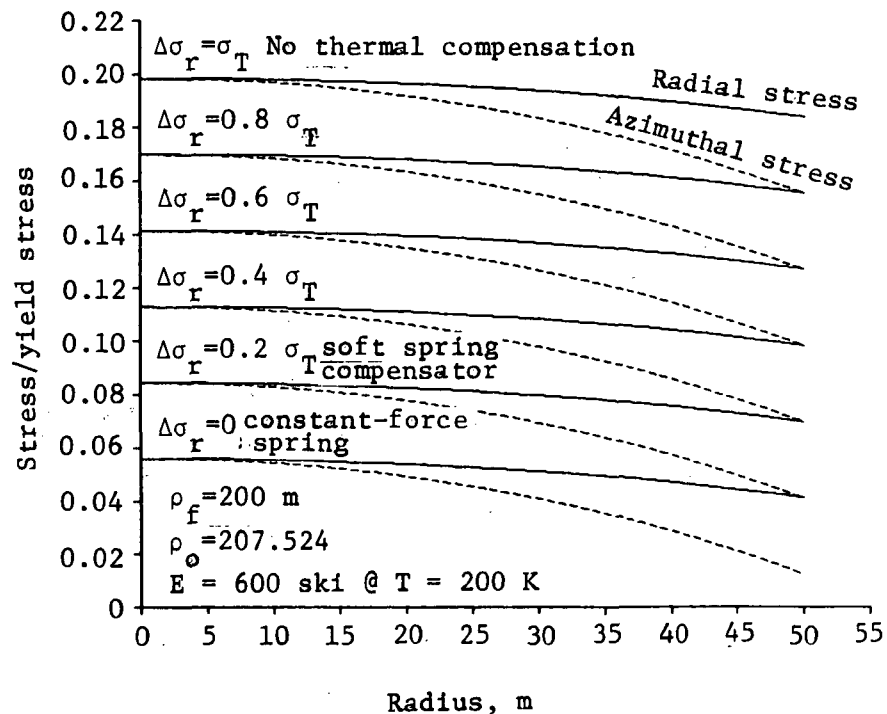s not optimized. It is the latest of a series of design analyses intended to use commercially available membranes. Custom-manufactured membranes appear unnecessary for the surface precision associated with this mission. A high-strength commercial polymer such a Kapton[1] or Mylar is assumed for all three membrane surfaces. The membrane reflector is custom-coated with aluminum on both sides to a thickness of about 500 $\overset{\circ}{A}$. A high level of quality control in the basic material and fabrication techniques is assumed. Similarly, a high level of manufacturing sophistication is required to splice flat panels into a pre-formed spherical dish the size of a football field.

A substantial smoothing of the surface occurs with application of electro-static pressure. The flat panels that comprise the preformed shape become doubly curved. A strain elongation of 0.001 is imparted; therefore, if the surface accuracy is to be 1-mm, the membrane reflector can be fabricated from 1-m wide flat sheets. For higher surface quality, the field strength and strain must be increased, or preformed spherical panels manufactured. Very precise membranes can be obtained by either vacuum deposition or low-pressure polymerization on a master form.

Advantages of Mylar or Kapton are their high melting temperature and low glass transition temperature. Further, both materials have been previously qualified for diverse aerospace applications.

---

[1] Kapton: Registered trademark of E.I. du Pont de Nemours & Co., Inc.

The ECMM will not be subjected to stresses that could tear it during operation. Handling and deployment, however, can introduce substantial stresses. It is contemplated that a heavy catenary tape would border the membrane reflector. Also, a scrim of reinforcing fibers in the membrane reflector surface is planned. A zero-order analysis was performed on scrim properties. The scrim must not have a substantially different thermal expansion coefficient than the basic reflector material, or a "billowing" between the scrim fibers would effectively destroy the membrane, or adequate strains in the membrane will not be possible and smoothness will not improve. Several polymer tapes for a scrim appear promising. This subject area requires further testing and analysis.
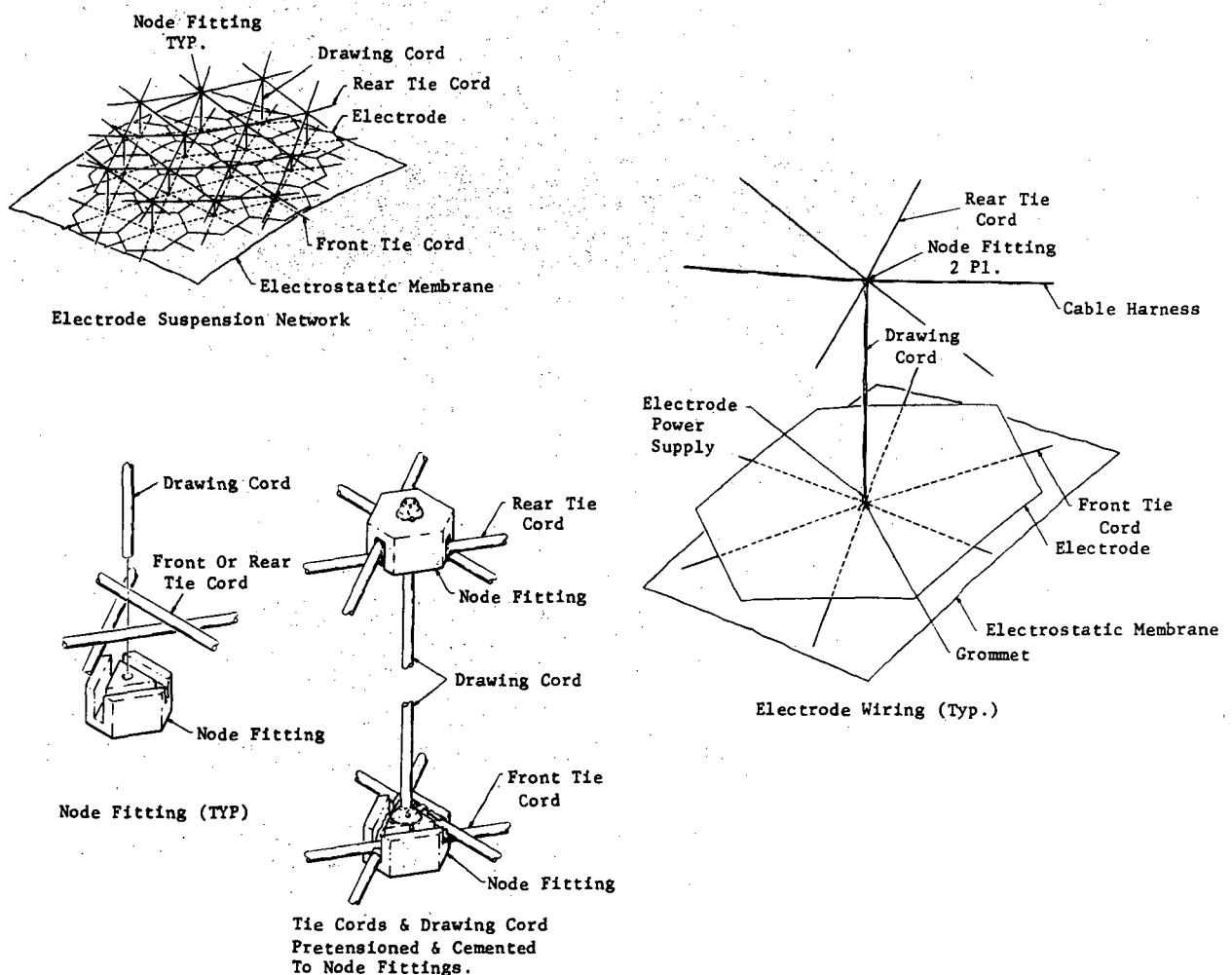
Figure 3.1.17. - Electrode suspension and wiring.

The stress level in the membrane reflector is subject to many considerations. There does not appear to be an optimum stress. We have postulated a stress level of 2 to 5 percent of yield because:

(1) Membrane stiffness produces a lowest mode frequency of the same order as the support structure. The membrane lowest mode frequency is slightly higher than 1.0 Hz.

(2) This stress level provides control over thermal stress. Shape control in the presence of temperature changes is very important in ECMM design.

(3) This stress is similar to that in the NASA 4.88-m testbed. Many surface imperfections and wrinkles are eliminated when this stress is applied.

(4) This stress level does not load the compression rim or continuous truss structure enough to govern the design of the structure. Minimum gauge and handling loads dominate the design. (Such a load does, however, cause design problems in the radial rib structure.)

The design philosophy is to impart a high degree of position stability to the membrane reflector. Static and dynamic stability are achieved without a control system. Although it is feasible to operate the ECMM in an unstable mode (i.e., with a small gap between reflector and electrode membranes), we see only a minor advantage and major disadvantages. High stability is obtained with a sizable gap between the membrane reflector and the electrodes. The surface tolerance on the electrode structure relaxes as the gap is enlarged. High-spatial-frequency electrode errors can be quite large without significant effect on the membrane reflector. The gap may vary by 50 percent about its mean value. The membrane reflector acts as a mechanical smoothing mechanism. With a small gap (and unstable membrane) the tolerances on the electrode structure must decrease to the point that the electrode surface would also have to be a quality reflector.

The membrane reflector's shape is maintained by independent control of the electrode voltage. The high-voltage supplies are regulated by an onboard processor. A surface-monitoring sensor measures the location of discrete points on the membrane reflector from a reference. This figure sensor is an important item for the ECMM. There must be at least one sensed point for each control electrode. Obviously, the desired reflector rms smoothness dictates the sensor's position accuracy. Its update rate is determined by the mission requirements. A single high-rate sensor could scan multiple points. Off-the-shelf sensors that meet the mission requirements are not available today. However, there are several commercial absolute-ranging devices that could, with small improvements, meet the mission goals. Special laboratory bread-board interferometers could provide significant capability.

The number of electrodes and their position accuracy are dictated by thermal shape-control requirements. The pressure distribution and voltage will be a function of temperature changes in the membrane reflector surface. Obviously, a finite number of control electrodes cannot provide an exact pressure adjustment. Each electrode, however, produces a shape that is very smooth and has a long-scale length. Because of the wide influence of a single electrode, surprisingly few electrodes are required for shape control. To maintain a surface quality of 1 cm, approximately 40 electrodes are required. For a 1-mm quality, 220 electrodes are required. These numbers are first-order estimates, considering only corrections for the simplest error sources. Substantial voltage changes are required for shape adjustments. Hence, a separate voltage supply is prescribed for each control electrode. Each voltage supply is very small and light (about 0.25 kg) because very little power is required.

The average surface density of the ECMM is about 0.10 kg/m^2, including the weight of the three membranes, drop cords, and scrim reinforcement. This density does not include the support structure and power supplies.

Note that the three membranes cannot be open mesh surfaces. With access holes, the space plasma would cause an ion migration to the control electrodes, producing a power drain. Both the membrane reflector and the Faraday membrane enclose the "hot" electrode surface. Fortunately, the enclosure is not required to be airtight, although it is desirable to minimize the

openings. A distributed opening of 1.0 m^2 is quite acceptable. Power requirements would be 10 to 40 watts in the presence of densities of 10^4 to 10^5 particles/cm^3.

ECMM Design Parameters. - The important design parameters that characterize the ECMM are summarized, with a short discussion for each parameter of specifications including the principal design constraints, tradeoffs in the selection process, and alternatives.

Membrane Reflector

Focal Length
to diameter: $f_n = 1.0$

The geometrical focal-length-to-diameter ratio is the same for all configurations. The aperture geometrical diameter is 100 m. The effective rf diameter is about 50 m, or $f_n = 2.0$. The reflector surface was prescribed to be spherical. The depth at the center is 6.25 m. With a slight adjustment in electrode voltage, the surface can be made parabolic.

Curvature: The formed spherical surface has a radius of curvature $\rho_f = 200$ m. However, the membrane is preformed with a larger radius of curvature. Preliminary design trades led to a preformed radius of curvature $\rho_o = 208$ m. This prestressed radius will subject the membrane to acceptable stress levels when the membrane is pulled down electrostatically to produce a final 200-m radius of curvature.

Stability: A high degree of static and dynamic stability is required. Static stability requires the membrane reflector to convergently return to its equilibrium position after being deflected from equilibrium. In an unstable design, a high-rate control system would have to prevent divergence in position as the membrane reflector is drawn toward the control surface. A high degree of static stability was prescribed for the NASA 4.88-m testbed model and validated.

50

Membrane

deflection: ΔZ = 25 cm

The central membrane deflection ΔZ is associated with the change in surface radius of curvature from ρ_0 = 208 m to ρ_f = 200 m.

Polymer

material: Three high-strength polymers have been actively investigated: Kapton, Mylar, and Parylene[1]. All three have a specific gravity between 1.3 and 1.4. They have been recommended in preference to other membranes because of:

(1) Commercial availability;

(2) Substantial use and fabrication knowledge in the aerospace industry;

(3) Prior space certification for thermal insulation;

(4) Elimination of meteoroid tear propagation;

(5) Reasonable recoverable elastic strain allowing substantial deflections and forming of the doubly curved surface with reasonable electrostatic pressure of about 1.0 N/m^2.

Secondary material candidates are Nylon[2] and Stratofilm[3]. They would be excellent space candidates if it were not for their poor thermal properties. These two materials are much less stiff than the high-strength polymers previously cited, so that the forming pressure and voltage could be much lower. Tests using Nylon and Stratofilm membranes can be performed at a much lower voltage than using the space-rated polymers, an advantage in atmospheric testing where high-voltage breakdown is a problem.

---

[1] Parylene: registered trademark of Union Carbide.

[2] Nylon: registered trademark of Dupont.

[3] Stratofilm: registered trademark of Winzen Intl.

Membrane

thickness: h = 7.6 to 12.5 m

This is the practical minimum thickness of polymer that can be "easily" handled. Minimal thickness is desired to minimize the pressure and voltage needed to formed the surface. A thin aluminum coating is applied to both sides of the polymer membrane. A two-layer conductor eliminates differential spacecraft charging and acts as a thermal control surface. Coating the inner side of the membrane reflector also neutralizes stray charge buildup and prevents the membrane from clinging to itself during deployment. Nominally, 500 $\overset{\circ}{A}$ of aluminum is applied to each side, yielding a surface resistivity of about 0.56 Ω/m^2.

Rip-Stop

strength-

eners: Developers of large upper-atmosphere balloons have indicated that safe deployment techniques for large polymer surfaces are known. Rip-free deployment even from highly compressed packages can be performed with a continuous film without rip-stop strengthening. The more conservative approach would be to use some type of rip-stop. Analyses have been performed on various rip-stop strengtheners. Problems develop if the thermal expansion coefficient of the rip-stop material is not the same as that of the membrane reflector. General Research's recommendation* is to fabricate the rip-stop from the same material as the membrane reflector, but 10 to 30 times thicker. The rip-stop is spaced at least 1 to 2 m apart. The preferred layup is an isotension pattern made of overlapping elements at angles of 0, 60, and 90 degrees.

---

*Subject of a patent disclosure.

Modulus: $E = 4.1 \times 10^9$ N/m^2

This value of Young's modulus of elasticity is for Kapton with both sides aluminized. The preference is for a low modulus coupled with a large elastic strain. Kapton has a modulus of an order of magnitude less than metals but an order of magnitude more than the weak polymer films. Values at two temperatures, both with and without aluminumizing, are as follows:

	Basic material	Two sides aluminized
T = 200 K	3.3×10^9 N/m^2	3.8×10^9 N/m^2
T = 300 K	2.96×10^9 N/m^2	4.14×10^9 N/m^2

Poisson's ratio: $\gamma = 0.3$

Poisson's ratio affects the radial voltage distribution. It also influences the ratio of azimuthal to radial stress σ_θ / σ_r in the membrane reflector. The value is estimated, as little quantitative data have been found.

Yield stress: $\sigma_y = 8.3 \times 10^7$ N/m^2

The stress level for a strain of 0.02 (2 percent offset) is estimated for a temperature of 200 K. At 300 K the strength is reduce to about 6.89×10^7 N/m^2.

Central stress: $\sigma_c = .058 \, \sigma_y$

This stress occurs in the center of the 100-m aperture. This stress, $\sigma_c = 4.8 \times 10^6$ N/m^2 results from a membrane deflection of 25 cm.

This stress level provides significant smoothing of the membrane reflector. Material imperfections and manufacturing flaws, particularly about the seams, are substantially diminished. A nominal surface accuracy exceeding 1-mm rms is projected.

Rim Stress:

$$\sigma_r \text{ (Rim)} = .043 \, \sigma_y$$

$$\sigma_\theta \text{ (Rim)} = .013 \, \sigma_y$$

The membrane stress decreases from the center to the rim. The ratio σ_θ / σ_r equals Poisson's ratio at the rim. The membrane stress is dictated by the initial untensioned shape and the final formed shape. The final reflector surface is spherical with radius of curvature $\rho_f = 200$ m. The initial shape is also specified as a sphere for simplicity in manufacturing. Stress requirements led to the specification of the initial radius of $\rho = 208$ m.

Fabrication: The preformed spherical surface must be fabricated from many panels. Commercial polymers are generally available in rolls with a maximum width of 1.32 m. Using flat panels of this width, a doubly curved surface with a smoothness of 1.0-mm rms is projected. Better smoothness could be achieved by the following:

(1) Higher stress;

(2) Narrower panels;

(3) Preforming the panels to spherical segments.

Linear expansion:

$$\alpha = 2. \times 10^{-5} \qquad \text{Kapton}$$

$$\alpha = 1.7 \times 10^{-5} \quad \text{m/m/K} \quad \text{Mylar}$$

$$\alpha = 3.5 \times 10^{-5} \qquad \text{Parylene}$$

The coefficient of linear expansion for these polymer films is the same order of magnitude as aluminum. Significant radial expansions or contractions develop with a 100 K temperature change. A perimeter thermal compensation technique has been developed to prevent excessive thermal stress when the temperature changes.

Thermal

constants: $\alpha_T = 0.12$, $\varepsilon_1 = .004$

Solar absorptivity and emissivity of the aluminized membrane reflector.

Griffith

crack length: $L_G > 1.0$ m

A long "razor" slit in a tensioned membrane may self-propagate into a longer slit if a crack length L_G is exceeded. The important parameters are the stress, crack length, and membrane material. The polymers are less critical than metal films in propagation of tears. At the nominal stress levels, the membrane will not propagate tears due to meteoroid damage.

Frequency: $f = 1.43$ Hz

The lowest-mode frequency of the membrane reflector is approximately 1.43 Hz, assuming the 100-m surface to be rigidly attached to the rim. Thermal compensation actuators at the end of the catenaries were not modeled. The membrane stiffness is quite high. This frequency is satisfactorily high for an aperture this large. All the stiffness is derived from internal membrane tension. The eigenvalues are proportional to the square root of stress. This frequency is associated with the nominal stresses and an operating temperature of 300 K. At lower temperature (and depending on the type of thermal compensator), the stress and eigenvalues will be larger.

Electrodes and Electrode Suspension Surface

Number of

Electrodes: First-order calculations indicate that 220 electrically isolated control panels are needed for a surface quality of 1.0-mm rms, and that 40 are needed for 1.0-cm rms. It is envisioned that each electrode is hexagonal or wedge-shaped. The electrodes would be formed by a very thin aluminized layer on the

suspension surface, on the side facing the membrane reflector. The separation between electrodes would be 8 to 15 cm. To eliminate long heavy high-voltage wires, a power supply is located on the back of each electrode. Only low-voltage, dc wiring is routed to the reflector perimeter.

Power:

P < 10 watts, 40 watts end of life

The power requirement is determined by the control rate of voltage adjustment. Secondary considerations are leakage current between the control electrodes and ion transport between the membrane reflector and electrodes caused by high-energy particles from Sun storms. Maximum current flow for charge replenishment is about 10 μA, and maximum current flow for the maximum rate of voltage change is about 100 μA (for each electrode). This low-current flow allows the use of very thin wire for the low-voltage dc supply and the high-voltage grounding wire. Based upon CRT technology, an all-solid-state high voltage supply would weigh less than 0.25 kg.

Nominal field
strength:

F_E = 280 kV/m

The field strength determines the pressure on the membrane reflector. It is also the variable that defines breakdown in a vacuum or in air. The nominal field strength is 280 kV/m as compared to 600 kV/m for the 4.88-m ground test article at NASA Langley Research Center. The nominal operating voltage, V, is 58 kV. A voltage as low as 26 kV was considered, but rejected because it would require the electrode surface to be held to an unacceptably high surface accuracy.

Control
voltage:

V = ±30 kV

Disturbances to the membrane reflector require voltage adjustments of ±30 kV to reposition the surface. The largest error sources are the thermal environment and static misalignment of the electrode surface and the rim. The perimeter loads are

influenced by the thermal compensators attached to the caten-
aries. With the nominal compensators, a 100 K drop in tempera-
ture results in a 20 percent increase in tension and a 14 kV
adjustment. Additional voltage control is used to provide
static (servo) adjustments. Voltage adjustments will compensate
for inaccuracy of the electrode surface and the rim.

Membrane
electrode
separation: $G = 20$ cm

The peak-to-peak waviness of the electrode surface relative to
the membrane surface, δ_e, can be ± 8 cm. This irregularity
translates into a much smaller waviness of the membrane reflec-
tor, attenuating electrode errors. The attenuation depends on
the period of the δ_e disturbances. As the spatial frequency
increases, the transmitted errors decrease. Limiting the mem-
brane reflector error to 1.0 mm dictates a spatial electrode
period of 4.5 m or less.

Electrode
surface
drop cords: Drop cords are used to form the curved electrode surface. The
maximum separation is 4.5 m. The electrode surface and drop
cords form a tension structure. The drop cords and the rip-stop
scrim reinforcement in the electrode surface must have a small
thermal expansion coefficient. Quartz appears to be a likely
candidate.

Electrode
membrane: Kapton or Mylar appears to be a preferred choice for the elec-
trode surface. They both have a high bulk resistivity. Quartz
tapes would be integrated into the surface to form a thermally
stable network for the electrode surface. Loads are transmitted
through the quartz tapes to the electrode surface. The thickness
of the electrode surface is not significant. From weight con-
siderations a 0.012 to 0.025 mm thickness is recommended.

Capacitance: C = 0.3 μF

The total capacitance of the 100-m reflector is only about
0.3 μF, despite the large surface area. The nominal energy
storage for this capacitor is only 533 J as compared to a
typical automotive battery of 10^5 J.

3.1.1.7 Cradle and Erection Systems

For ground handling, ground transportation, STS launch, and delivery to
low-Earth orbit, a combination cradle and deployment canister will be used
(fig. 3.1.18). The stowed spacecraft is installed in the canister at the
manufacturing facility and remains there until it is ejected into its deploy-
ment orbit. The canister is then restowed in the STS payload bay and returned
to Earth for possible reuse.

Four rails guide the folded spacecraft into the canister and act as guide
rails during ejection from the Shuttle cargo bay. The energy required to
eject the spacecraft from the canister is provided by four linear springs, one
at each of the four guide rails. The ejection springs release when the space-
craft is approximately 50 percent withdrawn from the canister. The final 50
percent withdrawal is by spacecraft inertia. Because the spacecraft is still
being guided out of the canister by the internal launch rails during the final
inertial withdrawal, it is expected that spacecraft tumbling will be minimized.

Power and systems checkout signal interface with the STS orbiter is
provided from the forward cargo bay bus.

3.1.1.8 Weight Summary

Table 3.1.3. presents the box truss ring spacecraft mass breakdown.

TABLE 3.1.3. - VEHICLE MASSES.

Subsystem	kg	
Membrane subsystem		
Reflecting membrane	270	
Electrode	270	
Faraday membrane	<u>270</u>	
Total	810	810
Hoop		1032
Thermal compensators (28)		59
Astromasts		51
Electric power & power distribution subsystem		
Type I (2) 50-Ah batteries, electronics (4)	644	
Type II (3) 50-Ah batteries, electronics(2)	<u>531</u>	
Total	1175	1175
Flex rolled up solar array		
Type I (4 units)	191	
Type II (2 units)	<u>125</u>	
Total	316	316
Power cabling		
Primary & redundant		100
Transfer propulsion (hydrazine) (278 km to 650 km)		
Dry weight	40	
Orbit transfer propellant	485	
Orientation propellant	<u>20</u>	
Total	545	545
Attitude control propulsion		
PPT (29.5 kg each x 24)		709
Communication subsystem		
Transponder electronics		56

TABLE 3.1.3. - VEHICLE MASSES (continued).

Subsystem	kg	
Attitude control system		
IRU (2)	18	
Fixed-head star tracker (2)	15	
Remote interface unit (2)	5	
Navigation & guidance computer (2)	10	
Power conditioning	2	
Module structure	25	
Total	75	75
Data management		
OBC	5	
Multiplex data bus (MDB)	60	
Central unit	9	
Module structure	14	
Total	88	88
Antenna feeds		
Electronics (0.229 kg x 188)	43	
Cabling/waveguides	9	
Microwave horns	200	
Structure	500	
Total	752	752
Figure sensing and actuation system		
H.V. Supplies (220 baseline x 0.5 kg)	110	
Figure sensor	5	
Shape control microprocessor	3	
Dedicated shape processors (4 x 5 kg)	9	
Total	127	127
Spacecraft total mass		5895

3.1.2 Hybrid Wrap Radial Rib/Rim

The hybrid wrap radial rib/rim radiometer design meets the mission requirements but integration of subsystems is more difficult than the box truss ring due to the lack of hard points on the structure. The feed support and reflector hub provide the primary hard points for subsystem integration. The basic radial rib design was modified through addition of a rim to support the loads due to the ECMM. The rim also improves the dynamic performance of the structure.
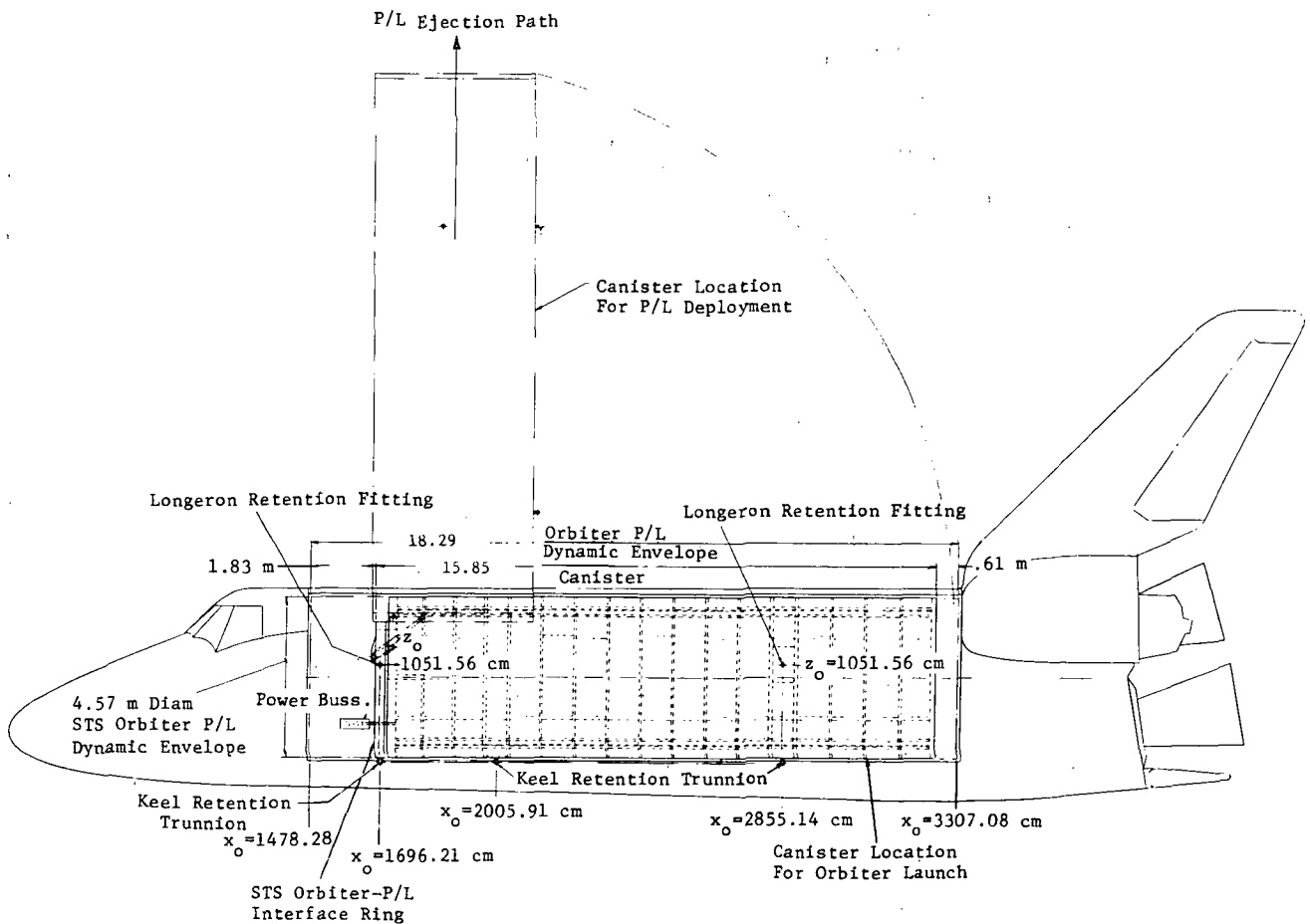
Figure 3.1.18. - Launch cradle.

3.1.2.1 Stowage and Deployment

The stowed configuration is shown in Figure 3.1.19. A distributed horn feed support structure is folded identically to that used for the box truss ring. The two feed mast beams are composed of two Astromasts, each stowed in a canister. Stowage of the wrap radial ribs are very efficient as demonstrated by the small stowage volume.

The hybrid wrap radial rib/rim antenna consists of a hollow, doughnut-shaped hub to which 24 radial ribs, formed to the shape of an arc, are attached. To furl the reflector the ribs are wrapped around the hollow hub with the membrane folded between them.
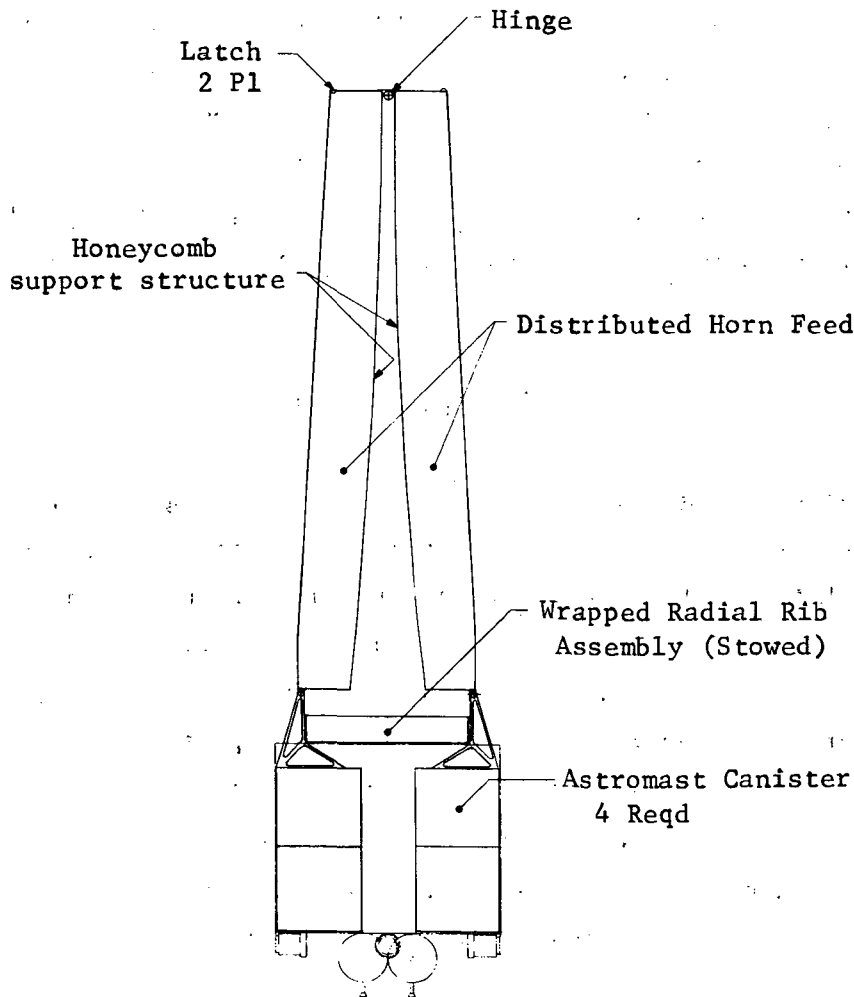
Figure 3.1.19. - Stowed hybrid wrap radial rib.

The hollow, doughnut-shaped support hub has mounting pads to interface the radiometer system with a spacecraft. It provides the support points for each radial rib and stowage area for the radial ribs and the reflective membrane. The hub supports the deployment and refurl mechanism.

The flexible ribs are wrapped around a power-driven rotating spool that constrains the stored energy of the wrapped ribs and deploys the reflector surface at a controlled rate. The stowage mechanism uses a sliding (or rolling) guide to "wipe" the ribs in a rotating manner into their stowed configuration. The stowed configuration is 1/30 of the deployed diameter of the antenna.

Deployment of the spacecraft is initiated by simultaneously unfolding the feed structure while deploying the two horizontal Astromasts. When the feed structure is deployed and latched, the horizontal Astromast deployment is stopped, and two other vertical Astromasts deploy the feed to its full extension. On completion of this step, the horizontal Astromast deployment is completed. Deployment of the 24 ribs and reflector surface is then performed using the power-driven rotating spool for controlling the deployment rates. Miscellaneous subsystems are then deployed to complete the spacecraft deployment.

3.1.2.2 Deployed Design

The deployed spacecraft configuration is shown in Figures 3.1.20 and 3.1.21. The reflector structure is a modified wrap radial rib concept for incorporation of the ECMM and relatively large distributed horn feed system. A rim has been added to the 24-rib configuration to accomodate the larger ECMM loads and also to improve dynamic performance. The rib and rim are a graphite epoxy lenticular (or closed) cross section. A nontapered rib depth of 43.7 cm was selected with the help and guidance of Mr. Art Woods at LMSC. The rib has a width taper of 40.6 cm at the base to a 17.0 cm width at the tip. No depth taper was allowed due to the spacing requirements of the ECMM three-layer surface. The rim is 53.7-cm deep by 17-cm wide. The ribs and rim are a

three-layer graphite epoxy structure producing a lenticular beam wall thickness of 0.04 cm. The layup is 45, 0, and 45 degrees where 45-degree plies are HMF cloth and the 0-degree ply is T50.

The feed mast beams are 1.523-m diameter Astromasts with graphite epoxy longerons. The feed is stabilized by graphite epoxy tension guylines that are attached to the rim. Although the rim is significantly more flexible than the box truss ring, it provides some added stiffness to the nonstraight feed mast. The double feed mast was selected because of the geometry and mass of the feed.

3.1.2.3 Electrical Generation and Power Interface Design

The two solar arrays, their associated battery packs and electrical subsystems are located at the intersection of the Astromast canisters (figs. 3.1.20 and 3.1.21). These two locations are the only structural hard points available that have adequate view of the Sun. The solar arrays are larger than those on the box truss ring because the two arrays must have the equivalent area of the six solar arrays on the box truss ring.

3.1.2.4 Hydrazine Thrusters

Four hydrazine thrusters, tanks, and subsystems are mounted directly behind the central hub of the reflector. The hydrazine thrusters are used for orbital insertion and initial stabilization after reaching operational orbit. The thrusters are in pairs to provide redundancy.

3.1.2.5 Pulsed Plasma Attitude Control

Attitude control is provided by four pulsed plasma thrusters mounted behind the central hub and two thruster triads mounted at the ends of the distributed horn feed structure.
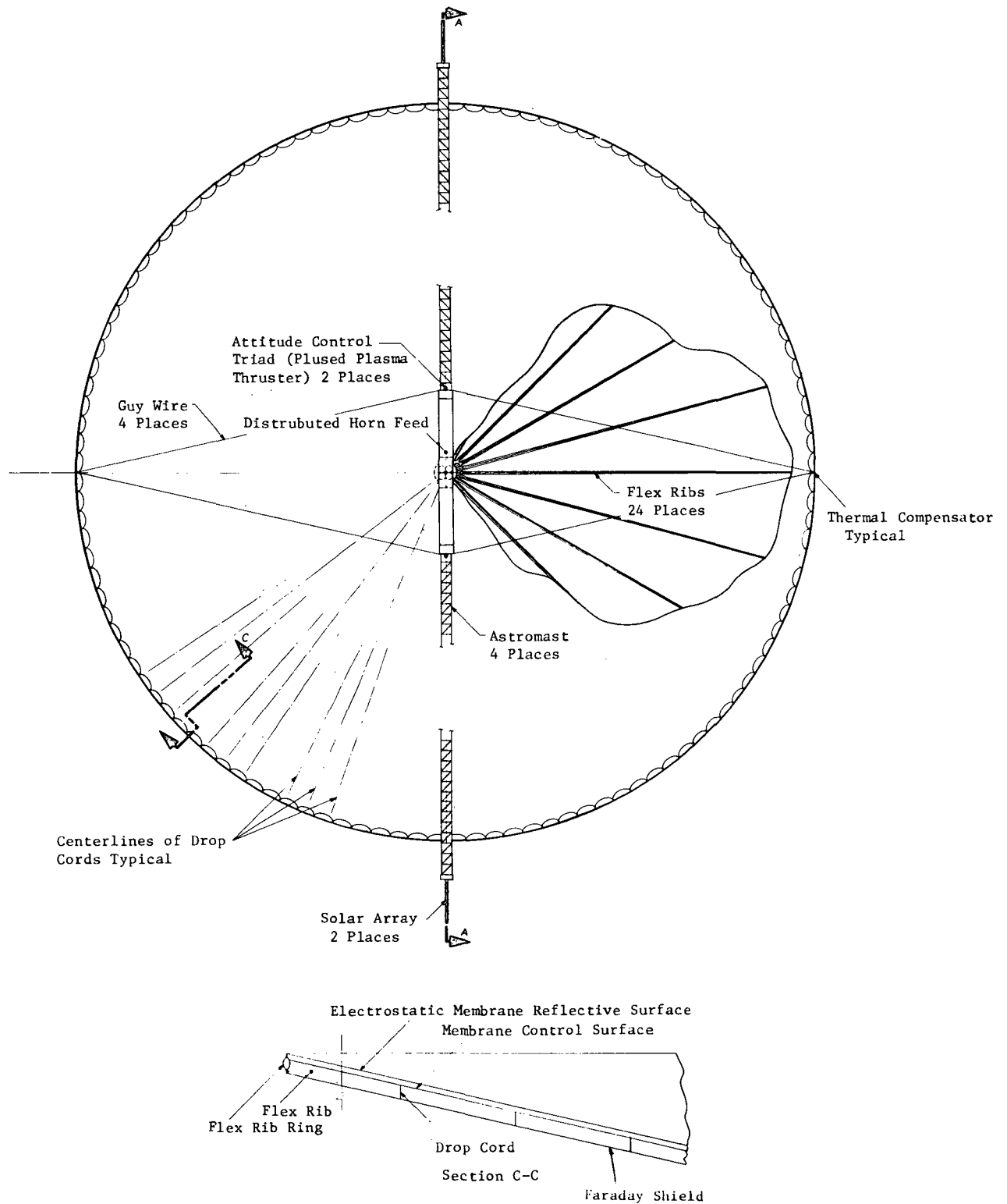
Figure 3.1.20 - Wrap radial rib concept.

3.1.2.6 Thermal Interface Design

The reflective membrane is attached to a thermal compensator, which is attached to the rim around the circumference of the ribs. The thermal compensators are similar to those designed for the box truss ring. The compensators minimize thermally induced membrane stresses with a low spring-constant spring. A linear actuator eliminates the rib deflections produced by membrane loads and rib thermal deflections.
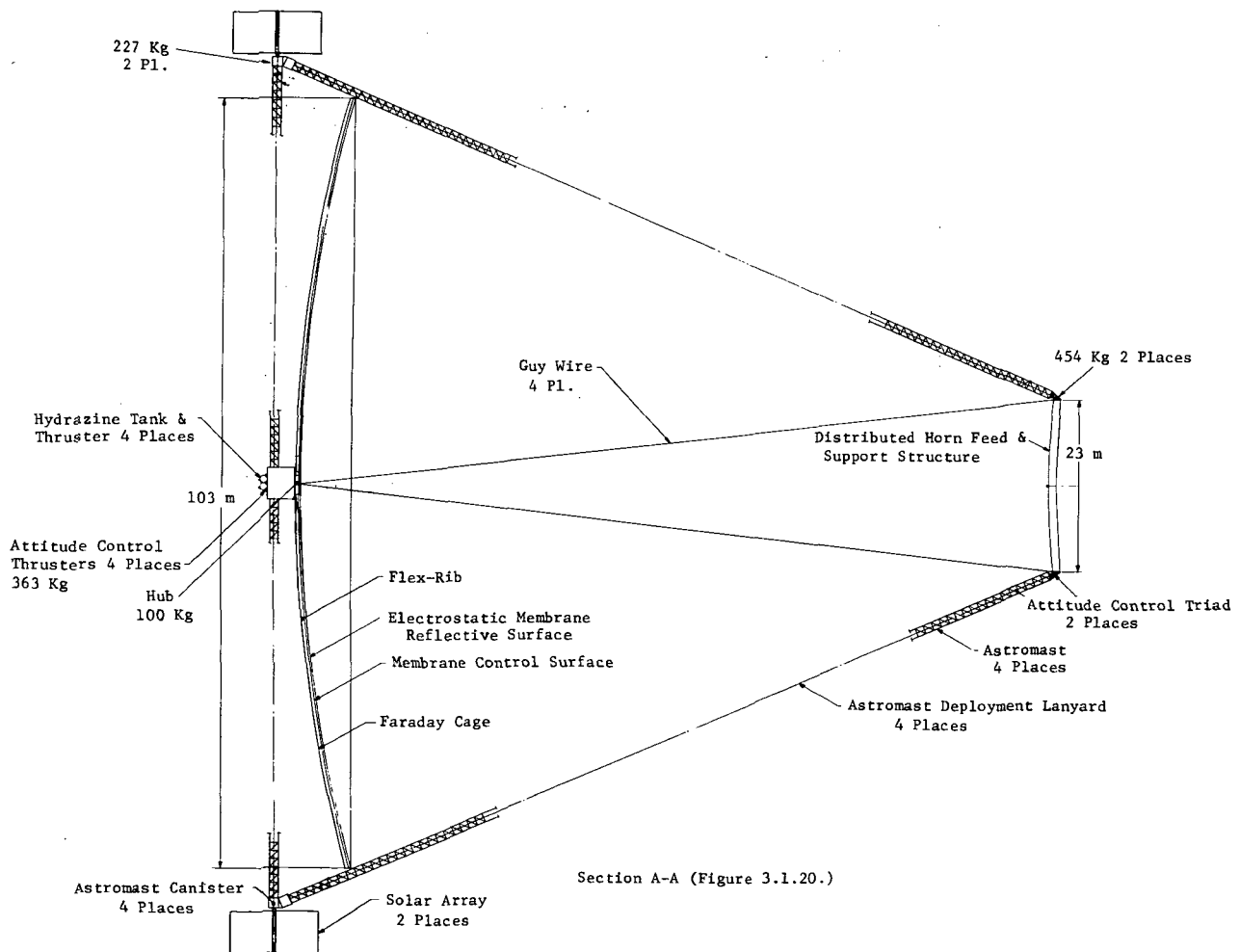
Figure 3.1.21. - Wrap radial rib concept.

3.1.2.7 Weight Summary

Because subsystems on the hybrid wrap radial rib/rim system are similar in nature to the box truss ring, only structural subsystem masses are presented in this section. Other subsystem masses are presented in the weight summary section 3.1.1.8 for the box truss ring.

Radial ribs (24 @ 35.3 Kg)	= 847 kg
Thermal compensators	= 100 kg
Hub	= 165 kg
Rim	= 225 kg
Astromasts and canisters	= 75 kg
Total	=1412 kg*

Estimated Total Spacecraft Mass = 6165 kg
(270 kg greater than box truss ring design)

3.2 SUBSYSTEM DESIGNS

3.2.1 Electric Power and Power Distribution

The electric power subsystem supplies power to all power loads. It consists of the Flexible Rolled Up Solar Array (FRUSA), Sadu (slip rings), Modular Power Subsystem module (MPS), and electric cabling as summarized in Table 3.2.1.

The MPS provides controlling, distributing and monitoring power derived from the solar array. The FRUSA is flight qualified. Power cabling distributes electric power throughout spacecraft and services all power loads.

Figure 3.2.1 illustrates power loss versus wire gage and motivates discussion in section 3.2.1.4.3.

3.2.1.1 Interface Requirements

The mechanical and electrical interface requirements for the electric power subsystem follow.

3.2.1.1.1 <u>Mechanical</u> – The complete mechanical specifications of the Electric Power Module are contained in GSFC S-700-13, Multimission Spacecraft Mechanical System. Mechanical and electrical connections of the FRUSA are made through slip rings. Mechanical interfaces of the power cabling cover bonding to structure, strain relief provisions, and interfacing with joints.

3.2.1.1.2 <u>Electrical</u> – All electrical connections of the MPS are on the inboard panel. Provisions are made for command/telemetry, power cabling, and STS umbilical.

TABLE 3.2.1. - ELECTRIC POWER SUBSYSTEMS SUMMARY.

Components	Mass, kg	Dimensions, m	Power, W
Electric power module (MPS)			
(excluding batteries, electronics)			50
RIU	4.50		
Connector bracket	2.75		
Module/structure connector	5.00		
Module frame	24.00		
Module mounting hardware	11.40		
Thermal louvers	6.00		
SPRU	15.00		
MPS type I (2) 50 A-h battery	160.0		
MPS Type II (3) 50 A-h battery	265.0		
Flexible rolled up solar array			
Type I	48	$23 \ m^2$	
Type II	63	$25 \ m^2$	
Solar array drums	145.00	0.33 x 3.3	--
SADU	125.00	0.33 x 3.3	--
Power Cabling			
Primary	23	400-m length	--
Redundant	32	690-m	--
Total subsystem	1724		300
Total power capability, watts			7200
Total energy storage: 800 A-h			

3.2.1.2 Constraints/Requirements

3.2.1.2.1 Mechanical – Packaging constraints imposed by STS require changes in the basic configuration of the MPS. The proposed 3-year resupply provision requires removable fasteners. Requirements on the FRUSA include packaging contraints imposed by orbiter and expanding existing array configuration for greater power output. Wire sizes smaller than No.-22AWG are discouraged for use in power cabling.

3.2.1.2.2 Electrical – The output voltage will be 125 Vdc ± 5%. The voltage ripple is held to 0.750 mV and capable of handling 1200 W continuous. The MPS must comply with EMI/EMC requirements as per MIL-STD-1541. The unregulated voltage from the FRUSA shall be approximately 150 Vdc. The total impedances of cables and return paths will be such that the potential difference between the source of voltage regulation and load will not exceed 5 V (MIL-W-5088).
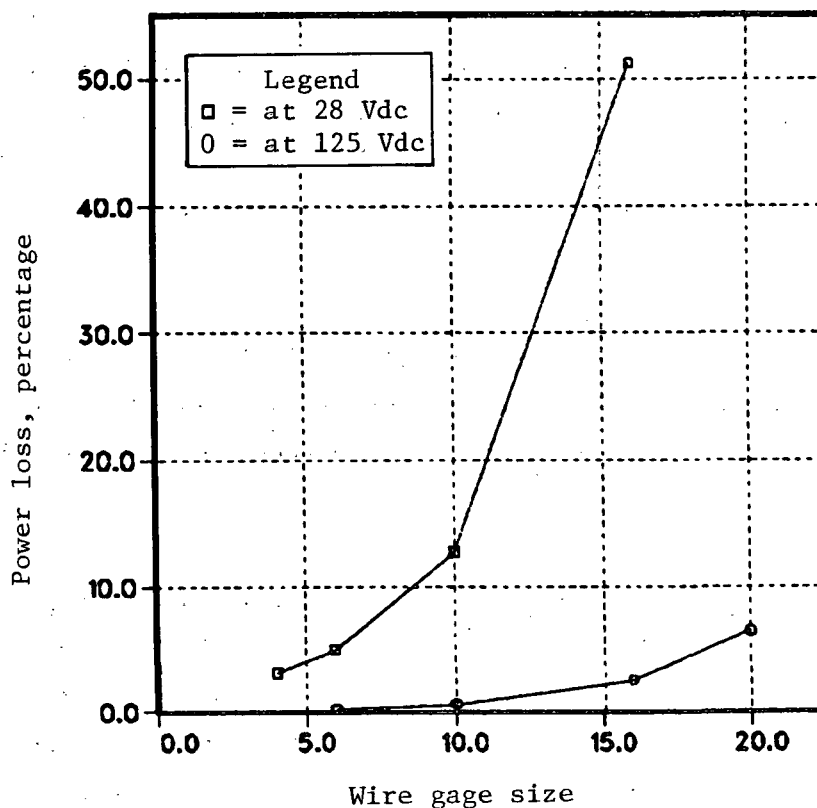
Figure 3.2.1. - Power loss versus gage size for 100-W load.

3.2.1.3 Duty Cycles/Operating Modes

3.2.1.3.1 Electric power module (MPS) - The MPS is used for all mission phases after deployment. During eclipses by the Earth's shadow, energy is stored in batteries. These batteries are sized for 30 percent depth of discharge (DOD) and 16 400 recharging cycles over the 3-year resupply time. In case of total MPS failure, redundancy provisions will require faster DOD cycling and operation closer to the 1200-W maximum of the modules when called on to relieve the additional load.

3.2.1.3.2 Wire and cabling - The primary power distribution network is used for all phases of the 10-year mission. It is also employed in the STS orbiter to power up subsystems and check the engineering status prior to deployment.

3.2.1.4 Design Criteria

3.2.1.4.1 Electric power module (MPS) - The electric power module is designed according to contemplated power loads and redundancy. They are illustrated in Figure 3.2.2. The MPS is designed around the baseline specifications of the Multimission Modular Spacecraft - Modular Power Subsystem (MMS-MPS). In distributing electric power, EMI/EMC must be considered. A total of six modules are distributed around the rim, servicing the four quadrants and power loads on the feed.

The MMS-MPS was selected because standard NASA subassemblies are used in this module. This choice essentially provides an off-the-shelf design, although the power regulator unit (PPU) must be redesigned for the higher operating voltage.

3.2.1.4.2 Flex rolled up solar array - The solar array derives power from sunlight. The packing constraints require a flexible, easily contained, and flight-qualified solar array. The FRUSA concept with expanded surface area will be employed. FRUSA can be modified to accommodate the larger array area and satisfy packing constraints. It was flown on STP 71-2 in October of 1971.

3.2.1.4.3 **Power cabling** - Electric power cabling must conform to the con-
straints specified in Section 2.0. Primary and redundant wiring must be
considered and routed over long distances (100-m).

Power wiring is distributed via twisted pairs. Redundant wiring is
provided so that each quadrant can continue to operate given the total failure
of the primary MPS for that quadrant. Due to the large power requirements,
the single power bus that is required to supply electric loads on the feed
beam is composed of several wire pairs.

Type 1 peak loads (four modules), W

- Propulsion	960
- Data management	120
- ACS	60
- Shape control	100
- Thermal control	15
- Power sink	90
	1,345
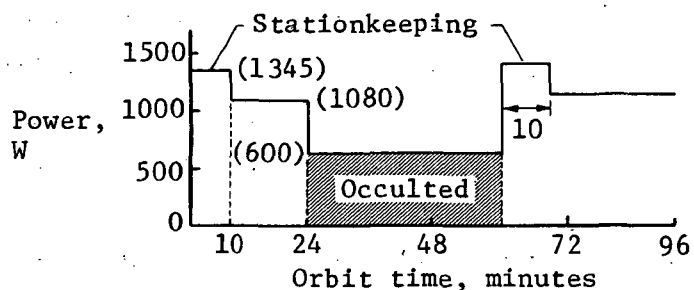
Type 2 peak loads (two modules), W

- Propulsion	340
- Data management	100
- ACS	60
- Shape control	200
- Thermal control	15
- Power sink	90
- Communication or guidance	70
- Feed horns & amplifiers	450
- Harness	30
	1,355
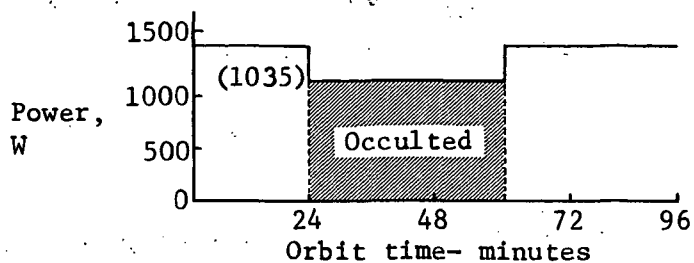
Figure 3.2.2. - Electrical power subsystem requirements.

3.2.2 Transfer Propulsion

The orbit transfer propulsion consists of four hydrazine, blowdown, mono-propellant thrusters. They are throttleable from 3 to 18 N. These thrusters provide the impulse required to transfer from the deployment altitude of 240 km to the operating altitude of 650 km. They are in pairs for redundancy.

The suggested propulsion system consists of four space-qualified MRE-4-A-1 hydrazine thrusters produced by TRW and RCA. These thrusters have an I_{sp} of about 220 to 230 s.

3.2.2.1 Interface Requirements

3.2.2.1.1 <u>Mechanical</u> - The hydrazine thrusters will be hard-mounted on the mechanical surface of the structure. Gimbaling provisions are not required.

3.2.2.1.2 <u>Electrical</u> - Command and telemetry commands are accomplished through the MDB. The control electronics and power processor interface to the MDB through an RIU. Electric power is supplied from a power bus.

3.2.2.2 Constraints/Requirements

3.2.2.2.1 <u>Mechanical</u> - Mounted at four places on rim.

3.2.2.2.2 <u>Electrical</u> - Electrical connections include power and multiplex data bus (MDB).

3.2.2.2.3 <u>Thermal</u> - Hydrazine and catalytic bed temperature maintained by heaters. Hydrazine freezes at $1.5^{\circ}C$.

3.2.2.3 Duty Cycles/Operating Modes

The hydrazine thrusters are used primarily for orbit transfer and perhaps for correcting for altitude. Therefore, they are required to operate between 5 to 10 cycles.

3.2.2.4 Design Criteria

Transfer to desired orbit must not exceed a maximum acceleration of 0.01 g. Relatively simple low cost hydrazine system was selected. A system was required to have good storage capability, flight qualified, throttleable, and reliable.

3.2.3 Attitude Control Subsystem

The attitude control system (ACS) is used to stabilize the spacecraft during orbital transfer, to orient and stabilize the spacecraft relative to nadir, and provide general station keeping as desired.

The major component of the attitude control system is the ACS module (ACM), which is located on the rim. It contains an inertial reference unit (IRU), fixed head star tracker (FHST), interfacing electronics, and computers. Four hydrazine thrusters and 24 pulsed plasma thrusters are arranged around the spacecraft. The hydrazine thrusters are used for attitude control during orbital transfer and nadir orientation. The PPTs are used for attitude control during subsequent orbital operations. Command and telemetry signals are transmitted via the MDB. Figure 3.2.3 shows the relationship of these components.

The IRU will provide a fine resolution, 3 axis, strap-down attitude reference as well as navigational incremental velocities for spacecraft applications. IRU requirements can be met by off-the-shelf units, except possibly the 3-year lifetime requirement that may necessitate an additional level of redundancy or serviceability.

The components of two typical ACS modules are summarized in Table 3.2.2. The star tracker searches, detects, and provides star positions. A description is contained in GSFC-712-9. The attitude control module contains the dual, pilot/copilot navigation and guidance control system. Each separate

74

system consists of navigation and guidance control computer, IRU, star tracker, and secondary sensory input (accelerometers, magnetometers). The ACM also provides an interface with the general purpose, housekeeping processor of the data management subsystem, attitude control thrusters, and transfer propulsion.
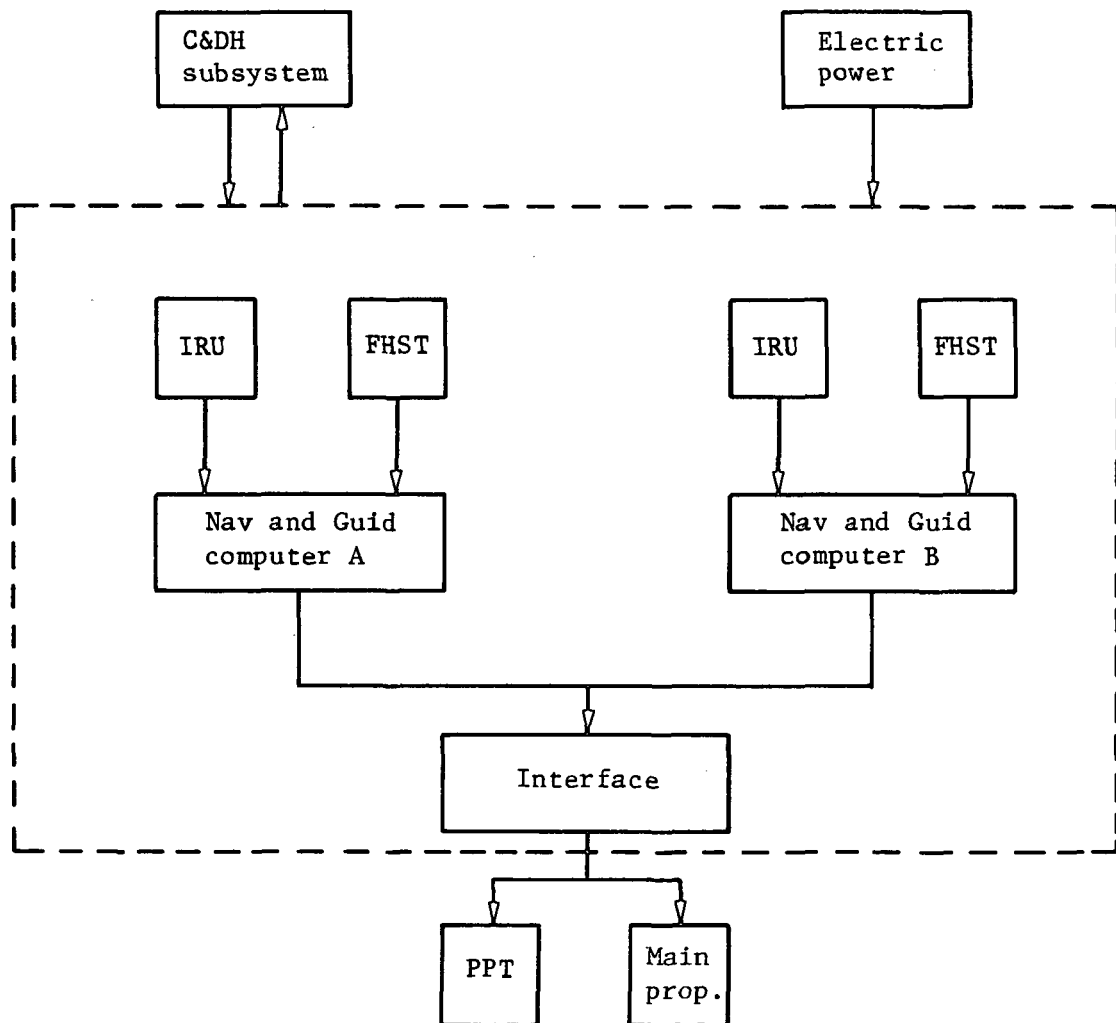
Figure 3.2.3. - ACS block diagram.

TABLE 3.2.2. - ACS SUMMARY.

Components	Mass, kg	Dimensions m	Power, W
Inertia reference unit	9.0	$15 \times 10^{-3} m^3$	
Gyro heater	30.0	-----	
Steady state current	----	-----	35
FHST	7.7	0.2 x 0.2 x 0.3	
Star tracker	----	-----	18
Shutter	----	-----	3
Attitude control module			
IRU (2)	18.0	-----	130
FHST (2)	15.5	-----	40
RIU	4.5	-----	
Nav & guid control comp (2)	10.0	-----	50
Power conditioning	2.5	-----	10
Modular structure	25.0	-----	
Total	75.5	-----	230

3.2.3.1   Interface Requirements

3.2.3.1.1   Mechanical – The IRU will be rigidly attached to the ACM and is an integral part of the module. Actual mechanical requirements for the star trackers are hardware dependent. The attitude control module is hard mounted to structure and limited by structural constraints and deployment considerations.

3.2.3.1.2   Electrical – Electrical interface with the IRU consists of electric power and operating commands. The outputs are incremental velocities, incremental angle pulse rate, clock reference, and engineering telemetry.

The electrical interface of the star tracker consists of electric power, input operating commands, digital data output, and analog data output. These hardwire connections directly couple the star tracker with the interface assembly.

Electrical interfaces between components in the module are not considered. External connections include electric power at 125 Vdc, and command and telemetry via MDB to command and data handling (C&DH) interface unit.

3.2.3.2 Constraints/Requirements Typical

3.2.3.2.1 Mechanical - In order to achieve the required accuracy, the angle between the IRU and star tracker is to be known to 15 arc-sec.

3.2.3.2.2 Electrical - Noise and ripple to the IRU and star tracker should be limited to about 1.5 V peak to peak, 1 Hz to 10 MHz. Input power transients and IRU-induced transients should be held to a minimum.

3.2.3.2.3 Thermal - The IRU and star tracker should operate in a range of approximately $0^{\circ}C$ to $40^{\circ}C$ with a temperature variation limited to $0.5^{\circ}C$ per hour.

3.2.3.2.4 Environmental - All components of the subsystem will be provided radiation protection and will be capable of tolerating the integrated radiation dose over the designed mission lifetime.

3.2.3.3 Duty Cycles/Operating Modes

There are four modes imposed on the attitude control subsystem:

1) Orbit transfer mode during the powered and unpowered portions of the transfer. During this phase, the attitude control module directly controls the operation of the transfer propulsion subsystem.

2) Normal operating mode with a pointing accuracy of 0.01 degrees achievable after few hours.

3) Calibration mode which generates calibration data relative to the IRU(s) and FHST.

4) Slew mode which reorients the spacecraft relative to an initial inertial reference.

3.2.3.4 Design Criteria

3.2.3.4.1 <u>Inertial reference unit</u> - The inertial reference unit provides high accuracy attitude reference data relating the principal axis of the spacecraft and the bore sight of the antenna to the fixed stars. The IRU also provides incremental velocity data to the navigational logic in the computer, permitting computation of the spacecraft's position in inertial space, and also its position with respect to Earth known targets. Due to gyro drift considerations and computational uncertainties, periodic attitude and positional updates will be required. These updates are obtained by employing the star tracker to relate the IRU's own axis to the directons to the fixed stars and by obtaining a positional update from the global positioning satellites (GPS), ground link, or truth site correlation. The GPS will probably be the cheapest method of obtaining the necessary positional update, and its proposed 12-m accuracy is sufficient.

3.2.3.4.2 <u>Fixed head star tracker</u> - This star tracker is suitable for the mission and its selection could reduce overall cost.

3.2.3.4.3 <u>Attitude control module</u> - The attitude control module will provide the mounting structure, environmental, and thermal protection for the IRU, star tracker, navigation and guidance control computers, and interface units. The ACM provides the interface between all components of the ACS on-board computer (OBC).

The actual design implementation is beyond the scope of this effort. At this point the module can only be described in terms of known component design, design considerations/requirements, and STS orbiter constraints. The use of dual IRU, star trackers, and computers provides redundancy and additional accuracy. Dedicated navigation and guidance computers relieve the OBC of these functions and provide additional redundancy.

3.2.3.4.4 <u>Navigation and guidance control computers</u> - The navigation and guidance computer provides the coordinate transformation from the stellar-

inertial to an Earth-centered reference. The computer must be capable of computing the spacecraft ephemeris to the accuracy of about 190 m. This will minimize the error in the determination of the local nadir.

It was not necessary in this study to define actual computers, although various suitable computers exist that can be employed. Implementing existing hardware reduces cost and expedites design.

3.2.4 Attitude Control Propulsion

The on orbit attitude control propulsion subsystem is used to correct for perturbing forces such as solar radiation pressure, aerodynamic drag, and general stationkeeping. The location of the 24 thrusters is illustrated in Section 4.9. Two suitable thrusters were considered, an 8-cm mercury ion thruster, and a pulsed plasma thruster using Teflon[1] as fuel. Both these thrusters are in the milli-newton range and are described in Table 3.2.3.

Pulsed plasma thrusters were selected, although a problem exists in packaging these units on the spacecraft's feed. Their size is such that the boom cannot be properly folded for stowage in the cargo bay of the orbiter. Three solutions are possible and are discussed in Section 4.9: PPTs could be used on the spacecraft ring and mercury ion thrusters on the feed boom, PPTs could be repackaged to meet the boom volumetric constraints, or mercury ion thrusters could replace PPTs entirely. Because no final resolution to the problem has been made, both PPTs and mercury ion thrusters are discussed below.

The pulsed plasma thrusters are used primarily for attitude control and station keeping. Their locations are illustrated in Section 4.9. During one orbit, they are operated to compensate for perturbations due to aerodymanic drag, radiation pressure, and gravity gradient torques. Assuming a yearly fuel consumption of 2.6 kg/thruster, the lifetime of the thrusters until fuel is exhausted approaches 6 years. Refueling will probably not be necessary because of the dual redundancy.

---

[1] Teflon: Registered trademark of Dupont.

TABLE 3.2.3. - ACS THRUSTER CANDIDATES.

	Mass, kg	Dimension m	Power, W
Pulsed plasma thrusters		0.43 dia x 0.25 high	170
Thruster	0.45		
Exhaust cone	0.45		
Capacitors	10.50		
Power converter/MDB interface	4.00		15
Gimbal assembly	5.00		15
Teflon fuel	15.00		
Radiation hardening	1.00		
RFI structure enclosure	2.50		
	38.90		200
Mercury ion thrusters			
Thruster	3.90	0.17	125
Propellant tank, valve	1.45	0.13 x 0.17 high	
Power electronic unit	7.50	0.39 x 0.20 x 0.11	165
Digital interface unit	3.75	0.25 x 0.24 x 0.12	10
Mercury fuel	8.75		
	25.35		300
Total subsystem			
PPT	813		
Mercury ion	557		
Average power (PPT) (based on estimated torques and forces in one orbit)			1632

The mercury ion thrusters provide an alternative to the PPT and provide some packaging advantages. The charged nature of the exhaust requires further consideration, and may not be compatible with the ECMM.

3.2.4.1 Interface Requirements

3.2.4.1.1 <u>Mechanical</u> – The PPTs are mounted on double gimbaled platforms. These mechanisms provide for vectoring of thrust. A spring-deploying mechanism is required to allow packaging within the STS orbiter and later to deploy in its proper operating attitude. Special consideration must also be given to damping the impulsive nature of the thrusters so that modes of the structure are not exicted.

667-N force

30 μs = t   T = 5s

5   10   15   20
Seconds
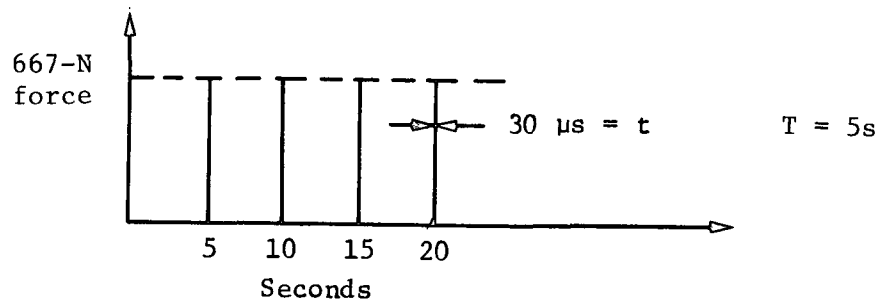
The average force over 5 seconds is 4.5×10^{-3} N. The output represents a periodic sequence of rectangular pulses. The frequency spectrum of the PPT pulse train can be visualized by plotting the amplitude of the Fourier coefficients C_n

$$|C_n| = \frac{At}{T} \left| \frac{\sin(n\pi f_o t)}{n\pi f_o t} \right|$$

where $T = f_o = 1/t$

and generate the envelope. Although C_n is a discrete function, it was considered as continuous to generate this envelope.

The amplitude spectrum is shown in Figure 3.2.4. It represents a frequency range from 10^3 to 5×10^5 Hz. The second lobe is about -6dB down. The output is essentially constant between 0 and 1000 Hz. It is possible that these frequency components depicted could excite structural modes.

81

3.2.4.1.2 <u>Electrical</u> - For pulsed plasma thrusters, the electric interface consists of electric power, command bus, and telemetry. These last two functions are accomplished with the multiplex data bus. The baseline information required for these thrusters is shown below.

Command	Telemetry
Thrusting pulse	Discharge voltage
Gimbaling (x,y)	Initiating voltage
	Capacitor temperature
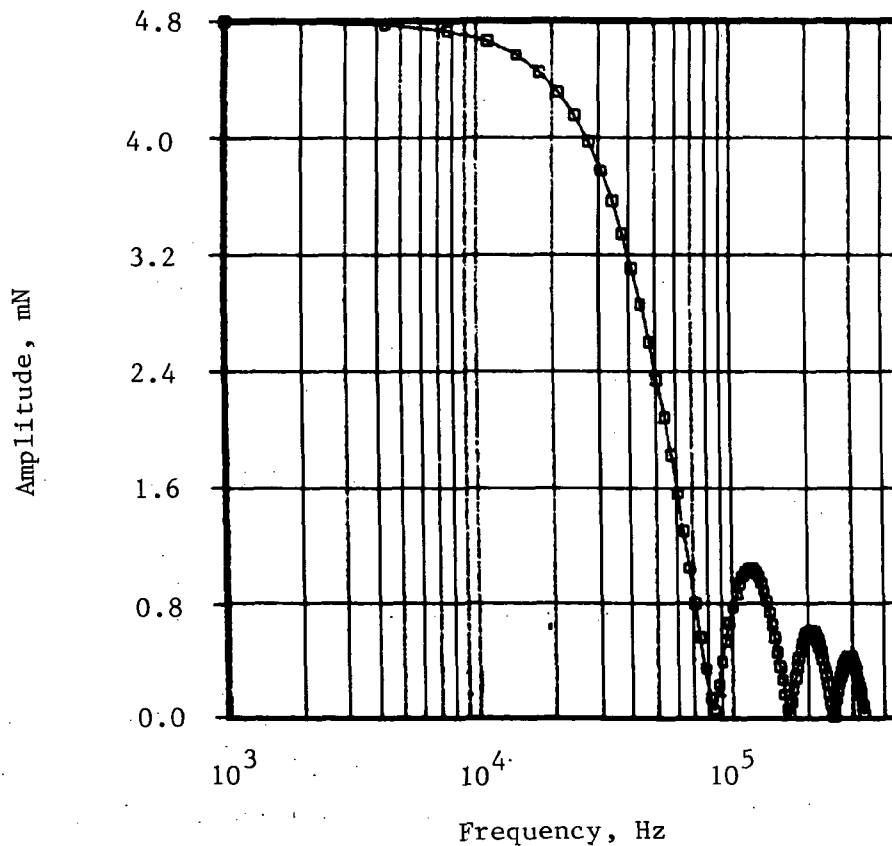
Figure 3.2.4. - Fourier spectrum of pulsed plasma thrusters.

For mercury ion thrusters, the electronics, developed by Hughes Aircraft are comprised of a digital interface unit (DIU) and a power electronics unit (PEU). The electrical interface with the spacecraft is at the DIU. This unit requires three digital command words (command data, command enable, and command clock), and 28-Vdc housekeeping power.

3.2.4.2 Constraints/Requirements

3.2.4.2.1 Mechanical - The pulsed plasma thrusters must be mounted on a deployable, gimbaled platform probably on vertice of 4 structral elements (vertice of cube) to distribute impulse of thrust.

The eight-cm mercury ion thrusters have the same constraints as the PPTs. In addition, the DIU and PEU have a thermal dissipation of 10 and 40 W respectively and must be positioned to allow unrestricted radiation of heat. Locations must be selected that will minimize exhaust plume impingement and interaction with the charged membrane.

3.2.4.3 Duty Cycles/Operating Modes

The pulsed plasma thrusters are employed for attitude control and station keeping. During one orbit, they are operated in the continuous pulse mode to compensate for aerodynamic drag. They must also operate continuously (except in shadow) to compensate for radiation pressure, especially when β = 45 deg. Operation in the discrete mode is employed to compensate for other disturbances and torques. Mercury ion thrusters would be used in the same manner as the pulsed plasma thrusters.

3.2.4.4 Design Criteria

3.2.4.4.1 Pulsed plasma thrusters - A suitable attitude control and station-keeping method is required without using momentum exchange devices. An all-propulsive system was selected because momentum exchange devices such as reaction wheels impose a prohibitive size and weight penalty. In addition, a residual angular momentum exists that cannot be unloaded when at certain solar incidence angles. See Section 4.8 for a more detailed analysis.

3.2.4.4.2 Mercury ion thrusters - An alternative to the PPT system is the mercury ion thruster. The mercury ion thrusters provide certain packaging advantages, especially in the feed horn assembly. However, the charged exhaust plume, the charged membrane surface, and the effect on the composite structural elements need more consideration.

3.2.5 Communications Subsystem

The communication subsystem provides the spacecraft to Earth communications link. The uplink channel provides spacecraft commands while the downlink transfers engineering telemetry data and radiometer experimental data. The communications subsystem is illustrated in Figure 3.2.5. Table 3.2.4 summarizes the features of the broad beam antennas and communications module which comprise this subsystem.

3.2.5.1 Interface Requirements

3.2.5.1.1 Mechanical - Broad beam antennas and the communications module are mounted on rim of spacecraft.

3.2.5.1.2 Electrical - Electric inputs to the communications module include electric power and the data input link from the communications multiplexer located in the C&DH module. The four antennas are interfaced to the subsystem through appropriate transmission cables and the antenna selector switch.

3.2.5.2 Constraints/Requirements

3.2.5.2.1 Mechanical - Physical location of the broad beam antennas does not affect the radiometer operations.

3.2.5.2.2 Electrical - The communications subsystem is designed to handle the required data rates at the maximum range from the spacecraft to synchronous tracking and data relay satellites (TDRS) (47 000 km) and direct-to-ground stations (STDN) (2800 km).

84
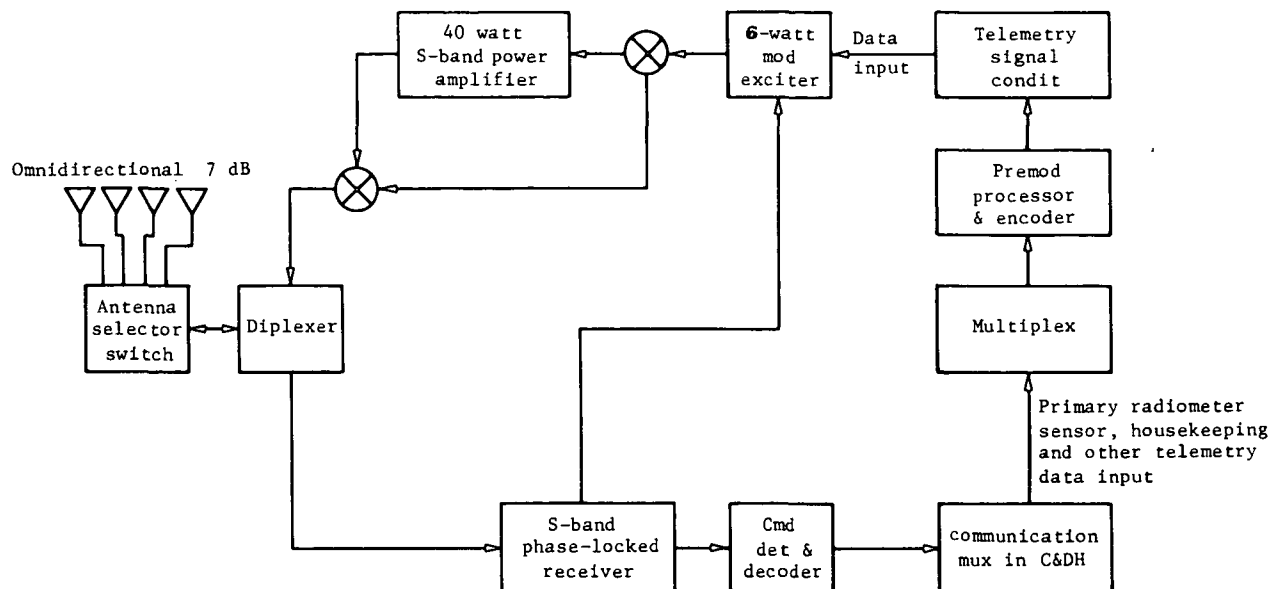
Figure 3.2.5.- LSS communication subsystem.

TABLE 3.2.4. - LSS COMMUNICATION SUBSYSTEM.

Subsystem element	Type/comments	Input frequency	Output frequency	Output power	Operating power	Size	Weight
S-band transponder consisting of transmitter and receiver.	Phase-coherent TDRS on STDN Compatible	2025-2120 MHz	2200-2300 MHz	6 watts	37.5 watts	——	0.9 Kg
Receiver	Phase-locked $2B_{LO}$ = 1000 Hz; all solid state includes ranging module				2.5 watts	5x13x5 cm	0.5 Kg
Transmitter	All solid-state exitation signal coherently derived from received signal	——	2200-2300 MHz	6 watts	35 watts	5x5x13 cm	0.5 Kg
S-band power amplifier	Solid state used for DOD missions	2200-2300 MHz	2200-2300 MHz	40 watts	160 watts	23x25x5 cm	1.8 Kg
Diplexer	Allows simultaneous transmission/reception	2025-2120 MHz	2200-2300 MHz	——	——	13x13x5 cm	0.5 Kg
Antenna selector switch	Signal comparitor to connect to antenna with strongest signal	2025-2120 MHz	——	——	5 watts	7x7x4 cm	0.25 Kg
(4-5) Broad beam antennas	Used to achieve near-omnidirectional coverage	2025-2120 MHz	2200-2300 MHz	——	——	15 cm	0.25 Kg

Total 202.5 watts   56 Kg

3.2.5.3 Duty Cycles/Operating Modes

The rate of radiometer data transmission to ground was not addressed in this study.

3.2.5.4 Design Criteria

The command data may be in the form of a baseband signal or a binary serial data bit stream that biphase modulates on sinusoidal subcarriers. The command rates range up to 2000 bps on a 16-kHz subcarrier.

The telemetry data may be an NRZ or Manchester serial format biphase modulated on subcarriers. The telemetry rates range from 250 bps to 40 kbps. When subcarriers are employed, standard subcarrier frequencies of 1.024 or 1.7 MHz are required.

Tables 3.2.5 through 3.2.7 show the data rates required for radiometer data, other telemetry data, and command data.

3.2.6 Data Management

The Data Management Subsystem integrates all aspects of spacecraft housekeeping and engineering status. The main onboard computer (OBC) is located in the command and data handling (C&DH) module. The system employs a time division multiplex data bus to communicate with all spacecraft components. The subsystem consists of the command and data handling module, remote interface units (RIU), and multiplex data bus (MDB). The C&DH module contains the OBC, peripheral varibus distributed processors, central unit (CU) interface, and communication multiplex processor. It is illustrated in Figure 3.2.5 and summarized in Table 3.2.8.

The OBC performs the high-speed housekeeping functions. The computer receives data and transfers control commands to the remote interface units by transferring telemetry gate addresses or command address words.

TABLE 3.2.5. - COMMUNICATION SUBSYSTEM DATA RATES.

The required data rates are:	Bit error rates	10^{-5}
	Commands	2 kbps
	Telemetry	40 kbps
Antennas:	(2 each) TDRS link	7 dB (0.12-m aperture)
	(2 each) STDN link	0 dB (omnidirectional)
Transponder:	Transmit frequency	(2200 to 2300 MHz)
	Receive frequency	(2025 to 2120 MHz)

TABLE 3.2.6. - BASIC RADIOMETER DATA RATE.

Case	(3dB) Resolution, m	No. of horns	Swath length wt factor	no. of samples in low-freq swath width
A	4410	41	1.0	41.0
B	2346	77	2.03	156.3
C	962	188	4.95	931.0

Total number of samples per swath = 1128.3

No. digits/per sample = 18 (This includes 12 digits for signal intensity granularity and 6 digits for data time & location)

Satellite valocity in 650 km orbit = 7500 m/s.

Time to cross low-freq. swath element = $\dfrac{4410}{7500}$ = 0.588 s.

Basic radiometer = $\dfrac{\text{(total samples/swath)} \times \text{(No. digits/sample)}}{\text{Time/swath}}$

$= \dfrac{1128.3 \times 18}{0.558}$ = 36.4 kbps

TABLE 3.2.7. - PCM S-BAND INFORMATION TRANSMISSION (KBPS).

Rf link	Cmd[a]	TLM[b]	Total (uncoded)
To LSS from ground			
STDN direct	2		2
STDN relay - TDRS	2		2
To LSS from Orbiter			
	2		2
From LSS to ground			
STDN direct		40	40
STDN Relay-TDRS		40	40
From LSS to orbiter			
		16	16

[a]Cmd data are primarily for deployment and GN&C purposes.

[b]TLM data includes primary radiometer sensor data,
engineering housekeeping, plus caution & warning
data.

TABLE 3.2.8. - DATA MANAGEMENT COMPONENT SUMMARY

Components	Mass . kg	Dimensions, m	Power, W
General purpose on board computer	4.5	0.4 x 0.3 x 0.2	25
Multiplex data bus (MDB)	286	992	--
Remote interface units (RIU)	(Charged to each module)		
Totals	291	-----	25

The data bus provides the interface media between the C&DH module, and the RIU services all outlying spacecraft components. It will probably consist of PG-142 coax line, although twisted shielded pairs might also be suitable.

Remote Interface Units provide the standard means of process to the C&DH subsystem and coupling to the MDB. In operation, the RIU will recognize its address and pass information to the subsystem (or part of subsystem) that it governs. Redundant RIUs are a baseline requirement.

3.2.6.1 Interface Requirements

3.2.6.1.1 <u>Mechanical</u> - The OBC is contained within the C&DH module. Therefore, mechanical interface is through the module structure.
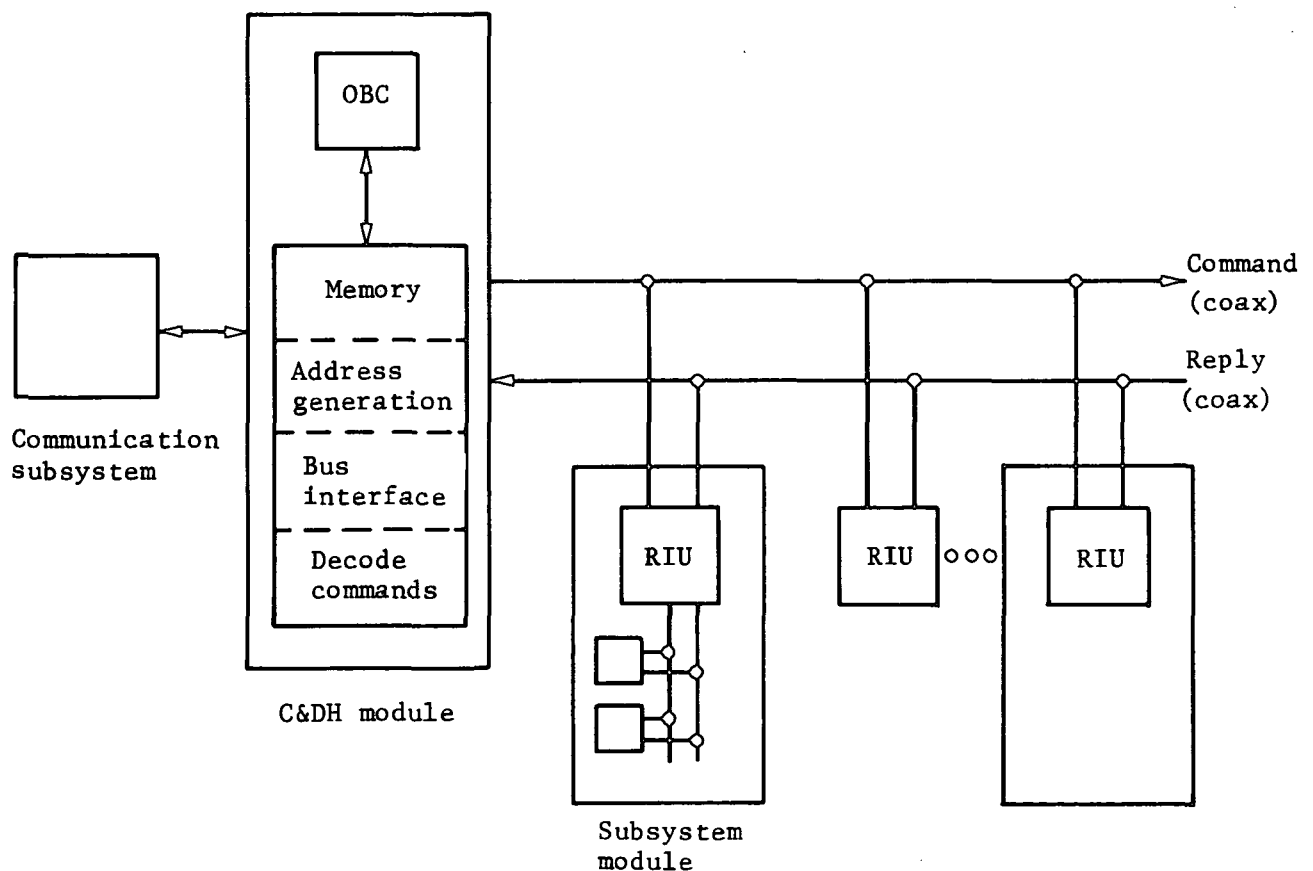
Figure 3.2.6. - Command and data handling subsystem.

The coaxial cable of the multiplex data bus is bonded or attached to the graphite-epoxy tubes. The simplest and most reliable method to negotiate the joints is through a loop, allowing the cable to straighten out during space-craft deployment. An alternative solution is to provide an electrical connector as an integral part of the joint.

The remote interface units are located in all modules requiring access to the MDB and, as such, do not impose any elaborate mechanical requirements.

3.2.6.1.2 Electrical — The MDB is the interfacing medium between the C&DH module and all other spacecraft components. Each RIU is directly coupled to the MDB.

3.2.6.2 Constraints/Requirements

3.2.6.2.1 Mechanical — The OBC is hard mounted within the C&DH module. The minimum radius of the bend of the data bus should not be less than six times the outside diameter of the coaxial cable. Each RIU is located within the module that it governs.

3.2.6.2.2 Electrical — Coaxial cables used in the structure and modules will be similar to RG-142 and conform to specifications described in MIL-C-17/60. This is required to minimize electromagnetic interference.

3.2.6.2.3 Thermal — All components of the subsystem must operate in range of $0^{\circ}C$ to $40^{\circ}C$. Thermal control is provided by thermal louvers, suitable component placement, and electric heaters.

3.2.6.2.4 Environmental — All components must withstand the integrated radiation load over the mission lifetime.

90

3.2.6.3 Duty Cycles/Operating Modes

The OBC controls all housekeeping aspects of the spacecraft, and as such requires continuous operation. During launch, the OBC is in a standby mode. The OBC also governs the communication subsystem and will be required to perform control and multiplex functions during transmission.

3.2.6.4 Design Criteria

3.2.6.4.1 General purpose OBC - A general purpose computer using timely technology and internal redundancy is required for this application. An example of the type of computer required is the NSSC-II implemented in the MMS program; although the OBC proposed for this mission does not perform navigation and guidance computations. Using such a computer will reduce design and manufacturing costs.

3.2.6.4.2 Multiplex data bus - A simple and reliable interface media is required to link all subsystems into the MDB. A dual redundant, coaxial transmission line is suggested. Coaxial cable will fulfill the required performance constraints. Nontraditional interface media, such as fiber optics provide an alternative; although such schemes are not flight qualified and would require extensive engineering to be compatible with the proposed data management subsystem. However, they do offer advantages in data capacity and EMI susceptability. Mechanical considerations of fiber optics, as related to the deployment of the spacecraft, also require consideration.

3.2.7 Antenna Feeds

The antenna feed subsystem consists of three rows of microwave sensor horns and associated signal conditioning electronics. These horns in conjunction with the membrane reflector, sense the microwave characteristics of the area under the vehicle's flight path. The characteristics of the sensors are summarized in Table 3.2.9.

3.2.7.1 Interface Requirements

3.2.7.1.1 Mechanical – All three types of sensors will be mounted within the confines of the feed horn.

3.2.7.1.2 Electrical – All sensor electronics will interface with a common, redundant power bus. The output of the signal processing electronics will interface with a dedicated microprocessor.

3.2.7.2 Constraints/Requirements

Based on the operating frequencies and the derived requirements defined in Section 2.2, the radiometer requirements are tabulated in Table 3.2.7.

3.2.7.3 Duty Cycles

The sensors will be operated for a short time after deployment to verify their health. After the spacecraft reaches operational altitude, the sensors will be run continuously.

3.2.7.4 Design Criteria

The microwave horn layout is determined by the 2λ width and the number of horns that can be placed on the 23-m long feed.

3.2.8 Figure Sensing and Actuation System

The figure sensor and a control microprocessor are located on the feed horn. These, in combination with four distributed processors, high voltage (HV) supplies, and thermal compensators maintain the accuracy of the mirror. The membrane is divided into four control quadrants, each with a dedicated processor under direction of the main processor. The characteristics of these components are summarized in Table 3.2.10. Each power supply provides power for a single electrode. The shape maintenance of the membrane is achieved by providing independent voltage control of each electrode. Additional information regarding membrane shape control and shape sensing can be found in sections 4.5 and 4.7 respectively.

92

TABLE 3.2.9. - RADIOMETER FEED CHARACTERISTICS.

Horn layout

Frequency, GHz	1.08	2.03	4.95
Wavelength, cm	27.8	14.8	6.1
Resolution, m	4410	2346	962
Number of beams	41	77	188

Sensed footprint

- Horn aperture $4\lambda \times 2\lambda$
- Swath width   150 km
- Altitude   650 km
- Field of view   13.2 deg
- Reflector aperture   50 m
- Focal length   100 m
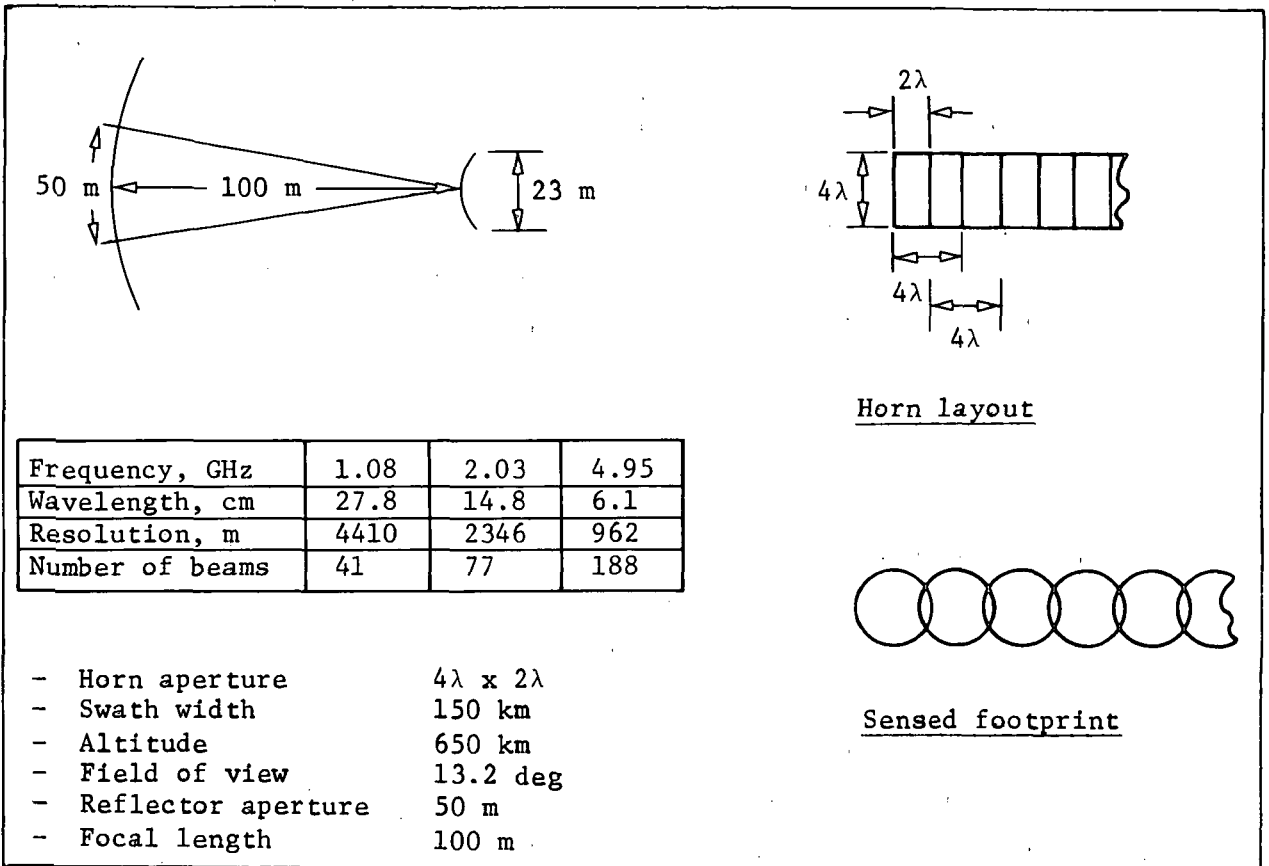
3.2.8.1   Interface Requirements

3.2.8.1.1   **Mechanical** - High voltage supplies are located underneath the electrodes as shown in Figure 3.1.17. The figure sensor is located on the feed with a direct view of the membrane surface. The membrane shape control microprocessor is located on the feed, near the figure sensor. Dedicated shape processors are located in each quadrant on the rim.

3.2.8.1.2   **Electrical** - The figure sensor has a dedicated data line to the main microprocessor which has direct data lines to the dedicated processors. Each dedicated shape processor has a multiplex data bus to the high voltage supplies in each quadrant. The high voltage supplies have a low primary dc voltage input along with the command line.

3.2.8.2 Constraints/Requirements

3.2.8.2.1 **Mechanical** - The exact method of attaching the high voltage supplies to the electrodes has not been determined. The figure sensor must have an unrestricted view of membrane surface.

3.2.8.2.2 **Electrical** - The electrical requirements of the electrode power supplies, figure sensor, and control microprocessor are summarized in Tables 3.2.11 through 3.2.13, respectively.

TABLE 3.2.10. - FIGURE CONTROL COMPONENT SUMMARY

Components	Mass, kg	Dimensions, m	Power, W
Figure sensor	5.0	0.5 x 0.4 x 0.3	10
Main processor	2.3	0.4 x 0.3 x 0.2	10-50
Remote processors (4)	9.1	0.4 x 0.3 x 0.2 each	60
High voltage supplies (220)	350.0	0.13 x 0.08 x 0.02 each	660
Totals	370	———	780

TABLE 3.2.11. - ELECTRODE POWER SUPPLY SPECIFICATIONS

	10-cm gap		20-cm gap	
	1-mm rms	1-cm rms	1-mm rms	1-cm rms
Voltages, V	0-60 000	0-60 000	0-100 000	0-100 000
Voltage steps, V	10	100	20	200
Nominal update rate, s	1/20	1/60	1/20	1/60
Nominal rise time, s	2.0	2.0	2.0	2.0
Fast update rate, update/s	20	2	20	2
Fast rise time, s	0.025	0.25	0.025	0.25

TABLE 3.2.12. - SENSOR REQUIREMENTS.

	1-mm rms	1-cm rms
Low rate measurements:		
Measurement rate, points/s	11	0.6
Measurement accuracy, mm	0.2	20.0
High rate measurements:		
Measurement rate, points/s	100	10
Measurement accuracy, mm	0.2	20.0

95

The dedicated shape processors require redundant electric power lines, a multiplexed data bus between electrodes, and a dedicated data link to the main shape control processor.

3.2.8.2.3 Thermal - All electrical components must be in the operating range -10° C to 50° C.

3.2.8.2.4 Environmental - All electrical components must be able to withstand the integrated radiation burden for design lifetime of 10 years.

TABLE 3.2.13. - CONTROL MICROPROCESSOR SPECIFICATIONS

	1-mm rms	1-cm rms
Memory size, thousand words	128	10
Word size, bits	16	12 - 16
Rate, multiplication per s	50 000	2000
Weight, kg	2.3	2.3
Volume, m^3	0.014	0.014
Power use, W	20-50	1-10
Reliability	Very high	Very high

3.2.8.3 Duty Cycles/Operating Modes

The steady state disturbances of the membrane reflector are compensated by voltage adjustments to reposition the surface. This condition occurs approximately 90 percent of the time in one orbit. Therefore, all components will operate continuously after deployment.

3.2.8.4.1 High-voltage supplies - HV supplies must be packageable and able to be integrated with the membrane. The electrical interfaces must be held to a minimum. The supplies must be capable of operating over specified voltage range.

The local dedicated processors are distributed in quadrants on the rim. They modulate the electrodes with digitally coded signals according to information supplied by the main processor. A functional diagram of the HV supplies is shown in Figure 3.2.7. The 66 supplies per quadrant are addressed by a unique location code. The format of the transmission frame consists of 16 bits to define voltage variation and 8 bits for the location address. Digital information is transmitted to each supply via a loop-configured, simplex, multipoint data line. The low dc primary voltage is distributed using parallel wiring.

A multiplexed bus will greatly reduce wiring requirements and hence alleviate deployment problems of the membrane. This scheme employs approximately 1320 m of wire. Implementing this system will increase the size of each supply due to the additional electronics. It will also increase multiplexing and software requirements. These disadvantages, however, offset the problems associated with separate, variable low-voltage lines and proportional output.

3.2.8.4.2 Figure sensor - The preferred near-term approaches for the figure sensor are laser ranging or optical interferometry. A detailed discussion of the available options is contained in Appendix D. Laser ranging methods have received the most attention, as demonstrated with the JPL self-pulsed laser surface-measurements system, the surface accuracy measurement sensor for deployable reflector antennas (SAM-DRA) sponsored by Langley, and commercial range finders. The two-color heterodyne CO_2 interferometer exceeds the measurement accuracy required, although phase stability and the inherently nonrobust nature of the system will probably be limiting factors. Therefore, some form of range finding technology is, at present, the most practicable alternative for the figure sensor.

19.0 cm

2.0 cm

7.6 cm

Bus voltage,
12 Vdc

Input buffer → Serial input shift register → Address decode

Serial input shift register → D/A convert → Control → High voltage step up → Filter

Figure 3.2.7. - High-voltage supply.
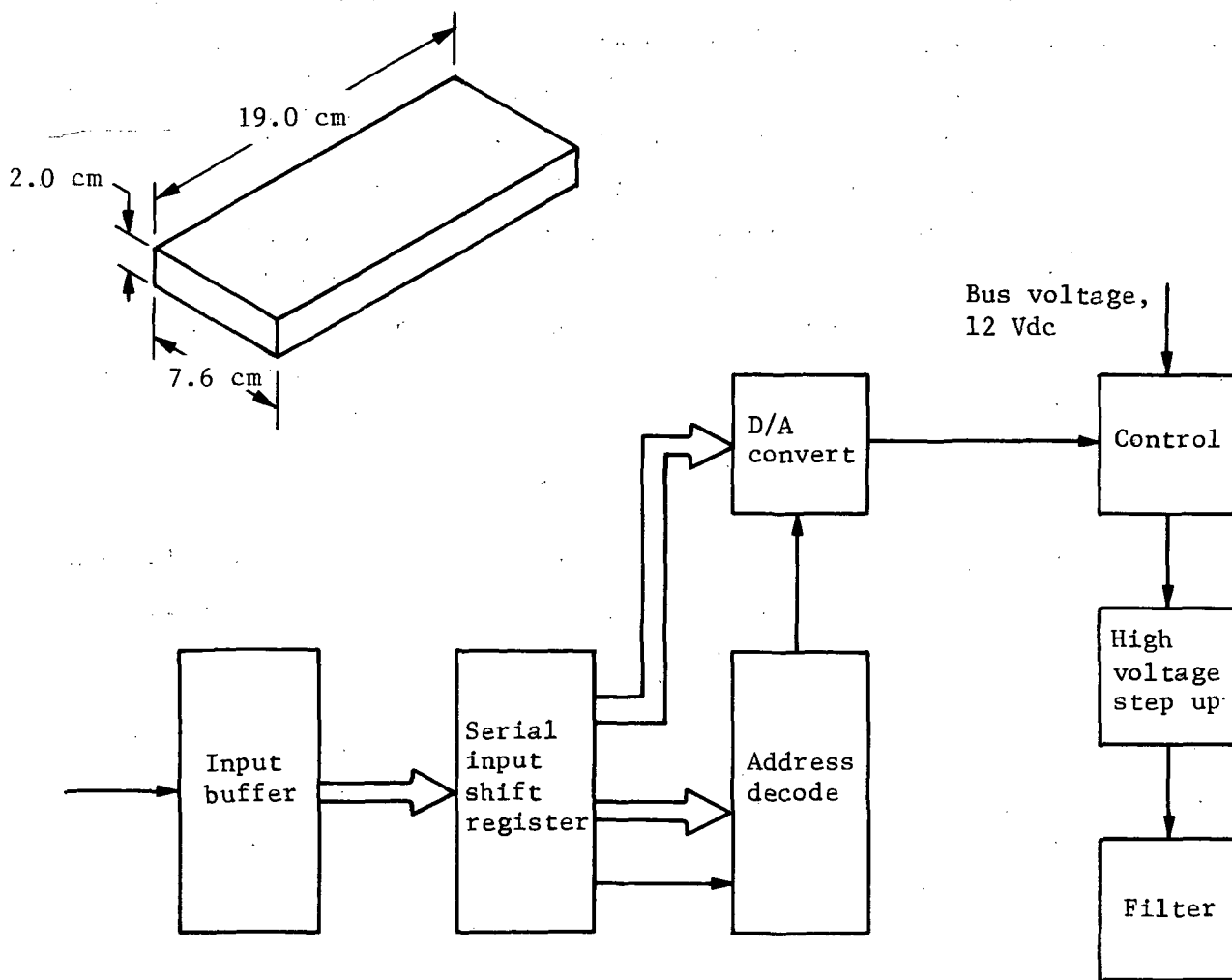
Component Description

Serial input shift register — Converts serial input to parallel data.

Address decode — Determines if particular supply is being commanded to change output.

— If yes, D/A enable goes high and conversion takes place.

D/A Convert — Supplies analog control voltage (envisioned as type of transistor bias)

3.2.8.4.3 <u>Membrane shape control microprocessor</u> – The measurement rate and voltage update rate influence the microprocessor sizing. A single main microprocessor is located on the microwave feed horn. Four separate dedicated lines are used to communicate with the dedicated processors. The membrane is assumed to be in a quasi-steady state requiring a minimum of 220 measurements every 20 seconds to maintain surface quality. During large thermal variations, the data update rate and matrix multiplication exceed the computer's capability. In addition, a single microprocessor does not provide for any form of redundancy. Therefore, a main processor is employed with four other dedicated processors, each governing a quadrant. This vectored approach will expedite calculations and provide redundancy, although at a slower data rate.

3.2.9 <u>Membrane Attachment Subsystem</u>

The membrane attachment subsystem provides a mechanical interface between the three membrane surfaces and the support structure. All three membranes are suspended along the perimeter and form a tensioned structure. The components of this subsystem include electrode drop cords used to form the curved electrode surface and thermal compensators. The membrane perimeter is terminated by a catenary. At the apex of each catenary is a spring, jack screw, and stepper motor that provide a large degree of thermal compensation. These components are summarized in Table 3.2.14.

3.2.9.1 Interface Requirements

The reflector, electrode, and Faraday membranes are attached to the structure at 56 locations. The 28 connections on the reflector are through the compensator/actuator system. Mechanical interface between the electrostatic membrane and the Faraday membrane is through the drop cords. The thermal compensator/actuator must accomodate 8.9-cm membrane thermal deflection and 2.6-cm truss hoop thermal deflection.

TABLE 3.2.14. - MEMBRANE ATTACHMENT COMPONENT SUMMARY.

Component	Mass, kg	Dimensions m	Power, W
Drop cords, 350	15	5×10^{-4} dia each	---
Thermal compensator, 28 ea	78	0.01 x 0.16 each	· 140
Totals	93	-----	140

3.2.9.2 Constraints/Requirements

Electrode drop cords must have a low thermal expansion. The thermal compensators/actuators must be capable of handling the largest anticipated thermal variations.

3.2.9.3 Duty Cycles/Operation Modes

The membrane attachment subsystem is an integral part of the spacecraft and provides the tension required to maintain the shape of the membranes during the operating lifetime. It is continuously cycled to adjust membrane shape and stressed once per orbit to compensate for thermal stresses.

3.2.9.4 Design Criteria

Design must provide for a tensioned surface between electrode membrane and Faraday membrane. A catenary perimeter is employed with a thermal compensator consisting of a spring, a jackscrew, and a stepper motor attached at 28 points on the rim (fig. 3.2.8). The steppers are under direct control of the local dedicated processor (Sect 3.2.8). The degree of thermal compensation is determined by the figure sensor. Loads to the support structure along the perimeter are about 26 N/m. The linear spring and jackscrew combination allows significant perimeter in-plane motion. With external disturbances to the membrane reflector, the perimeter compensator minimizes required voltage adjustments.

3.2.10 Membrane Subsystem

The membrane is defined as everything between the continuous box truss support structure. This definition includes the electrode surface that is enclosed by the membrane reflector, draw strings and the Faraday membrane, but not power supplies or cabling. The surface irregularities of the reflector are smoothed with the application of electrostatic pressure. Figure 2.4.3 illustrates the major components (Table 3.2.15).

3.2.10.1 Interface Requirements

3.2.10.1.1 **Mechanical** - The mechanical interface between individual membranes and between the membranes and the structure is contained in Section 3.2.9. Membrane load on the box truss hoop is limited to 26 N/m around its circumference.

3.2.10.1.2 **Electrical** - The electrical interface between membrane and structure is contained in Section 3.2.8.
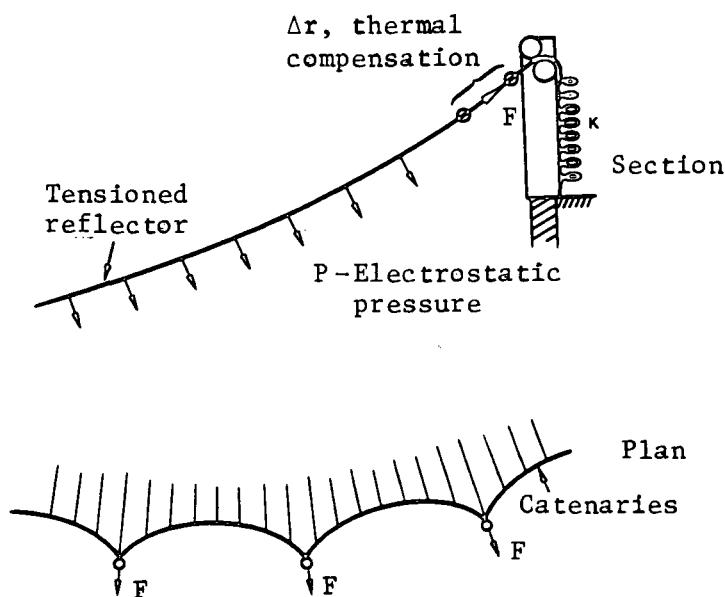
Figure 3.2.8. - Conceptual perimeter attachment.

TABLE 3.2.15. - MEMBRANE COMPONENT SUMMARY.

Component	Mass, kg	Dimension, m	Power, W
Reflector	270[b]	100 Dia x 0.12 x 10^{-3}	---
Electrode surface	270	100 Dia x 0.12 x 10^{-3}	---
Faraday cage	270[c]	100 Dia x 0.12 x 10^{-3}	---
Totals	810	------	40[a]

[a]Power drain in presence of 10^4 to 10^5 particles/cm^3.

[b]Reflector weight includes budget for aluminization, electrode surface, and electrode weight.

[c]Faraday cage includes budget for drop cords.

3.2.10.2 Constraints/Requirements

3.2.10.2.1 Mechanical - The membrane must have minimal openings for plasma penetration. The number of electrically isolated control panels required are shown in Table 3.2.16.

TABLE 3.2.16. - ELECTRODE QUANTITY.

Surface Quality	N, number
1.0 mm (rms)	220
1.0 cm (rms)	40

The allowable irregularity of the electrode surface is ± 8 cm. Limiting reflector error to 1.0 mm dictates a spatial electrode period of 4.5 m or less.

3.2.10.2.2 <u>Electrical</u> - The reflecting and Faraday membrane should be at ground potential. Electrical constraints on the electrodes are contained in Section 3.2.8, Figure Sensing and Actuation System.

3.2.10.3 Duty Cycles/Operating Modes·

The three membranes are essentially passive devices and deploy with the spacecraft. They are employed during the 10-year mission.

3.2.10.4 Design Criteria

3.2.10.4.1 <u>Reflecting membrane</u> - Design considerations:

1) Ease of deployment;

2) Mechanical properties, i.e., tear resistance;

3) Achieving the required surface quality.

The membranes consist of commercial Kapton or Mylar polymer, with a 500-$\overset{o}{A}$ thick aluminum coating. A stress level of 2 to 5 percent of yield is postulated.

Design rational:

1) Safe deployment techniques for large polymer surfaces are known, and the aluminum coating also eases deployment.

2) Although rip-free deployment is possible, a more conservative approach would be to fabricate the rip-stop from the same material at 20 to 30 times the thickness of the basic membrane reflector. At the nominal stress levels, the membrane will not tear due to meteoroid damage. In addition, a scrim is planned for the membrane reflector.

3.2.10.4.2 <u>Electrode</u> - Design considerations:

1) Electrical insulation;

2) Suitable physical properties.

From weight considerations, an electrode membrane thickness of 0.12×10^{-3} m is recommended. Each electrode is hexagonally shaped, and would face the membrane reflector. The design implementation is based on constraints and requirements previously imposed.

3.2.10.4.3 <u>Faraday membrane</u> - Design considerations:

1) Form space plasma shield;

2) Provide structure for draw strings.

The Faraday membrane forms the back and sides of the membrane subsystem

3.2.11 System Conclusions

3.2.11.1 New Developments

Large space structures create difficulties normally not encountered with conventional spacecraft. In this study an effort was made to use current and state-of-the-art (SOA) technology whenever possible. However, there are aspects of the ASSA design where SOA advancement is required. This section will detail these subsystems within the SOA and identify some critical technology areas.

The single subsystem requiring the most development is the figure sensor and actuation system, although the technology is near term. Refer to Appendix D for a discussion of some of the options available. Essentially, the problem is to develop a figure sensor of sufficient robustness, stability, accuracy, and scanning speed. Generally, the two figure sensors considered are an optical range finder or an interferometer.

For this particular surface, a minimum of 220 measurements must be made in approximately 20 seconds to an accuracy of a few mm over the 100-m diameter reflector. In order to reduce the sampling times at each point, the current stability, precision, and operating speed of these instruments must be increased. These requirements are beyond current technology capability, although the range finder system is probably closer in achieving a viable system. Another lead item is the development of control algorithms.

The long distances encountered in large space structures impose diffi- culties in electric power distribution. Conventional designs usually employ a 28 Vdc to handle the current. The long distances and higher power levels encountered in this spacecraft require an increase from 28 Vdc to 125 Vdc, enabling the wiring to be held to a manageable size (10-12 gage). This alteration will reduce weight and conform to stiffness and size constraints imposed by the deployable structure. The electrical problems imposed by the composite structural material have not been addressed in this study. These include grounding, shielding and FMC/EMI provisions.

The electrostatic membrane reflector employs the development and maturing of a new technology. The lead items in development of the ECMM appear to be the following.

1)   Reliable deployment of membranes;
2)   Quality membranes fabricated to a specified regularity and smoothness;
3)   High rate thermal transients and control.

Important ECMM experiments and testing can be performed on the ground. Testing should be pursued with rigor in order to answer design concerns and direct program development.

3.2.11.2 Available Designs

The transfer propulsion subsystem is of flight-proven, conventional design. In this spacecraft, hydrazine SOA systems are acceptable with essentially no modification except for the nominal mechanical integration to the structure.

The attitude control system is entirely SOA. Using suitable available components, an attitude control system can be implemented with a minimum of modification to the equipment.

4.0 SUPPORTIVE ANALYSIS

The analyses supporting the ASSA design are grouped into five major groups: structure and membrane dynamics; structure and membrane thermal effects; membrane electrode geometry and sizing; membrane shape-sensing and control; and thruster selection. This section describes these analyses and their results.

4.1 STRUCTURAL DYNAMICS

This section details the structural dynamics analyses performed to support the design of the 100-m radiometer using the box truss ring design and the radial rib/external hoop design. The basic geometric configurations are detailed in Sections 3.1.1 and 3.1.2. The analyses performed established structural frequencies and mode shapes for the two configurations. The NASTRAN computer code was used for all studies. A finite element approach was used for the modal analysis. This procedure involved definition of structural geometry, connectivity, member sizes, and material properties needed to construct the finite element model. A standard eigenvalue analysis was performed to establish the modal parameters.

4.1.1 100-m Box Truss Radiometer

The basic configuration consists of 28 identical boxes arranged in a circular configuration with an inside radius of 50.29 m, an outside radius of 61.57 m; and a box depth of 14 m. The line feed is located 100.58 m above the center plane of the hoop array and is supported by two Astromasts and four tension stays. This basic geometry is shown in Figure 4.1.1.

4.1.1.1 Model Parameters

An individual box of the 28-bay hoop configuration can be characterized in terms of two vertical members, four surface tubes (two inboard and two outboard), two radial tubes (upper, lower), and 10 diagonal members as shown in the sketch. The tube members/diagonals are axial load carrying members only, and constructed of graphite/epoxy. Member properties are summarized in Table 4.1.1.
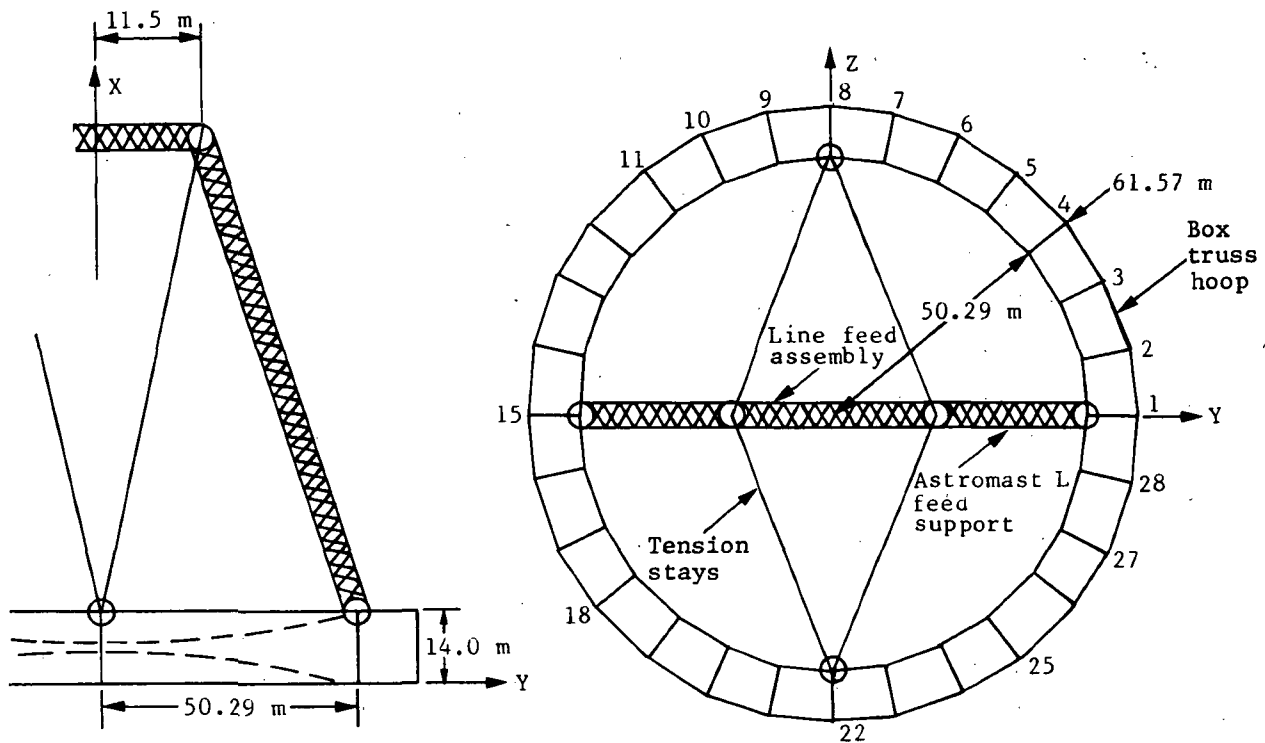
Figure 4.1.1. - 100-m box truss radiometer, basic geometry.

TABLE 4.1.1. - HOOP TRUSS MEMBER PROPERTIES.

Member	Comment	Cross sectional area, cm^2	Torsion constant, cm^4
S_1, S_2	10.2 cm x 0.046 wall	1.46	0.38
S_3, S_4	8.9 cm x 0.046 wall	1.28	0.25
R_1, R_2	7.6 cm x 0.046 wall	1.09	0.16
V_1, V_2	6.6 cm^2 x 0.097 wall	2.51	0.30
Diags.	0.091 cm^2 (6-ply)	0.23	---

Material
properties: Young's modulus $E = 1.38 \times 10^{11}$ N/m^2
              Shear modulus $G = 2.00 \times 10^{10}$ N/m^2
              Density $\rho = 1939.3$ kg/m^3
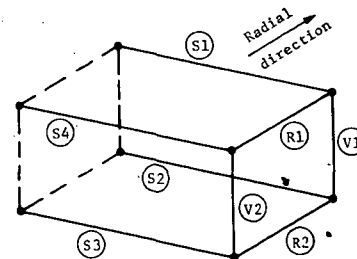
Note

Diagonals are not shown.

The electrostatically supported membrane reflecting surface is charac-
terized in terms of mass properties only; no system stiffness is assumed. For
a membrane surface mass density of 0.14 kg/m^2, the total reflecting surface
mass is 1166 kg, which is then distributed uniformly over the 28 x 2 = 56
internal diameter box joints. Fittings mass of 0.91 kg is assumed for the 4 x
28 = 112 box joints. Additional masses as shown in the following figure, are
used to accommodate the estimated values for attitude control packages, elec-
tronic/power supply subsystems, and the feed array.

The feed support subsystem, consisting of two Astromasts and four tension
stays, was modeled using the structural stiffness and mass properties shown in
Table 4.1.2. An "equivalent beam" representation was used to characterize the
Astromasts.
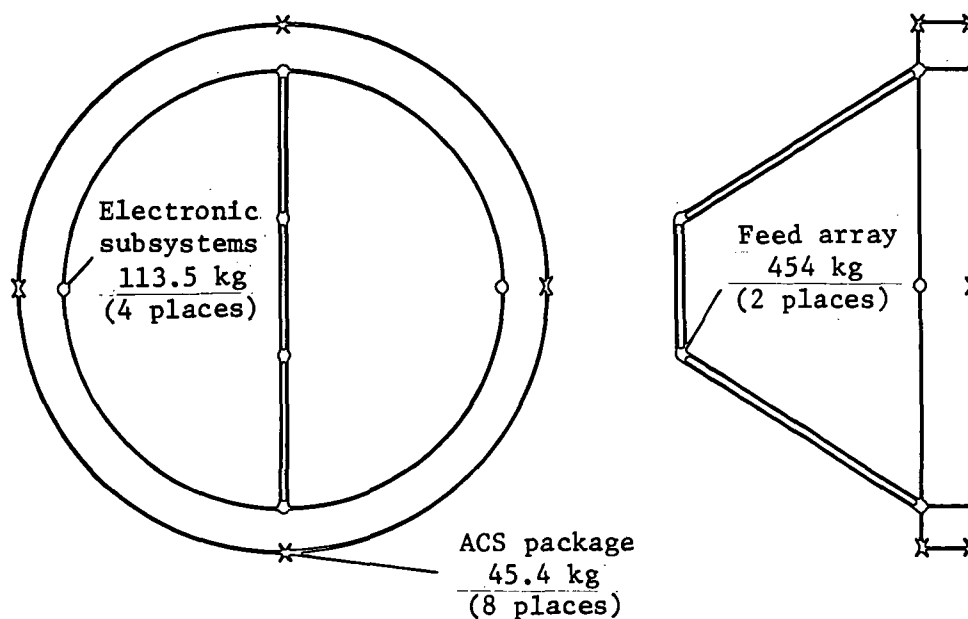
Figure 4.1.2. - Locations of additional masses.

TABLE 4.1.2. – FEED ARRAY SUPPORT SUBSYSTEM CHARACTERISTICS.

Tension stays	Young's modulus	$E = 1.38 \times 10^{11}$ N/m^2
	Density	$\rho = 1939.3$ kg/m^3
	Area	$A = 6.45 \times 10^5$ m^2
Astromasts	Young's modulus	$E = 1.38 \times 10^{11}$ N/m^2
	Shear modulus	$G = 2.06 \times 10^{10}$ N/m^2
	Density	$\rho = 15\ 357$ kg/m^3
	Area	$A = 1.29 \times 10^{-5}$ m^2
	Bending inertia	$I = 2.37 \times 10^{-6}$ m^4
	Torsion constant	$J = 5.43 \times 10^{-7}$ m^4

4.1.1.2 Rigid-Body Mass Properties.

Using the structural parameters described previously, the rigid-body mass properties are as shown in Table 4.1.3.

TABLE 4.1.3. – RIGID-BODY MASS PROPERTIES

Mass = 4205 kg

Principal inertias

$I_{xx} = 9.59 \times 10^6$ kg-m^2

$I_{yy} = 1.22 \times 10^7$ kg-m^2

$I_{zz} = 1.23 \times 10^7$ kg-m^2

Mass center

$\overline{X} = 23.78$ m above hoop midplane

$\overline{Y} = \overline{Z} = 0$
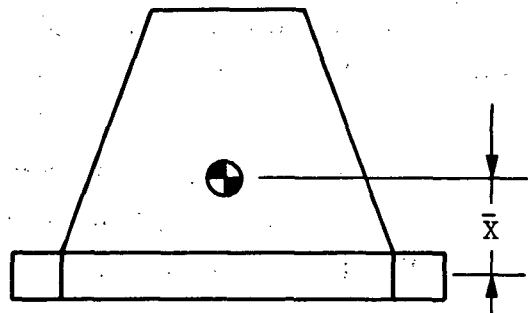
4.1.1.3 Modal Characteristics

The total structural system consists of 366 dynamic degrees of freedom. An eigenvalue analysis was performed and 60 natural frequencies/normal mode shapes were extracted. The lowest 36 system frequencies (modal content through 5 Hz) are shown in Table 4.1.4 and several mode shapes are given in Appendix A. The strain energy distribution in the individual modes is also indicated.

4.1.2 100-m Radial Rib/External Hoop Radimeter

The basic configuration consists of 24 identical radial ribs that emanate from a central hub to form a spherical surface with a radius of 51.1 m. The line feed is located 102 m above the center point of the dish and is supported by an Astromast configuration consisting of four masts arranged as shown in Section 3.1.2. Additional support stability is provided by four tension stays. The tips of the 24 individual ribs are connected by an external hoop.

4.1.2.1. – Model Parameters

For purposes of the structural model, an individual rib is characterized in terms of seven grid points spaced from root to tip, resulting in six individual segments. The root/tip cross sectional geometry and material properties are summarized in Figure 4.1.3 and Table 4.1.5. With reference to Figure 4.1.3, Table 4.1.5, and the given geometric relationships, the section properties for the six individual segments that comprise a single rib are given in Table 4.1.6.

The external hoop is assumed to be constructed similarly to the ribs, i.e., its cross-sectional properties (as described in Table 4.1.7) are derived using the rib relationships presented in the table.
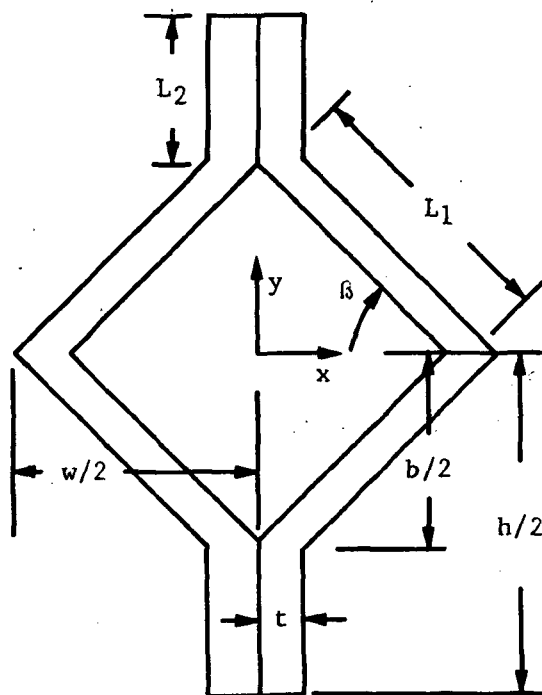
$$A = 4t(L_1 + L_2)$$

$$I_{xx} = 4t\left[\frac{L_1^3}{3}\sin^2\beta + L_1^2 L_2 \sin^2\beta + L_1 L_2^2 \sin\beta + \frac{L_2^3}{3}\right]$$

$$I_{yy} = 4t\left[\frac{t^2 L_2}{4} + \frac{L_1^3 \cos^2\beta}{3}\right]$$

$$J = I_{xx} + I_{yy}$$

Figure 4.1.3. – Rib cross sectional geometry.

112

TABLE 4.1.4. - MODAL CONTENT THRU 5 Hz.

Mode	Freq, Hz	Comment	Strain energy, percentage
1-6	0.0	Rigid Body	----------
7	0.1986	Astromast bending	100 Masts
8	0.2046	Astromast bending	100 Masts
9	0.2668	Astromast & feed bending	100 Masts & feed
10	0.2915	Astromast & feed bending	100 Masts & feed
11	0.8048	Astromast bending, stay extension	87 Masts, 13 stays
12	0.9317	Astromast bending	100 Masts
13	0.9417	Astromast bending	99.6 Masts
14	1.0945	Astromast & feed bending	100 Masts & feed
15	1.1252	Astromast bending	100 Masts
16	1.1297	Astromast bending	100 Masts
17	1.2047	Astromast & feed bending	100 Masts & feed
18	1.4051	Stay extension	99.5 Stays
19	1.4314	Astromast bending & ring mode	37 Masts, 63 ring
20	1.5648	Ring mode	92.4 Ring
21	1.6496	Ring mode	100 Ring
22	1.8261	Ring mode	100 Ring
23	2.0804	Stay extension	99 Stays
24	2.7528	Astromast bending & stay extn	9 Masts, 91 stays
25	2.8652	Feed bending	85 Feed, 15 stays, & ring
26	2.9930	Astromast bending	100 Masts
27	3.0321	Astromast bending	100 Masts
28	3.1307	Astromast & feed bending, stay extn	20 Mast & feed, 80 stays
29	3.2545	Astromast & feed bending	97 Masts & Feed, 3 Ring
30	3.5881	Ring mode	2 Masts, 98 Ring
31	3.7687	Feed bending	94 Feed, 6 Ring
32	3.8270	Feed bending & stay extension	6 Feed, 94 Stays
33	3.9317	Ring mode	100 Ring
34	3.9646	Ring mode	100 Ring
35	4.6578	Ring mode	99 Ring
36	4.8057	Astromast & feed bending	99 Mast & feed

TABLE 4.1.5. - RIB-MEMBER PROPERTIES.

Dimension	Root geometry m	Tip geometry m
t	4×10^{-4}	4×10^{-4}
w	0.406	0.170
h	0.437	0.437
b	0.380	0.380

Material properties:		
	Young's modulus	$E = 7 \times 10^{10}$ N/m^2
	Shear Modulus	$G = 1 \times 10^{10}$ N/m^2
	Density	$\rho = 1939.3$ kg/m^3

TABLE 4.1.6. - RIB SECTION PROPERTIES (AVERAGE) FOR SIX-BAY SEGMENTATION.

Bay	Cross sectional area m^2	Bending inertia	
		Plane 1, I_{xx} m^4	Plane 2, I_{yy} m^4
1 (root)	0.478×10^{-3}	0.711×10^{-5}	0.534×10^{-5}
2	0.455×10^{-3}	0.683×10^{-5}	0.402×10^{-5}
3	0.436×10^{-3}	0.650×10^{-5}	0.304×10^{-5}
4	0.418×10^{-3}	0.638×10^{-5}	0.223×10^{-5}
5	0.401×10^{-3}	0.618×10^{-5}	0.157×10^{-5}
6 (tip)	0.386×10^{-3}	0.600×10^{-5}	0.104×10^{-5}
Note $J = I_{xx} + I_{xy}$ (torsion constant)			

114

TABLE 4.1.7. - HOOP-MEMBER PROPERTIES.

Property	Value
Cross-sectional area	4.48×10^{-4} m^2
Bending inertia	
Plane 1, I_{xx}	1.04×10^{-5} m^4
Plane 2, I_{yy}	9.63×10^{-7} m^4
Torsion Constant, J	1.14×10^{-5} m^4
Material properties: Young's modulus	$E = 7 \times 10^{10}$ N/m^2
Shear modulus	$G = 1 \times 10^{10}$ N/m^2
Density	$\rho = 1939.3$ kg/m^3
Note: Geometry (with reference to previous table)	
$t = 4 \times 10^{-4}$ m $h = 0.537$ m	
$w = 0.17$ m $b = 0.47$ m	

The membrane reflecting surface is characterized in terms of mass properties only; no system stiffness is assumed. For a membrane surface mass density of 0.1 kg/m^2, the total reflecting surface mass is 840 kg, which is then lumped at the rib grid points as shown in Table 4.1.8.

Additional mass, as shown in Figure 4.1.2 is added to account for the rigid hub, ACS packages, feed array, solar panels, and Astromast canisters.

The feed support subsystem, consisting of four Astromasts and four tension stays, was modeled using the structure stiffness and mass properties shown in Table 4.1.9. An "equivalent beam" representation was used to characterize the Astromasts.

TABLE 4.1.8. - SURFACE MASS DISTRIBUTION.

Grid	Bay	Length, L	Mean arc Length, s	Bay mass, kg	Grid mass, kg
1 (root)					.78
	1	9.5 m	1.64 m	1.56	
2					2.36
	2	8.02 m	3.93 m	3.15	
3					4.00
	3	8.05 m	6.02 m	4.85	
4					5.71
	4	8.10 m	8.12 m	6.57	
5					7.45
	5	8.16 m	10.21 m	8.33	
6					9.58
	6	8.75 m	12.3 m	10.82	
7 (tip)					5.41
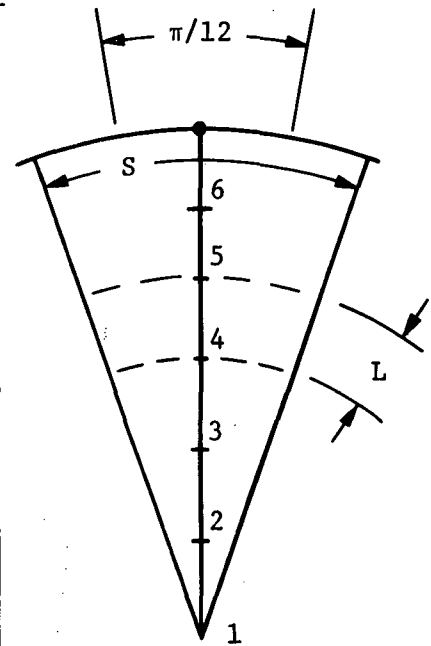
TABLE 4.1.9. - FEED ARRAY SUPPORT SUBSYSTEM CHARACTERISTICS.

Tension stays	Young's modulus	$E = 1.38 \times 10^{11}$ N/m^2
	Density	$\rho = 1939.3$ kg/m^3
	Area	$A = 1.29 \times 10^{-4}$ m^2
Astromasts	Young's modulus	$E = 1.38 \times 10^{11}$ N/m^2
	Shear modulus	$G = 2.06 \times 10^{10}$ N/m^2
	Density	$\rho = 12325$ kg/m^3
	Area	$A = 2.0 \times 10^{-5}$ m^2
	Bending inertia	$I = 4.74 \times 10^{-6}$ m^4

4.1.2.2 Rigid Body Mass Properties

Using the structure parameters described previously, the rigid-body mass properties are as shown in Table 4.1.10.

TABLE 4.1.10. - RIGID-BODY MASS PROPERTIES

Mass = 4161 kg

Principal inertias

$$I_{xx} = 4.56 \times 10^6 \text{ kg-m}^2$$
$$I_{yy} = 9.13 \times 10^6 \text{ kg-m}^2$$
$$I_{zz} = 1.06 \times 10^7 \text{ kg-m}^2$$

Mass center

$\overline{X}$ = 28.48 m above mounting hub

$\overline{Y} = \overline{Z} = 0$
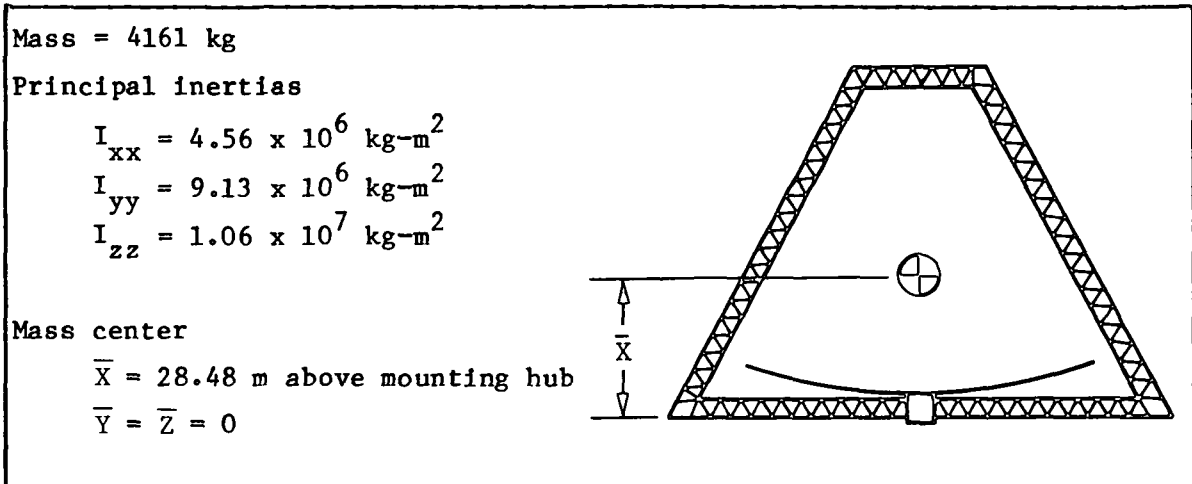
4.1.2.3 Model Characteristics

The total structural system consists of more than 1200 dynamic degrees of freedom. An eigenvalue analysis was performed and the frequency spectrum is shown in Table 4.1.11. Representative mode shapes are shown in Appendix B.

TABLE 4.1.11. - MODAL CONTENT THROUGH 0.5 Hz.

Mode	Freq, Hz	Mode	Freq, Hz	Mode	Freq, Hz
1-6	0.0 (rigid body)	12	0.1651	18	0.3500
7	0.03933	13	0.2161	19	0.3605
8	0.04207	14	0.2559	20	0.3800
9	0.04562	15	0.2560	30	0.4318
10	0.07090	16	0.3356	40	0.4444
11	0.1263	17	0.3389	50	0.5749

4.2 MEMBRANE STATICS AND DYNAMICS

This section discusses the statics of the electrostatic membrane and the dynamics of the membrane reflector.

4.2.1 Membrane Static Analysis

The electrostatic membrane is a tension structure. Its smoothness and stiffness are related directly to the internal membrane stress. The preferred membrane stress level is an involved subject. Table 4.2.1 lists the 9 different issues that dictate a high and low-stress level. Through repeated studies and testing, a consensus has developed on the operating stress level. The principal factors are the following:

(1) Materials and manufacturing flaws must be ameliorated;

(2) Thermal strains must be controlled;

(3) Micro-creep must be minimized;

(4) Tear propagation from holes or slits must not occur.

The membrane reflector undergoes large deflections but only moderate strains. Figure 4.2.1 is a schematic of the membrane reflector. The initial untensioned and tensioned shapes are both spherical. The center enlargement shows a typical membrane separation and deflection. Basic design variables are ΔZ, the membrane centerline deflection and the gap between the taut reflector and the control electrode. The stress in the taut reflector is proportional to ΔZ. The position stability of the membrane is proportional to the ratio of gap/ΔZ. The perimeter constraint is very important in membrane mechanics. In subsequent discussions on membrane thermal compensations, the fixed rim state will be replaced with an adjustable rim, which alters the stress state.

Possible operating voltages for the membrane are shown in Figure 4.2.2. The primary factors that influence voltage selection are seen in the following

TABLE 4.2.1. - MEMBRANE STRESS LEVELS.

Increasing membrane stress provides:
Higher stiffness ω $\alpha\sqrt{\sigma_c}$
Reduced amplitude of wrinkles
Attenuation of control electrode billow errors
Easier control over thermal stress
Looser tolerances in membrane manufacturing and splicing

Reducing membrane stress provides:
Lighter support structure to carry compressive loads
Lower voltages   V $\alpha\sqrt{\sigma_c}$
Less long-term micro-creep
Increased critical tear propagation length

expression:

$$V \ \alpha \ (EH)^{0.5} \left(\frac{gap}{\Delta Z}\right) (\Delta Z)^{1.5}$$

where EH is the product of Young's Modulus times thickness, gap/ΔZ = 0.4 is a
position stability parameter, and ΔZ = 0.25. This deflection corresponds to
a stress $\sigma(0)$ = 4.8 x 10^6 N/m^2. The centerline deflection is propor-
tional to stress. The solid line in Figure 4.2.2 corresponds to the minimal
safe voltage as a function of the centerline deflection, ΔZ.

The baseline membrane was not designed to a minimal voltage. The gap
between membrane reflector and control electrode was increased from 0.1 m to
0.2 m, which doubled the nominal operating voltage. The larger gap allows
more tolerant electrode designs. Allowable irregularities in the control
electrode surface increase dramatically as the gap is increased. This subject
will be discussed in detail later in this section. The nominal centerline
voltage for the baseline is 58 kV. This voltage is imparted to all elec-
trodes; however, the average gap increases as a function of radius which
effectively reduces the pressure near the edge.
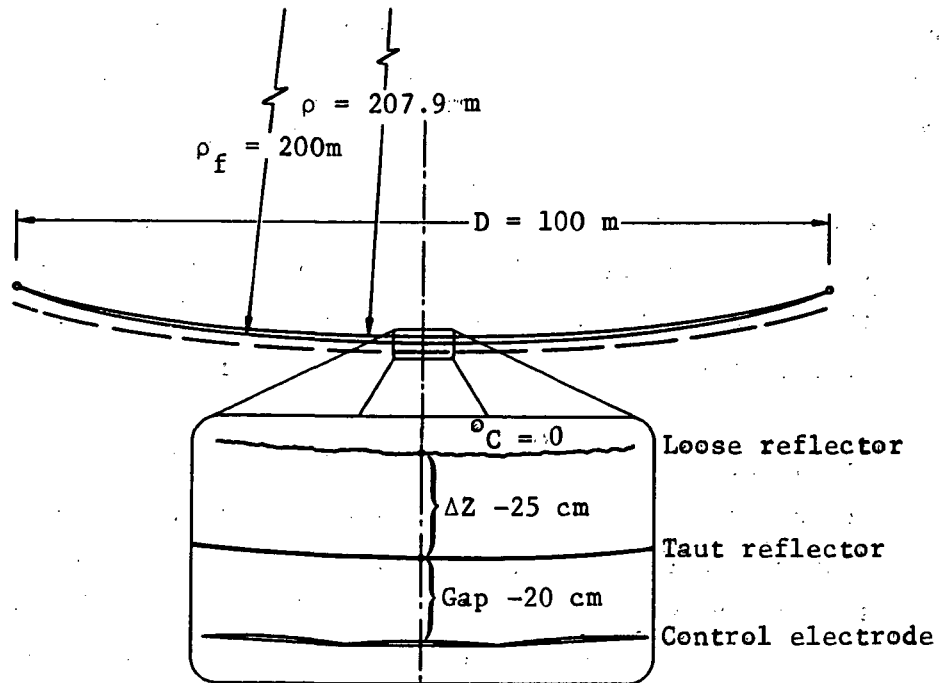
Figure 4.2.1. - Parameters of reflector preforming.
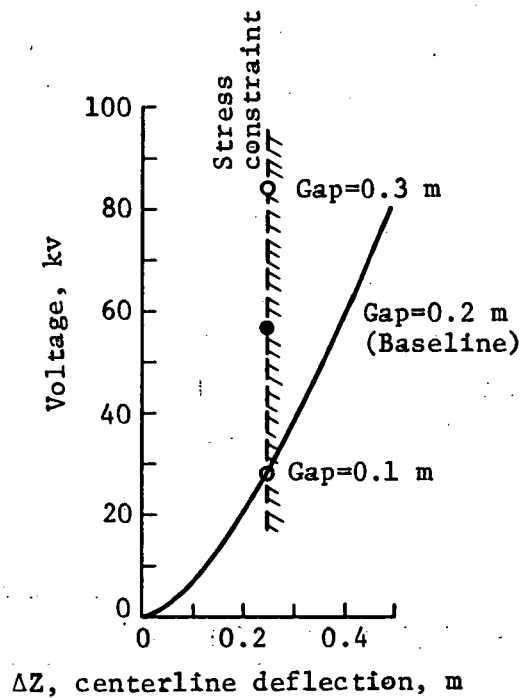
Figure 4.2.2. - Possible operating voltages with a stable surface.

The computer solution, based on large deflections of membranes (ref. 1), is used to determine the static state of the membrane reflector. Figures 4.2.3 and 4.2.4 and Table 4.2.2 summarize the more important parameters. The radial and azimuthal stress as a function of radius is shown in Figure 4.2.3. The stresses are given as fractions of the yield stress (σ_y = 82.7 x 10^6 N/m). The parameter in each set of curves is ΔZ or the preformed radius of curvature. It is seen that stress varies linearly with ΔZ. As a function of radius, the azimuthal stress varies considerably more than the radial stress. The radial stress only decreases 20 percent from centerline to the rim, but the azimuthal stress varies by 75 percent.

The electric field strength as shown in Figure 4.2.4 decreases from the centerline to the rim by 31 percent. The electrostatic pressure, proportional to field strength squared, decreases by 52 percent from centerline to the rim. As mentioned previously, the average gap rather than voltage (on each electrode) is used to obtain the decreasing field strength, and pressure. The gap is 0.2 m at the center and 0.29 m near the rim.

A tabular summary of the important parameters is presented in Table 4.2.2. Stress and electrostatics data are shown every 2 m. The radial and azimuthal stresses are identical and have a maximum value at the centerline. At the rim their ratio is γ, Poission's ratio for the membrane.

4.2.2 Membrane Dynamic Analysis

To this point, statics of the membrane base have been discussed. This section will discuss dynamics of the membrane reflector. The results are presented for free vibrations (i.e., without a control system). The eigenvalue solution is a set of linearized equations that use a prior nonlinear

---

1. D. J. Mihora: Stresses in an Adaptive Membrane Reflector—the Electrostatically Controlled Membrane Mirror. General Research Corporation IM-2335, Presented at Eighth U.S. National Congress of Applied Mechanics, June 26-30, 1978, University of California, Los Angeles.
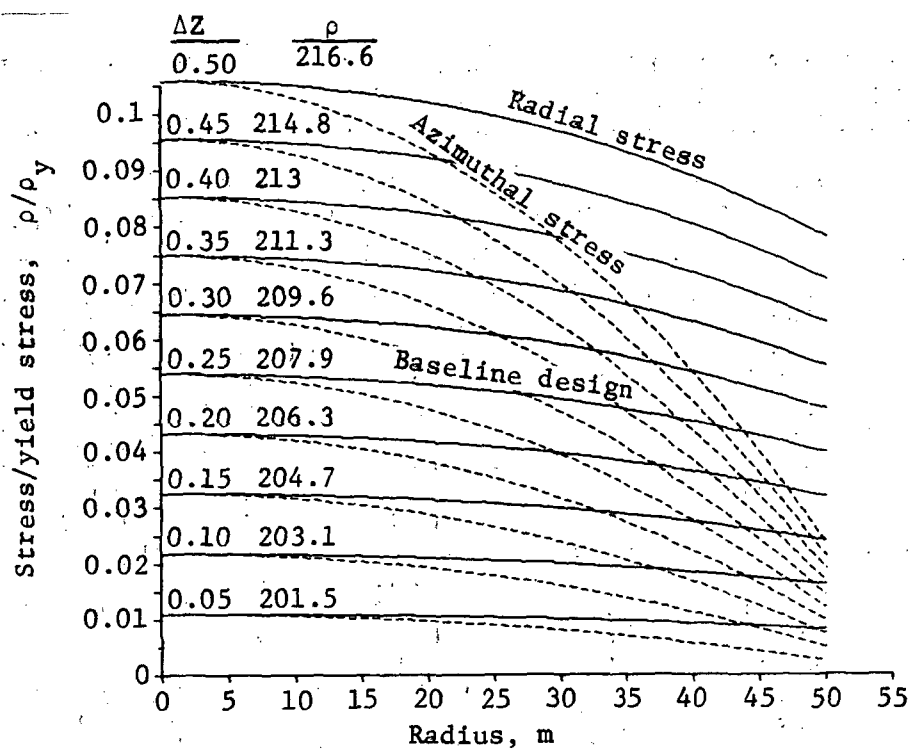
Figure 4.2.3. – Stress distribution.
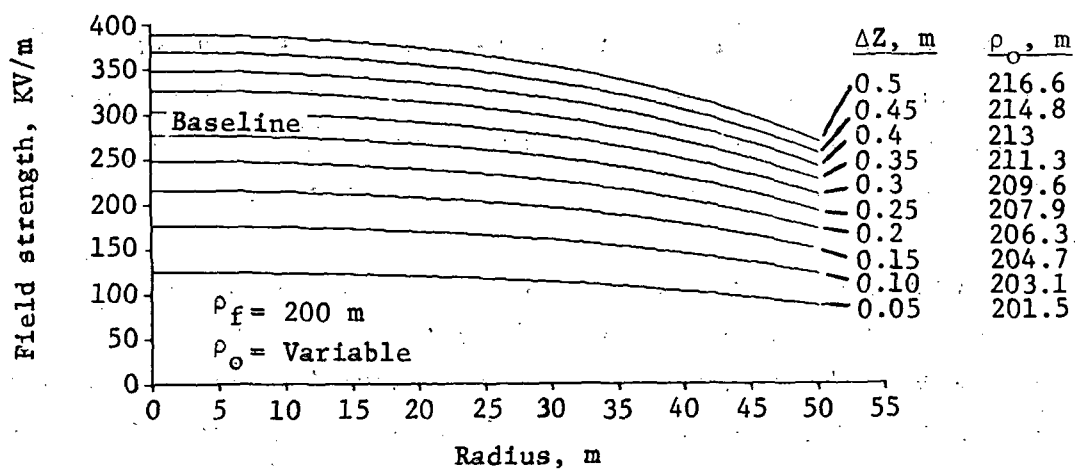
Figure 4.2.4. – Electric field strength distribution.

TABLE 4.2.2. – BASELINE PROPERTIES OF 100-m APERTURE, $f_N = 1.0$ AT T = 300 K
(ρ_f = 200 m, ρ_o = 207.94 m, f_N = 1.0, G = 0.2 m)

Radius, m	Pressure, N/m²	Height tensioned m	Height untensioned, m	Radial stress, fraction of yield	Azimuthal stress, fraction of yield	Azim/Rad stress	Electric Field, V/m
0.00000	0.34004	6.35083	6.10083	0.05391	0.05391	1.00000	277365
2.00000	0.33986	6.34083	6.09123	0.05389	0.05386	0.99946	277292
4.00000	0.33906	6.31083	6.06242	0.05384	0.05366	0.99768	276966
6.00000	0.33772	6.26081	6.01439	0.05374	0.05334	0.99261	276419
8.00000	0.33585	6.19077	5.94713	0.05360	0.05289	0.98678	275650
10.00000	0.33343	6.10068	5.86062	0.05341	0.05230	0.97926	274655
12.00000	0.33047	5.99051	5.75483	0.05319	0.05159	0.97000	273433
14.00000	0.32696	5.86023	5.62973	0.05292	0.05075	0.95896	271978
16.00000	0.32290	5.70981	5.48528	0.05261	0.04977	0.94608	270284
18.00000	0.31828	5.53919	5.32143	0.05225	0.04866	0.93129	268435
20.00000	0.31310	5.34832	5.13813	0.05185	0.04742	0.91452	266153
22.00000	0.30736	5.13715	4.93533	0.05141	0.04604	0.89569	263700
24.00000	0.30104	4.90561	4.71296	0.05091	0.04453	0.87467	260974
26.00000	0.29413	4.65363	4.47096	0.05037	0.04288	0.85134	257963
28.00000	0.28663	4.38113	4.20923	0.04978	0.04110	0.82557	254655
30.00000	0.27854	4.08803	3.92771	0.04914	0.03917	0.79717	251031
32.00000	0.26983	3.77424	3.62630	0.04844	0.03711	0.76595	247075
34.00000	0.26049	3.43965	3.30490	0.04769	0.03490	0.73167	242764
36.00000	0.25052	3.08415	2.96341	0.04689	0.03254	0.69406	238074
38.00000	0.23991	2.70765	2.60171	0.04602	0.03004	0.65279	232975
40.00000	0.22863	2.31001	2.21969	0.04509	0.02739	0.60747	227432
42.00000	0.21667	1.89111	1.81722	0.04410	0.02459	0.55763	221405
44.00000	0.20402	1.45081	1.39417	0.04305	0.02164	0.50272	214845
46.00000	0.19066	0.98896	0.95038	0.04192	0.01853	0.44207	207690
48.00000	0.17657	0.50541	0.48571	0.04072	0.01526	0.37483	199868
50.00000	0.16173	0.00000	0.00000	0.03944	0.01183	0.30000	191284

solution to obtain static properties of the membrane. The notation used to index the mode shapes is presented in Figure 4.2.5. For shallow membrane surfaces, the lowest mode (1 = 0, m = 0) has no node lines. It is a simple convex shape. The left three modes (m = 0) are the lowest symmetric modes.

Twelve of the modes associated with the baseline reflector are presented in Figure 4.2.6. Normalized modal amplitude is shown as a function of radius. Associated with the mode shape is its natural frequency. A consequence of the deep dish (N = 1) is an unusual lowest mode shape. The shape is quite different from the drumhead mode shown in Figure 4.2.5. The natural frequency of the lowest mode is 8.92 rad/s (1.42 Hz).

123

n=0, m=0 ——————— ω_{00}

n=0, m=1 ——— ω_{10}

n=1, m=0 ——— ω_{01}

n=1, m=1 ——— ω_{11}

n=2, m=0 ——— ω_{02}
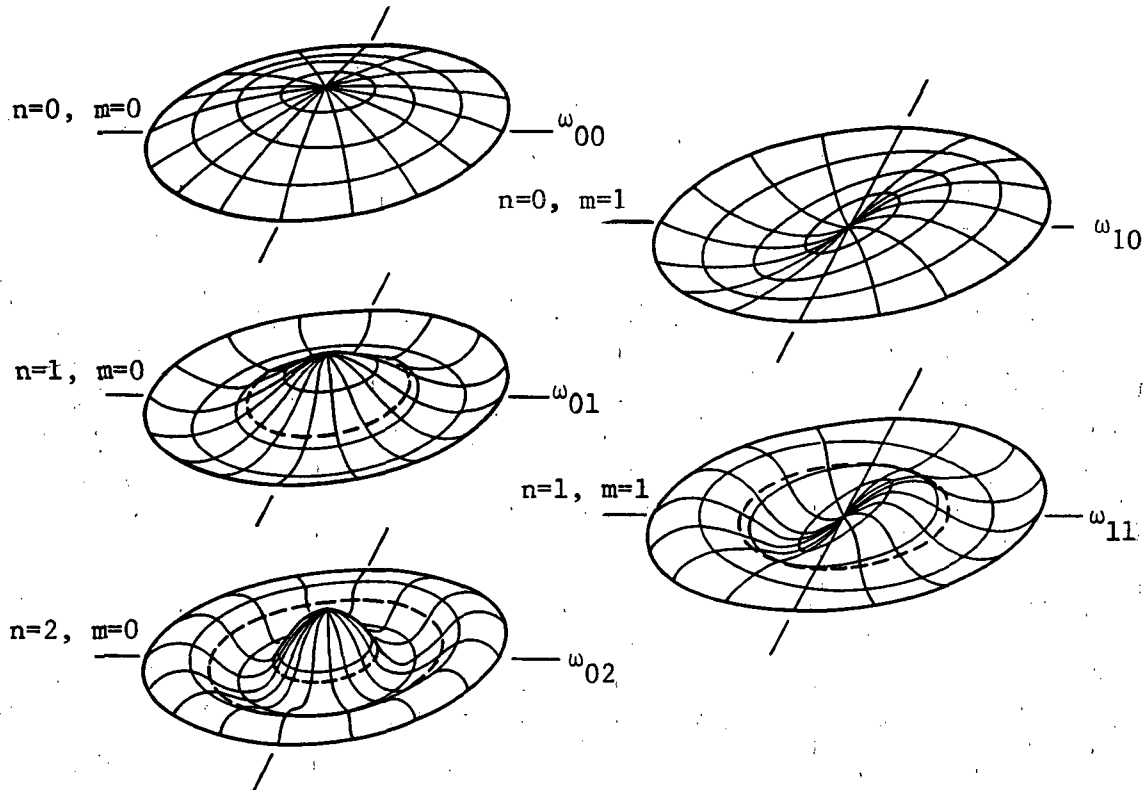
Figure 4.2.5. - Notation associated with radial (n) and
azimuthal (m) mode shapes.

The membrane reflector is a very stiff structure. It has a substantially
higher natural frequency than the feed structure and beams. It has about the
same natural frequency as the deep-box compression rim designed by Martin
Marietta Corporation. These cases are all at the lowest tension condition,
corresponding to a temperature of 300 K. Depending on the final selected
perimeter compensation, the membrane reflector natural frequency can be higher
at colder temperatures, because the membrane frequency varies in proportion
to $\sqrt{\sigma_c}$.
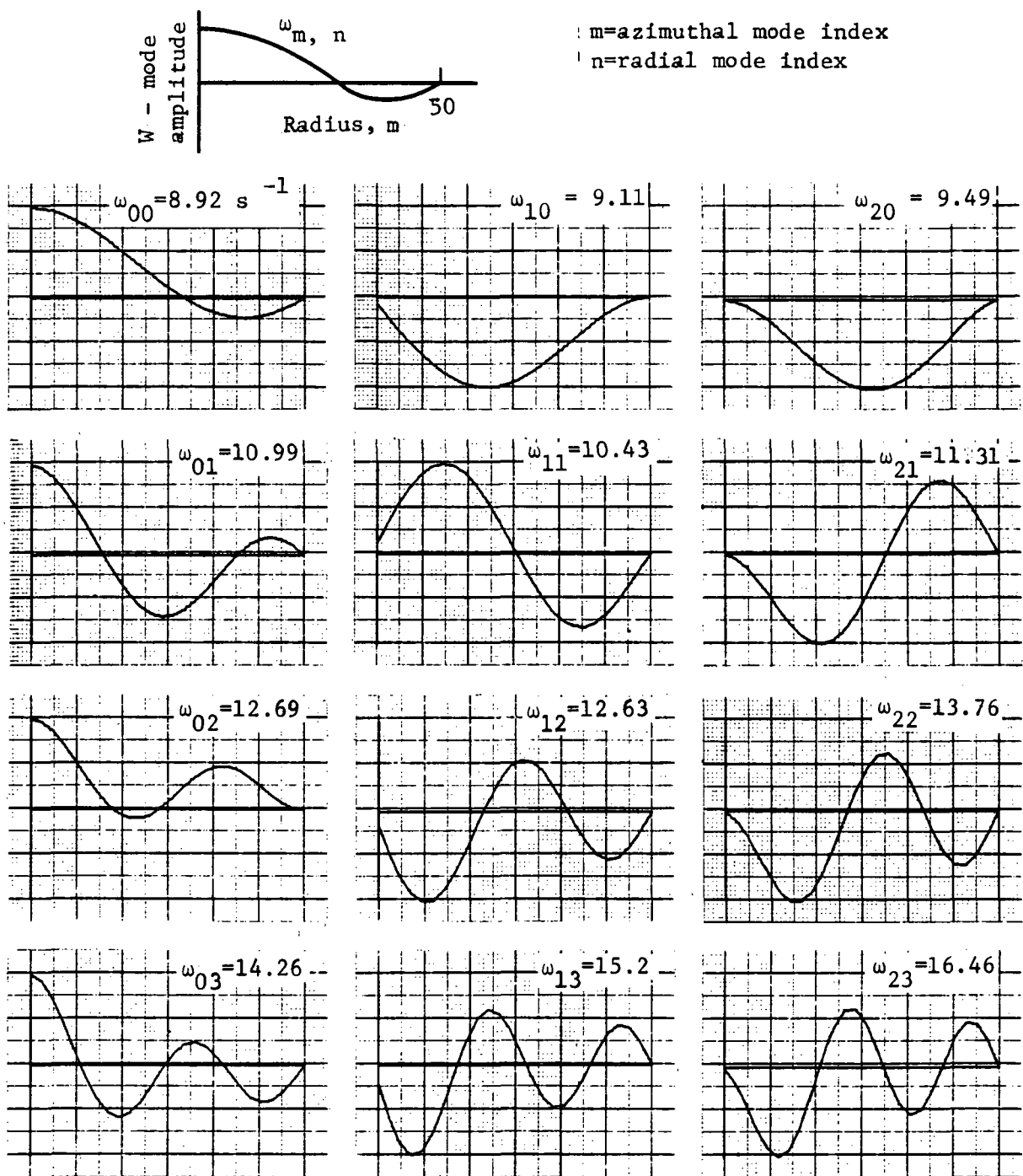
Figure 4.2.6 - Summary of lowest modes.

4.3 THERMAL EFFECTS

This analysis provides a first-cut presentation of antenna thermal performance in the form of structural temperature data, defines potential problems, and recommends favorable thermal options.

4.3.1 Summary of Results and Conclusions

The results of this study depend entirely on the thermo/optical property values. The major focus has been placed on what are termed as Case 1 thermal properties. For this case membrane surface properties were assumed to be:

(1) Solar absorptivity = 0.12
(2) Emissivity = 0.04

All ECMM membranes were assumed to be double-aluminized polymeric films having the above properties on both sides.

Using Case 1 properties, at no time will the ECMM reflector change in temperature at a rate greater than $2^\circ C/s$. This includes the time at which the spacecraft enters the penumbra, the Earth's shadow sweeping across the reflector, and the times when the rim shadow moves across the reflector surface.

The reflector will have minimum and maximum temperatures of -7.8 and $100^\circ C$, respectively. By coating surfaces black (see Case 2 results) this temperature differential can be reduced to approximately $100^\circ C$. At no time will a gradient larger than $47^\circ C$ exist on its surface. ECMM minimum and maximum temperatures, plus the maximum gradient for the outer shroud, drawing, electrode, and reflector membranes are summarized in Table 4.3.1 for Case 1 and 2 properties. Box truss temperatures, including surface tubes and diagonal tapes, range in temperature from -104 to $82^\circ C$.

Analysis of the Astromast and box truss used simplified assumptions. Cost limitations prevented a complete detailed analysis of both structures. It should be noted the temperatures presented in this study may be different from actual mission temperatures because they depend on an assumed worst-case spacecraft orientation in orbit.

TABLE 4.3.1. - SUMMARY OF CASE 1 AND CASE 2 RESULTS.

	Reflector membrane			Electrode membrane			Drawing membrane			Outer shroud		
	Tmin	Tmax	Max grad	Tmin	Tmax	Max grad	Tmin	Tmax	Max grad	Tmin	Tmax	Max grad
Case 1: (°C)	-7.8	100	47	34	64	6.6	-71	221	60	-61	216	233
Case 2: (°C)	-39	103	28	24	83	16	-59	208	38	-46	202	213

TABLE 4.3.2. - SUMMARY OF THERMAL PROPERTIES.

	α, (exterior)	ε, (exterior)	α, (interior)	ε, (interior)
Case 1	0.12	0.04	—	0.04
Case 2	0.12	0.04	—	0.9
Case 3	0.09	0.01	—	0.01
Case 4	0.9	0.9	—	0.9

A 670-km circular orbit in the solar ecliptic plane (beta angle = 0) was assumed in this analysis. Detailed transient orbital temperatures for Case 1 and Case 2 are in Appendix C. Other cases presenting possible thermal options and problems are discussed later in this report.

4.3.2 Discussion of Analysis

The majority of analysis effort was involved in developing an appropriate computer model for predicting antenna temperatures. Two Martin Marietta in-house computer programs were used for this effort. The first program, TRASYS, calculates incident space heat fluxes and radiation exchange factors. The second, MITAS, uses TRASYS output to compute resultant ECMM structural temperatures.

The ECMM consists of three membranes - the exterior reflector, the electrode, and drawing membranes. Bounding their outer circumference is another cylindrical membrane, which shall be referred to as the outer shroud. When taken in its entirety, the ECMM appears as a large opaque concave lens. The membrane was divided into small sectional areas, each area serving as a temperature node for predicting membrane temperature distributions. All ECMM membranes were apportioned into eight circumferential sections. The reflector, electrode, and drawing membranes were divided axially into three additional sections making a total of 24 nodes for each of these membranes. The outer shroud was not divided axially leaving eight temperature nodes around its circumference. Figure 4.3.1 illustrates the ECMM temperature node scheme. The model also includes two sections of the deployable box truss and two Astromast longerons. Computer cost limitations made it impossible to model the entire box truss. However, using two sections located at 90 degrees from each other makes it possible to gain an estimate of the circumferential temperature distribution around it. Figure 4.3.2 shows the box sections in position relative to the ECMM. Temperatures have been predicted and are presented in this report for selected sections of each box indentified in the figure as Box 1 and Box 2. Both tube and tensioning tape temperatures are included in these data.

Astromast longeron temperatures were predicted at 10 longitudinal loca-
tions from the membrane up to the distributed feed horn and support struc-
ture. Once again cost limitations prevented modeling the entire Astromast.
Nevertheless, the most critical worst-case information needed to determine
Astromast thermal distortion should be provided by predicting longitudinal
temperatures. The analysis did not include guylines. It will, however,
provide suitable boundary conditions for predicting guyline temperatures.

TRASYS was used to calculate incident space heat fluxes and infrared
radiation interchange factors. In conducting this analysis the spacecraft was
assumed to be in a circular 670-km orbit, the orbital plane coinciding with
the solar ecliptic plane as shown in Figure 4.3.3. This is typically referred
to a 0-degree beta angle orbit. Although the nominal proposed orbit has a
30-degree angle of inclination with the equator, this orbit presents the
worst-case condition for temperature gradients. In other words, if the space-
craft does not exceed design limitations for a beta angle of 0 degrees, it
will not be exceeded for any other orbit.
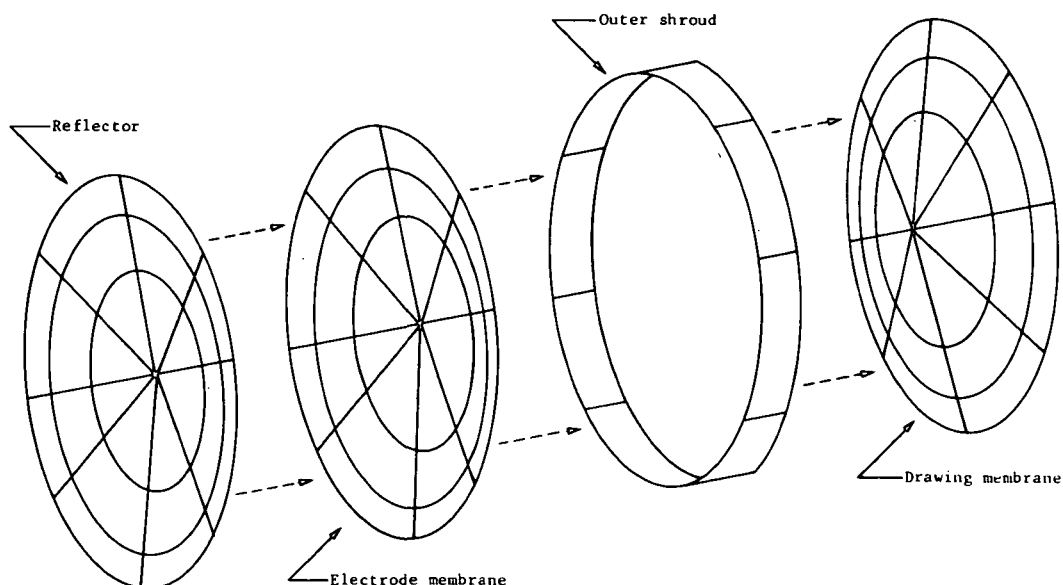
Figure 4.3.1. - ASSA-membrane modal breakdown scheme.
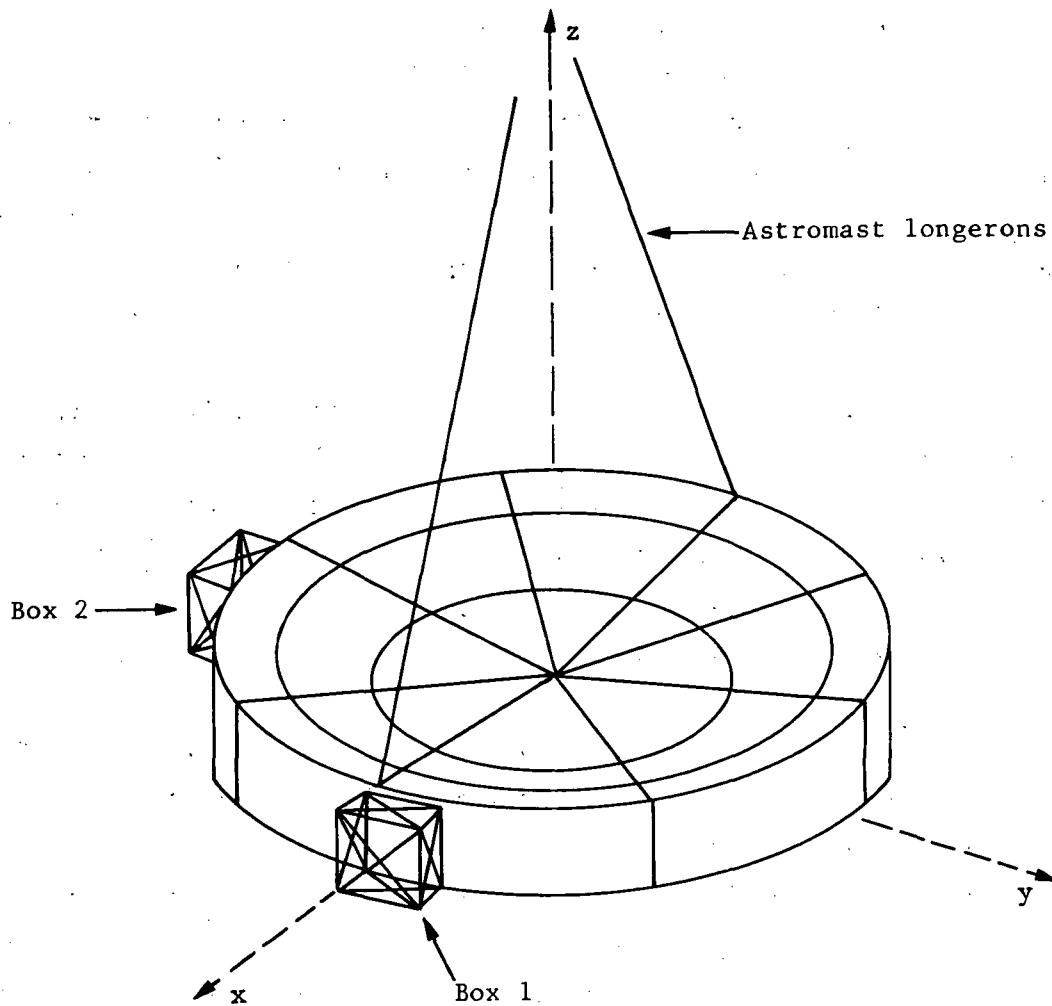
Figure 4.3.2. - Box section positioning.

A feature of TRASYS incorporated specifically for large space structure use is the capability to model large truss structures in a fast and efficient manner by minimizing the engineer's task of defining a complex truss geometry within any given coordinate system. For example, the deployable box truss, which consists of long narrow cylindrical tubes and long rectangular tensioning tapes, can be modeled in TRASYS as a group of structural elements and tapes. The elements and tapes option minimizes the amount of data necessary to define a cylindrical or rectangular surface. This feature is only

capable of calculating incoming and outgoing heat fluxes governed by the orbital environment and cannot be used to calculate radiation view factors. Usually this is sufficient when analyzing a box truss as the view from one structural element to another is small enough that it can be assumed negligible. This is true with the ECMM-deployable box truss. However, box truss-to-ECMM radiation exchange is not negligible. Therefore, it was necessary to calculate view factors from each box to the membrane.

TRASYS was also used to calculate internal radiation exchange couplings between ECMM membranes. The symmetrical geometry of the membranes was used to avoid making redundant views of the membranes and to avoid making redundant view factor calculations. Only view factors for a one-eighth segment were required. All other membrane surfaces have an identical geometry and calculating view factors from a one-eighth segment is transferable to all.

Space heat flux and infrared radiation exchange data generated by TRASYS was input into MITAS to calculate resultant structural temperatures. To calculate temperature profiles the thermal capacitance of each node must be calculated and input into MITAS. The spacecraft was allowed to initially come to a steady state condition at time equal to 0 hours. After this the transient response was calculated. Temperatures are reported in this study after two complete orbits, because it took this long before the antenna stabilized and the temperatures became repetitive. Figure 4.3.4 shows the orbitial time locations for which the data in Appendix C are presented.

To calculate thermal capacitance and define ECMM geometry, structural dimensions were taken from LSS drawing 82204000000 and the ASSA March 1981 midterm review. Graphite/epoxy tubes and graphite tapes were both assumed to have a density of 1600 kg/m^3 and specific heat of 0.25 cal/gm-$^\circ$K .

Although the deployable box truss is well defined in regard to both material and dimensional characteristics, the Astromast longerons are not. This made it necessary to assume both their physical and thermophysical properties. Their shape was assumed to be a solid cylinder having a radius equal to 0.357 cm, density of 4480 kg/m^3, and specific heat of 0.14 cal/gm-$^\circ$K.
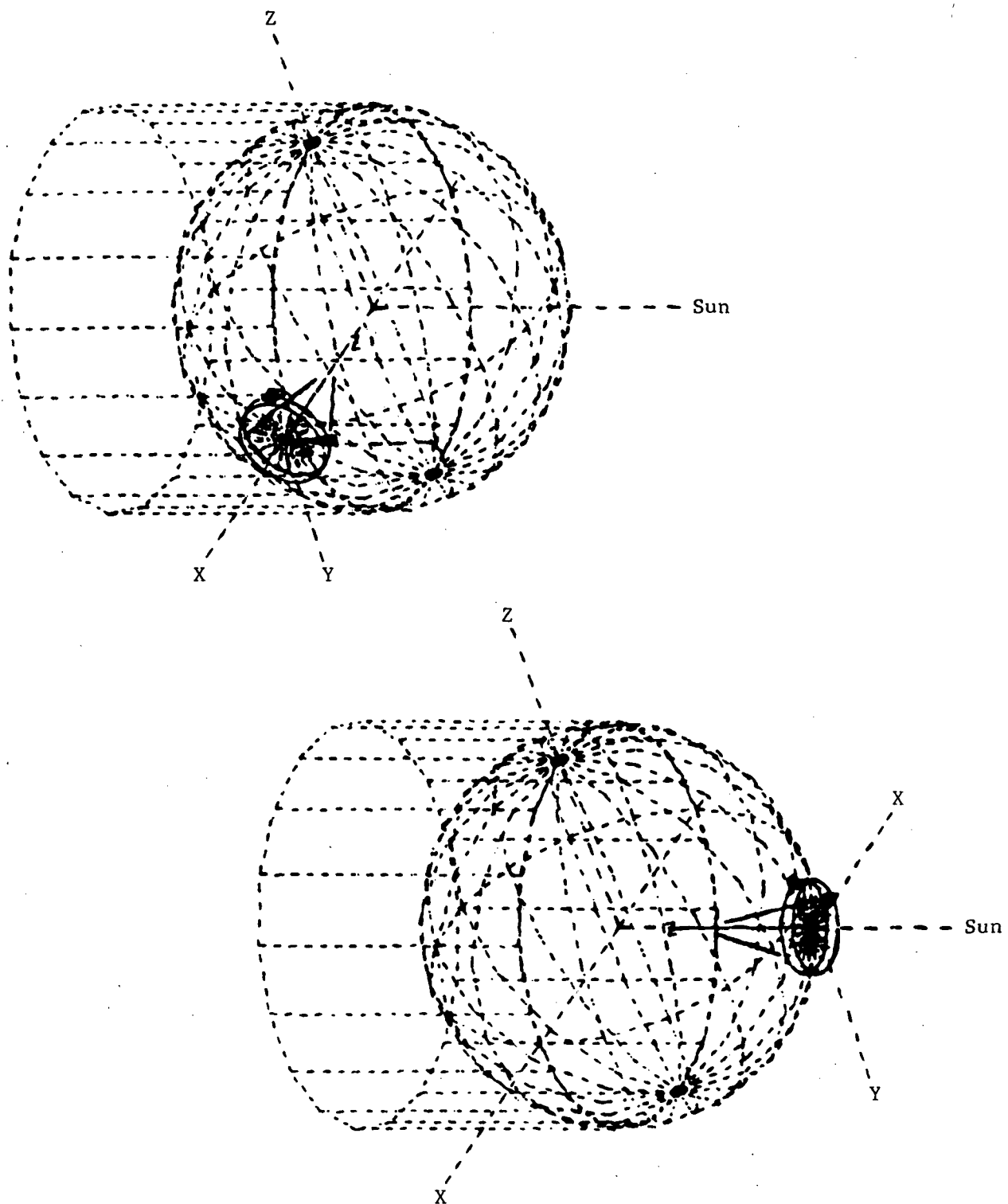
Figure 4.3.3. - Spacecraft orbit.
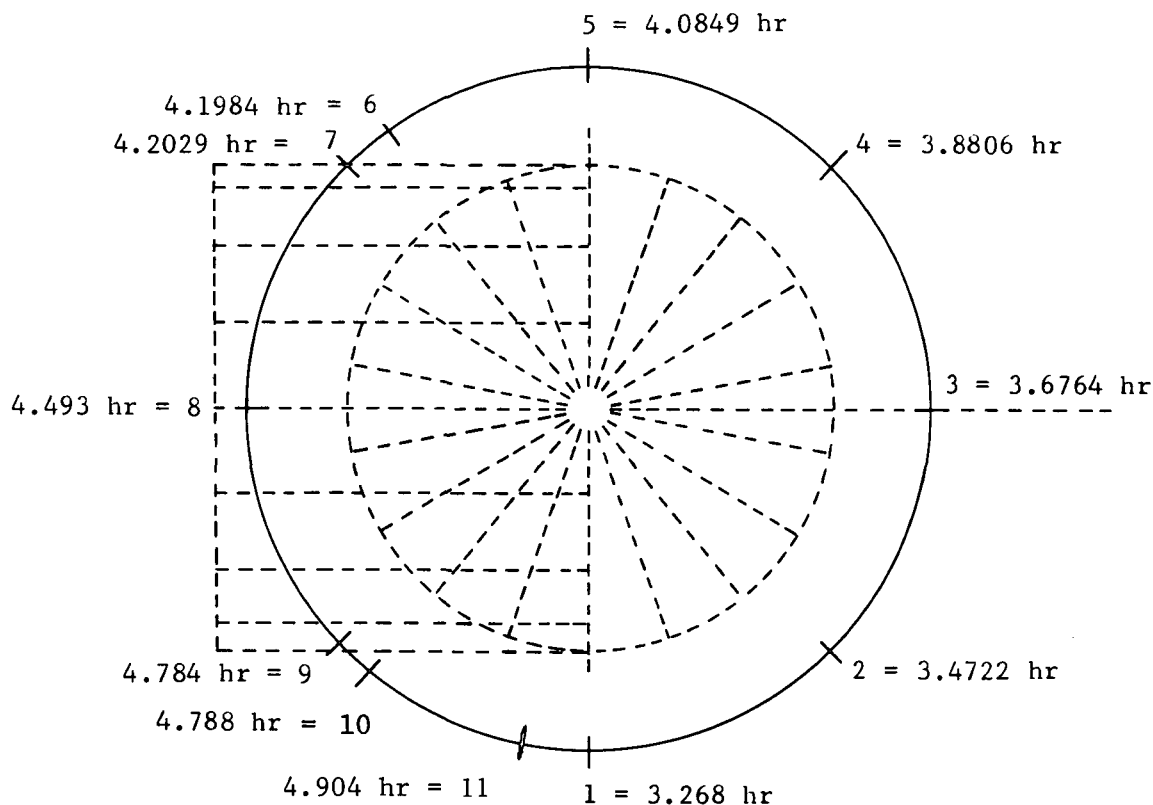
Figure 4.3.4. - Orbital time locations.

4.3.3 Discussion of Results

The thermal performance of any large space structure in Earth orbit primarily depends on the aggregate influence of several factors. One factor is the space heating environment, i.e., direct incident solar, and if applicable, planetary albedo and planetary thermal radiation in the infrared (IR) region. This study assumed the antenna to be in a 670-km orbit. At this altitude, the effects of planetary albedo and thermal are lessened, but by no means can they be ignored.

In conjunction with the space heating environment are structural interior and exterior surface thermo/optical properties. They determine the amount of all incoming heat fluxes that are absorbed, affect IR radiation exchange between different structural areas, and govern emitted reradiation to space.

Four cases are discussed in this study, each with different thermo/optical properties. They demonstrate the influence of thermo/optical properties on structural temperatures and their importance when formulating good thermal designs.

Another factor to be considered is structural thermal capacitance. This affects a structure's ability or inability to store internal thermal energy. Stored thermal energy (directly relatable to structural mass) affects transient temperature response. The ECMM has a very small capacitance in relation to its large area. This usually reduces the effect of capacitance because the magnitude of the absorbed and reradiated heat fluxes are usually much greater than the stored energy. The environmental fluxes will be the main drivers in the energy balance of a surface, thereby reducing the temperature time lag caused by capacitance effects.

Thermal capacitance, however, cannot be ignored as long as the ECMM has aluminized surfaces. An aluminized surface significantly reduces the absorbed and emitted fluxes allowing capacitance to become more influential. It becomes especially important at the point where the antenna passes out of the Sun into the Earth's shadow. A point of concern is the possible occurrence of large temperature gradients across the reflector as the Earth's shadow sweeps across it. At this time, the antenna has a large enough capacitance to negate extreme temperature gradients.

Lastly, thermal performance is affected by heat energy generated by electrical components. Internal heat generation is not a factor when examining the entire ASSA structure in bulk form as has been done in this study. It will be a factor, however, in the future when it becomes necessary to analyze smaller electrical components that are always auxiliary to any large space system.

The selection of thermo/optical properties will be the major factor influencing ECMM thermal performance. The orbital environment, i.e. solar, Earth thermal, and albedo fluxes, are fixed for the assumed 670-km orbit. Thus, the thermo/optical properties govern the amount of those fluxes that are absorbed by ECMM surfaces and the ability of those surfaces to reradiate IR to space. Four cases have been devised in this study, each case considers a

134

different set of properties on the membrane. The first case assumed all ECMM surfaces to have vapor-deposited aluminum on both sides. The solar absorptivity and emissivity were taken to be 0.12 and 0.04, respectively.

The second case assumed all external ECMM surfaces to be coated with vapor-deposited aluminum having the same properties as above. In this case, interior surfaces were assumed to be black (ε = 0.9). The rationale for devising this case is that coating interior surfaces will enhance internal radiation heat transfer thereby reducing temperature gradients between the different ECMM membranes. Having something other than a metallic coating on a surface that has to meet an electrical conductivity requirement is a valid concept. The metallic layer need only lie underneath thin nonmetallic coatings that are essentially rf transparent.

The third case presents the predicted temperatures that result from ref. 2 properties and illustrates the necessity of determining exactly the properties of aluminized Kapton. There is some discrepancy in the definition of the thermo/optical properties of metallized films. Ref. 1 indicates a solar absorptivity of 0.09 and emissivity of 0.01 for aluminized Kapton. This is a substantial deviation from properties assumed in Case 1.

The last case assumes the ECMM has an external coating with properties comparable to black paint. As mentioned previously, this is valid in that as long as the membrane has a metallic layer underneath the external coating, its rf capability is not inhibited. A black coating was chosen in this last case over other potential candidates because it is not subject to the normal thermo/optical property degradation problems that occur after a long period in the orbital environment. Black coatings typically have high values for solar absorptivity and emissivity, the ratio of these two values being approximately equal to 1.0. Unlike other nonmetallic coatings having a lower absorptivity/emissivity ratio, these properties will not change appreciably in the long term. An example of this type of coating would be white paint.

---

1. "Properties of Metallized Flexible Materials in the Space Environment." TRW Report 26177-6048-RU-00, SAMSO TR 78-31; Richard M. Kurland, G. L. Brown, J. F. Thomasson, J. T. Bevans, W. P. Bell; January, 1978.

When a structure's external coating is subject to degradation, it is difficult to predict its temperature at the end of mission life. Very little comprehensive information is available in the aerospace industry dealing with property degradation rates. Available data indicate that metallic surfaces do not degrade appreciably, nor will an organic coating that has a ratio of absorptivity to emissivity of one. If the ECMM cannot be designed within these constraints, i.e., if coatings having an absorptivity/emissivity ratio substantially lower than 1.0 are required, then the problem of degradation poses a formidable subject for future thermal analysis. This indicates that adequate thermal performance can be achieved using metallized Kapton, thereby rendering the degradation issue moot.

For all four cases the box elements and longerons were assumed to be black with a value of 0.9 for both absorptivity and emissivity. All thermo/optical property values are summarized in Table 4.3.2 for each case analyzed. Most of the results focus on Case 1 analysis because this configuration probably is the most likely candidate for selection as the ASSA baseline design. Only reflector temperatures are discussed in this text. Comprehensive data for all surfaces can be found in Appendix C. Focus has been placed on the reflector because its thermal performance is the most critical to the design. The box truss and Astromast will be treated independently of the membrane analysis. This has been done because this study is a first cut presentation and, except for Case 4, the temperatures remain substantially the same in all aluminized cases. Case 4 box truss and Astromast temperatures are not discussed because this case will not be recommended for reasons to be discussed later.

4.3.4 Results and Conclusions

Using Case 1 properties, a maximum temperature gradient of approximately $47^\circ C$ is predicted for the ECMM reflector surface. This gradient occurs just before the spacecraft enters the Earth's penumbra region. At no time will any reflector surface change at a rate faster than $2^\circ C/s$. This includes rim shadowing and penumbra passage. Concern has been expressed that as a shadow sweeps across the antenna, part of the reflector will be illuminated and part

136

will be shadowed, resulting in a severe temperature gradient that thermally stresses the membrane for a short period. This phenomenon will not occur with Case 1 properties.

Although reflector thermal capacitance is extremely small, it becomes significant when combined with low values of solar absorptivity and emissivity and when the transient change in orbital enviroment, i.e., heat fluxes, occurs quickly. These factors are all present in Case 1. First, low values for absorptivity and emissivity tend to reduce gradients. This means that if the reflector is partially in the Sun and partially shaded, the absorbed flux in the illuminated area is small in relation to the incident flux and the low emissivity of the surface is conductive to heat retention in the shadowed area because of lowered IR reradiation to space. Absorbed incident and emitted IR heat fluxes are the primary drivers in determining ECMM thermal response. Reducing the amount of absorbed heat allows the thermal capacitance to have a more important influence on transient temperature response, increasing structural temperature lag after the change in orbital environment. Second, the spacecraft is traveling at approximately 27 000 km/hr in its assumed orbit and entirely passes into the penumbra in approximately 0.02 seconds. The aggregate of these factors results in the reflector not being able to change more than $2^{o}C$ within this time. Analytical verification can be found by examining the change in reflector temperature from 4.1984 hours to 4.2029 hours in Appendix C. The time difference is approximately 16.2 seconds, and penumbra passage occurs sometime within it. During this time no reflector surface changes more than $1^{o}C$, yet the solar flux has gone from a full Sun to zero. The $47^{o}C$ gradient reported earlier occurs just after the reflector has undergone a rim shadow passage. Although the transient analysis was not done in sufficient detail to track the shadow across the reflector, this gradient can be used as a first-cut indicator of the maximum gradient to be expected. It is important to keep in mind that although the reflector is subject to rim shadowing, those portions of the reflector that are shadowed still receive an energy input via IR radiation from other membrane surfaces. In fact, this analysis indicates that radiation exchange with other membranes tends to modulate the heating and cooling rates of reflector surfaces to an appreciable degree.

Overall, the Case 1 reflector will achieve a minimum and maximum temperature of -7.8 and 100°C during the orbit. Other surfaces fluctuate between greater extremes. For example, the outer shroud has a minimum and maximum of -61 and 216°C. The drawing membrane varies from -71 and 221°C. It is impossible to negate large temperature swings when a spacecraft with a large area-to-mass ratio passes in and out of the Earth's shadow. The best that can be hoped is to alleviate temperature gradients thereby keeping thermal expansion and contraction symmetric, eliminating "slew" distortions.

Case 2 was run to show the effect that changing the internal emissivity to 0.9 would have on ECMM temperature gradients. Increasing internal emissivity while leaving external properties constant will modulate internal temperatures thereby reducing gradients. This is reflected in a maximum reflector temperature gradient of approximately 28°C, 19 degrees less than Case 1 results. The overall ECMM temperature swings are slightly less extreme with reflector temperature ranging from -38 to 103°C , drawing membrane from -59 to 208°C, and outer shroud from -46 to 200°C. No problems with penumbra passage should be expected for this case as the external ECMM properties have remained constant. The only negative aspect to an internal black coating would be the added weight to the ECMM. Because Case 1 results are probably adequate, it may not be necessary to undergo an additional weight penalty. ECMM Case 2 results are presented in Appendix C, along with Case 1.

The analysis in Case 3 was undertaken to illustrate that thermo/ optical properties of an aluminized surface must be accurately defined. Ref. 1 information indicates a solar absorptivity of 0.09 and an emissivity of 0.01 for aluminized Kapton. If these are valid numbers, ECMM temperatures could exceed 370°C, thereby approaching the temperature material limits of Kapton.

Case 4 was analyzed to show the temperatures that would result if a black exterior and interior coating were used on the ECMM. Very large temperature swings occur on the drawing membrane. It varies from -190 to 121°C. This large variation is probably undesirable, although at no time are gradients larger than in Case 2. The major problem with coating the ECMM black is that it increases absorptivity and emissivity, depressing the effect of thermal

capacitance. This allows membrane temperatures to change more rapidly with a changing orbital environment making penumbra passage and rim shadowing a potential problem. Case 4 temperatures are included in Appendix C but not in the same detail as Cases 1 and 2.

Although the primary focus of this analysis has been on the ECMM, an analysis in abbreviated detail of the Astromast, box truss, and guyline tapes has also been included. Astromast analysis assumed both longerons to be in the same plane so that shading (although it is minimal) would be included. In reality this probably will not be the actual orbital configuration. Nevertheless, it is the thermal worst case because nonparallel longerons have different angles of incidence in regard to solar heat flux resulting in worstcase temperature differences between them. The longerons range in temperature from -93 to 46°C. There is never a temperature difference greater than 47°C between them. Because of the different angles between tubes and tapes in the box truss, large temperature differences will result. Box temperatures will range from approximately -104 to 77°C. Tape temperatures are approximately the same with a range of -101 to 82°C. Temperature gradients in any one box section of the deployable box truss can run as high as 166°C.

Box truss temperatures are included in Appendix C along with Case 1 temperatures. As mentioned earlier, box temperatures are about the same for all aluminized cases. A black ECMM would produce different results as there would be greater radiation exchange between box truss and membrane; this situation is not presented.

In conclusion, the results of this study depend entirely on the accuracy of the thermo/optical properties used. If the assumed properties for Case 1 are accurate, then the ASSA baseline design is feasible from the thermal performance standpoint.

4.4 CONTROL ELECTRODE GEOMETRY

Control electrode analyses have been directed toward a very low-mass surface. It appears that a variety of membrane and reinforcing materials can be used to form and adjust the precision membrane reflector. The electrode geometry is intrinsically associated with the membrane reflector smoothness. Before describing the electrode surface geometry, the electrode influence characteristics are presented.

Figure 4.4.1 shows the effect of spatially distributed loads on an elastic string. The higher spatial frequencies result in a reduced rms irregularity. A tensioned membrane surface responds in a similar manner. In Figure 4.4.1, the electrode waviness is introduced as a spatial variable. The amplitude of the sinusoids, Δ as ratioed to the mean separation, gap, produces a varying loading. A higher number of cycles over the diameter will reduce the waviness imparted to the membrane. From the expression

$$P_o = \frac{\varepsilon_o}{2}\left(\frac{V}{\ell}\right)^2$$

where $\varepsilon_o = 8.84 \times 10^{-12}$ F/m, free space dielectric constant

V = electrode voltage

ℓ = membrane-to-electrode separation

substituting $P_o = P + \Delta P$ and $\ell = $ gap $ + \Delta$, one obtains

$$\frac{\Delta}{gap} = 1 - \sqrt{\frac{1}{1 + \frac{\Delta P}{P}}}$$

The relationship between amplitude and spatial wavelength of the loads for a fixed rms waviness is

$$\frac{\Delta P}{P} = 0.016 \ n^2$$

where n = number of cycles along the radius. The allowable membrane electrode waviness is then

$$\frac{\Delta}{\text{gap}} = 1 - \sqrt{\frac{1}{1 + 0.016 \, n^2}}$$

This relation is plotted in Figure 4.4.2. With very few radial cycles (e.g., n = 3), the Δ/gap must be quite small to not exceed $\sigma = 1.0$ mm. As the spatial frequency increases (e.g., n > 10), the allowable Δ/gap is large. Effectively the EMR is acting as a low-pass spatial filter. The low frequency errors are transmitted to the membrane reflector. At higher spatial frequencies the electrode errors are <u>not</u> transmitted into the membrane reflector. One can use these results to lay out simple membrane electrodes.

Figure 4.4.3 schematically illustrates a membrane electrode layout. In the arrangement, the membrane electrode surface is "contoured" by inelastic quartz drop cords. Because of the very low thermal expansion coefficient, quartz is also inlaid in the membrane electrode surface. The polymer membrane surface has a much larger thermal expansion coefficient than quartz. In orbit, the membrane electrode shape changes with temperature. As the temperature decreases from 300 K to 200 K, the amplitude decreases as the electrode surface contracts. For a peak-to-peak irregularity of ± 8 cm, a drop cord separation of no more than 4.5 m is recommended. The reflector's surface roughness would be less than 1.0 mm (rms). The drop cord separation could be substantially larger if the electrode surface was formed with flat "facets" between the quartz cords. Starting with flat facets at T = 300 K would produce a very taut electrode surface at T = 200 K. Further work is required on these electrode surface designs to arrive at the preferred layout.

The allowable amplitude of electrode surface billowing is a function of the gap and drop cord spacing. The criteria for selecting the number of drop cords is shown in Figure 4.4.4. The solid line indicates the half-amplitude billow of the electrode surface. The conservative assumption is implied — adequate billowing is assumed at T = 300 K so that at T = 200 K billowing also exists. The shaded boundary indicates the electrode smoothness requirements to limit waviness to 1.0 mm (rms). This curve was obtained from Figure 4.4.2

using a gap = 20 cm. The intersection of the two curves indicates that nine radial cycles (or drop cords) are adequate for a 1.0-mm membrane reflector surface. Increasing the membrane gap, increasing reflector stress, and decreasing membrane reflector surface quality all have the same effect of moving the shaded line upward, reducing the number of radial cycles. There are numerous design options that electrostatics afford for the electrode surface layout.

Even for the most conservative layout the number of drop cords is very low when compared to mesh-drawn surfaces. Assuming nine radial cycles, approximately 325 drop cords are required for a 100-m surface. A similar mesh-drawn surface would require tens of thousands of drop cords to approach the 1.0-mm geometric surface quality.
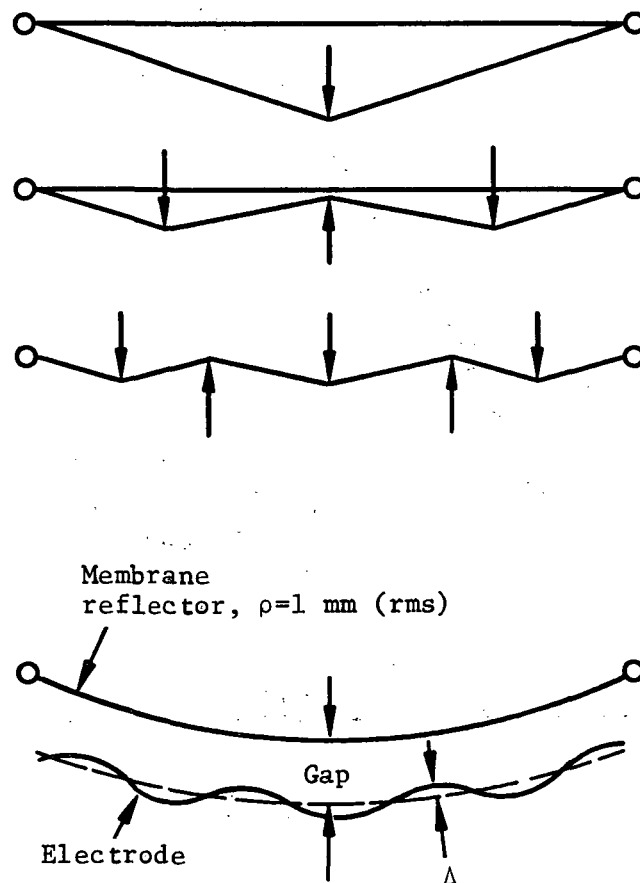
Figure 4.4.1. - Spatially distributed loads.

The induced membrane errors from billowed electrodes are only one of several errors imparted to the membrane reflector. An estimate of the principal membrane reflector errors is summarized in Table 4.4.1. Component errors are allocated with goal of 10-mm rms at 1 GH_z and 1-mm rms at 10 GH_z. The breakout is intended to show the magnitude of individual errors. A description of the errors generated from a finite number of electrodes is presented in section 4.7. The seam and surface preforming error is a statement of quality control. Some allowance must be made for residual controller errors or a "dead-band" about the desired quality.

$$\frac{\Delta}{G} = 1.0 - \sqrt{\frac{1}{1+0.016\ n^2}}$$

[n] radial cycles
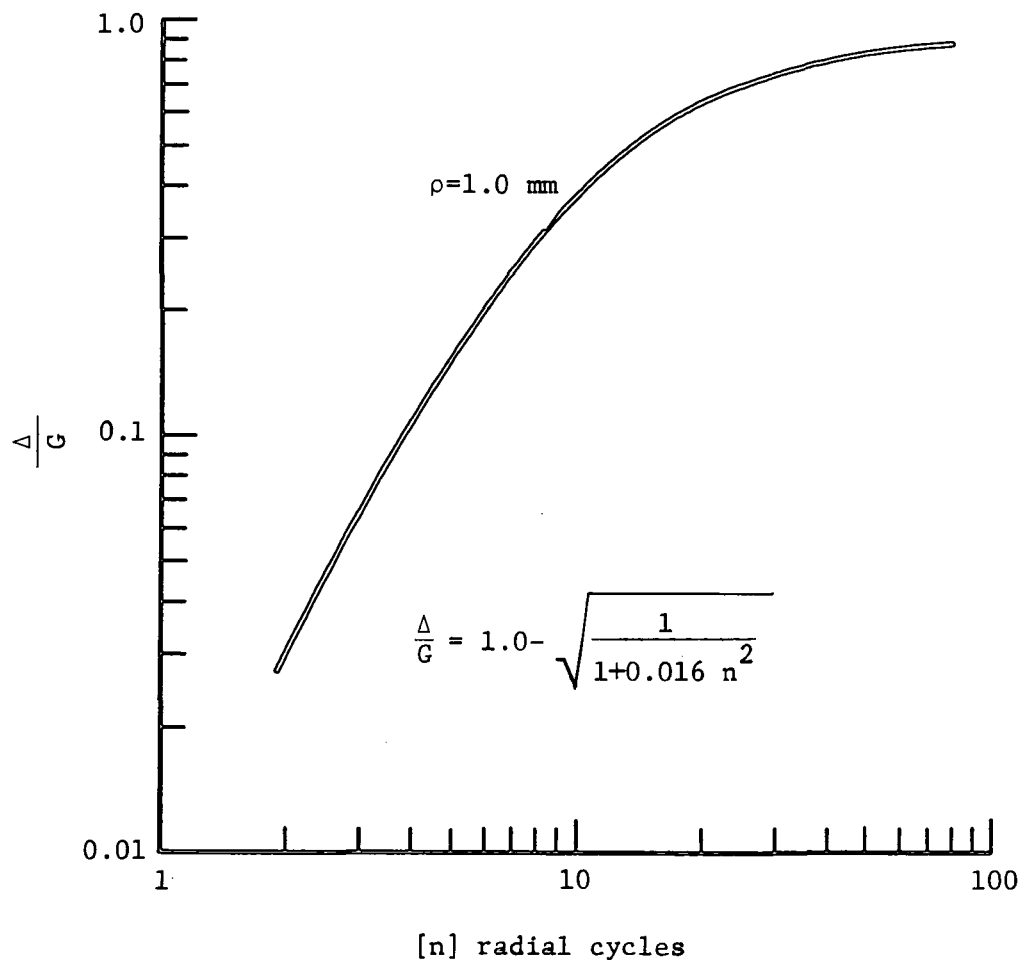
Figure 4.4.2. - Electrode surface smoothness for specified reflector smoothness.
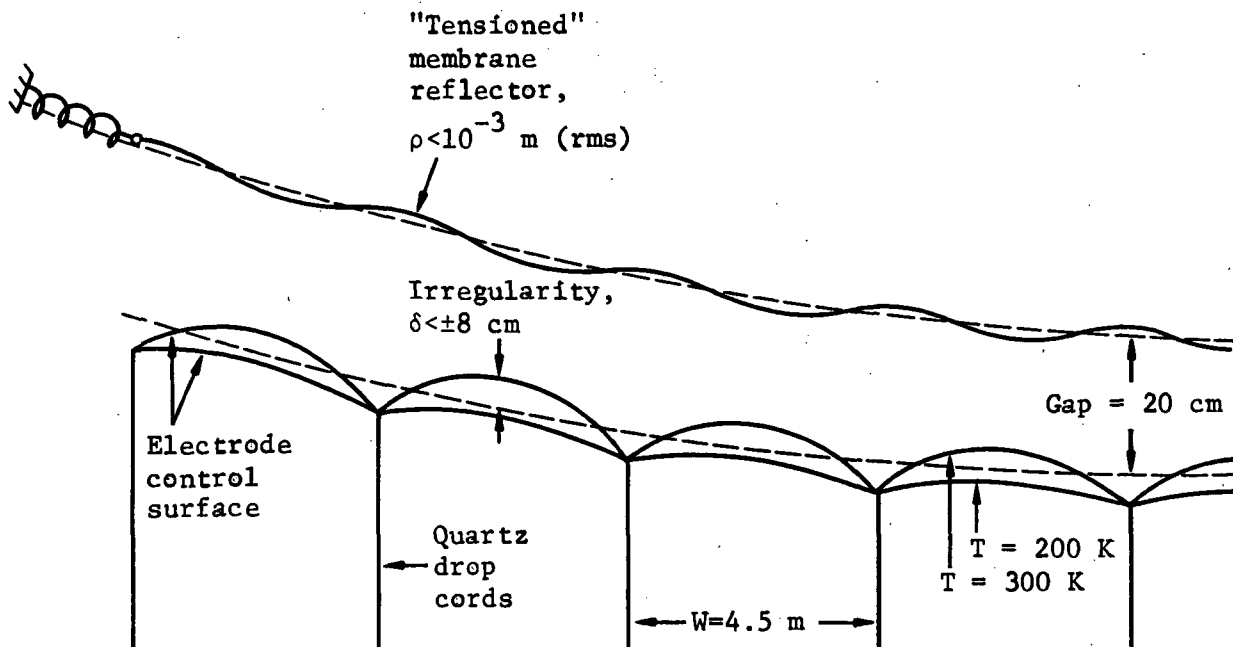
Figure 4.4.3. – Control electrode smoothness.
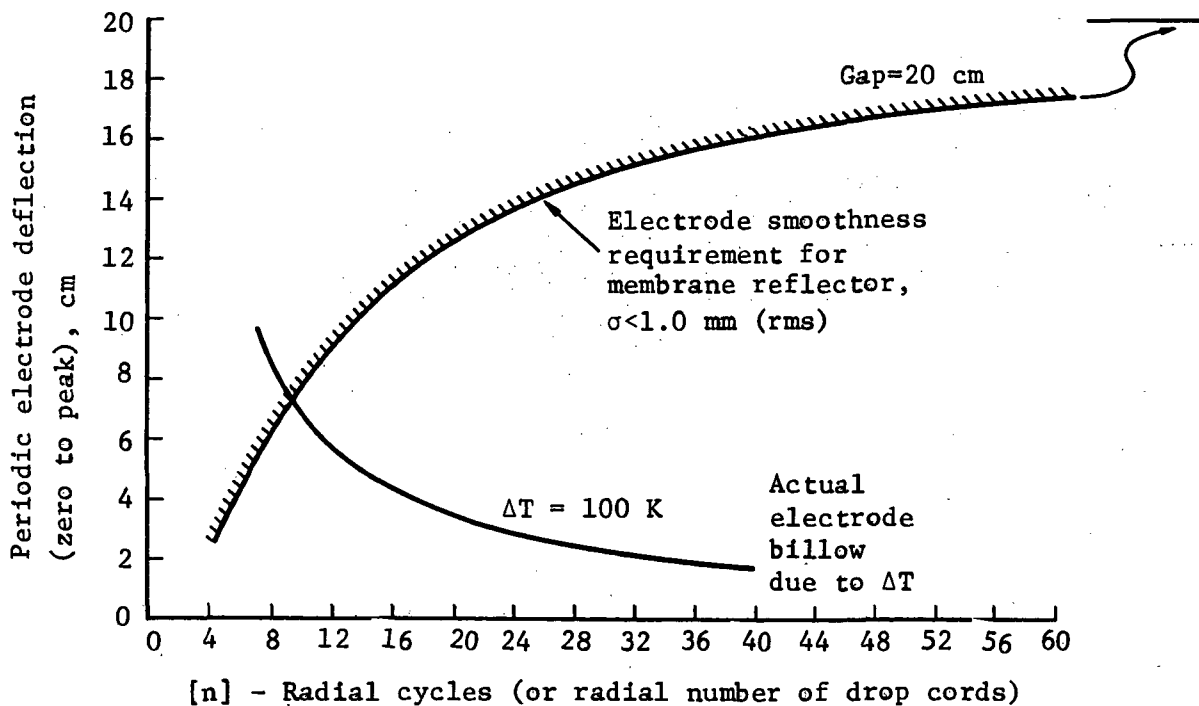
Figure 4.4.4. – Selection of number of drop cords.

TABLF 4.4.1. - ERPOR INVENTORY.

Principal Error Sources	Operating Frequency	
	f = 1 GHz	f = 10 GHz
"Billowed" electrode surface	0.3 mm	0.1 mm
Finite number of control electrodes	3.4 mm (40 electrodes)	0.3 mm (220 electrodes)
Perimeter and rim catenary	TBP	TBD
Seams and surface preforming	2.0 mm	0.3 mm (high QC)
Residual controller induced	3.0 mm	0.3 mm
Goal (rms)	10 mm	1 mm

Approximate analytic expressions that define the surface errors are
presented in Table 4.4.2. The error analysis used an axisymmetric model. The
spatial definition in the azimuthal direction would be similar. The spatial
frequency is defined by n, the number of radial cycles. For each type of
error distribution, the number of cycles, n, is different, resulting in a sum
of unrelated sinusoids. Certainly, there are also random materials and manu-
facturing imperfections. Their magnitude is slightly less than the cyclic
errors and is not included in the "waviness" summary. In the lay-up of the

membrane reflector, various seaming arrangements to form the preformed sphere
are possible. A range of n-values from 10 to 33 bounds the expectations.
This waviness is attributed to seams and membrane anisotropy. The 0.33-mm
waviness does not include the error of incorporating flat "facets" or panels
to construct the spherical shape.

TABLE 4.4.2. - MEMBRANE REFLECTOR WAVINESS IN THE RADIAL DIRECTION.

Finite electrodes introducing fluctuating spatial loading

15-m electrodes
$$\delta \sim 0.006 \ (r/50) \ \sin \ (2n\pi \ r/50) \qquad n \sim 3.5$$

10-m electrodes
$$\delta \sim 0.0017 \ (r/50) \ \sin \ (2n\pi \ r/50) \quad n \sim 4.5$$

5-m electrodes
$$\delta \sim 0.0003 \ (r/50) \ \sin \ (2n\pi \ r/50) \quad n \sim 9$$

Seams/anisotropy
$$\delta \sim 0.0003 \ \sin \ (2n \ \pi \ r/50) \qquad 10 < n < 33$$

Catenary perimeter
    Shape errors were not estimated

Billowed electrode surface
$$\delta \sim 0.0014 \ \sin \ (2n\pi \ r/50) \qquad n \sim 12$$

4.5 MEMBRANE SHAPE CONTROL

A control system for the ECMM must maintain the reflector surface within desired tolerances in the presence of various external disturbances and inherent system variations. Examples of external disturbances are temperature variations, solar pressure, and pointing control torques. System variations include membrane attachment ring out-of-roundness, electrode position offset, and nonhomogeneous membrane material. Minimizing control system complexity is very desirable, thus minimizing engineering problems and cost. Complex, real-time closed-loop control systems, which include a form of modal control and modern state-space control, have been previously considered in conceptual studies. These high-complexity control types were necessary due to very stringent surface quality requirements and a severe external disturbance spectrum. The 100-m ECMM design has less stringent surface quality requirements, and the external disturbance spectrum is not as severe as in the previous work. A less complex "quasi-steady-state" control system is able to perform all the required functions of the 100-m ECMM. This technique is workable due to the fact that the ECMM experiences long periods (tens of minutes, 80 percent of each orbit) in near steady-state conditions. These conditions include the spacecraft in eclipse, and the spacecraft in full Sun, with the Sun shining on the electrode support membrane and not on the reflector membrane. In these conditions, errors such as support rim out-of-roundness, electrode position errors, and the like are nearly steady, and a "quasi-steady-state" closed loop control system will be used to maintain surface quality tolerances. The most stressing situation on the control system occurs when the spacecraft goes into or out of eclipse, leading to rapid temperature variations and large changes in required electrode voltages. The "quasi-steady-state" control system will function properly under nonsteady-state conditions provided membrane natural mode frequencies are not excited by electrode voltage changes, and provided the measurement and voltage update rate is high enough to keep the reflector surface within tolerances. Excitation of the membrane natural modes can be prevented by separation of electrode control frequencies and membrane mode frequencies. Subsequent sections describe the analyses performed on the "quasi-steady-state" closed-loop control concept.

4.5.1 Quasi-Steady-State Control -- Influence Curves

To begin the design of a quasi-steady-state control system, the relation-
ship between static control forces and static membrane position must be known.
The solutions to the nonlinear membrane equations give the membrane nominal
shape as a function of a set of nominal pressures. Influence functions
$(\delta z(r)/\delta p_i)$ quantify how incremental pressure changes from the nominal value
on a single electrode produce displacement of points over the entire membrane
surface. Determination of influence curves is a difficult but necessary first
step in control system design.

As an example, consider the baseline membrane controlled by a set of ten
5-meter wide circular ring electrodes (fig. 4.5.1). Radial symmetry of
membrane deflections is assumed for this example. The influence curve of a
single electrode is shown in Figure 4.5.2. A first observation about this
influence curve is that it is very wide: a change in pressure at a single
electrode causes substantial deflections at points far removed from the elec-
trode itself. For this 100-m baseline, $(\delta z(r)/\delta p_j)$ is nearly linear over
the entire range of pressures from 0.0 to 0.5 N/m^2. When we consider small
variations in pressure away form the nominal, $(\delta z(r)/\delta p_i)$ can be considered
linear. Thus to determine Δz, the membrane deflection from nominal, the
influence curve $(\delta z(r)/\delta p_i)$ is multiplied by Δp_i. $\Delta z(r)$ curves from
each electrode can be linearly added to give a sum curve that represents the
membrane deflection for a given pressure distribution. In mathematical terms:

$$\Delta Z(r) = \frac{\delta Z(r)}{\delta P_1} \Delta P_1 + \frac{\delta Z(r)}{\delta P_2} \Delta P_2 + \ldots \frac{\delta Z(r)}{\delta P_{10}} \Delta P_{10}$$

Assume a sensor is available that gives Δz (membrane position error from
nominal) at a set of specific r values. A typical set might be at the center
of each electrode, i.e., r = 2.5, 7.5, 12.5, 17.5, 22.5, 27.5, 32.5 42.5,
and 47.5. Equation 1 is valid at each of the above r values, and the

148

following matrix equation can be written:

$$
\begin{bmatrix} \Delta Z_1 \\ \Delta Z_2 \\ \cdot \\ \cdot \\ \cdot \\ \Delta Z_{10} \end{bmatrix} = \begin{bmatrix} \dfrac{\delta Z_1}{\delta P_1}, & \dfrac{\delta Z_1}{\delta P_2}, & \cdots, & \dfrac{\delta Z_1}{\delta P_{10}} \\ \dfrac{\delta Z_2}{\delta P_1}, & \dfrac{\delta Z_2}{\delta P_2}, & \cdots, & \dfrac{\delta Z_2}{\delta P_{10}} \\ \cdot & \cdot & & \cdot \\ \cdot & \cdot & & \cdot \\ \cdot & \cdot & & \cdot \\ \dfrac{\delta Z_{10}}{\delta P_1}, & \dfrac{\delta Z_{10}}{\delta P_2}, & \cdots, & \dfrac{\delta Z_{10}}{\delta P_{10}} \end{bmatrix} \begin{bmatrix} \Delta P_1 \\ \Delta P_2 \\ \cdot \\ \cdot \\ \cdot \\ \Delta P_{10} \end{bmatrix}
$$

where the following notation has been used

$$\Delta z_1 = \Delta z(r = 2.5)$$
$$\Delta z_2 = \Delta z(r = 7.5)$$
$$\text{etc.}$$

and

$$\frac{\delta Z_1}{\delta P_1} = \frac{\delta Z(r = 2.5)}{\delta P_1}$$

$$\frac{\delta Z_2}{\delta P_1} = \frac{\delta Z(r = 7.5)}{\delta P_1}$$

Note that only a finite number of measurements is available. Even if every measurement point were exactly adjusted to its nominal position, other points may still be away from nominal. The attainable smoothness of the membrane deflection curve is in fact a function of the number of electrodes and this subject is examined in Sections 4.4 and 4.6.

Rewrite Eq 2 in the following form:

$$[\Delta z] = [IM] \, [\Delta p] \tag{3}$$

where   [Δz] = column matrix (10 x 1) of Δz values

[IM] = influence matrix (10 x 10)

[ΔP] = column matrix (10 x 1) of Δp values.

Inversion of Eq 4 yields:

$$[\Delta p] = [IM]^{-1} [\Delta z] \qquad\qquad (5)$$

Equation 4 provides a basis for a quasi-steady-state control law. With a set of measurements [Δz], the pressures [Δp] required to zero out the errors at each point can be calculated. Then using the relationship between pressure on the membrane and electrode voltage, the required voltage corrections can be determined.

Note that the dynamics of the motion of the membrane due to the voltage changes have been neglected. Previous studies have shown that the response of the membrane to electrode voltage changes is very fast. Step changes in electrode voltages can cause rapid membrane deflections, which may overshoot the desired final position, with the posssibility of exciting the membrane natural frequency modes. To avoid this possibility voltage changes for the quasi-steady-state control system must have rise times in the neighborhood of half a second.
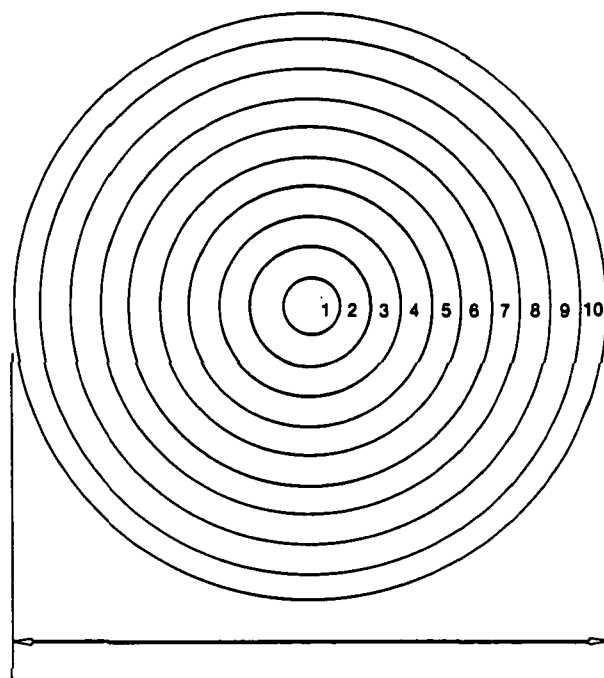
Figure 4.5.1. - Electrode layout for example case.
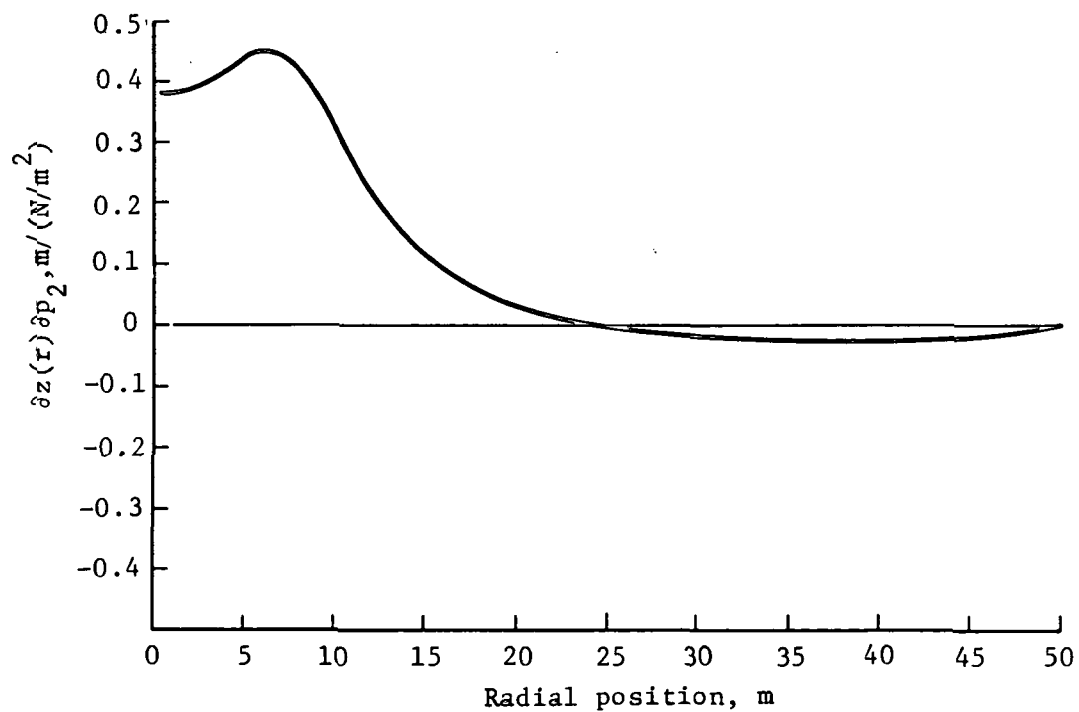
Figure 4.5.2. - Influence curve for electrode number 2.

4.6 MEMBRANE ELECTRODE SIZING

Attainable surface quality of the reflector membrane is a function of electrode size. The final membrane shape is a linear combination of the influence curve of each electrode. Because this is the case, only certain sum curves are attainable. Intuitively, one would expect that smaller electrodes would allow finer control of the electrode surface.

A computer program was written to compute the membrane final shape $\Delta z(r)$ as the linear sum of each electrode's influence curve times its pressure. Program inputs are the number of radial ring electrodes, the influence curve for each electrode, and the pressure on the membrane at each electrode. The program outputs are the sum curve $\Delta z(r)$, and an error curve given by:

$$\Delta z_{error}(r) = \Delta z_{sum}(r) - \Delta z_{nominal}(r) \qquad (6)$$

where $\Delta z_{nominal}(r)$ = the deflection corresponding to an exact sphere of 200-m radius.

This program has been run for three sets of ring electrodes:

1)   Ten 5-m wide electrodes;

2)   Five 10-m wide electrodes;

3)   Three 15-m and one 5-m wide electrodes.

Figures 4.6.1, 4.6.3, and 4.6.5 show the Δz curves due to each electrode, and the sum curve. Figures 4.6.2, 4.6.4 and 4.6.6 show the Δz_{error} curve.

The Figure 4.6.2 curve shows a 1.5-cm error at $r = 0$. This error is due to the nonlinearity of the membrane, and in fact the monimal pressures would give the exact shape. The 1.5-cm error indicates that $\delta z(r)/\delta p_i$ is not exactly linear over the entire range of pressures. The part of the error curve that is of interest then is the variation about the smooth curve that has maximum values of 0.6 mm, 3.4 mm, and 12.1 mm peak-to-peak for the three electrode sizes. It is assumed that 0-m wide electrodes would provide 0-mm

152

error in the limit case. These four values of peak-to-peak surface quality versus electrode width are plotted in Figure 4.6.7. The curve of Figure 4.6.7 shows that 1-mm peak-to-peak surface quality can be attained with 5-meter wide circular ring electrodes, and 1-cm peak-to-peak surface quality can be attained with 14-meter wide electrodes.

Note that the above numbers are for peak-to-peak surface accuracy. the rms surface quality is better than the peak-to-peak value by a factor of $1/2\sqrt{2} = 0.35$. Thus the attainable rms surface quality is considerably better than the preceding peak-to-peak figures for the same size electrodes. However, this analysis has only considered errors due to electrode size, when in fact other error sources do exist. It is reasonable at this point to assume 1-mm and 1-cm rms surface qualities are attainable with the above electrode sizes in the presence of all error sources.

This analysis has considered only radial direction errors, and further work will be required to determine azimuthal influence curves. This would reflect on the selection of circular rings or hexagonal electrodes.

The conclusions of this section are that to attain a 1-mm rms surface quality, 200 6-m x 6-m electrodes are required, and to attain a 1-cm rms surface quality, 40 14-m x 14-m electrodes are required. Contiguous electrodes should be used (hexagons or segmented circular rings) so not to waste any available electrode area and thus keep electrode voltages to a minimum.
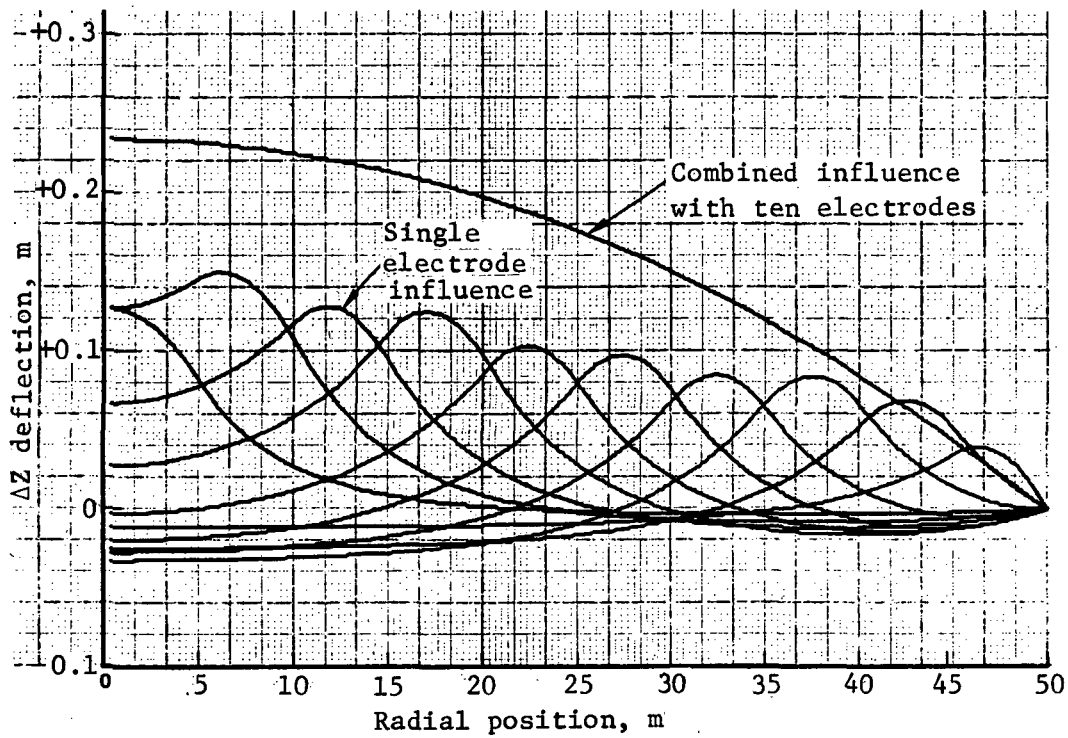
Figure 4.6.1. - Influence curves of ten 5-m wide electrodes.
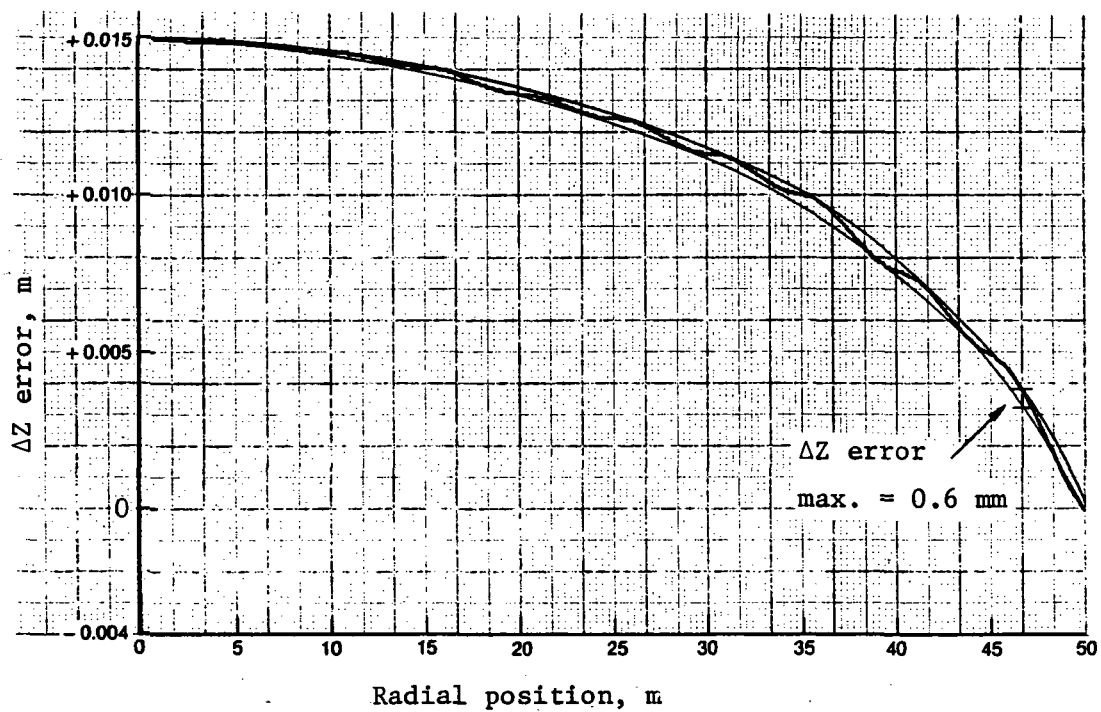
Figure 4.6.2. - Error curve of ten 5-m wide electrodes.

154
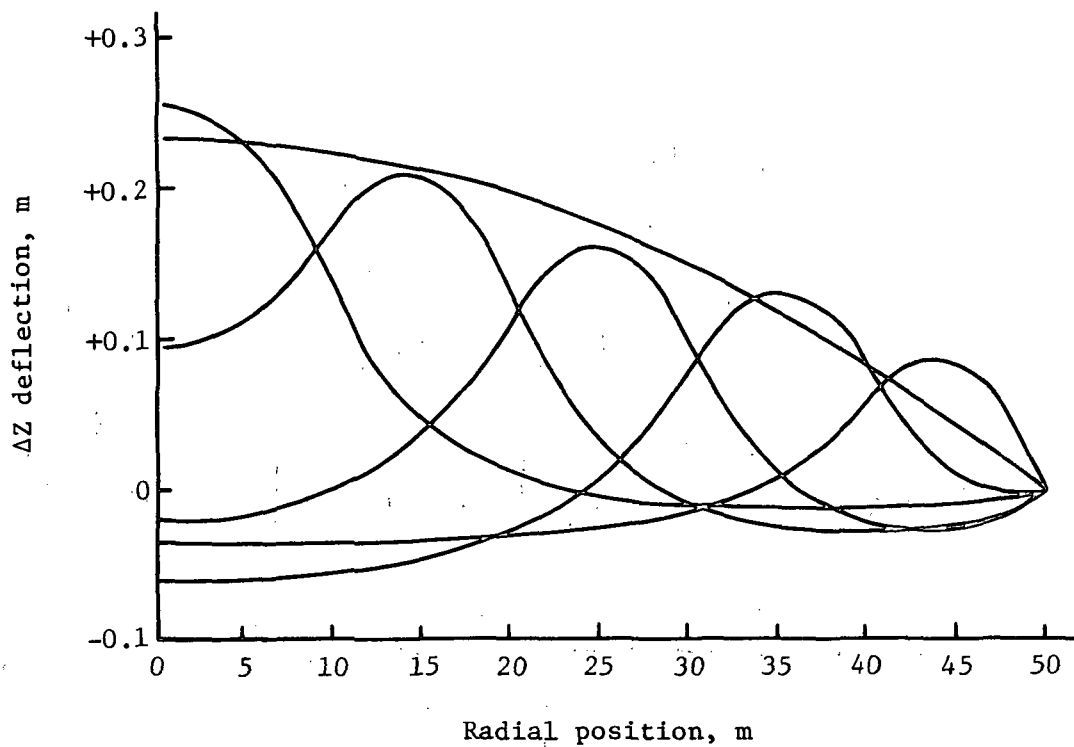
Figure 4.6.3. - Influence curves of five 10-m wide electrodes.
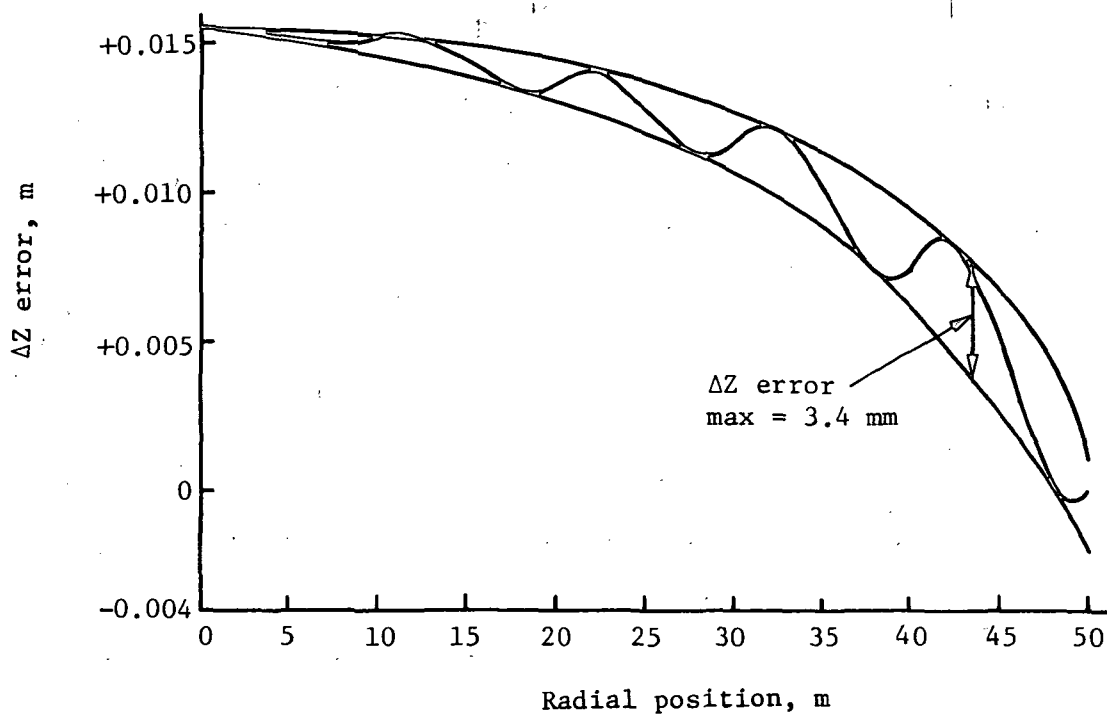
Figure 4.6.4. - Error curve of five 10-m wide electrodes.

155
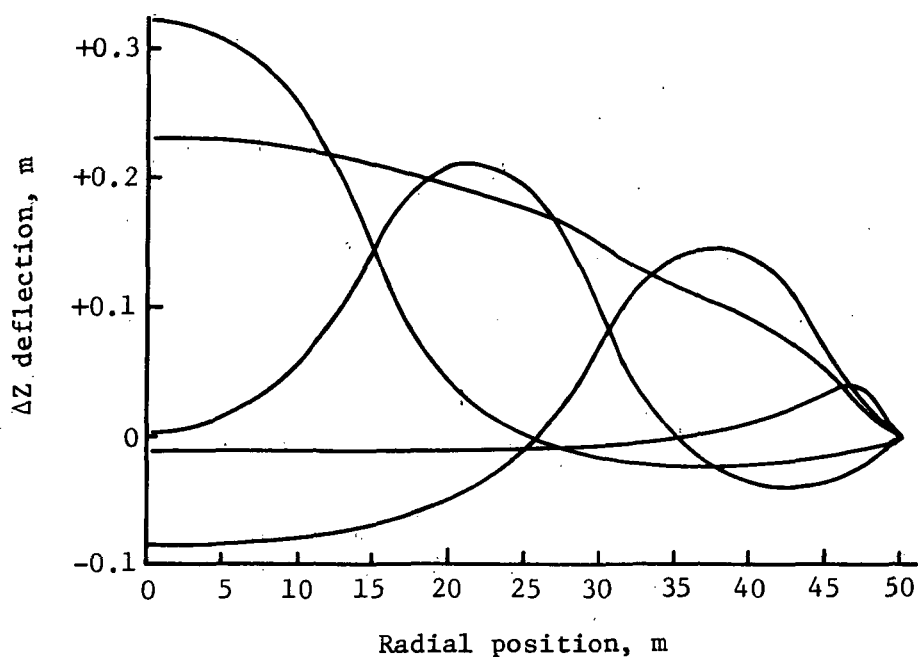
Figure 4.6.5. - Influence curves of three 15-m wide and 5-m wide electrodes.
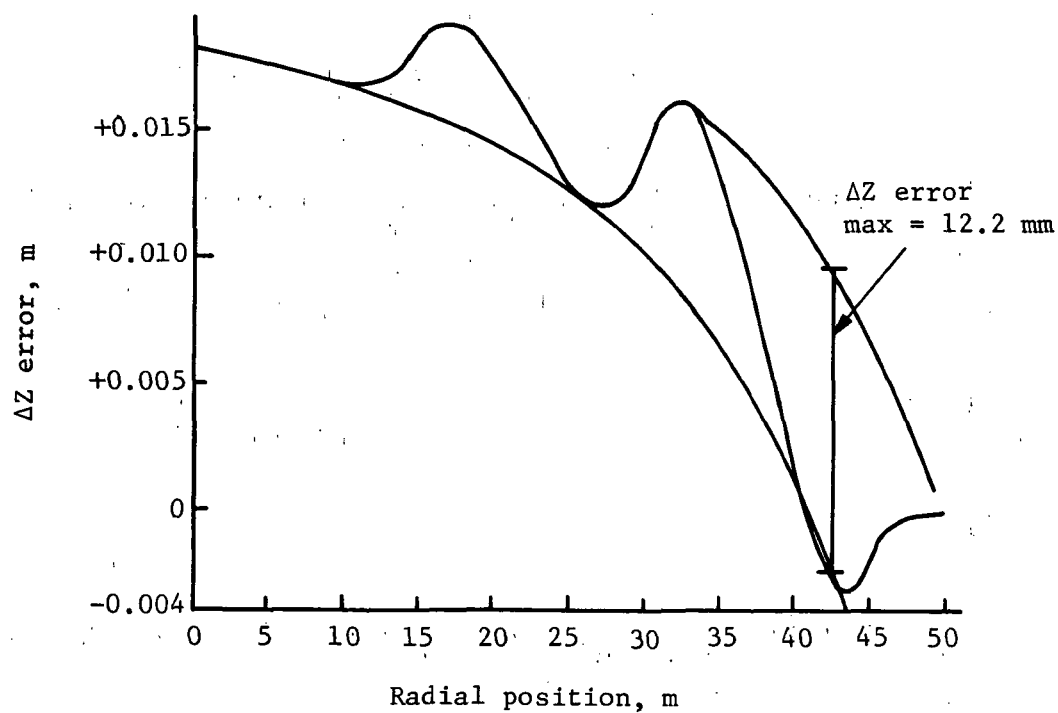
Figure 4.6.6. - Error curve of three 15-m wide and one 5-m wide electrodes.

o Influence curve addition errors
o Peak-to-peak and rms values
o Radial ring electrodes

Hypothetical total number of electrodes
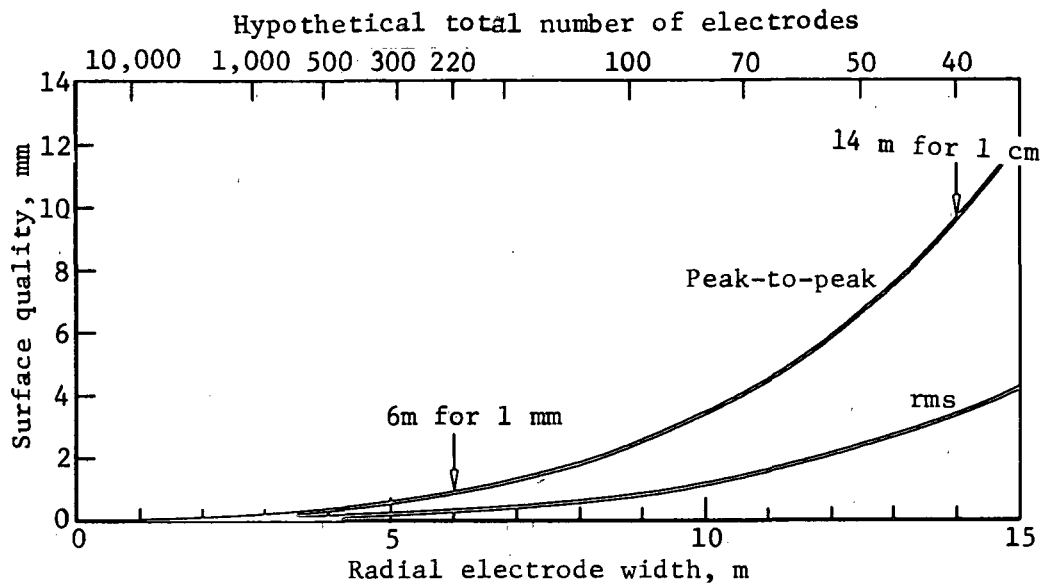
Figure 4.6.7 Electrode size versus surface quality

4.7 MEMBRANE SHAPE SENSING

A low-orbit large-membrane mirror will be subject to distortions caused by temperature variations, particularly when the mirror passes from the Earth's shadow to full sunlight. The figure control system must be able to maintain the required surface quality despite nominal temperature variations of 100 K.

There are several levels of control system complexity that can be designed to perform all, or part of, the figure control task. A brief overview of these levels of complexity is presented in the next section. A particular control model, based on an active real-time optical figure sensor, will then be used to select the criteria that must be met by the figure sensor.

4.7.1 Levels of Control Complexity

There are five levels of control complexity: a totally passive system based on spring-loaded catenaries; a semiactive system using temperature and strain measurements as sensors for computer adjustments of the electrode voltages; an active control system using proximity sensors for measuring the surface shape to control the electrode voltages; an active system using optical shape measurements; and a ground-linked control system. Each of these levels will be briefly discussed here.

4.7.1.1 Passive Control System

The simplest level of control passively compensates for temperature-induced deformations by mounting the membrane to the rim with spring-loaded catenaries. To some degree this permits the system to automatically adapt to elongations or contractions in the membrane. If oscillations should occur, the basic limitation of this approach is that there would be no way to monitor their amplitude and properly adjust the voltages on the electrodes to dampen the vibrations.

4.7.1.2 Semiactive Control System Using Strain Gages and Thermometers

The next simplest level of control complexity is to attach strain gages and thermometers at the catenary springs and other key points on the mirror mounting structure. The strain measurements at the catenary spring provide a measure of the net force at that attachment point. Conceivably, variations in this net force can be calculated from knowledge of the temperature distribution over the membrane surface. By feeding data from a network of such strain gages and thermometers to a computer, the correct adjustments to the electrode voltages can be calculated.

The temperature distribution, especially during the shadow crossings, varies rapidly and asymmetrically across the surface. Factors such as deformations in rim shape, flaws or degradations of the membrane, and perturbations from electrode edges, make it more difficult to accurately compute the membrane response, assuming that it is known. Consequently, a more complicated measurement system that directly measures the surface shape is needed.

4.7.1.3 Active Control System Using Proximity Detectors

An active control system of this type directly measures the shape of the front surface membrane by detecting its proximity to the back surface structure. One way to do this would be by using the capacitance of the electrodes. Another way would be mechanical or optical fiber proximity sensors. However, this method requires that the back support structure be stable and rigid enough to serve as a reference surface. This is possible for a continuous truss but infeasible with membrane electrodes suspended from a compression rim.

4.7.1.4 Active Control System Using Real-Time Optical Sensors

This is also a direct shape measurement system, but the sensors are optical sensors located on the rim or on the microwave feed structure. Microwave interferometric sensors are not considered appropriate because of their size and the possibility of interfering with the radiometer operations.

Because the surface is mirrorlike and the sensors will not be at the center of the curvature, it will be necessary to place small retroreflecting targets (curves or retroflector tape) on the mirror. Both day and night operation is required, which implies that the optical sensors must be self-illuminating.

4.7.2 Selection of Control Model and Optical Figure Sensor Criteria

At this time, the most conservative approach is the fourth control level: an active control system with an optical real-time figure sensor. A passive system probably would not be able to maintain surface control if transient vibrations were to occur. The semiactive system using temperature and strain measurements requires very good predictive knowledge of the membrane. The proximity-sensor system would probably constrain the structural options to an undesirable degree.

An active control system with a real-time optical sensor must be able to adequately sample the surface in a short time. The range of figure sensor requirements are the following:

	Simplest	Most Complex
Accuracy	2 mm	0.2 mm
Number of points	40	220
Measurement rate	1 Hz	100 Hz

The highest possible measurement rate is always advantageous. The lowest acceptable rate requires many figure sensors, each viewing only one point.

The required system characteristics are determined mostly by the measurement accuracy and calibration, the sensor position and target characteristics, and the measurement rate. These factors will be discussed next.

160

4.7.2.1 Measurement Accuracy and Calibration

The required measurement accuracy is a function of the microwave sidelobe level and the operating frequency. The increase in sidelobe power level relative to the mainlobe power level can be estimated from:

$$SLL = 632 \left(\frac{\sigma}{\lambda}\right)^2 \left(\frac{C}{D}\right)^2 \frac{1}{n} e^{-\left(\frac{\pi C \theta}{\lambda}\right)^2}$$
(7)

where: SSL = contribution to sidelobe power ratio due to rms surface error; i.e., ratio of sidelobe rms power to peak mainlobe power

     σ = rms surface error

     λ = wavelength

     n = efficiency

     C = spatial correlation of surface errors, assuming that the errors obey a gaussian distribution

     θ = angle off the mainlobe axis.

TABLE 4.7.1. - SIDELOBE LEVELS AS A FUNCTION OF RMS SURFACE ERROR AND THE ERROR CORRELATION DISTANCE[a].

Correlation Distance, m	On-axis sidelobe ratio. SLL, dB	
	$\sigma = \lambda/50$ (2 mm)	$\sigma = \lambda/25$ (4 mm)
10	-23.8	-17.8
5	-29.8	-23.8
1	-43.8	-37.8

[a] Assuming a 100-m diameter, 60 percent antenna efficiency, 3 GHz frequency and gaussian error statistics.

In equation 7 the rms surface deviation σ, the correlation of the surface error C, and the angle off the mainlobe center θ, are of particular interest. The surface error contribution is a maximum on the central axis. A decrease in rms surface accuracy from $\lambda/50$ to $\lambda/25$ will cause a 6-dB increase in sidelobes at $\theta = 0^{\circ}$, but can have an insignificant effect at even small angles off axis if the correlation term in the exponential is large. Consequently, the issue of rms surface quality must be carefully evaluated in terms of the specific system performance.

Table 4.7.1 shows the sidelobe levels assuming a 100-m diameter mirror operating with 60 percent efficiency at 3 GHz. At 3 GHz an rms error of $\lambda/25$ is 4 mm, which requires a measurement accuracy of $(0.707) \times 4 = 2.8$ mm. If the measurement system accuracy is 1 mm, then a $\lambda/50$ rms error can be maintained.

The measurement precision, or repeatability, must be quite high. Consequently, self-calibration capability must be designed into the system. This implies that there must be a number of key reference points that can be measured with an absolute distance sensor such as a range finder or interferometer. One calibration technique might be to design reference targets that can move known distances. The calibrated absolute sensor can then be the reference sensor for angle-only sensors, if these are used.

4.7.2.2 Sensor Position and Target Motion

The optical sensors must be positioned at structurally-allowed points near the microwave receiver, and/or on the rim. This prevents operation at the center of curvature, so that slope-type of measurements such as the optical Hartmann tests will not be feasible. For the initial design of the 100-m mirror, the sensor operating range must exceed 100 m. A conservative allowance would be to require a 100-m to 200-m operating range.

Because thermal effects can cause structural deformation, methods of monitoring the mounting position must also be designed. These should be built into the calibration system.

162

Because of the sensor location and the fact that a membrane mirror is highly specular, even at optical frequencies, small, lightweight, retro-reflecting targets must be placed on the mirror surface. Because the membrane in-plane distortion umder thermal stress can be as large as 0.1 m and out-of-plane distortions 0.25 m, the targets can wander from their desired position. Target wander led to a conservative requirement that the sensor be able to search for the target over a 1-m spot. At a 100-m operating distance, the minimum sensor field-of-view would then be 0.01 rads to perform searching. However, the sensor could reduce the field-of-view once the target was acquired. It is desirable to have a small field-of-view for it makes better use of the finite number of resolution cells in most electronic optical sensors such as vidicons or CCD arrays. The sensor mount must be stable to minimize jitter-induced errors. Because the sensor will have to scan for the target, it probably will be necessary to place optical encoders on the optical mount. It is possible that the scan function could be partially mechanical for large scans and partially optical for small scans. However, the search rates may be compatible with a mechanical scan for both the large target-to-target scan and the small search-for-target scan.

4.7.2.3 Summary of Optical Figure Sensor Requirements

It will be asssumed that there are 40 to 220 electrodes to control the membrane reflector. At least one optical measurement is made for each electrode. The membrane thermal analysis defines two different rates that accommodate slow membrane drift and rapid changes when the Earth's shadow crosses the aperture. The low-drift rate is associated with a membrane reflector temperature change of $\dot{T} \le 0.02$ K/s, which occurs at least for 90 percent of the orbit. A high rate ot $\dot{T} \le 6$ K/s occurs with sudden illumination when entering and departing the Earth's shadow. Fast rates would be handled with a few dedicated sensors. Slow rates and many sensed points would be scanned with a scanning sensor.

Table 4.7.2 summarizes the optical figure sensor requirements. These requirements will be used to select specific technologies discussed in Appendix D.

TABLE 4.7.2. – OPTICAL FIGURE SENSOR REQUIREMENTS[a]

	1 mm RMS	1 cm RMS
Minimum number of sensed points over 100-m aperture	220	40
Maximum measurement rate on "select" center points	40/s	4/s
Measurement accuracy	0.2 mm	2.0 mm
1 m search capability		
Automated, self-calibrating		
Day/night operation		

[a] In addition to the other criteria, the sensor should also be lightweight, robust, and cost-effective. Since no system, and few components, are currently space-qualified, it is difficult to make any projections on cost effectiveness. Size and weight will be commented on during discussion of specific technologies.

4.8 Rigid Body Analysis

This section consists of a rigid body analysis of a baseline Large Space System (LSS) which is to function as a radiometer. The LSS is placed in circular orbit about the Earth at an altitude of 650 km, subjected to environmental and vehicle interaction forces and torques without an active control system of any type on board, and is in a z-local vertical mode. The analysis is then used to demonstrate the ability or lack of the gravity gradient torques to stabilize the LSS over one complete orbit. The results generated by the analysis can then be used to size an active control system consisting of thrusters, momentum exchange devices, or a combination of the various active control devices, which when used in conjunction with gravity gradient torques would be required for attitude control and station keeping.

The baseline LSS is to be placed in an orbit at an inclination angle of 60 degrees. When this angle is added to the 23 degree angle the Earth's equatorial plane makes with the Earth's orbital plane, the LSS orbit moves through ± 83 degrees with respect to the Sun line. For the purpose of this analysis an inclination angle of 67 degrees was chosen thus making the orbit move through ± 90 degrees and makes checking the computer simulation results much easier. Shown in Figure 4.8.1 is the orbit plane with respect to the inertial reference frame and the Sun line for the various beta angles. A computer simulation of rigid body dynamics was performed for one complete orbit for beta angles of 0, 45, and 90 degrees. The resulting forces, torques, angular momentum, and Euler angles are then used to size an active control system to maintain the attitude and stationkeeping requirements of the spacecraft. The vehicle interaction torque defined by

$$\bar{T}_{INA}^{V} = \bar{\omega}_{V}^{V} \times [I] \, \bar{\omega}_{V}^{V} \tag{8}$$

165

and written in component form becomes:

$$T_{INAX} = \Delta I_x\, \omega_y\, \omega_z$$

$$T_{INAY} = \Delta I_y\, \omega_x\, \omega_z$$

$$T_{INAZ} = \Delta I_z\, \omega_x\, \omega_y$$

Because $\Delta I_z = 0$ for $I_{xx} = I_{yy}$ and for all cases considered $Wz = 0.0$, the torque due to vehicle interaction is zero.

Listed in Table 4.8.1 is a summary of possible control torque actuators that may be used for attitude control and station keeping requirements.

An analysis of the results concluded that momentum exchange devices are not practical control actuators to be used on the ECMM. The facts used to reach such a conclusion are as follows:

(1) The spacecraft would require a minimum of two momentum exchange devices per axis, with their respective spin vectors aligned opposite one another. The weight of the system becomes prohibitive.

(2) For the case of $\beta = 90$, there exists at the end of the orbit a residual momentum of 1.6426×10^3 N-m-sec. There does not exist for any time during the orbit an occulted region which would be required in order to perform a desaturation of the momentum control device.

(3) The size of the device was such that when it was attached to the box ring truss of the ECMM spacecraft, the packaging problems were such that the volume requirements of the Space Shuttle cargo bay were exceeded.

166

The entire control of the spacecraft now depends on some form of thruster system. Section 4.9 of this report presents an analysis of the types of thrusters that could be used for the attitude control propulsion system.
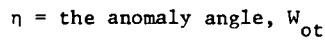
Figure 4.8.1. - Orbit plane with respect to the inertial reference frame and Sun lines.

TABLE 4.8.1. - CONTROL TORQUE ACTUATOR SUMMARY.

Torque Actuator	Advantage	Disadvantage
Thrusters	No cross-coupling with the vehicle motion to produce undesirable torques for which compensation must be made.	
Electric	High specific impulse, applicable to missions with a long lifetime.	Low-thrust high-power requirements.
Chemical	High thrust.	Low specific impulse, not applicable to missions with a long lifetime. Tankage and weight problems.
Momentum exchange devices Reaction wheels and CMGs	Ideal when disturbances are cyclic with respect to an inertial reference frame and the secular component (bias torque) is small. Could reduce the size and number of thrusters required for the mission.	Cross-coupling with the vehicle motion to produce undesirable torques that require compensation. Requires a desaturation control law scheme. Number required could be prohibitive in terms of size, weight, and power required.
Magnetic torquers	Used in conjunction with momentum exchnage devices for desaturation or momentum management purposes.	Magnetic field of the Earth is time variant and strongly altitude dependent. At any instant torque can be produced only along components normal to the local magnetic field vector. Practical limitations in power supply and coil size make the generation of large torques infeasible.

168

4.9 MICROTHRUSTER ANALYSIS FOR ATTITUDE CONTROL

Presented in this section is an analysis that compares chemical and electrical microthrusters, which could be used as the active control system for the spacecraft in lieu of momentum exchange devices. The data used in the comparative analysis were obtained from the results of the rigid-body analysis of Section 4.8.

Table 4.9.1 is a summary of the current state-of-the-art microthrusters available, including some that are not flight qualified. Considering only the flight-qualified and high-I_{sp} thrusters, the Pulsed Plasma Thruster (PPT) and Mercury Ion Thruster (HgIon) were selected as candidates to be used for the comparative analysis. The basic differences between the PPT and HgIon systems are summarized in Table 4.9.2.

A comparison of the two thruster systems, which are considered for use as the ECMM spacecraft attitude control system, is presented in Table 4.9.3.

Due to the membrane contamination considerations and space charging problems associated with the mercury ion systems, the PPTs were baselined for the ACS propulsion. However, due to the dimensions of the PPT packages, the feed boom could not be folded and stowed in the cargo bay with the PPTs attached. Therefore, either the PPTs used on the boom must be repackaged or mercury ion thrusters must be used on the boom. Alternatively, mercury ion thrusters could be used throughout if the contamination and charge problems could be solved.

4.9.1. Disturbances

The object of the thruster system is to counteract all disturbing forces. The major forces are aerodynamic force and solar pressure force. For an orbit between 600- and 1000-km altitude, these two forces are of the same magnitude.

Gravity gradient also plays a small part in helping to stablize the FCMM. Gravity torques will be produced even for principal axis of inertia (the case for ECMM) when the vehicle body does not coincide with the reference axis system.

The SOLRPR computer program was used to calculate forces and torques on the body. Section 4.9.1.1 deals with the torques and 4.9.1.2 considers the forces. SOLRPR was run for three different β angles as described in Figure 4.9.1. Solar radiation arrives perpendicularly to the face of the page.

TABLE 4.9.1. - MICROTHRUSTER CANDIDATES.

System	Thrust, N	I_{sp}, s
Chemical		
Inert gas	10^{-4} to 1.0	35 to 275
Vaporizing liquid	10^{-5} to 0.05	50 to 100
Subliming solids	10^{-4} to 10^{-2}	40 to 80
Hydrazine direct catalyst	0.05 to 1000	100 to 225
Bipropellant (storable)	0.05 to 10^4	170 to 320
Electric		
Resistojet	0.01 to 5.0	175 to 860
Electrolysis	10^{-4} to 5.0	100 to 350
Pulsed plasma	10^{-6} to 10^{-3}	1000 to 5000
Ion (mercury)	10^{-3} to 0.5	2000 to 9000
Ion (noble gas)[a]	2.1×10^{-3}	5500 to 6400
MPD[a]	2.3×10^{-2} to 3.2×10^{-2}	2000 to 9000
Mass driver[a]	10^{-5} to 10	10^4 to 5×10^4

[a]Not flight qualified.

TABLE 4.9.2. - PROPULSION SYSTEM COMPARISON.

Plasma propulsion	Ion propulsion
Electromagnetic forces	Electrostatic forces
Electrically neutral plasma accelerated	Charged ions accelerated
No neutralization required	Ions must be neutralized
Extremely short puffs of propellant are ejected (microseconds of flow time)	Steady flow of propellant is ejected (hours of flow time)
Instantaneous reaction forces are typically hundreds of Newtons	Reaction forces inherently fractions of a Newton

TABLE 4.9.3. - MERCURY ION AND PPT COMPARISON.

	Mercury Ion	PPT
Packaging	Very versatile[a]	Some size restriction[b]
Number of thrusters necessary	20	24
Total mass required (excluding fuel)	540 kg	550 kg
Total power required	4840 W	4080 W
Effects on structure	Possible degradation[c]	None
ACS requirements	Satisfied	Satisfied

[a]Modular components make many packaging schemes possible.

[b]Off-the-shelf PPTs are cylindrical, about 43.2 cm in diameter and 25.4-cm wide.

[c]Sufficient test data have not been acquired.

171
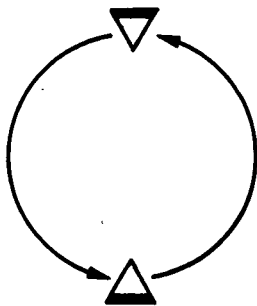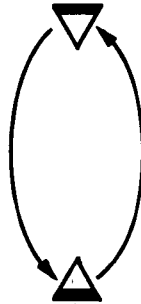
$\beta = 90$ deg $\beta = 45$ deg $\beta = 0$ deg

Figure 4.9.1. - Orbital appearance from Sun.

4.9.1.1. Torques

Figures 4.9.2, 4.9.3, and 4.9.4 are three graphs of torque versus orbital angle for β = 90, 45, and 0 degrees respectively.

The maximum torques about the x-axis are:

$\qquad$ -0.552 Nm at β = 90 deg

$\qquad$ +0.133 Nm at β = 45 deg

The maximum torques about the y-axis are:

$\qquad$ -0.735 Nm at β = 0 deg

$\qquad$ +1.269 Nm at β = 0 deg

There are no torques about the z-axis.
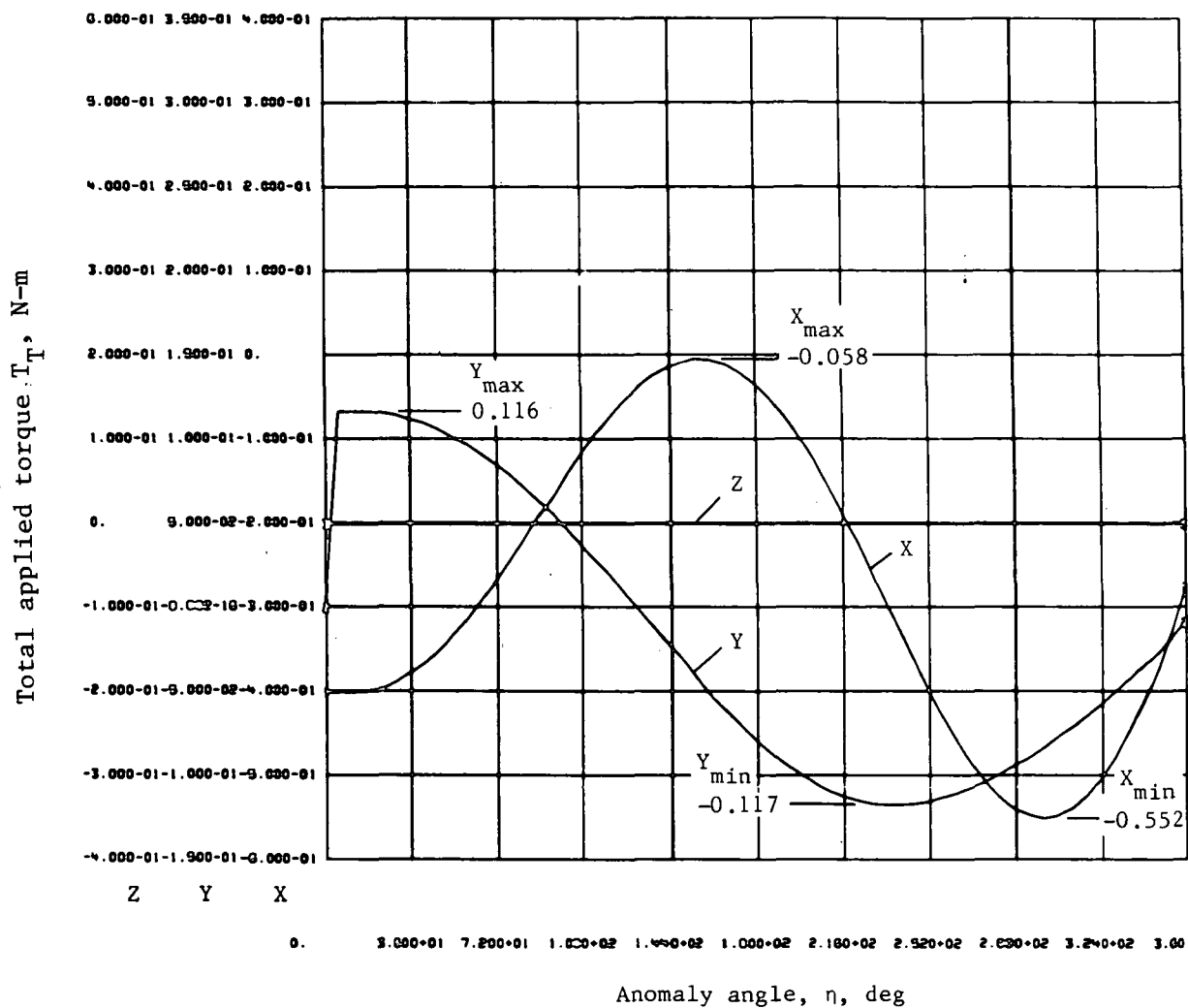
Figure 4.9.2. — Total applied torque versus anomaly angle, β = 90 deg.
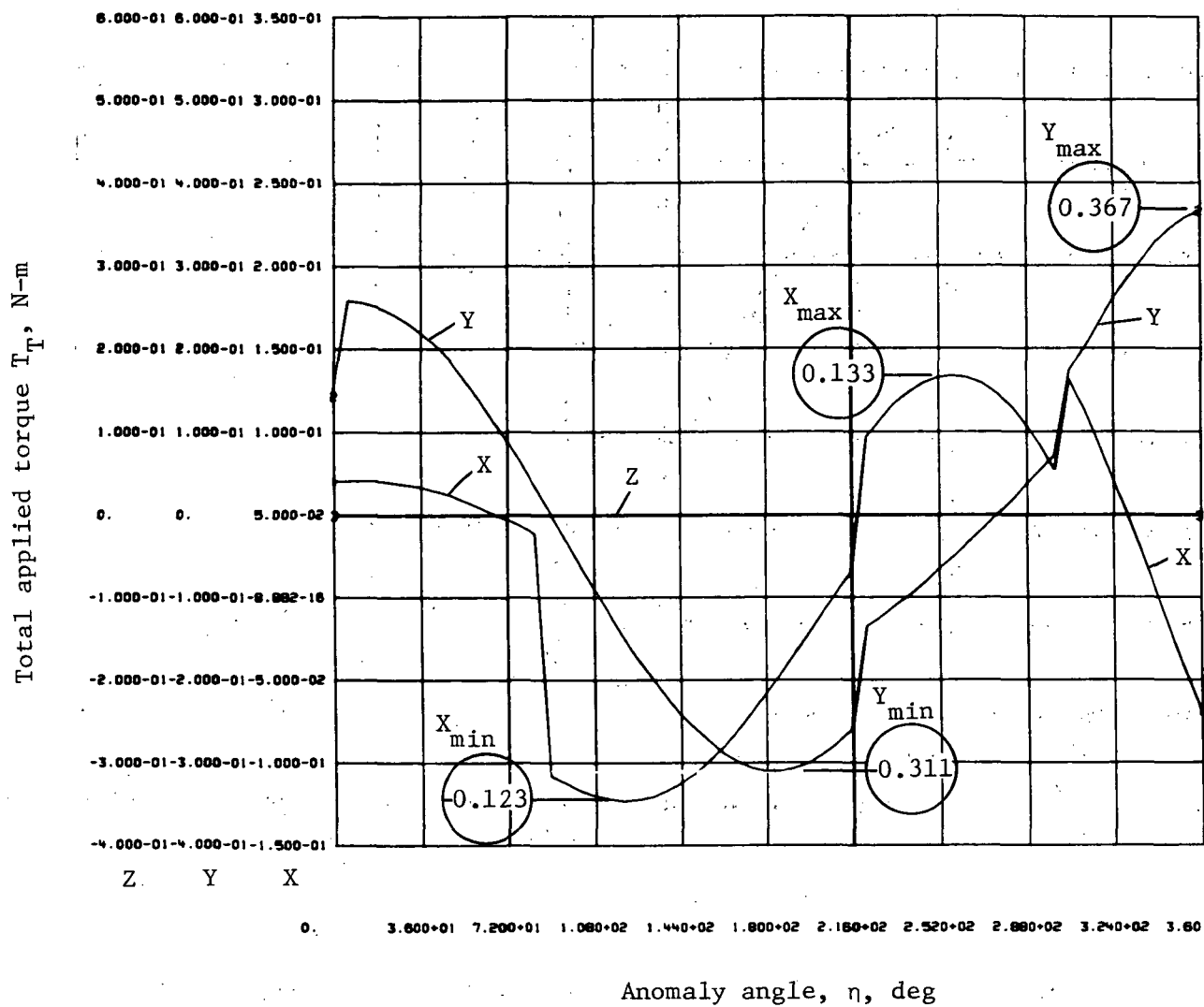
Figure 4.9.3. - Total applied torque versus anomaly angle, β = 45 deg.

174
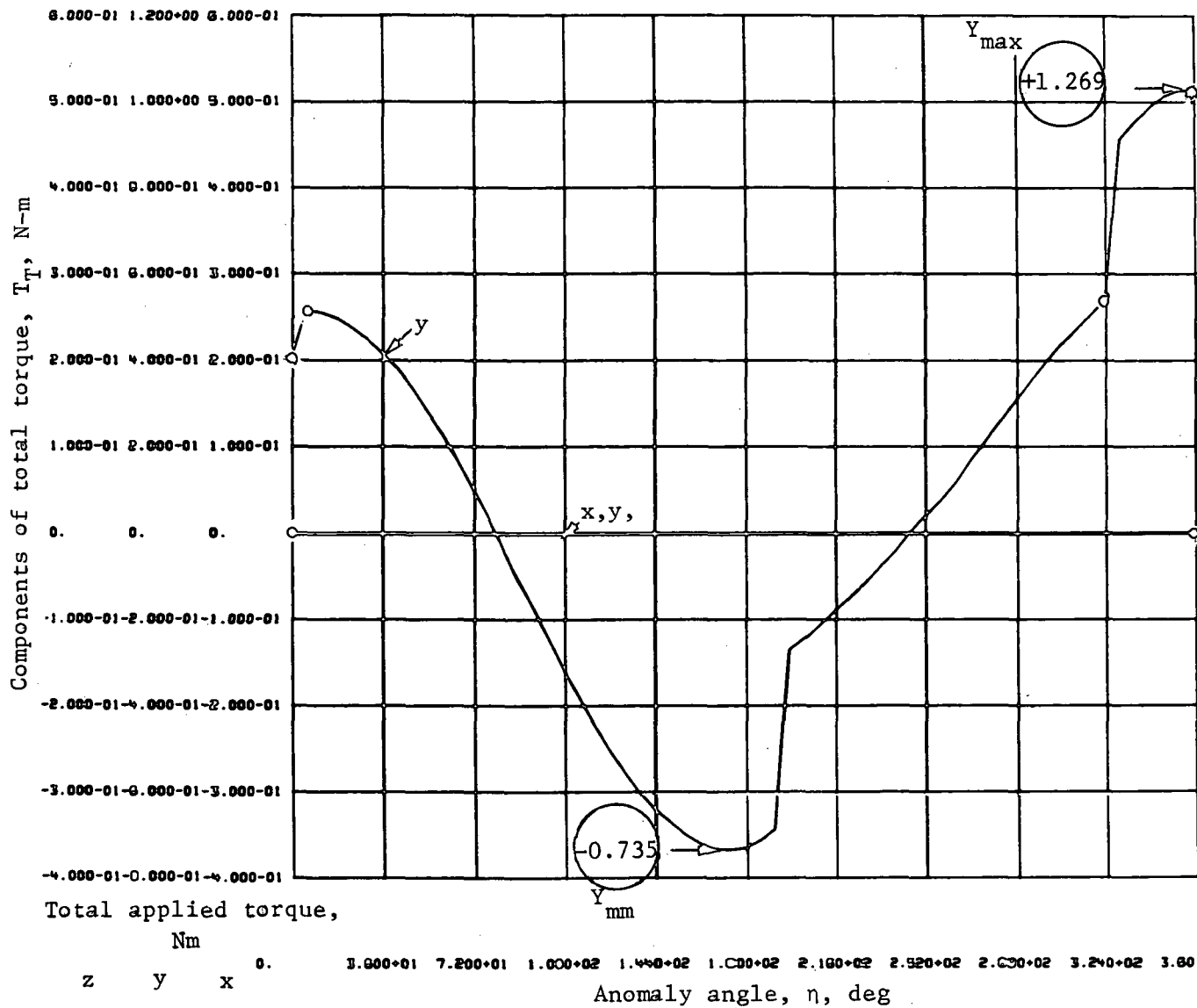
Figure 4.9.4. – Total torque components versus anomaly angle, β = 0 deg.

175
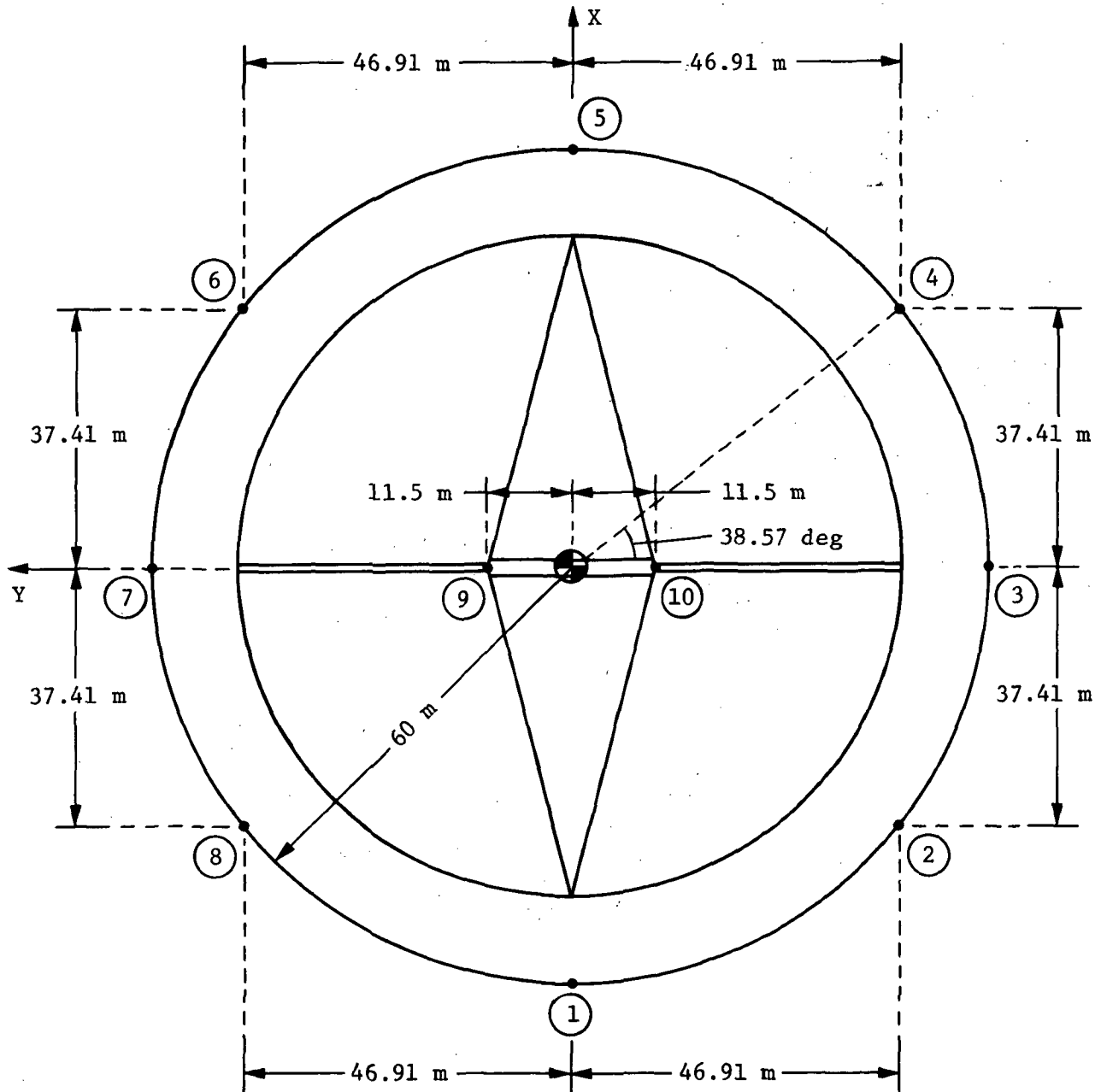
Figure 4.9.5. -. Thruster location, top view.
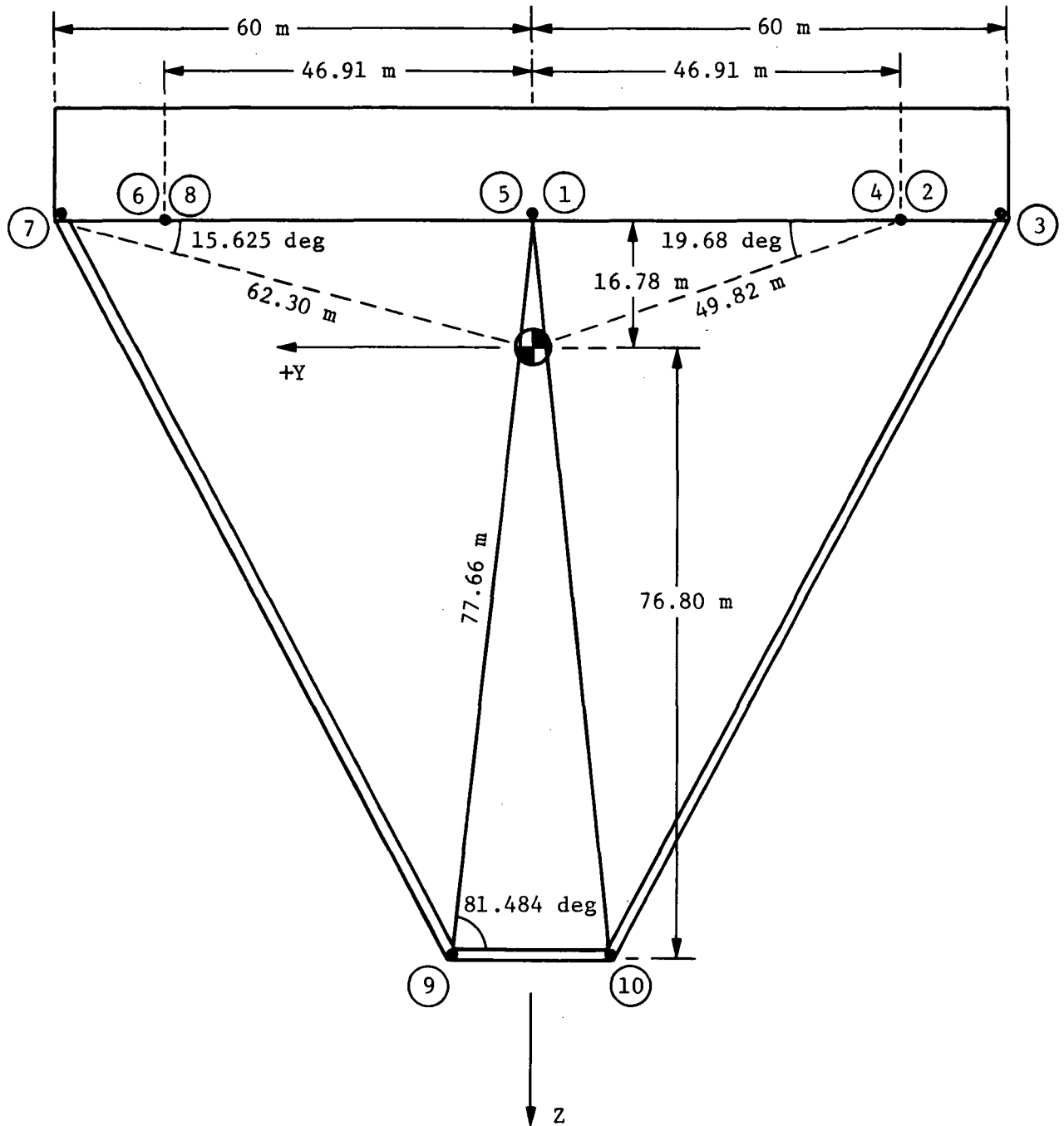
Figure 4.9.6. – Thruster location, front view.
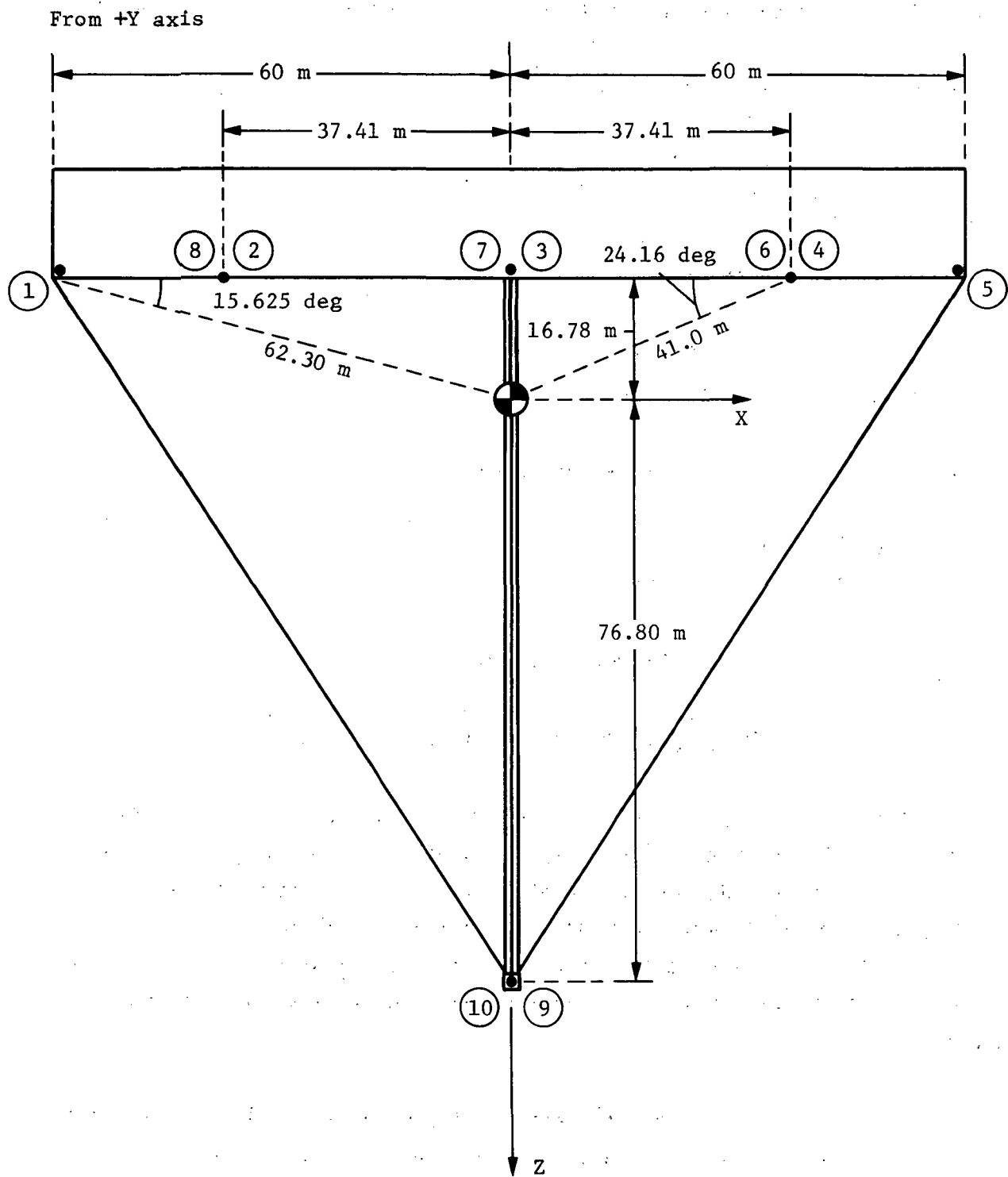
Figure 4.9.7. - Thruster location, side view.

4.9.1.2. Forces

The SOLRPR program also supplied information on the forces encountered.

The maximum forces in the x-direction are:

   -0.02169 N at β = 0 deg
   +0.004554 N at β = 0 deg

The maximum forces in the y-direction are:

   -0.01303 N at β = 90 deg
   +0.009318 N at β = 45 deg

The maximum forces in the z-direction are:

   -0.04217 N at β = 45 deg
   +0.07552 N at β = 0 deg

The largest force is in the positive z-direction.

4.9.2. Positioning of Thrusters on ECMM

Thrusters are to be positioned on the ECMM structure to overcome the external forces and torques. The maximum restoring torques are created when the thrusters fire in a direction perpendicular to the longest moment arm. The maximum force occurs when as many thrusters as possible fire in the proper direction. Finally, the strength of the structure, packaging considerations, and wiring problems also have to be considered to determine the positions of the thrusters.

Due to these considerations, thrusters are placed on the lower ring formed by the ECMM's box trusses, at locations 1 to 8 as shown in Figures 4.9.5 to 4.9.7. Thrusters were put on the feed horn, positions 9 and 10, to stabilize the vehicle and to create more restoring torque.

The pulsed plasma and the mercury ion thrusters have completely different geometries and packaging problems. The different packaging problems make it necessary to have different numbers of thrusters at the 10 locations. Two single-pulsed plasma thrusters (Section 4.9.3) are required at locations 2, 4, 6, and 8. Three single-pulsed plasma thrusters (Section 4.9.3) are needed at locations 1, 3, 5, and 7. At locations 9 and 10, one twin-pulsed plasma thruster (Section 4.9.3) is necessary. For the mercury thruster system, two thrusters are required at all locations.

4.9.3. The Pulsed Plasma Thruster

The PPT shown in Figure 4.9.8 and described in Table 4.9.4 was chosen because of its high I_{sp} and its uncharged noncorrosive exhaust.
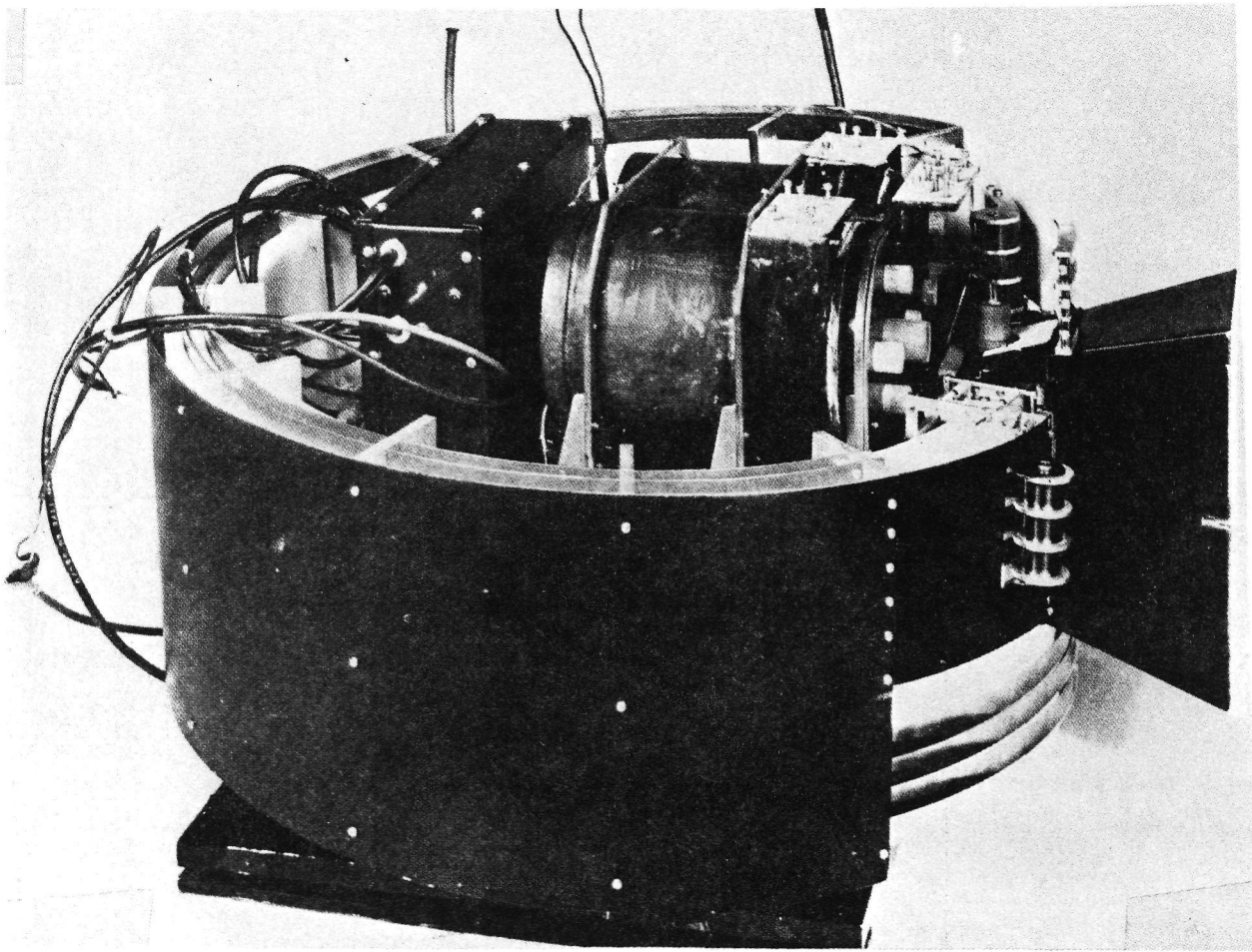
Figure 4.9.8. - Milli-lb pulsed plasma thruster subsystem.

180

TABLE 4.9.4. – PULSED PLASMA THRUSTER DATA.

Manufacturer	Fairchild Republic Co.
Status:	
– Qualified	Yes
– Flown	LES 6, 8, and 9; TIP 2 and 3; NOVA
Life:	
– Total Impulse	320 000 N-s
– Total Prop	15 kg
Steady State Vacuum Specific Impulse	2200 s
Propellant	Teflon
Power	170 watts per millipound thrust
Weight	23 kg

The thruster is mounted to a double gimbaling system shown in Figure 4.9.9 to direct the thrust in all directions. This creates a much more efficient station keeping system, and simplifies pure translational and pure rotational firing order.

Pulse plasma thrusters (PPT)

Bearings allow transfer of power and control signals.

Stepper motor – controls rotation of thrusters.

Turntable with stepper motor – controls revolution of thrusters.
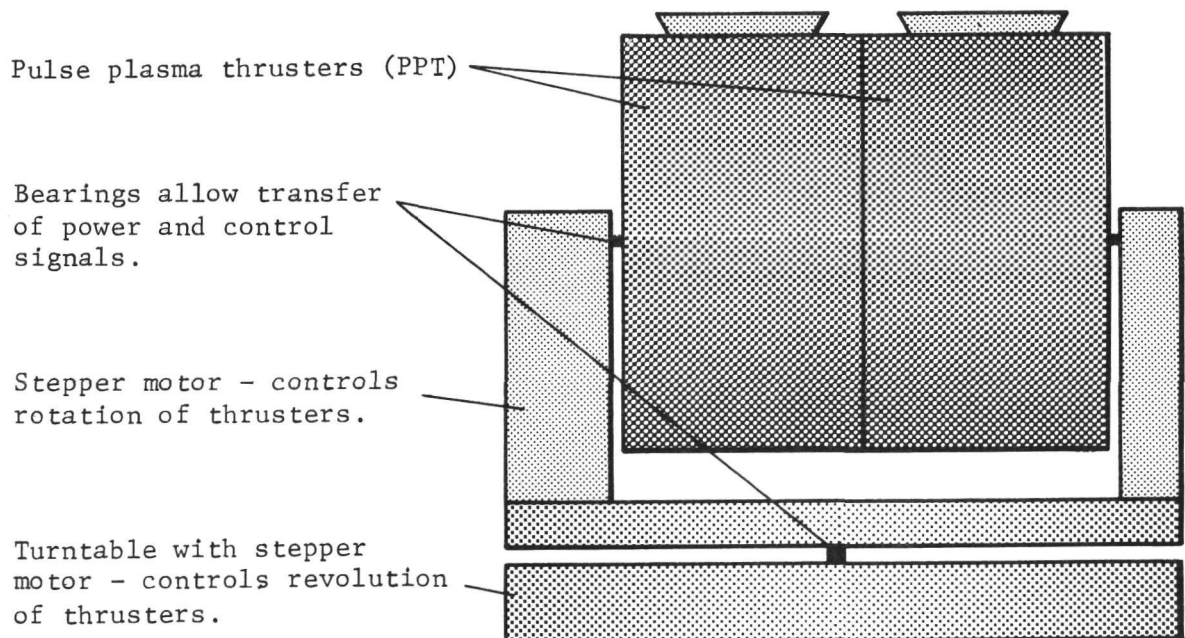
Figure 4.9.9. – PPT gimbal system.

Table 4.9.5 gives the maximum translational and rotational firing order. For translation, the direction of thrust of each thruster is broken down into its three body-axis components. The positive x-direction is always in the direction of orbit, the positive z-direction is pointing toward the center of Earth, and the positive y-direction is on the right side (facing positive x), orthogonal to the x and z axes.

The use of Table 4.9.5 is best visualized via an example. For maximum translation in the positive x-direction, thrusters 3c, all of thrusters 4, 5, and 6, and thruster 7a must be fired at fullpower in the negative x-direction. The y and z components for all these thrusters are zero. To prevent rotation, thrusters 9 and 10 are throttled to only 4.372×10^{-3} N thrust each (in the negative x-direction). The result is a pure translation in the positive x-direction.

The translation figures in Table 4.9.5 are for maximum translation without rotation (pure translation). The rotation figures are also for maximum pure rotation.

On the bottom of the chart there is a brief table showing how well the requirements of Section 4.9.1 are met. The worst case is the force causing a translation in the positive z-direction. With the proposed PPT system this force can be countered with over 40 percent to spare.

Table 4.9.6 takes the maximum rotational thrust in Table 4.9.5 and displays the rotational torque caused about all three axes for each thruster. Interpretation, again is aided via an example. In Table 4.9.6. thruster 1c is fired in the negative y-direction, with a 3.372×10^{-3} N force, to achieve a positive rotation about the x-axis (positive ϕ rotation). Table 4.9.6 shows that a positive torque of 0.098×10^{-3} Nm occurred. In addition, there is a negative 0.202×10^{-3} Nm torque about the z-axis (negative ψ rotation).

The bottom section of Table 4.9.6 compares the available maximum torque with the expected maximum torque from Section 4.9.1. In the worst case of rotation about the positive y-axis ($+\theta$), there is over 250 percent extra torque with the PPT system.

182

TABLE 4.9.5. – THRUSTER FIRING ORDER.

Thruster		Translation +X	-X	+Y	-Y	+Z	-Z	Rotation About X-axis +φ	-φ	About Y-axis +θ	-θ	About Z-axis +ψ	-ψ
1a	X	-	1.0	-	0	0	0	-	0	0	-0.194	0	-
	Y		0		1.0	0	0		0.758	0	0	1.0	
	Z		0		0	-1.0	1.0			1.0	0.981	0	
1b	X	-	1.0	-	-	0	0	-	-	0	-0.194	-	-
	Y		0			0	0			0	0		
	Z		0			-1.0	1.0			1.0	0.981		
1c	X	-	1.0	0	-	0	0	0	-	0	-0.194	-	0
	Y		0	-1.0		0	0	-0.758		0	0		-1.0
	Z		0	0		-1.0	1.0	0		1.0	0.981		0
2a	X	-	1.0	0	-	0	0	0	0	0	-0.334	-0.782	-
	Y		0	-1.0		0	0	-0.095	0	0	0	0.623	
	Z		0	0		-1.0	1.0	0.942	1.0	0.928	0.943	0	
2b	X	-	1.0	0	-	0	0	0	0	0	-0.334	-	0.782
	Y		0	-1.0		0	0	-0.095	0	0	0		-0.623
	Z		0	0		-1.0	1.0	0.942	1.0	0.928	0.943		0
3a	X	-	1.0	0	-	0	0	0	0	-	-1.0	-1.0	-
	Y		0	-1.0		0	0	-0.027	0		0	0	
	Z		0	0		-1.0	1.0	0.963	1.0		0	0	
3b	X	-	-	0	-	0	0	0	0	-	-	-	-
	Y			-1.0		0	0	-0.027	0				
	Z			0		-1.0	1.0	0.963	1.0				
3c	X	-1.0	-	0	-	0	0	0	0	1.0	-	-	1.0
	Y	0		-1.0		0	0	-0.027	0	0			0
	Z	0		0		-1.0	1.0	0.963	1.0	0			0
4a	X	-1.0	-	0	-	0	0	0	0	0.334	0	-0.782	-
	Y	0		-1.0		0	0	-0.095	0	0	0	-0.623	
	Z	0		0		-1.0	1.0	0.942	1.0	-0.943	-0.928	0	
4b	X	-1.0	-	0	-	0	0	0	0	0.334	0	-	0.782
	Y	0		-1.0		0	0	-0.095	0	0	0		0.623
	Z	0		0		-1.0	1.0	0.942	1.0	-0.943	-0.928		0
5a	X	-1.0	-	0	-	0	0	0	-	0.194	0	0	-
	Y	0		-1.0		0	0	-0.758		0	0	-1.0	
	Z	0		0		-1.0	1.0	0		-0.981	-1.0	0	
5b	X	-1.0	-	-	-'	0	0	-	-	0.194	0	-	-
	Y	0				0	0			0	0		
	Z	0				-1.0	1.0			0.981	-1.0		
5c	X	-1.0	-	-	0	0	0	-	0	0.194	0	-	0
	Y	0			1.0	0	0		-0.758	0	0		1.0
	Z	0			0	-1.0	1.0		0	-0.981	-1.0		0
6a	X	-1.0	-	-	0	0	0	0	0	0.334	0	0.782	-
	Y	0			1.0	0	0	0	0.095	0	0	-0.623	
	Z	0			0	-1.0	1.0	-1.0	-0.942	-0.943	-0.928	0	
6b	X	-1.0	-	-	0	0	0	0	0	0.334	0	-	-0.782
	Y	0			1.0	0	0	0	0.095	0	0		0.623
	Z	0			0	-1.0	1.0	-1.0	-0.942	-0.943	-0.928		0
7a	X	-1.0	-	-	0	0	0	0	0	1.0	-	1.0	-
	Y	0			1.0	0	0	0	0.027	0		0	
	Z	0			0	-1.0	1.0	-1.0	-0.963	0		0	
7b	X	-	-	-	0	0	0	0	0	-	-	-	-
	Y				1.0	0	0	0	0.027				
	Z				0	-1.0	1.0	-1.0	-0.963				
7c	X	-	1.0	-	0	0	0	0	0	-	-1.0	-	-1.0
	Y		0		1.0	0	0	0	0.027		0		9
	Z		0		0	-1.0	1.0	-1.0	-0.963		0		0
8a	X	-	1.0	-	0	0	0	0	0	0	-0.334	0.782	-
	Y		0		1.0	0	0	0	0.095	0	0	0.623	
	Z		0		0	-1.0	1.0	-1.0	-0.942	0.928	9.43	0	
8b	X	-	1.0	-	0	0	0	0	0	0	-0.334	-	-0.782
	Y		0		1.0	0	0	0	0.095	0	0		-0.623
	Z		0		0	-1.0	1.0	-1.0	-0.942	0.928	9.43		0
9(2)	X	-0.983	0.983	-	0	-	0	0	0	2.0	-2.0	2.0	-2.0
	Y	0	0		1.97		0	1.98	0	0	0	0	0
	Z	0	0		0		1.0	0.296	0.639	0	0	0	0
10(2)	X	-0.983	0.983	0 ·	-	-	0	0	0	2.0	-2.0	-2.0	2.0
	Y	0	0	-1.97			0	0	-1.98	0	0	0	0
	Z	0	0	0			1.0	0.639	0.296	0	0	0	0
Total thrust for translation (in mlbs)	X	-10.97	10.97	0	0	0	0	0	0	0	0	0	0
	Y	0	0	-10.97	10.97	0	0	0	0	0	0	0	0
	Z	0	0	0	0	-20.0	24.0	0	0	0	0	0	0
Thrust in lbs		0.010966	0.010966	0.010966	0.010966	0.0200	0.0240						
Thrust in N		0.048777	0.048777	0.048777	0.048777	0.08896	0.106752						
Maximum Expected in N.		0.013886	0	0	0	0	0.075512						
Error, %		251	∞	∞	∞	∞	41.4						

TABLE 4.9.6. – RESULTANT ROTATIONAL TORQUES.

Thruster		About X-axis +φ	−φ	About Y-Axis +θ	−θ	About Z-axis +ψ	−ψ
1a	φ	-	-22.1	0	0	-16.8	-
	θ		0	60.0	-62.1	0	
	ψ		45.5	0	0	+60.0	
1b	φ	-	-	0	0	-	16.8
	θ			60.0	-62.1		-
	ψ			0	0		
1c	φ	22.1	-	0	0	-	16.8
	θ	0		60.0	-62.1		0
	ψ	-45.5		0	0		-60.0
2a	φ	45.8	-46.9	-43.7	44.2	-10.5	-
	θ	-35.2	37.4	34.7	-40.9	-13.1	
	ψ	-3.55	0	0	15.7	60.0	
2b	φ	45.8	-46.9	-43.7	44.2	-	10.5
	θ	-35.2	37.4	34.7	-40.9		13.1
	ψ	-3.55	0	0	15.7		-60.0
3a	φ	58.2	-60.0	-	0	0	-
	θ	0	0		-16.8	-16.8	
	ψ	0	0		60.0	60.0	
3b	φ	58.2	-60.0	-	-	-	-
	θ	0	0				
	ψ	0	0				
3c	φ	58.2	-60.0	0	-	-	0
	θ	0	0	16.8			16.8
	ψ	0	0	60.0			60.0
4a	φ	45.8	-46.9	44.2	-43.5	10.5	-
	θ	35.2	-37.4	40.9	-34.7	-13.1	
	ψ	3.55	0	15.7	0	60.0	
4b	φ	45.8	-46.9	44.2	-43.5	-	-10.5
	θ	35.2	-37.4	40.9	-34.7		13.1
	ψ	3.55	0	15.7	0		60.0
5a	φ	22.1	-	0	0	16.8	-
	θ	0		62.1	-60.0	0	
	ψ	45.5		0	0	60.0	
5b	φ	-	-	0	0	-	-
	θ			62.1	-60.0		
	ψ			0	0		
5c	φ	-	-22.1	0	0	-	-16.8
	θ		0	62.1	-60.0		0
	ψ		45.5	0	0		-60.0
6a	φ	46.9	-45.8	-44.2	43.5	10.5	-
	θ	-37.4	35.2	40.9	-34.7	13.1	
	ψ	0	3.55	-15.7	0	60.0	
6b	φ	46.9	-45.8	-44.2	43.5	-	-10.5
	θ	-37.4	35.2	40.9	-34.7		-13.1
	ψ	0	3.55	-15.7	0		-60.0
7a	φ	60.0	-58.2	0	-	0	-
	θ	0	0	16.8		16.8	
	ψ	0	0	-60.0		60.0	
7b	φ	60.0	-58.2	-	-	-	-
	θ	0	0				
	ψ	0	0				
7c	φ	60.0	-58.2	-	0	-	0
	θ	0	0		-16.8		-16.8
	ψ	0	0		-60.0		-60.0
8a	φ	46.9	-45.8	43.5	-44.2	-10.5	-
	θ	37.4	-35.2	34.7	-40.9	13.1	
	ψ	0	-3.55	0	-15.7	60.0	
8b	φ	46.9	-45.8	43.5	-44.2	-	10.5
	θ	37.4	-35.2	34.7	-40.9		13.1
	ψ	0	-3.55	0	-15.7		-60.0
9(2)	φ	155	-7.35	0	0	0	0
	θ	0	0	154	-154	-154	154
	ψ	0	0	-23.0	23.0	23.0	-23.0
10(2)	φ	155	-155	0	0	0	0
	θ	0	0	154	-154	154	-154
	ψ	0	0	23.0	-23.0	23.0	-23.0
Total Rotation (in mlb-meters)	φ	932	-932	1010	-1010	526	-526
	θ	0	0	0	0	0	0
	ψ	0	0	0	0	0	0
in ft-lbs		3.06	-3.06	3.31	-3.31	1.73	-1.73
in Nm		4.15	-4.15	4.49	-4.49	2.34	-2.34
Expected maximum in Nm		0.133	0.552	1.269	0.735	0	0
Error, %		3020	651	254	511	∞	∞

184

After calculating the average force and torque for each beta angle orbit, the amount of fuel required can be calculated. The forces cause a direct thrust requirement for translation. The torques, however, are related to thrust by a moment arm. This problem is solved through use of Tables 4.9.5 and 4.9.6. For example, the average torque over one second about the x-axis is 0.1292 Nm for β = 90 deg. The absolute value of the vector sum of all the thruster used for maximum rotation about the x-axis is summarized in Table 4.9.5. This gives the total thrust used per second in the maximum rotation configuration of 0.08098 N/s. The average torque of 4.15 Nm achieved via this thrust is given in Table 4.9.7. Setting up a simple proportional calculation gives the force needed to match the required torque (0.002521 N/s).

Table 4.9.7 shows the total force requirement by the thrusters for each orbit. It also shows what part of this is due to translational and rotational thrust requirements. This is done for three different beta angle orbits.

TABLE 4.9.7. - THRUSTER FORCE REQUIREMENTS PER ORBIT.

β Angle, deg	Translational, N	Rotational, N	Total, N
0	39.66×10^{-3}	2.891×10^{-3}	0.04255
45	41.79×10^{-3}	0.935×10^{-3}	0.04273
90	20.70×10^{-3}	1.189×10^{-3}	0.02189

The worst case is for β = 45 deg where a total force of 0.0427 N per orbit must be supplied. From this a total impulse (I_t) can be calculated (I_t = 250.6 N.s). Then using the formula

$$m = \frac{I_t}{I_{SP} \cdot g}$$

where: I_{sp} = specific impulse (s)
    g = gravitational constant
    m = mass of fuel in kg

the mass of fuel can be calculated per orbit (0.01163 kg). For a 10-year
mission, the total fuel used is 625.4 kg.

There are 24 thrusters; therefore, about 26 kg per thruster (average) is
necessary. Note that from Table 4.9.5 there is only 15 kg of fuel per
thruster. If we could double the fuel supply there would be approximately 15
percent extra fuel. This could be done via resupply, or larger initial fuel
tanks.

4.9.4. Eight-Centimeter Mercury Ion Thruster System

The mercury ion thruster system is modularized and can be packaged for
many different constraints. As shown in Figure 4.9.10 four components make up
each system: thruster and gimbaling assembly, fuel tank, power electronics
unit, and a digital interface unit. Tables 4.9.8 through 4.9.11 give speci-
fications of these components.

The principal concern with this thruster is its "dirty" exhaust, consis-
ting of positively charged mercury ions. The ions tend to drain electrical
energy from the ECMM's membrane control surface. Also, the mercury may be
harmful to the Mylar membrane, the graphite structure, and the feed horns on
the ECMM. However, further analysis is required to determine the effect of
such contamination.

Table 4.9.12 gives the schemes for a maximum translational and rotational
firing order. In the translational section the direction of thrust is broken
down into its three components for each thruster. For example, to get maximum
translation in the positive x-direction, thrusters in locations 1, 2, 3, 7,
and 8 (Section 4.9.2) must be fired at full power, 9.96×10^{-3} N, in the
negative x-direction. The y and z components of thrust for all of these
thrusters are zero. To prevent rotation, thrusters at locations 9 and 10
(Section 4.9.2) are throttled to 5.42×10^{-3} N of thrust in the negative
x-direction. The result is a pure translation in the positive x-direction.

The bottom of the chart compares the external forces (Section 4.9.1) to
the thruster-produced forces. The rotation figures give the thrust in the x-,

186
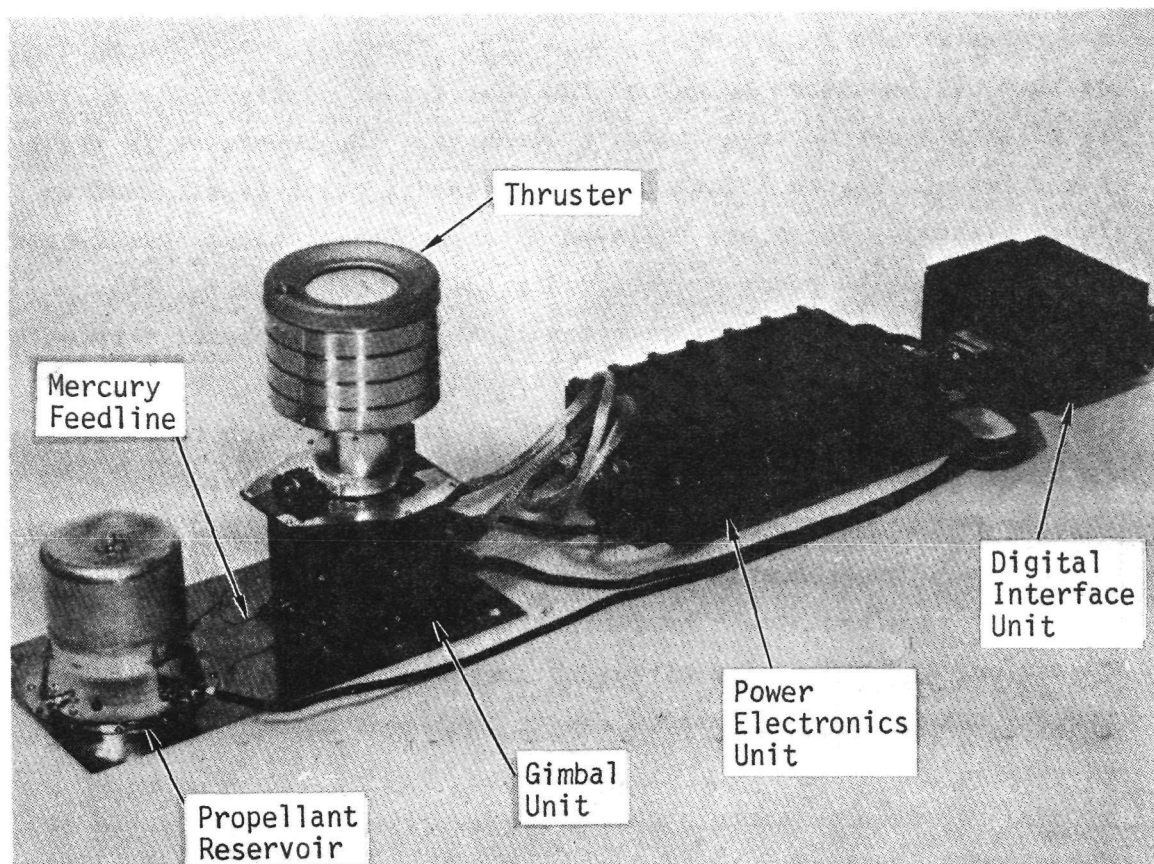
Total Weight 27.2 kg   Total Power   212 W

Figure 4.9.10. - Eight-cm ion thruster subsystem.

TABLE 4.9.8. - DIGITAL CONTROLLER AND INTERFACE UNIT.

Provides simple command and telemetry interfaces via autonomous control of PEU and thruster; uses digital microprocessor logic	
Weight	3.75 kg
Size	25 x 24 x 12 cm
Power (max.)	10 watts at 28 Vdc
Thermal dissipation	10 watts
Input	16-bit serial digital command
Processor	8-bit CMOS-RCH 1802
Memory	2K read and write
	8K read only
Output	32 8-bit words
Temperature	-20 to +50°C

TABLE 4.9.9. – THRUSTER, GIMBAL, AND BEAM SHIELD UNIT.

Thruster converts electrical power and propellant into thrust	
Thrust level	4.98×10^{-3} N
Specific impulse	2700 s
Weight	3.88 kg
Size	
Beam diameter	8 cm
Gimbal adapter diameter	7.6 cm
External diameter	17 cm
Length	22.6 cm
Power to thruster	125 watts
Electrical efficiency	72 percent
Propellant efficiency	77 percent
Total efficiency	55 percent
Beam current	72 mA
Net acceleration voltage	1208 volts
Thermal dissipation	35 watts
Propellant flow rate	0.7 g/hr
Temperature range	-20 to 80°C
Design life	20 000 hours
	10 000 off/on cycles
Gimbal Unit	
Deflection in any azimuth	10 deg
Motor steps per degree deflection	2421
Time from +10 deg to -10 deg deflection	120 s
Motor drive power (max.)	7 W
Mass[a]	150 kg
Size Base	14.41 cm x 15.15 cm
Height	13.48 cm

[a] Includes mass of internal propellant feedline and manifold.

TABLE 4.9.10. – PROPELLANT TANK, VALVE, AND FEED UNIT.

Provides supply and control of mercury propellant to thruster	
Capacity	8.75 kg Mercury
	12 500 hr nominal operations
Size	
Tank diameter	13 cm
Overall diameter	18.42 cm
Bolt-circle·diameter	17.5 cm
Height	17 cm
Empty weight	1.45 kg
Pressure (max.)	241×10^6 N/m^2
Valve	Electromagnetic latching
Temperature range	-20 to +6°C

TABLE 4.9.11. – POWER ELECTRONICS UNIT.

Converts solar array voltage into 12 different voltages and currents required by the thruster	
Weight	7.5 kg
Size	39 x 20 x 11 cm
Power	
Nominal	165 watts at 70 Vdc
Max	200 watts at 70 Vdc
Efficiency	75 percent
Thermal dissipation	40 watts
Temperature range	-20 to +50°C

y-, and z-directions at each thruster location to provide the maximum rotation possible without translation. For example, to get maximum torque about the positive x-axis from thrusters in location 6 (Section 4.9.2), one would use full thrust in the direction that was perpendicular to a line drawn from the vehicle center of mass to the thruster location. This would yield 0.0 N of thrust in the x-direction, 3.35×10^{-3} N of thrust in the y-direction, and 9.39×10^{-3} N of thrust in the z-direction.

As a final note: ϕ is rotation about the x-axis, θ is rotation about the y-axis, and ψ is rotation about the z-axis.

Table 4.9.13 takes the maximum rotational thrusts on the previous chart and shows the torque imparted to the vehicle. For example, the thrusters at location 1 produce 0.242×10^{-3} N of thrust in the negative y-direction to get a positive rotation around the x-axis. They cause 4.07×10^{-3} Nm of torque around the x-axis, 0.0 Nm of torque around the y-axis, and -14.51×10^{-3} Nm of torque around the z-axis.

Finally, the bottom of the chart compares the external torques (Section 4.9.1) to the thruster-produced torques.

4.9.5. Momentum Exchange For Attitude Maintenance

Momentum exchange devices were considered for the attitude maintenance requirements of the spacecraft, but despinning of the momentum devices proved very costly.

The worst case was for $\beta = 90$ deg, because this orbit is never shadowed from the solar pressure force. Table 4.9.14 shows this case, with the number of thrusters and power required discussed in Section 4.9.3 using the pulsed-plasma thrusters.

Continuous thruster firing would be much more efficient if it were used directly for attitude maintenance; therefore, momentum exchange devices were not used.

TABLE 4.9.12. - THRUSTER FIRING ORDER.

Thruster	Translation +x	-x	+y	-y	+z	-z	Rotation +φ	-φ	+θ	-θ	+ψ	-ψ	
1	-2.24	0	0	0	0	0	0	0	0	-.603	0.	0	
	0	0	-2.24	2.24	0	0	-.0545	.0545	0	0	2.24	-2.24	
	0	0	0	0	-2.24	2.24	0	0	-2.24	2.16	0	0	
2	-2.24	0	0	0	0	0	0	0	0	-.917	1.75	-1.75	
	0	0	0	2.24	0	0	0	.754	0	0	1.40	-1.40	
	0	0	0	0	-2.24	2.24	-2.24	2.11	-2.24	+2.24	0	0	
3	-2.24	2.24	0	0	0	0	0	0	-1.02	-1.02	+2.24	-2.24	
	0	0	0	2.24	0	0	0	.603	0	0	0	0	
	0	0	0	0	-2.24	2.24	-2.24	-2.16	.24	.24	0	0	
4	0	2.24	0	0	0	0	0	0	.917	0	1.75	-1.75	
	0	0	0	2.24	0	0	0	.754	0	0	-1.40	1.40	
	0	0	0	0	-2.24	2.24	-2.24	2.11	2.04	-2.24	0	0	
5	0	2.24	0	0	0	0	0	0	.603	0	0	0	
	0	0	-2.24	2.24	0	0	-.0545	.0545	0	0	-2.24	2.24	
	0	0	0	0	-2.24	2.24	0	0	2.16	-2.24	0		
6	0	2.24	0	0	0	0	0	0	.917	0	1.75	1.75	
	0	0	-2.24	0	0	0	-.754	0	0	0	-1.40	1.40	
	0	0	0	0	-2.24	2.24	2.11	-2.24	2.04	-2.24	0	0	
7	-2.24	2.24	0	0	0	0	0	0	1.02	-1.02	-2.24	2.24	
	0	0	-2.24	0	0	0	-.603	0	0	0	0	0	
	0	0	0	0	-2.24	2.24	2.16	-2.24	.24	.24	0	0	
8	-2.24	0	0	0	0	0	0	0	0	-.917	-1.75	1.75	
	0	0	-2.24	0	0	0	-.754	0	0	n	1.40	-1.40	
	0	0	0	0	-2.24	2.24	2.11	-2.24	-2.24	2.04	0	0	
9	-1.22	1.22	0	0	0	0	0	0	-2.24	2.24	-2.24	2.24	
	0	0	-2.24	0	0	0	0	-2.22	0	0	0	0	
	0	0	0	1.38	0	2.24	-.672	-.332	0	0	0	0	
10	-1.22	1.22	0	0	0	0	0	0	-2.24	2.24	2.24	-2.24	
	0	0	0	2.24	0	0	2.22	0	0	0	0	0	
	0	0	1.38	0	0	2.24	-.332	.672	0	0	0	0	
Total thrust for trans	-13.64	13.64	0	0	0	0	0	0	0	0	0	0	x Thrust in
	0	0	-13.44	13.44	0	0	0	0	0	0	0	0	y mlbf
	0	0	1.38	1.38	-17.92	22.4	0	0	0	0	0	0	z
Thrust in prin dir in N	-.0607	.0607	-.0598	.0598	-.0797	.0996							
Max. ext force in N	0	.0139	0	0	.0755	0							
Error in canciling ext force %	—	337	—	—	31.9	—							

TABLE 4.9.13. - RESULTANT ROTATIONAL TORQUES.

Thruster	$+\phi$	$-\phi$	$+\theta$	$-\theta$	$+\psi$	$-\psi$	
1	.914 0 -3.27	-.914 0 3.27	.0 134. 0	0 140. 0	-37.6 0 134.	37.6 0 -134.	
2	105 83.8 0	-112. -78.9 28.2	105. 83.8 0	-95.7 -91.7 -43.0	-13.5 29.4 134.	23.5 -29.4 -134.	
3	134. 0 0	-140. 0 0	-14.4 17.1 61.2	-14.4 -17.1 -61.2	0 37.6 134.	0 -37.6 -134.	
4	105. -83.8 0	-112. 78.9 -28.2	-95.7 91.7 43.0	105 -83.8 0	23.5 29.4 134.	-23.5 -29.4 -134.	
5	.914 0 3.27	-.914 0 -3.27	0 140. 0	0 -134. 0	37.6 0 134.	-37.6 0 -134.	
6	112. 78.9 28.2	-105. -83.8 0	95.7 91.7 -43.0	-105. -83.8 0	23.5 -29.4 134.	-13.5 29.4 -13.4	
7	140. 0 0	-134. 0 0	14.4 17.1 -61.2	14.4 -17.1 61.2	0 -37.6 134.	0 37.6 -134.	
8	112. -78.9 -28.2	-105 83.8 0	-105. 83.8 0	95.7 -91.7 43.0	-23.5 -29.4 134.	23.5 29.4 -134.	
9	7.73 0 0	-174. 0 0	0 172. 25.8	0 -172. -25.8	0 172. 25.8	0 -172 -25.8	
10	174. 0 0	-7.73 0 0	0 172. -25.8	0 -172. 25.8	0 -172. 25.8	0 172. -25.8	
Total torque ϕ θ ψ	892. 0 0	-892. 0 0	0 1003. 0	0 -1003. 0	0 0 1124.	0 0 -1124.	Torque in mlbf - m
Total torque	2.93	-2.93	3.29	-3.29	3.69	-3.69	In ft - lb
Total torque	3.97	-3.97	4.46	-4.46	5.00	-5.00	In N-m
Max. ext. torque	.133	-.552	1.269	-.735	0	0	In N-m
Error, %	2885	619	251	507.	—	—	

TABLE 4.9.14. - MOMENTUM EXCHANGE DATA FOR β = 90 deg.

Thruster firing time	Number of thrusters	Thruster total power requirement
1 minute	132	20.4 kW/s
1 second	7900	1220.0 kW/s

5.0 ANTENNA QUALITY AND PERFORMANCE

The antenna quality and performance task was directed toward an evaluation of the effects of reflector surface irregularities on the performance of the antenna. It consisted of a modeling of the reflector surface irregularities in accordance with descriptions given by General Research Corporation followed by a computation of the effects of these irregularities on the gain and the sidelobe levels of the antenna. The latter step was done using a recently developed surface current integration program. The program had been used previously on some relatively small reflectors, but this was its first use on a very large reflector and also its first use on the Langley computers, so some effort was invested in debugging and on validating the performance of the program.

It is the requirement of the adaptive surface control system, i.e., the electrostatically-controlled membrane, to control the surface irregularities to a level sufficiently small so that there is no significant rf performance degradation in the antenna relative to that of an ideal reflector. It was found that the irregularity model given to us by General Research meets this requirement.

5.1 MODELING OF THE SURFACE IRREGULARITIES

The reflector, as discussed elsewhere in the report, has a diameter of 100 m. It has a spherical surface with a radius of curvature equaling 200 m. The focal region where the feeds are located is on a concentric sphere at a radius of curvature of 100 m, giving a focal length of 100 m. Each feed illuminates a spot on the reflector of 50 m in diameter, which partially overlaps the spots of nearby feeds. Considering just this spot, the antenna has an effective f/D of 2.0. The surface irregularity model shows a slight increase in the magnitude of the irregularities with distance from the reflector center, so the worst-case spot is one that just touches the edge of the reflector, as illustrated in Figure 5.1.1. This is the spot location selected for our analysis.

194

The General Research input defines expected distortions due to three distinct causes. These distortions are: spacing between the electrodes; spacing between the ties on the electrode surface; and spacing between seams in the electrodes and reflector surfaces. Each of these distortions is periodic and repetitive if the electrodes, ties, and seams are located on a systematic grid. This is important for the antenna pattern because the effect of any repetitive distortion in a cartesian grid is to divert gain from the main beam and generate spurious pattern lobes ("grating lobes") at specific angular locations in the pattern. In contrast to this, random distortions, which also divert gain from the main beam, distribute their effect on the pattern over a wide angle, with no generation of specific lobes. All the electrodes, ties, and seams can be on separate grids and in general probably would be. However, we have elected for this analysis to put all of them on the same grid as sketched in Figure 5.1.2. This represents the worst case for grating lobe formation. If the actual construction puts the electrodes, ties, and seams on distinct grids the grating lobes will be less than those calculated here. The dimension on the grid, 5 by 5 m along the diagonals, was selected in order to hold the overall rms error to around 1 mm. Applying this layout to the model given us by General Research gives:

$$\delta(X, Y) = \left(0.17 + \frac{0.03}{R}\right) \sin\left(\frac{2\pi X}{707}\right) \sin\left(\frac{2\pi Y}{707}\right) \tag{1}$$

The ties are the dominant factor in the distortion, so the principal way to reduce distortion is to reduce the spacing between ties on the electrode surface. Dimensions are in centimeters. The dependence on R, the distance from the reflector center (not the spot center), is not large, so the pattern should not change significantly as the spot is moved across the reflector. This model gives a gently undulating surface with lows at the electrode centers and highs at the tie points.
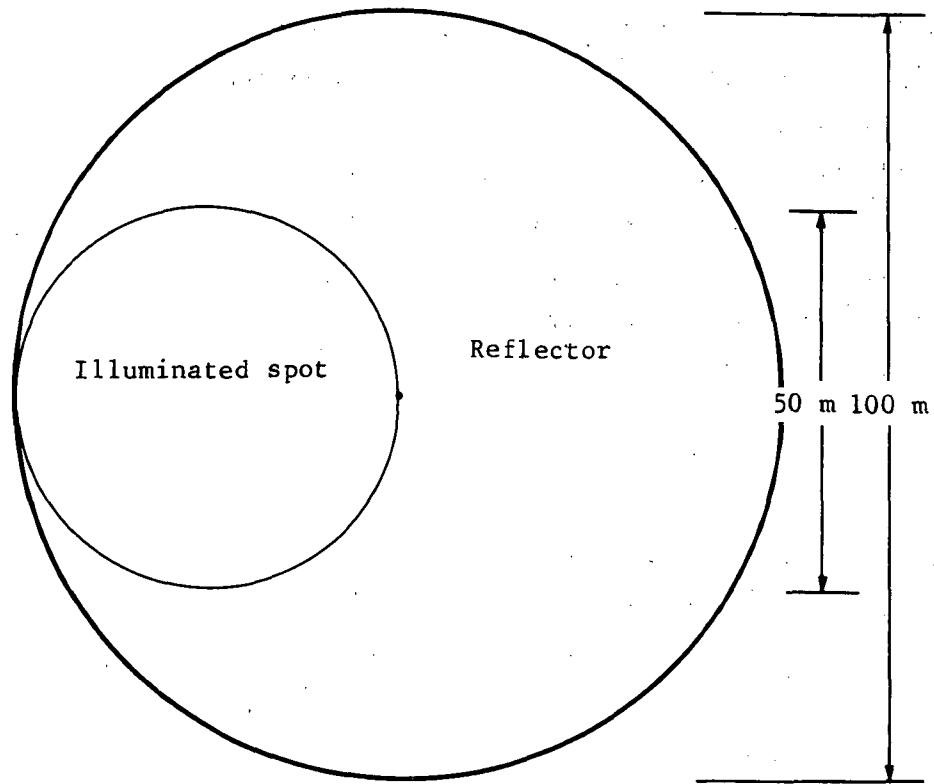
Figure 5.1.1. - Location of illuminated spot.
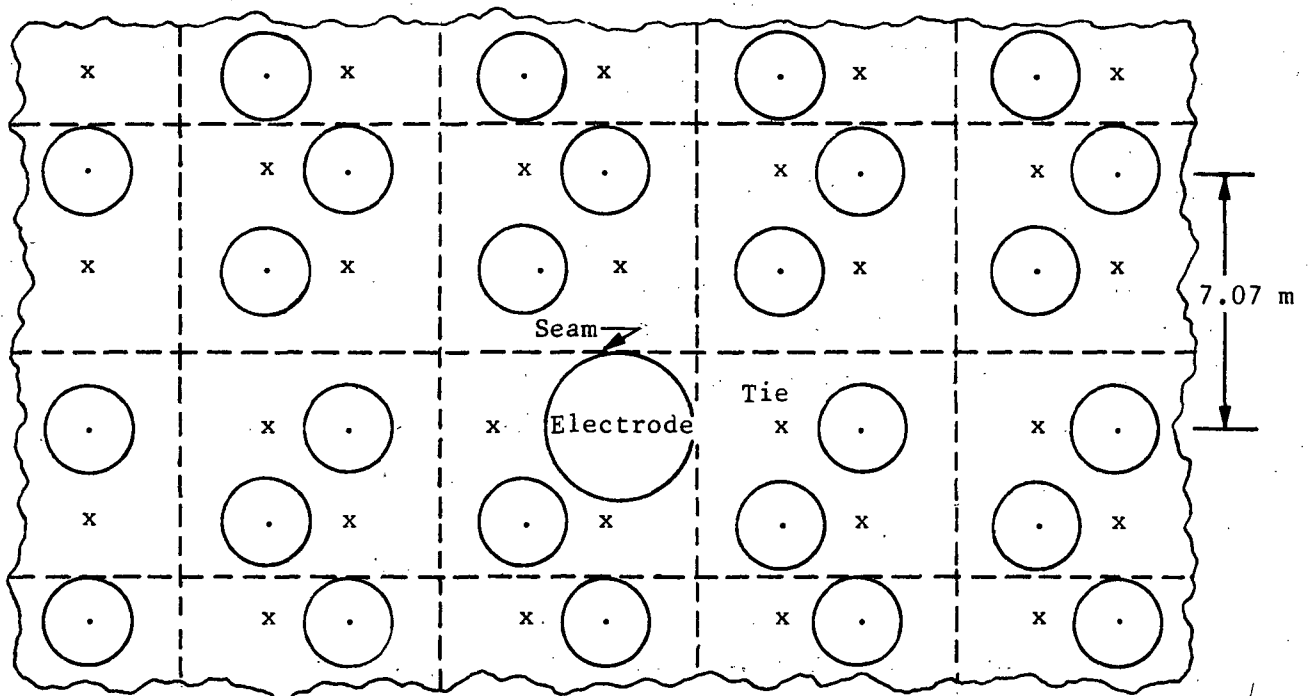
Figure 5.1.2. - Electrode, tie, and seam grid layout (worst case).

There are effects that will tend to spread out the grating lobes. The irregularities are not in the aperture plane. They are on the curved reflector surface. The X and Y dimensions in the expression given above are not actually in the planar coordinates of the aperture. They were computed as arc lengths along the curved reflector surface. Their projection on the aperture varies slightly from a uniform grid. This more nearly models the actual construction that would be used, and will reduce the computed grating lobes below those that would be given by using coordinates in the aperture plane. These effects increase with distance away from boresight, so the first grating lobe will be the largest one.

5.2 VALIDATION OF THE SURFACE CURRENT INTEGRATION PROGRAM

Pattern and gain computations were done only at the highest frequency of interest, 5 GHz, (wavelength λ = 6 cm), because the irregularity effects are greatest at the highest frequency. The program will not give accurate results for nonideal reflector surfaces unless the spacing between computed surface points is around 0.7λ or less, so a sample point spacing of 4.5 cm was selected. This gives 1113 points across the 50-m spot or approximately 973 000 points at which normals and surface currents are calculated, and a 973 000 point integration for each computed point in the far-field pattern. The program is not set up at this time to easily handle spherical surfaces, so we assumed a 50-m parabola with f/D = 2 for pattern computation purposes. The actual antenna would use a spherical reflector and an aberration-correcting feed, which should give essentially the same secondary pattern. The program was run for the distorted surface described above and also for an ideal paraboloid. One part of the validation was to compare the ideal paraboloid results with results generated by another program. The second program is a ray trace and aperture integration program, which can only be used for ideal paraboloids. The two computed patterns are shown in Figures 5.2.1 and 5.2.2. A $\cos^{20}$ feed amplitude pattern was used for both runs. This gives a 5-dB amplitude taper at the reflector edge, which results in relatively high sidelobes. A feed giving lower sidelobes would be used in an operational radiometer antenna. The key parameters of the two computed patterns are compared in Table 5.2.1. The 3-dB beam width and the null positions agree to

within the accuracy of the plots. There is a small difference in the first sidelobe height and this difference increases with distance away from the main beam. This can probably be explained by the greater accuracy of the current integration method. Accuracy of the aperture integration method is not extremely good beyond the first few sidelobes. The biggest difference is in the computed peak gain. The gain computation of the aperture integration program has been validated by measurements and should be accurate.
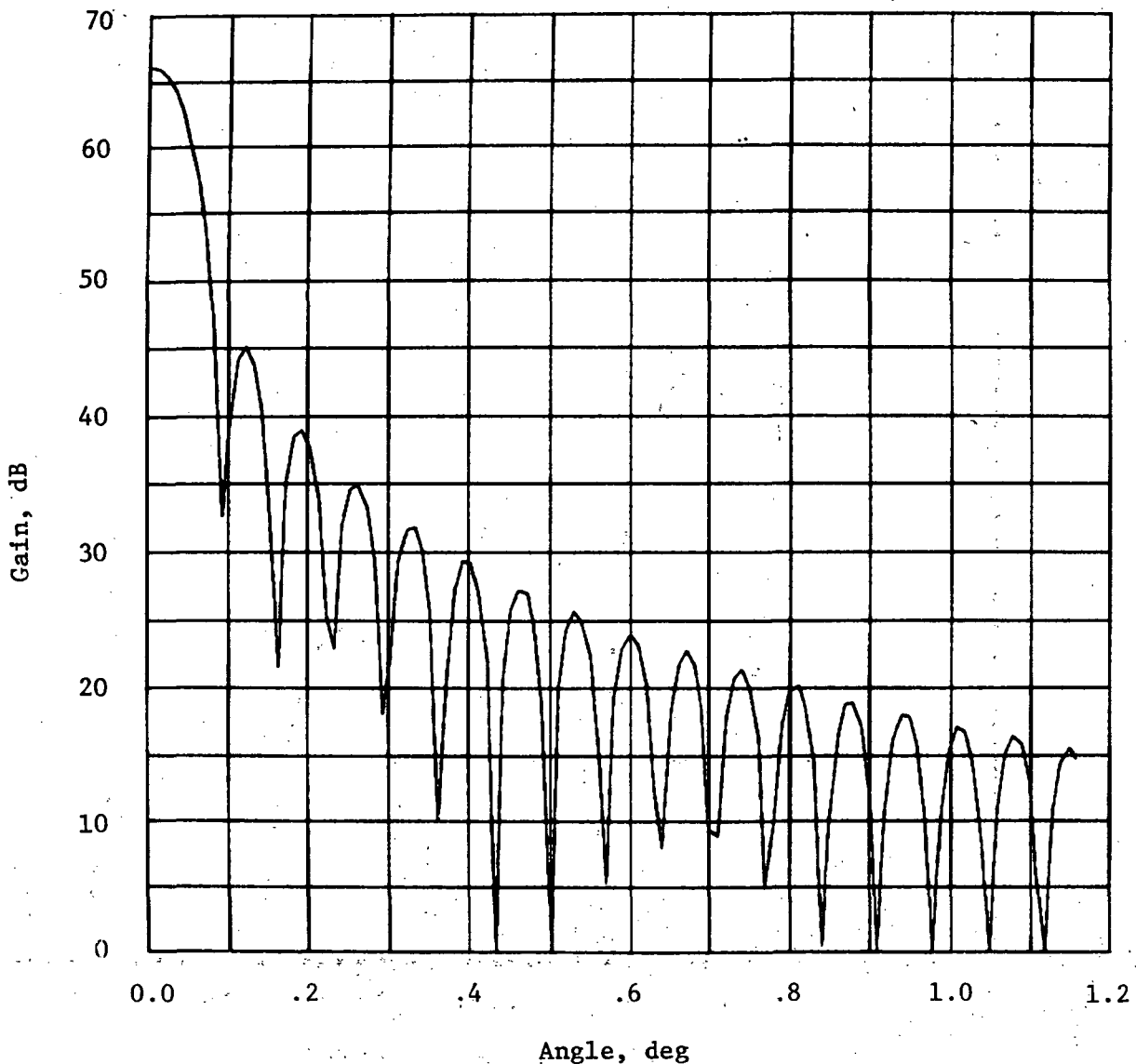
Figure 5.2.1. – Radiation pattern, surface current integration, ideal surface.

The absolute gain computation in the current integration program needs to be reviewed carefully. The main difference appears to be in the computation of the spillover loss. The relative gain computations are more important to us for present purposes, and they appear to be good.
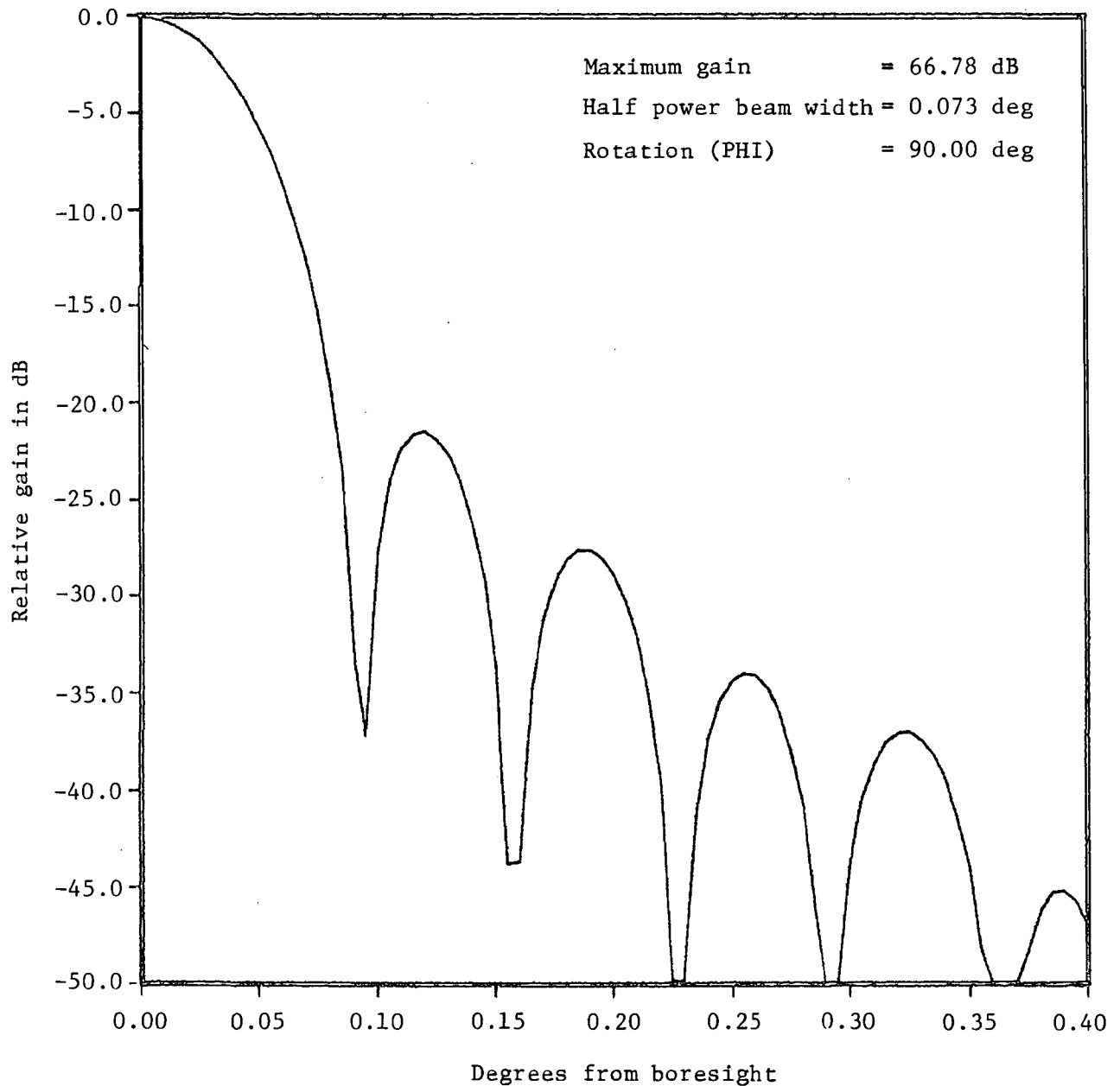
Figure 5.2.2. – Secondary pattern computed
by aperture integration.

TABLE 5.2.1. - COMPARISON BETWEEN SURFACE CURRENT AND
APERTURE INTEGRATION RESULTS.

Parameter	Aperture integration	Surface current integration
3 dB beamwidth	0.073 deg	0.074 deg
Position of first null	0.092 deg	0.090 deg
Position of second null	0.159 deg	0.159 deg
Position of third null	0.227 deg	0.225 deg
Position of fourth null	0.290 deg	0.293 deg
Position of fifth null	0.363 deg	0.363 deg
First sidelobe level	-21.32 dB	-21.09 dB
Second sidelobe level	-27.74 dB	-27.11 dB
Third sidelobe level	-34.15 dB	-31.24 dB
Fourth sidelobe level	-36.99 dB	-34.43 dB
Fifth sidelobe level	-45.01 dB	-36.93 dB
Peak gain	66.78 dB	66.18 dB

The peak gains for the ideal and distorted surface were computed to be 66.183 dB and 66.019 dB respectively, a difference of 0.164 dB. This is the loss in gain due to the surface irregularities. It has been found on other programs that if surface irregularities are small and of short correlation distance (relative to the reflector diameter), the loss in gain is well predicted by the Ruze expression for random distortions of short correlation distance,

$$\text{Loss (dB)} = 686\left(\frac{\sigma}{\lambda}\right)^2 \tag{2}$$

where σ is the rms surface distortion. The rms value of our surface was computed to be 0.09271 cm. Putting this value into the Ruze expression gives exactly our computed gain difference, 0.164 dB. This result gives a strong validation to the accuracy of the program in computing the effects of surface irregularities.

200

5.3 COMPUTED RESULTS

The modeled surface has an rms deviation from the ideal of 0.09271 cm and this reduces the gain by 0.164 dB, a neglible amount. The other question of interest is the size of the grating lobes arising from the near-uniform pattern of the distortions. The distortions are very small and not quite on a uniform grid, so the grating lobes should be small. Figure 5.3.1 shows the pattern computed for the irregular surface along the $\phi = 0$ plane. Effective element spacing along the principal planes, as shown in Figure 5.1.2, is 353.5 cm and 500 cm in the diagonal planes. Given the wavelength $\lambda = 6$ cm, this gives two predicted locations for the first grating lobe of $\sin^{-1} (6/353.5) = 0.9725$ deg along the principal planes ($\phi = 0$ and 90 deg) and $\sin^{-1} (6/500) = 0.6876$ deg along the diagonal planes ($\phi = \pm 45$). The farther-out grating lobes would be at integer multiples of these values. Figure 5.3.1 shows the computed location for the first grating lobe at 1.00 deg, slightly farther out than the predicted value. This is due to the fact that the grid is on the curved reflector surface, not in the aperture plane. As shown, the first grating lobe height relative to the main beam is -38.98 dB. The pattern in the diagonal plane should be similar except the lobe would occur around 0.7 deg. The farther-out grating lobes would be smaller than the first one. Isolated lobes at this low level should not seriously affect the operation of the radiometer. They could be reduced if necessary by decreasing the spacing between ties on the electrode surface, which would reduce the rms distortion.

Table 5.3.1 shows the difference in lobe gain between the patterns given by the ideal and distorted surfaces. It covers the lobes out to the first grating lobe. As shown, most of these differences are approximately equal to the main lobe gain loss of 0.164 dB, with small variations from this delta, increasing near the grating lobe. Except in the vicinity of the grating lobes, the two patterns are almost identical and the effects of the surface irregularities are essentially confined to the grating lobes.
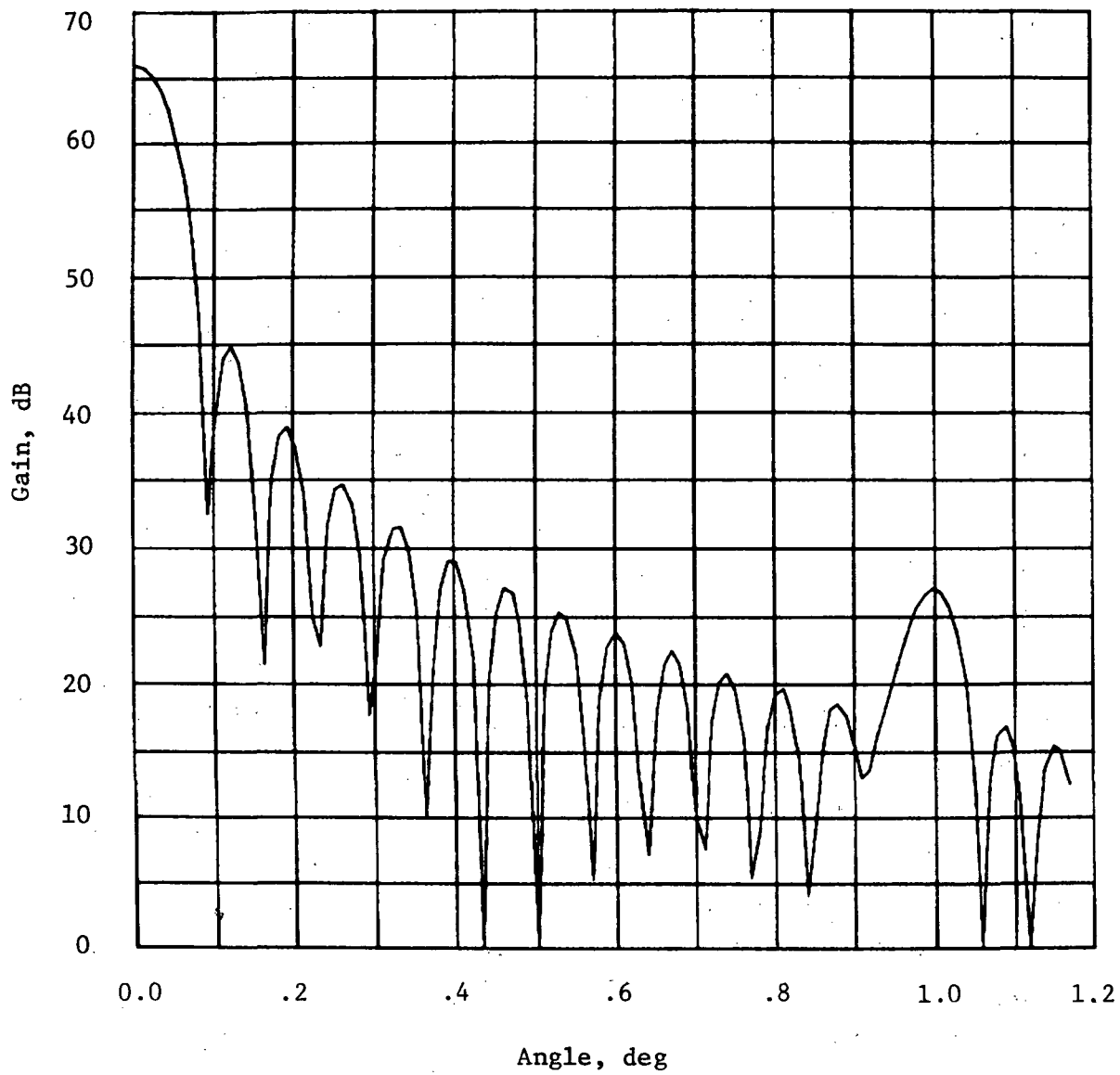
Figure 5.3.1. – Radiation pattern, surface current integration, modulated surface.

TABLE 5.3.1. - COMPARISON OF LOBE PEAKS, IDEAL AND DISTORTED REFLECTORS.

Lobe number	Location, deg	$\phi = 0$ Ideal-Distorted, dB
Main	0.00	0.164
1	0.12	0.164
2	0.19	0.156
3	0.26	0.194
4	0.33	0.151
5	0.39	0.157
6	0.46	0.233
7	0.53	0.215
8	0.60	0.170
9	0.67	0.253
10	0.74	0.461
11	0.81	0.480
12	0.88	0.315

5.4 DESCRIPTION OF THE SURFACE CURRENT INTEGRATION PROGRAM

The FIRE (Fast Integral rf Evaluation) code was developed as a design tool to be used in assessment of the performance of large reflector-type antennas. The following is a brief description of the model as applied to the performance analysis of the ASSA radiometer antenna.

The model is segmented into four major parts: surface generation, surface normals, surface currents, and far-field gain and pattern determination.

The surface generation module, SURFGEN, presently is using a closed-form function defining a delta divergence superimposed on an ideal parabola that geometrically defines the ASSA antenna. This function was user-supplied and generates the cartesian (x, y, z) file necessary for use by the other sections of the program. The sampling interval across the user's surface is determined

by the integration technique. This interval is 3/4 λ, where λ = .06 m and the diameter is 50.04 m. This generates $\pi/4 \cdot 1113^2$ = (.973 X 10^6) points across the entire surface.

Using the data generated in SURFGEN, the next overlay calculates a normal unit vector to each point on that surface. As the normal is perpendicular to planar sections on the surface, a three-point sample in both x and y was used to determine the normal. Two points were used on the edge.

The equations used in this calculation are given here:

$$\Delta = \left[1 + \frac{\lambda^2}{4F^2} + \frac{d\delta}{dX}\bigg|_{X,Y}^2 + \frac{Y^2}{4F^2} + \frac{d\delta}{dY}\bigg|_{X,Y}^2 \right]^{1/2}$$

$$X_{normal} = -\frac{1}{\Delta}\left[\frac{X}{2F} + \frac{d\delta}{dX}\bigg|_{X,Y} \right]$$

(3)

$$Y_{normal} = -\frac{1}{\Delta}\left[\frac{Y}{2F} + \frac{d\delta}{dY}\bigg|_{X,Y} \right]^{1/2}$$

$$Z_{normal} = -\frac{1}{\Delta}$$

where F is the focal length, 100 m.

(x, y) is the surface distortion, taken from the expression given in Section 5.1. Each component magnitude is solved for and saved separately. With the surface geometry and normals to that surface defined, a gain pattern for the reflector can be determined.

The surface-current method used by the FIRE code differs from the more commonly used aperture integration method in that the scalar integration over the aperture is replaced by a vector integration of surface current density over the reflector surface. If the reflector surface is illuminated by a feed antenna at the reflector focus, then the magnetic intensity vector $\tilde{H}_f$ may be calculated at any point on the reflector surface. If $\tilde{N}$ is the normal to the

surface at any point on the surface of the reflector, the electromagnetic boundary conditions of vanishing fields at the surface of a perfect conductor yield the current density at that point on the surface:

$$\tilde{J} = 2\left[\tilde{N} \times \tilde{H}_f\right] \tag{4}$$

where $\tilde{J}$ is the surface current density.

This surface current density is then integrated over the entire reflector surface to calculate the electric intensity vector in the far-field of the antenna:

$$E_{X,Y} = \frac{e^{-jk\tilde{R}}}{|\tilde{R}|} \cdot \tilde{i}_{X,Y} \cdot \iint 2\left(\tilde{N} \times \tilde{H}_f\right)e^{jk\bar{\rho}\tilde{R}}ds \tag{5}$$

where: $\tilde{R}$ = the vector from the focus to the far-field point.

$\bar{\rho}$ = the vector from the focus to a point on the reflector surface.

$\tilde{i}_{X,Y}$ = the unit vectors in the x or y sense.

k = 2π/wavelength

j = $\sqrt{-1}$

ds = the elemental reflector surface area.

It can be seen that the calculation of far field patterns involves:

Feed characteristics ($\tilde{H}_f$)
Reflector surface modeling
Geometric calculations ($\bar{\rho}$, $\tilde{R}$)
Integration

For this program, a simplified feed model is used:

$$G_F \approx \cos^n \theta$$

where G_F is the feed power pattern and θ is the polar angle in a spherical coordinate system with the origin at the feed phase center and focus of the reflector. This permits tapering the illumination in a simple manner. $n = 40$ was selected to give an edge taper of approximately 5 dB.

The reflector surface specification has been chosen to service a wide area of applications. No symmetry need be assumed for the reflector surface, because the ability to handle random asymmetric distortions is a key element of the FIRE code. Most rf analysis programs use Romberg or Simpson's integration to compute such integrals. A faster technique has been developed by Ludwig (ref. 1). This Ludwig Technique, together with the extensive use of overlayed code, are the major design assets of the program.

During the analysis of the ASSA radiometer antenna, which was carried out on the Langley computer system, optimum use was made of the restartability built into the program. The major problem encountered concerned computer time limitations. This problem was solved by the fact that once the surface is generated, normals are computed and surface currents are solved; all this data is stored on permanent disc storage. This allows the user to evaluate as much far-field data as needed. The far-field pattern was divided into groups of 14 points. Each group was analyzed in separate runs, which did not exceed the allowable time limit.

---

[1] "Computation of Radiation Patterns Involving Numerical Double Integration"; J.P.L. Technical Report 32-1430; A.C. Ludwig; Jet Propulsion Lab; California Institute of Technology; Pasadena, California; July 10, 1968.

APPENDIX A

MODAL CHARACTERISTICS OF THE
100-METER BOX TRUSS RADIOMETER

Page intentionally left blank
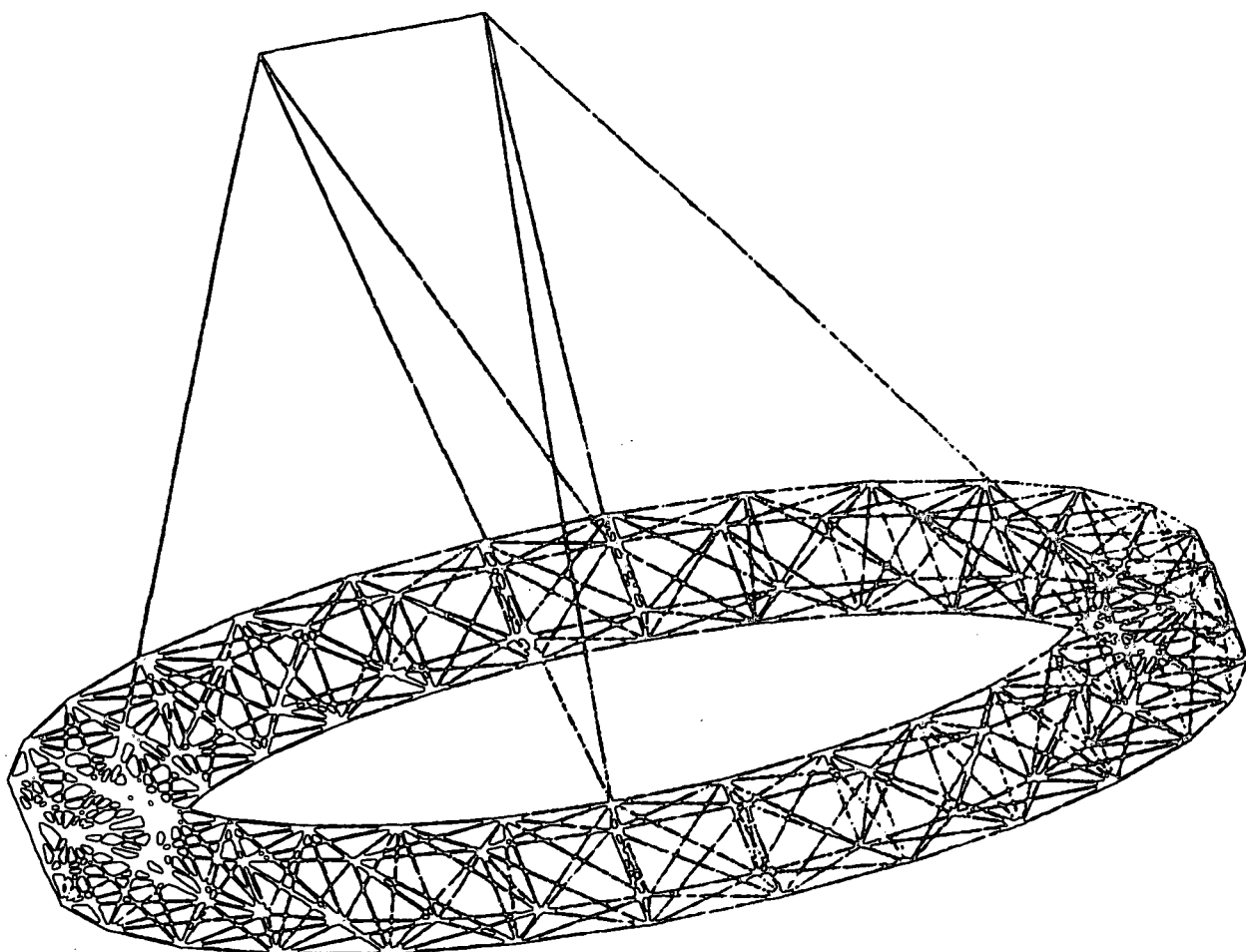
ASSA baseline 2 Two masts Line feed
Modes for ASET = 366 DOF
Undeformed shape
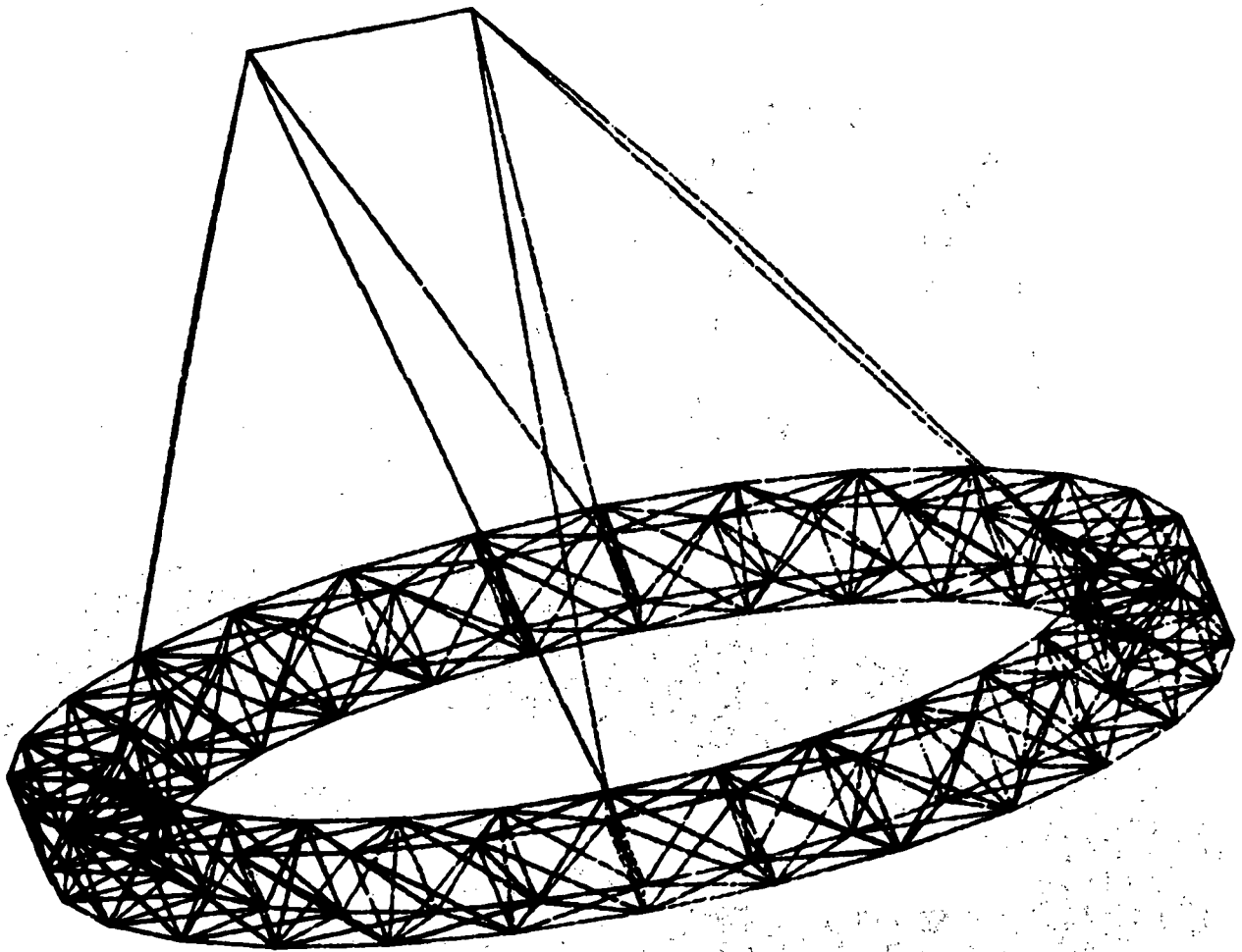
ASSA baseline 2 Two masts Line feed
Modes for ASET = 366 DOF
Modal deform, Subcase 7 Mode 7 Freq 0.198601
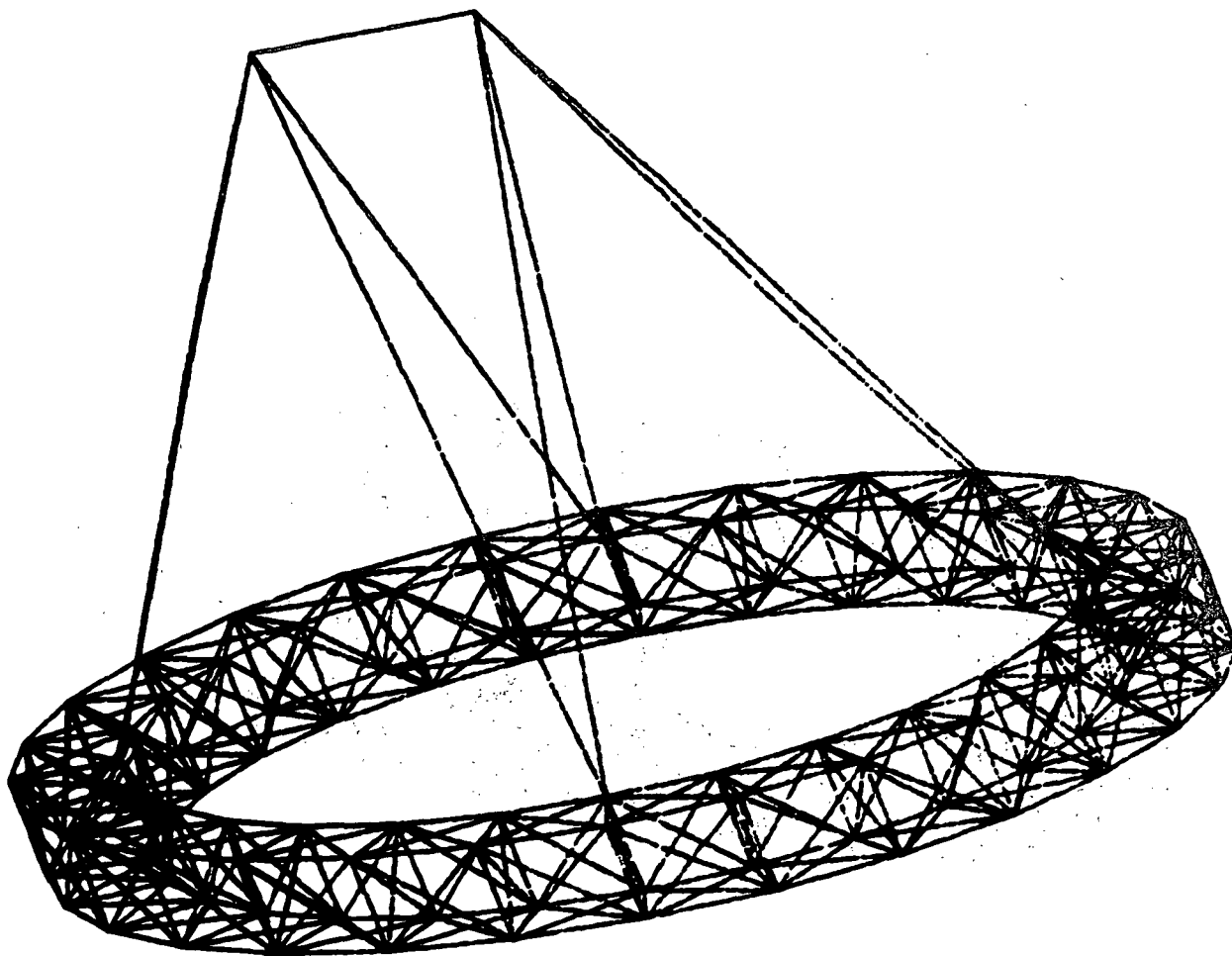
ASSA baseline 2   Two masts   Line feed
Modes for ASET = 366 DOF
Modal deform. Subcase 8   Mode 8   Freq 0.204635
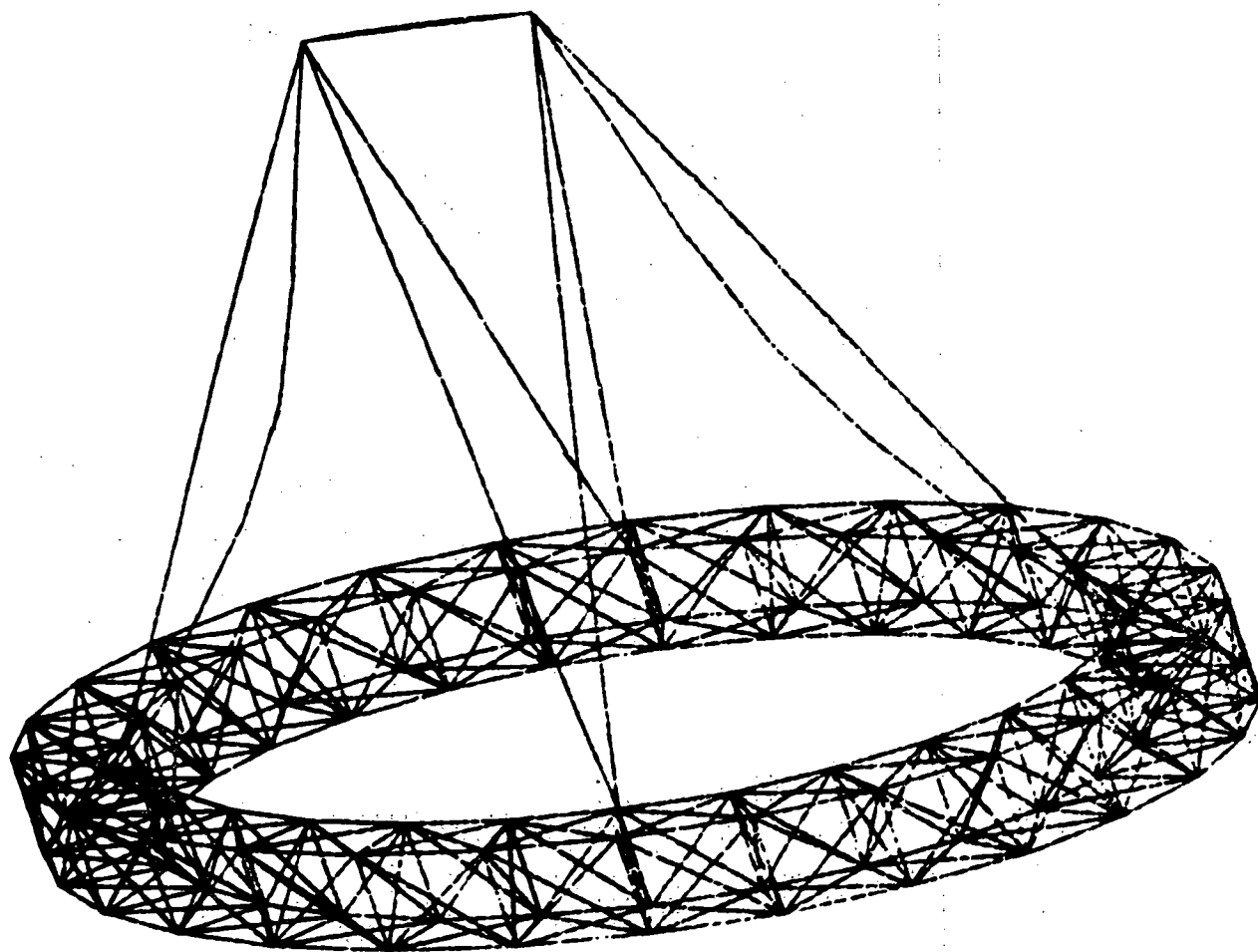
ASSA baseline 2   Two masts   Line feed
Modes for ASET = 366 DOF
Modal deform. Subcase 9   Mode 9   Freq 0.266796

212
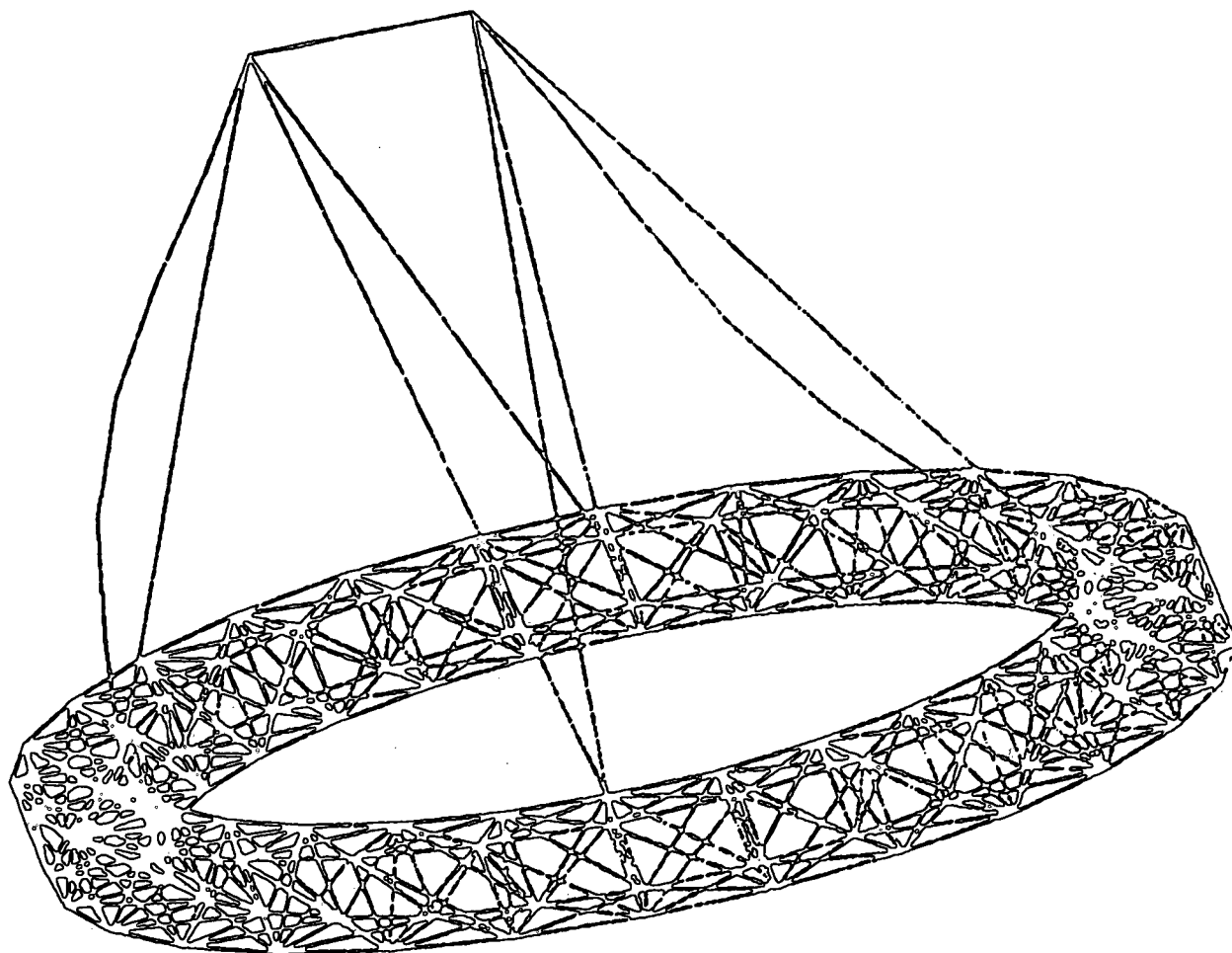
ASSA baseline 2   Two masts   Line Feed
Modes for ASET = 366 DOF
Modal deform. Subcase 10   Mode 10   Freq 0.291533
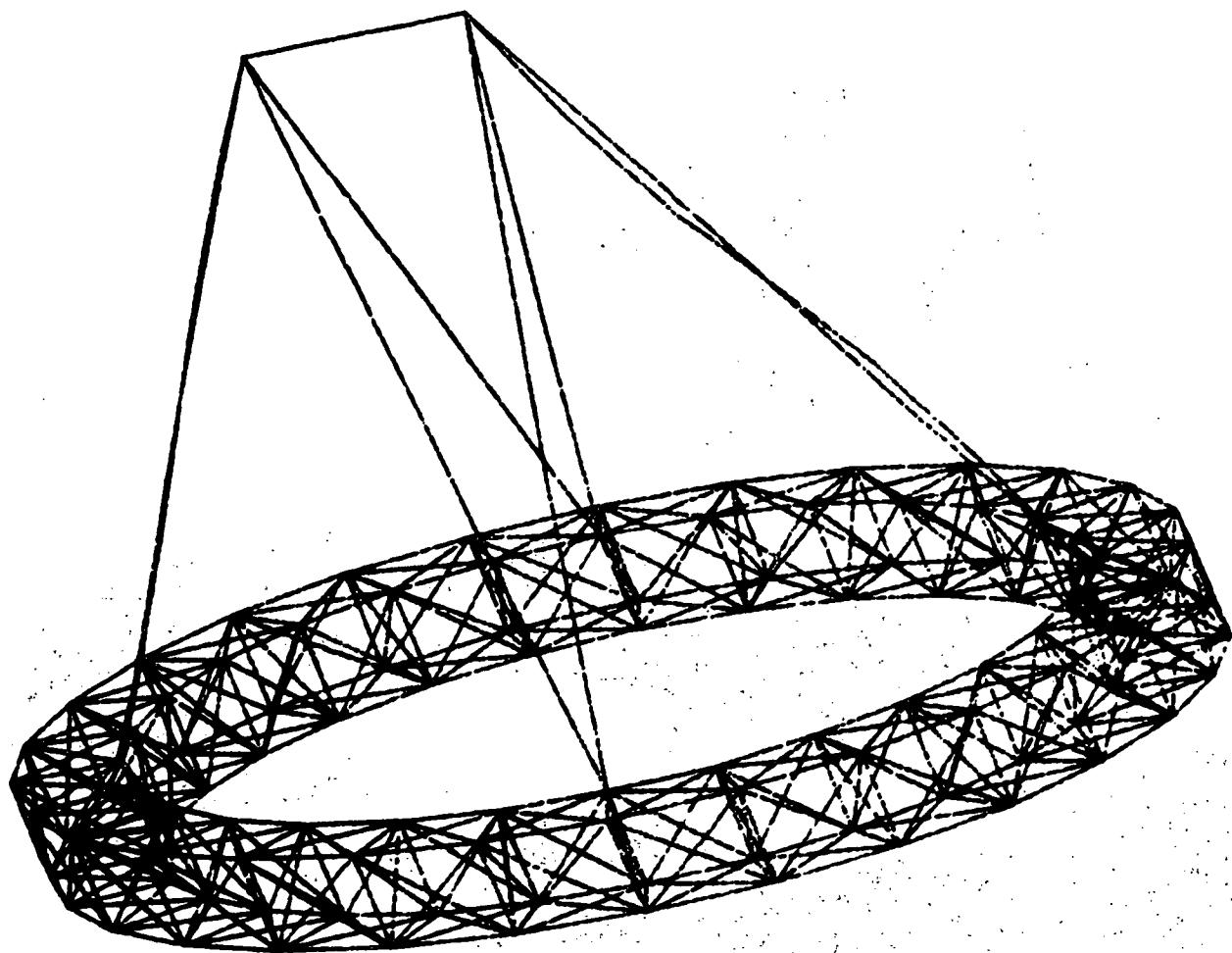
ASSA baseline 2   Two masts   Line feed
Modes for ASET = 366 DOF
Modal Deform. Subcase 13   Mode 13   Freq 0.341744
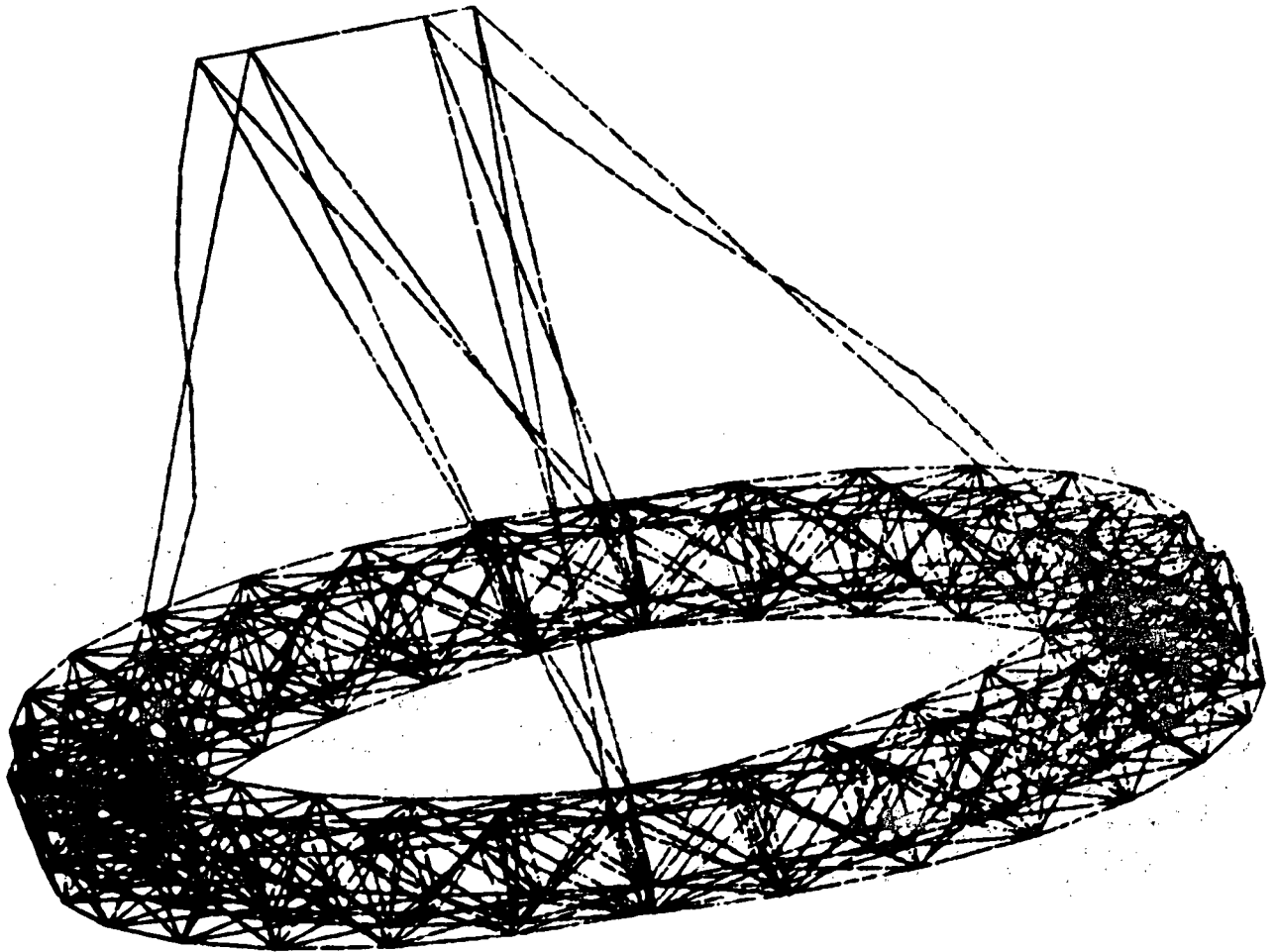
ASSA baseline 2 Two masts Line feed
Modes for ASET = 366 DOF
Modal deform. Subcase 11 Mode 11 Freq 0.864776

Page intentionally left blank

APPENDIX B

WRAPPED RADIAL RING MODE SHAPES

Page intentionally left blank
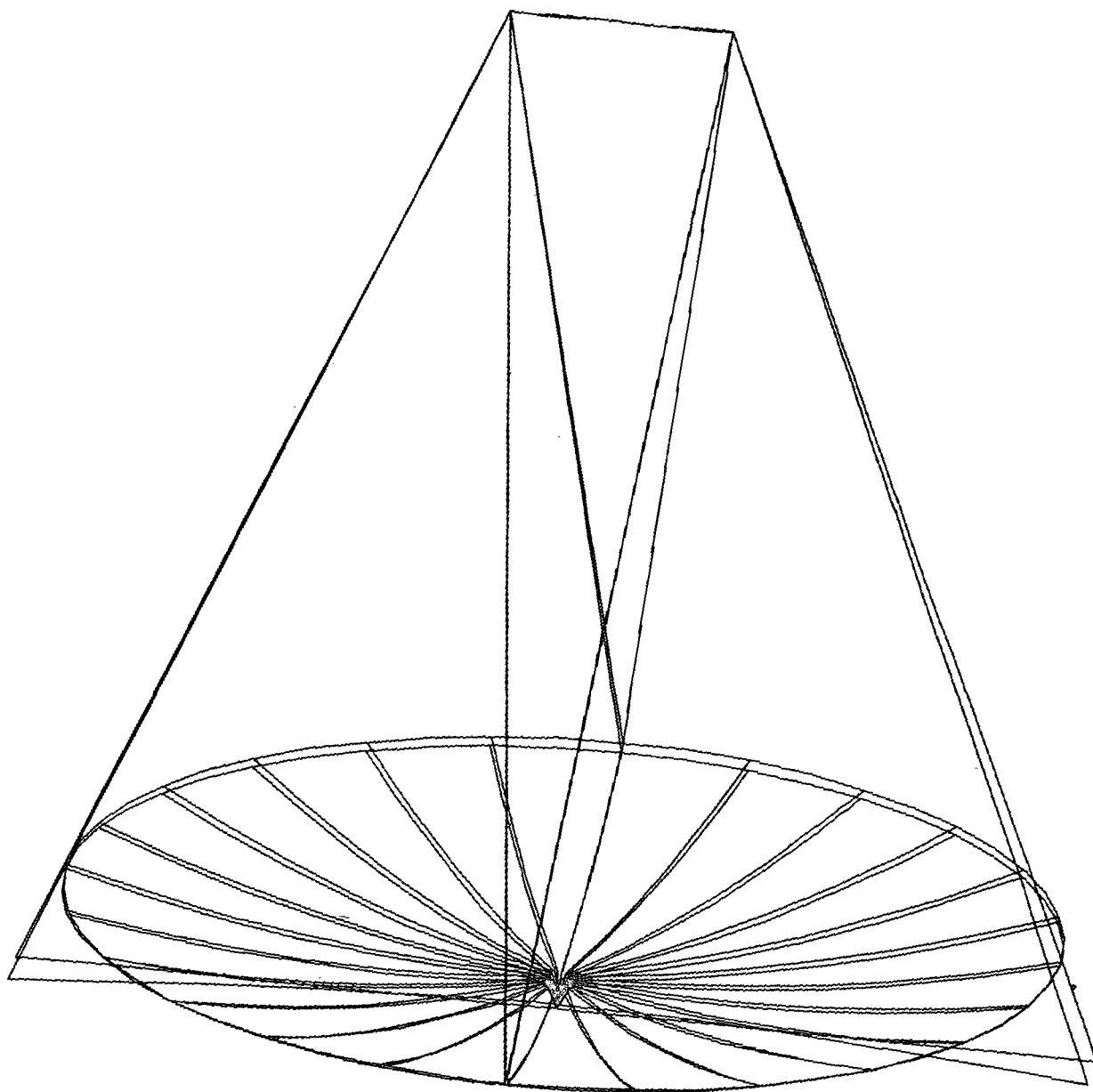
ASSA radial rib config 1 100 meters with line feed
Modal analysis ASET = 198 DOF
Modal deform, Subcase 1 Mode 8 Freq 0.042066
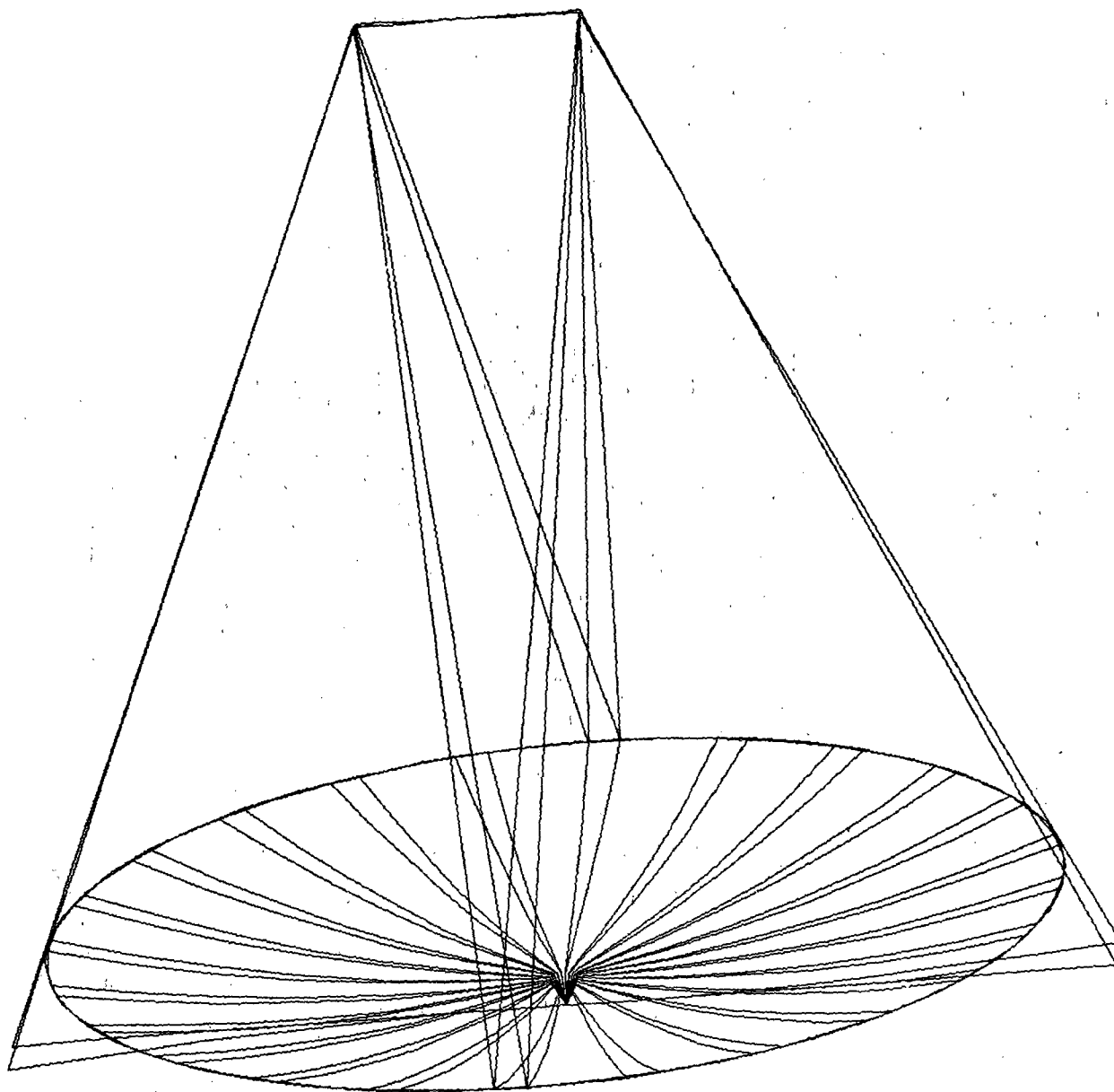
ASSA radial rib config 1 100 meters with line feed
Modal analysis ASET = 198 DOF

Modal deform, Subcase 1 Mode 4 Freq 0.046621
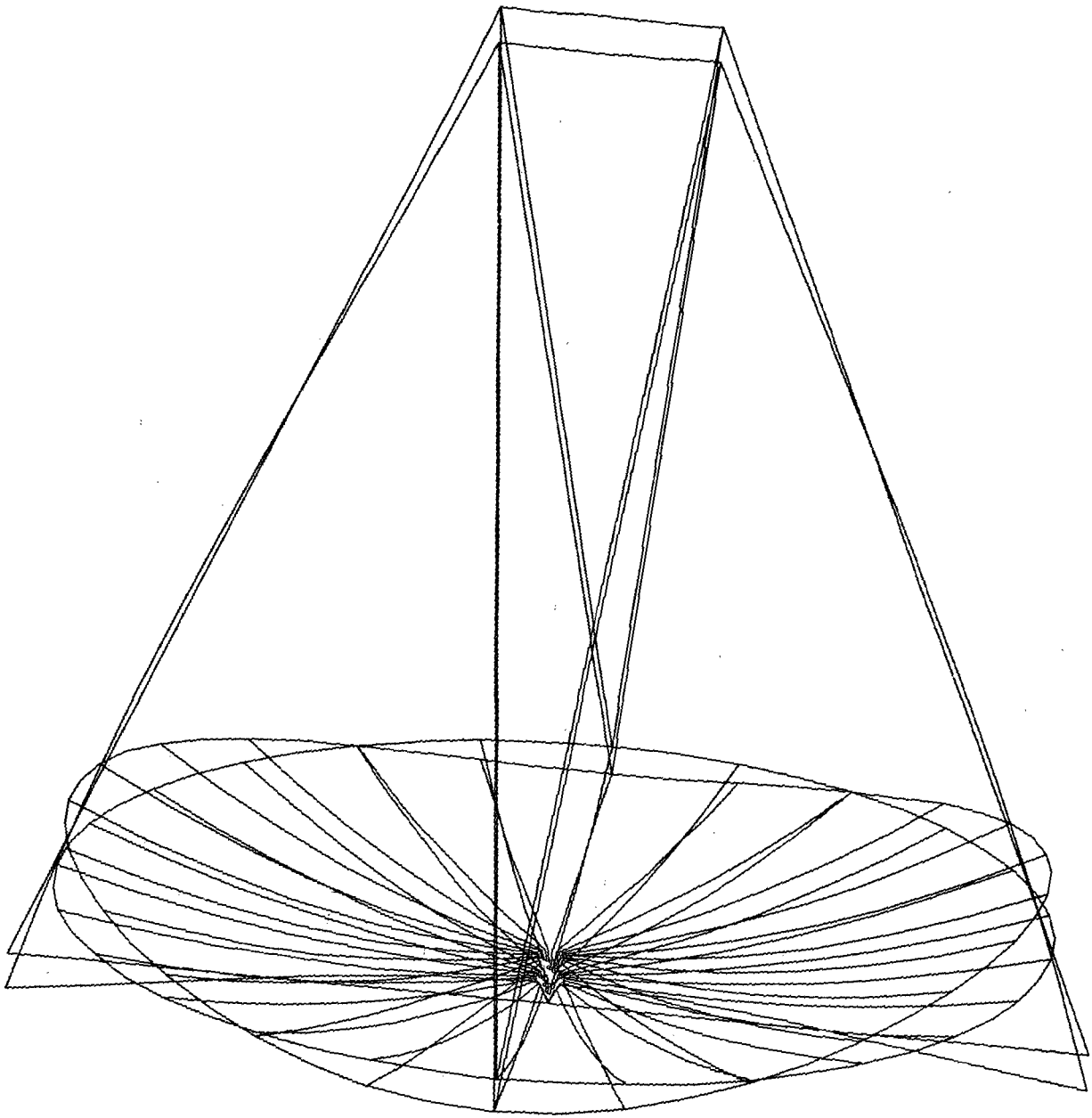
220

ASSA radial rib config 1 100 meters with line feed
Modal analysis ASET = 198 DOF
Modal deform. Subcase 1 Mode 10 Freq 0.070896
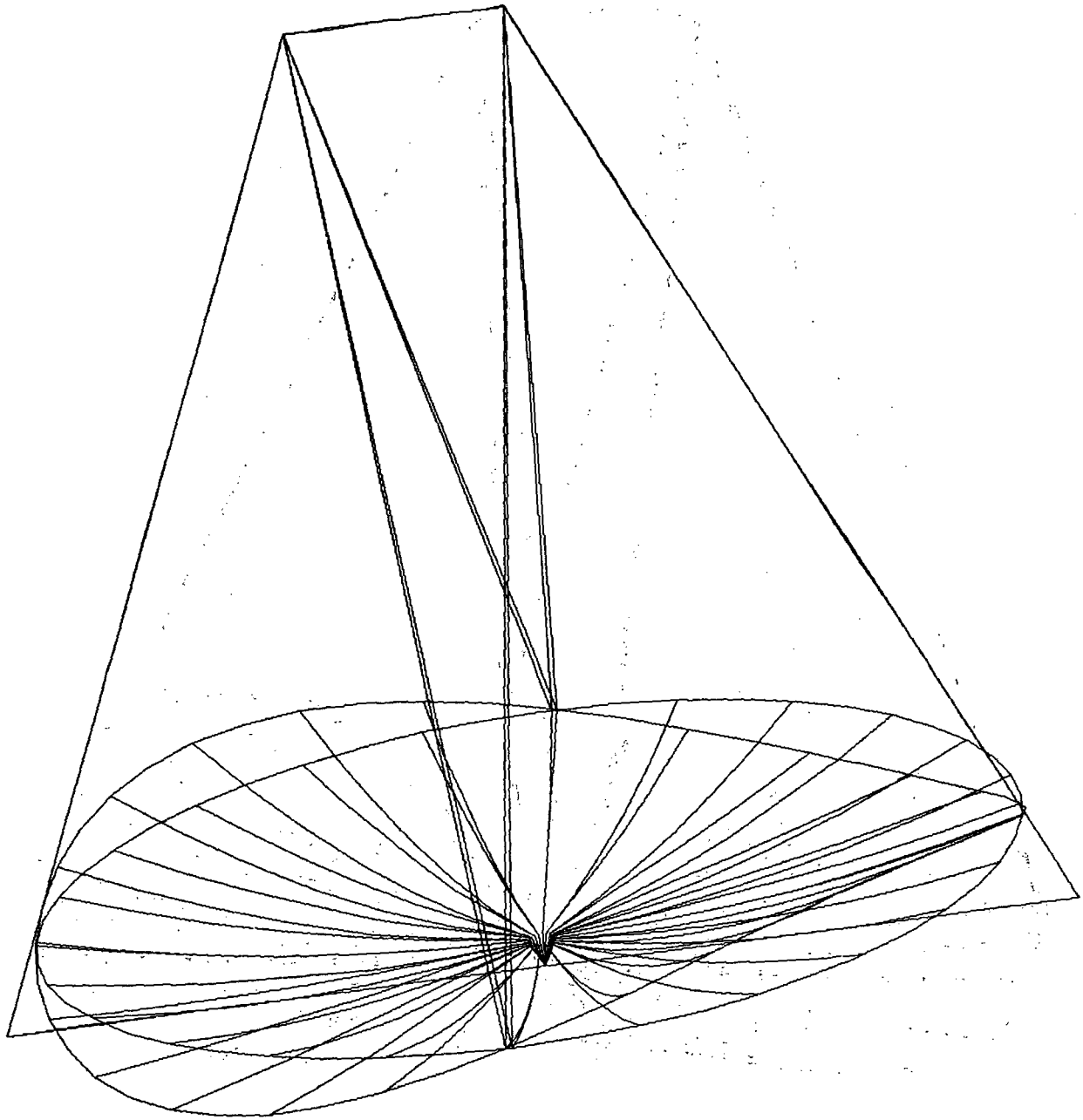
ASSA radial rib config 1   100 meters with line feed
Modal analysis ASET = 198 DOF

Modal deform. Subcase 1   Mode 11   Freq 0.126846
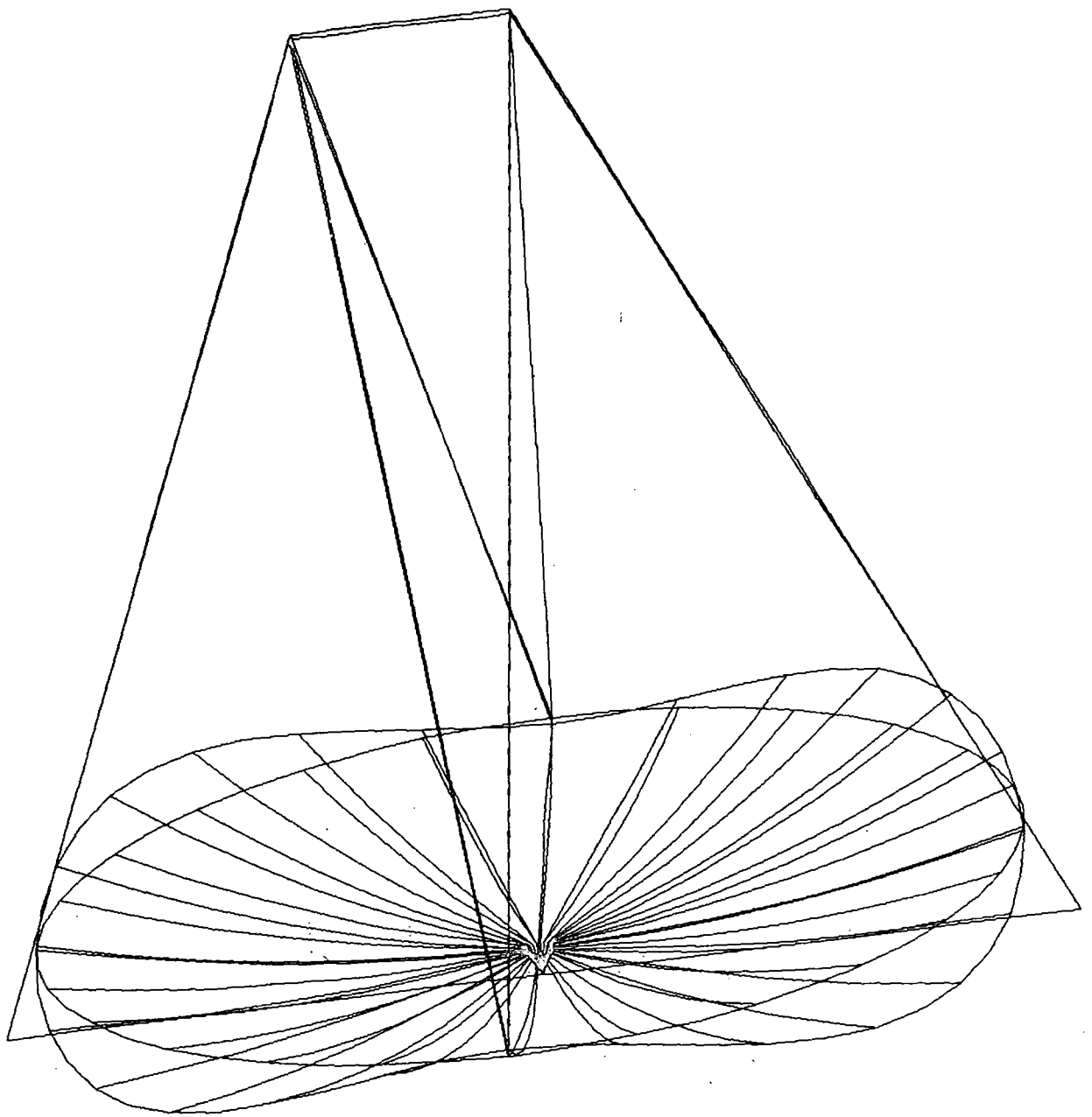
ASSA radial rib config 1 100 meters with line feed
Modal analysis ASET = 198 DOF

Modal deform. Subcase 1 Mode 12 Freq 0.166188
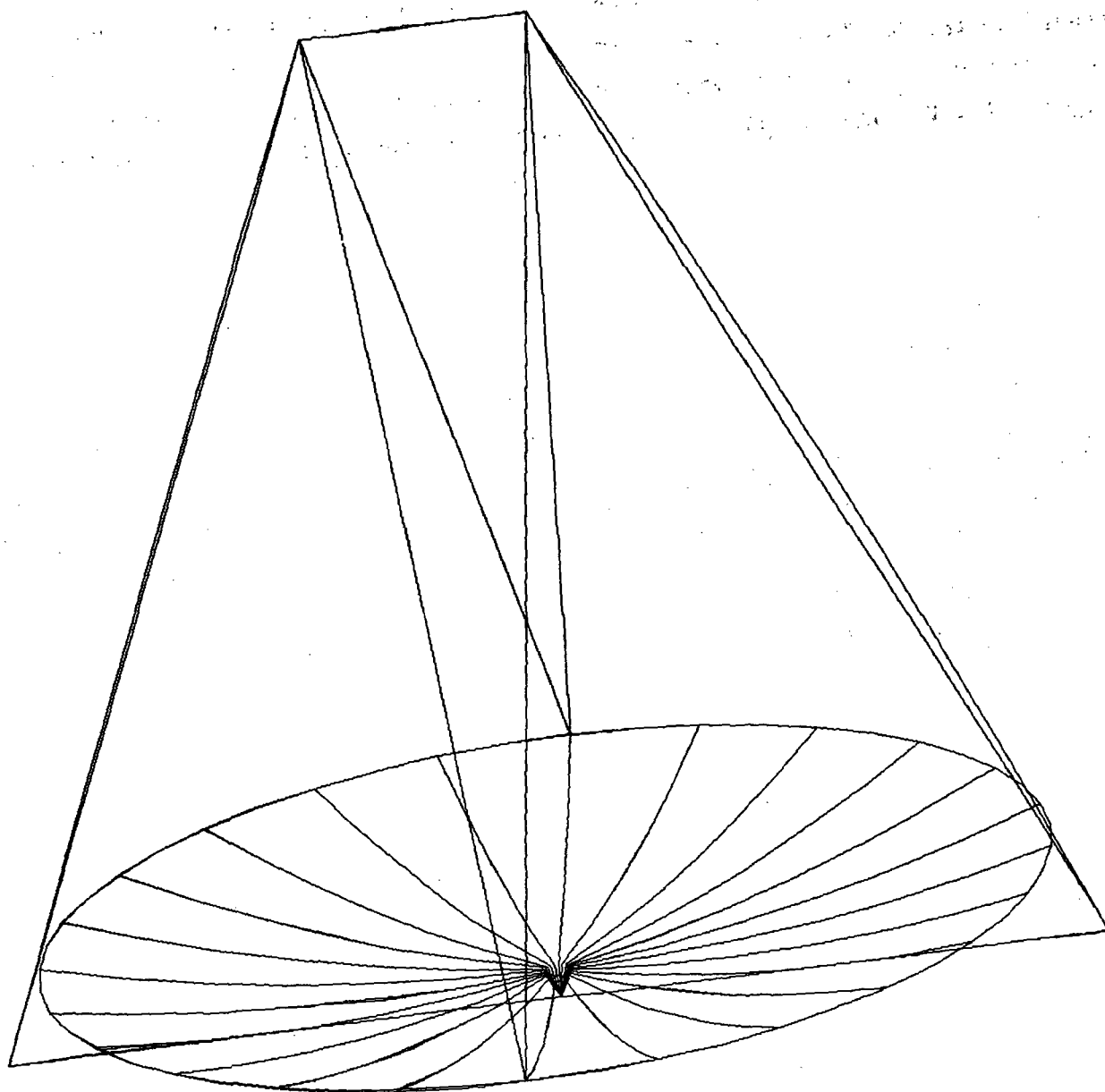
ASSA radial rib config 1 100 meters with line feed
Modal analysis ASET = 198 DOF

Modal deform. Subcase 1 Mode 18 Freq 0.216146

224

APPENDIX C

ORBITAL TEMPERATURES

The data contained in this appendix supports the thermal analysis discussed in Section 4.3. A 670-km circular orbit in the solar ecliptic plane ($\beta = 0$) was assumed. All temperatures are expressed in degrees Celsius. Figures 1.1 through 1.7 give the node-numbering scheme used in the analysis.

Page intentionally left blank
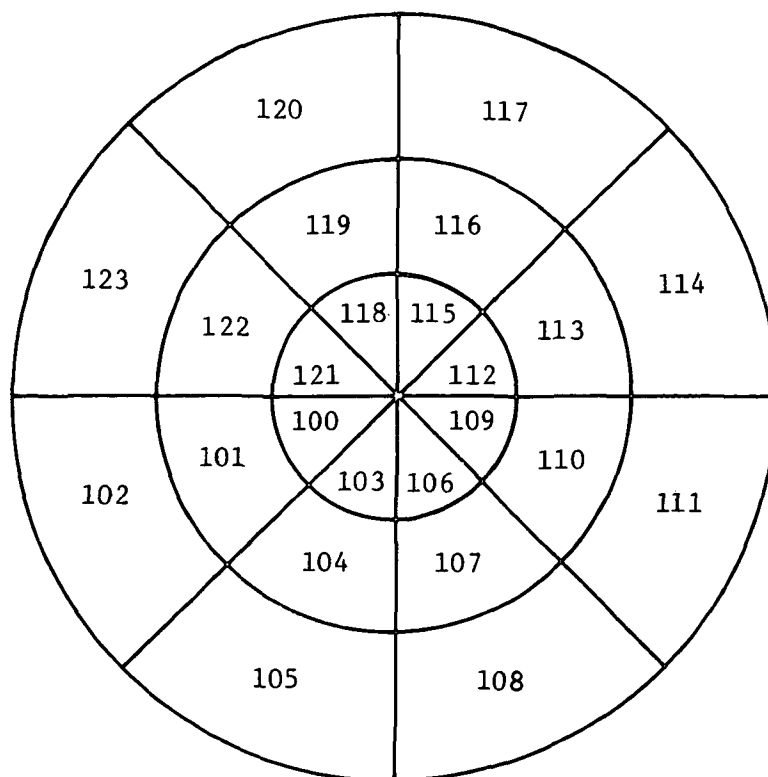
Figure 1.1. - Reflective membrane.
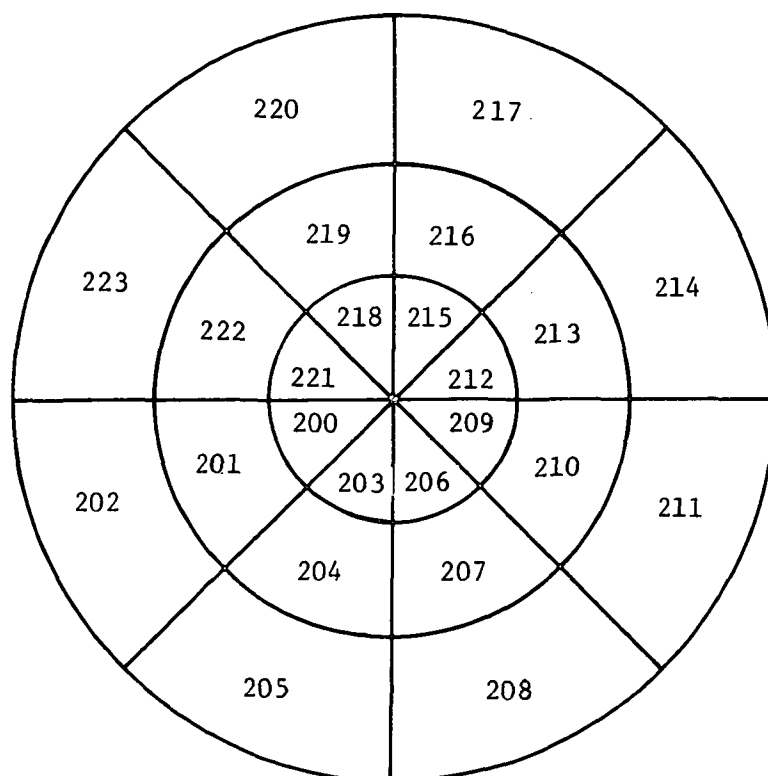
Figure 1.2. - Electrode membrane.

227
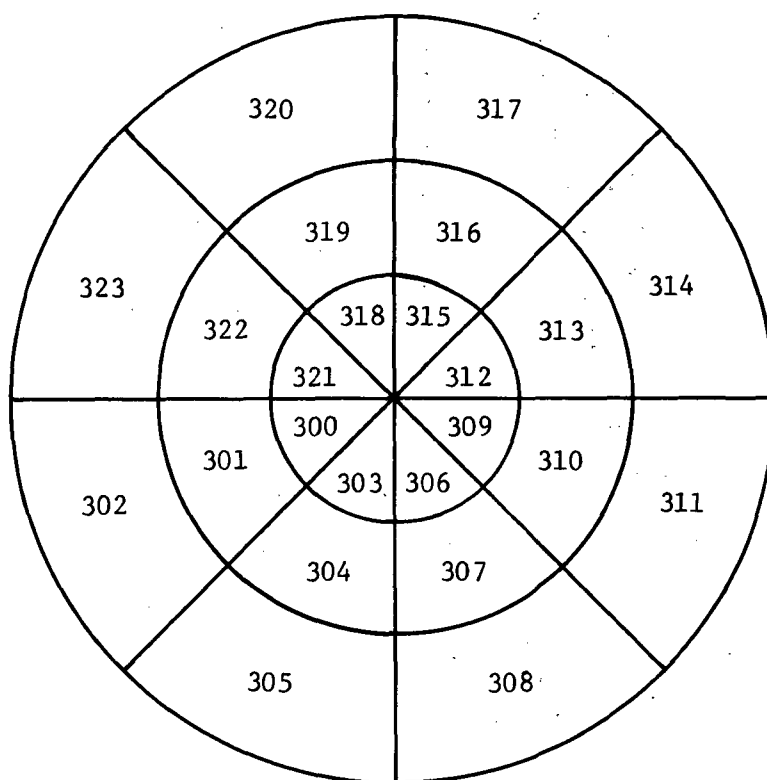
Figure 1.3. - Draw membrane.
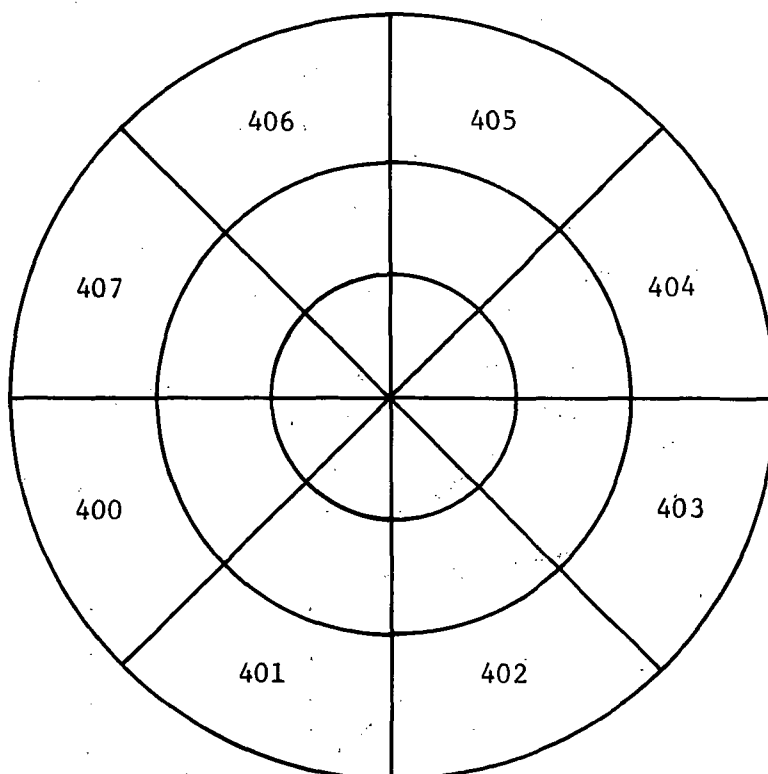
Figure 1.4. - Outer shroud.
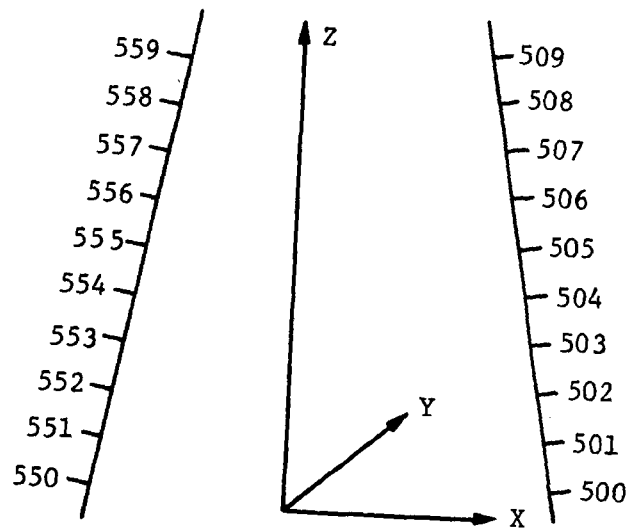
Figure 1.5. — Astromast longeron temperatures.
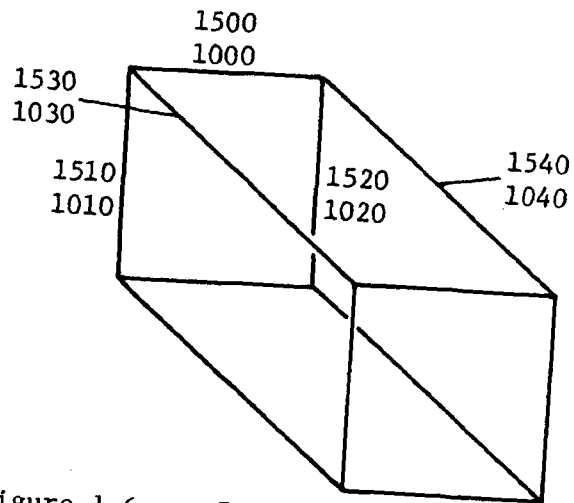
Figure 1.6. — Box truss tube members.
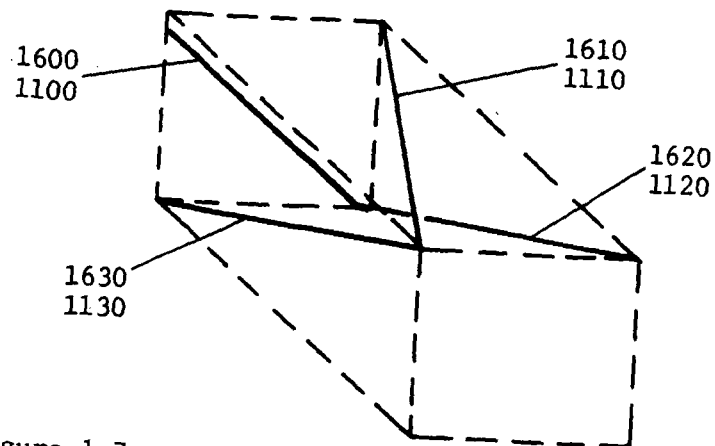
Figure 1.7. — Box truss diagonal tape members.

229

Page intentionally left blank

Page intentionally left blank

CASE 1 RESULTS

Page intentionally left blank

REFLECTOR MEMBRANE
NODES AND TEMP
(SEE FIGURE 1.1)

```
***************************
*TIME IN ORBIT =3.6764HRS.*
***************************
```

NODE	TEMPERATURE		NODE	TEMPERATURE
100	80.2		101	78.3
102	76.7		103	80.5
104	78.9		105	77.5
106	81.0		107	80.0
108	78.9		109	81.6
110	80.9		111	80.1
112	81.6		113	80.9
114	80.1		115	81.0
116	80.0		117	78.9
118	80.5		119	78.9
120	77.5		121	80.2
122	78.3		123	76.7

ELECTRODE MEMBRANE
NODES AND TEMP
(SEE FIGURE 1.2)

```
***************************
*TIME IN ORBIT =3.6764HRS.*
***************************
```

NODE	TEMPERATURE		NODE	TEMPERATURE
200	47.1		201	46.0
202	45.2		203	45.8
204	44.2		205	42.6
206	45.8		207	44.1
208	42.5		209	47.0
210	46.1		211	45.1
212	47.0		213	46.1
214	45.1		215	45.8
216	44.1		217	42.5
218	45.8		219	44.2
220	42.6		221	47.1
222	46.0		223	45.2

DRAWING MEMBRANE
NODES AND TEMP
(SEE FIGURE 1.3)

```
*************************
*TIME IN ORBIT =3.6764HRS.*
*************************
```

NODE	TEMPERATURE		NODE	TEMPERATURE
300	219.1		301	214.7
302	211.0		303	220.9
304	218.3		305	216.0
306	223.4		307	222.8
308	221.9		309	225.1
310	225.7		311	225.5
312	225.1		313	225.7
314	225.5		315	223.4
316	222.8		317	221.9
318	220.9		319	218.3
320	216.0		321	219.1
322	214.7		323	211.0

OUTER SHROUD
NODES AND TEMP
(SEE FIGURE 1.4)

```
*************************
*TIME IN ORBIT =3.6764HRS.*
*************************
```

NODE	TEMPERATURE		NODE	TEMPERATURE
400	109.8		401	70.3
402	-25.7		403	-25.2
404	-25.1		405	-25.6
406	70.1		407	110.3

234

ASTROMAST LONGERONS
NODES AND TEMP
(SEE FIGURE 1.5)

```
***************************
*TIME IN ORBIT =3.6764HRS.*
***************************
```

NODE	TEMPERATURE	NODE	TEMPERATURE
500	-24.1	501	-23.2
502	-29.2	503	-34.5
504	-34.5	505	-34.5
506	-34.5	507	-34.5
508	-34.5	509	-34.5
550	-33.8	551	-33.0
552	-38.8	553	-44.0
554	-44.0	555	-44.0
556	-40.7	557	-26.5
558	-26.5	559	-26.5

GR/EP BOX TRUSS TUBE MEMBERS
NODES AND TEMP
(SEE FIGURE 1.6)

```
***************************
*TIME IN ORBIT =3.6765HRS.*
***************************
```

BOX 1

NODE	TEMPERATURE	NODE	TEMPERATURE
1000	65.6	1010	-43.1
1020	-48.0	1030	65.6
1040	74.3		

BOX 2

NODE	TEMPERATURE	NODE	TEMPERATURE
1500	64.9	1510	-45.1
1520	-45.5	1530	65.7
1540	74.3		

GR/EP BOX TRUSS DIAGONAL MEMBERS
NODES AND TEMP
(SEE FIGURE 1.7)

```
***************************
*TIME IN ORBIT =3.6765HRS.*
***************************
```

BOX 1

NODE	TEMPERATURE		NODE	TEMPERATURE
1100	54.7		1110	-39.5
1120	70.7		1130	63.6

BOX 2

NODE	TEMPERATURE		NODE	TEMPERATURE
1600	56.7		1610	-36.7
1620	70.6		1630	63.4

REFLECTOR MEMBRANE
NODES AND TEMP
(SEE FIGURE 1.1)

```
*****************************
*TIME IN ORBIT =4.1984HRS.*
*****************************
```

NODE	TEMPERATURE	NODE	TEMPERATURE
100	89.1	101	95.9
102	99.7	103	83.0
104	85.1	105	85.9
106	74.6	107	69.8
108	66.4	109	68.7
110	59.1	111	52.6
112	68.7	113	59.1
114	52.6	115	74.6
116	69.8	117	66.3
118	83.0	119	85.1
120	85.9	121	89.1
122	95.9	123	99.7

ELECTRODE MEMBRANE
NODES AND TEMP
(SEE FIGURE 1.2)

```
*****************************
*TIME IN ORBIT =4.1984HRS.*
*****************************
```

NODE	TEMPERATURE	NODE	TEMPERATURE
200	64.2	201	62.6
202	61.1	203	62.9
204	60.7	205	58.5
206	62.7	207	60.3
208	58.2	209	63.8
210	62.4	211	61.1
212	63.8	213	62.4
214	61.1	215	62.7
216	60.3	217	58.2
218	62.9	219	60.7
220	58.5	221	64.2
222	62.6	223	61.1

DRAWING MEMBRANE
NODES AND TEMP
(SEE FIGURE 1.3)

****
TIME IN ORBIT =4.1984HRS.
****

NODE	TEMPERATURE		NODE	TEMPERATURE
300	37.7		301	38.9
302	39.6		303	36.5
304	36.8		305	36.9
306	34.9		307	33.9
308	33.1		309	33.9
310	32.0		311	30.6
312	33.9		313	32.0
314	30.6		315	34.9
316	33.9		317	33.1
318	36.5		319	36.8
320	36.9		321	37.7
322	38.9		323	39.6

OUTER SHROUD
NODES AND TEMP
(SEE FIGURE 1.4)

****
TIME IN ORBIT =4.1984HRS.
****

NODE	TEMPERATURE		NODE	TEMPERATURE
400	-17.5		401	-19.9
402	120.2		403	216.3
404	216.3		405	120.3
406	-19.7		407	-17.3

ASTROMAST LONGERONS
NODES AND TEMP
(SEE FIGURE 1.5)

```
***************************
*TIME IN ORBIT =4.1984HRS.*
***************************
```

NODE	TEMPERATURE		NODE	TEMPERATURE
500	25.0		501	25.9
502	19.2		503	13.3
504	13.3		505	13.3
506	13.3		507	13.3
508	13.3		509	13.3
550	45.2		551	46.1
552	39.4		553	33.3
554	33.3		555	33.3
556	33.3		557	33.3
558	33.3		559	33.3

GR/EP BOX TRUSS TUBE MEMBERS
NODES AND TEMP
(SEE FIGURE 1.6)

```
***************************
*TIME IN ORBIT =4.1984HRS.*
***************************
```

BOX 1

NODE	TEMPERATURE		NODE	TEMPERATURE
1000	-3.8		1010	-26.3
1020	-87.1		1030	45.9
1040	53.7			

BOX 2

NODE	TEMPERATURE		NODE	TEMPERATURE
1500	45.8		1510	38.1
1520	57.7		1530	-2.4
1540	4.5			

239

REFLECTOR MEMBRANE
NODES AND TEMP
(SEE FIGURE 1.1)

```
***************************
*TIME IN ORBIT =4.2029HRS.*
***************************
```

NODE	TEMPERATURE		NODE	TEMPERATURE
100	88.7		101	95.5
102	99.3		103	82.7
104	84.7		105	85.6
106	74.2		107	69.5
108	66.0		109	68.3
110	58.7		111	52.2
112	68.3		113	58.7
114	52.2		115	74.2
116	69.5		117	66.0
118	82.7		119	84.7
120	85.6		121	88.7
122	95.5		123	99.3

ELECTRODE MEMBRANE
NODES AND TEMP
(SEE FIGURE 1.2)

```
***************************
*TIME IN ORBIT =4.2029HRS.*
***************************
```

NODE	TEMPERATURE		NODE	TEMPERATURE
200	64.3		201	62.7
202	61.3		203	63.0
204	60.8		205	58.7
206	62.7		207	60.4
208	58.2		209	63.9
210	62.4		211	61.2
212	63.9		213	62.4
214	61.2		215	62.7
216	60.4		217	58.2
218	63.0		219	60.8
220	58.7		221	64.3
222	62.7		223	61.3

DRAWING MEMBRANE
NODES AND TEMP
(SEE FIGURE 1.3)

```
***************************
*TIME IN ORBIT =4.2029HRS.*
***************************
```

NODE	TEMPERATURE		NODE	TEMPERATURE
300	36.0		301	37.2
302	37.9		303	34.8
304	35.1		305	35.2
306	33.2		307	32.2
308	31.5		309	32.3
310	30.4		311	29.1
312	32.3		313	30.4
314	29.1		315	33.2
316	32.2		317	31.5
318	34.8		319	35.1
320	35.2		321	36.0
322	37.2		323	37.9

OUTER SHROUD
NODES AND TEMP
(SEE FIGURE 1.4)

```
***************************
*TIME IN ORBIT =4.2029HRS.*
***************************
```

NODE	TEMPERATURE		NODE	TEMPERATURE
400	-18.1		401	-20.5
402	117.5		403	209.7
404	209.7		405	117.6
406	-20.2		407	-17.9

ASTROMAST LONGERONS
NODES AND TEMP
(SEE FIGURE 1.5)

```
***************************
*TIME IN ORBIT =4.2029HRS.*
***************************
```

NODE	TEMPERATURE		NODE	TEMPERATURE
500	16.7		501	17.6
502	10.9		503	5.0
504	5.0		505	5.0
506	5.0		507	5.0
508	5.0		509	5.0
550	34.4		551	35.4
552	28.6		553	22.6
554	22.6		555	22.6
556	22.6		557	22.6
558	22.6		559	22.6

REFLECTOR MEMBRANE
NODES AND TEMP
(SEE FIGURE 1.1)

```
*****************************
*TIME IN ORBIT =4.7840HRS.*
*****************************
```

NODE	TEMPERATURE	NODE	TEMPERATURE
100	-4.1	101	-4.1
102	-4.2	103	-4.7
104	-5.1	105	-5.5
106	-5.3	107	-6.2
108	-6.9	109	-5.6
110	-6.7	111	-7.6
112	-5.6	113	-6.7
114	-7.6	115	-5.3
116	-6.2	117	-6.9
118	-4.7	119	-5.1
120	-5.5	121	-4.1
122	-4.0	123	-4.2

ELECTRODE MEMBRANE
NODES AND TEMP
(SEE FIGURE 1.2)

```
*****************************
*TIME IN ORBIT =4.7840HRS.*
*****************************
```

NODE	TEMPERATURE	NODE	TEMPERATURE
200	44.8	201	44.1
202	43.5	203	43.6
204	42.1	205	40.8
206	42.8	207	40.9
208	39.2	209	43.1
210	41.3	211	39.9
212	43.1	213	41.3
214	39.9	215	42.8
216	40.9	217	39.2
218	43.6	219	42.1
220	40.8	221	44.8
222	44.2	223	43.5

DRAWING MEMBRANE
NODES AND TEMP
(SEE FIGURE 1.3)

```
**************************
*TIME IN ORBIT =4.7840HRS.*
**************************
```

NODE	TEMPERATURE		NODE	TEMPERATURE
300	-60.4		301	-60.5
302	-60.6		303	-60.6
304	-60.9		305	-61.1
306	-60.9		307	-61.3
308	-61.6		309	-60.9
310	-61.6		311	-62.0
312	-60.9		313	-61.6
314	-62.0		315	-60.9
316	-61.3		317	-61.6
318	-60.6		319	-60.9
320	-61.1		321	-60.4
322	-60.5		323	-60.6

OUTER SHROUD
NODES AND TEMP
(SEE FIGURE 1.4)

```
**************************
*TIME IN ORBIT =4.7840HRS.*
**************************
```

NODE	TEMPERATURE		NODE	TEMPERATURE
400	-60.4		401	-61.0
402	-37.1		403	-31.5
404	-31.5		405	-37.1
406	-61.1		407	-60.2

ASTROMAST LONGERONS
NODES AND TEMP
(SEE FIGURE 1.5)

```
**************************
*TIME IN ORBIT =4.7840HRS.*
**************************
```

NODE	TEMPERATURE		NODE	TEMPERATURE
500	-85.4		501	-84.8
502	-89.3		503	-93.4
504	-93.4		505	-93.4
506	-93.4		507	-93.4
508	-93.4		509	-93.4
550	-85.5		551	-84.9
552	-89.4		553	-93.5
554	-93.5		555	-93.5
556	-93.5		557	-93.5
558	-93.5		559	-93.5

GR/EP BOX TRUSS TUBE MEMBERS
NODES AND TEMP
(SEE FIGURE 1.6)

```
**************************
*TIME IN ORBIT =4.7840HRS.*
**************************
```

BOX 1

NODE	TEMPERATURE		NODE	TEMPERATURE
1000	-71.0		1010	-90.7
1020	-94.2		1030	-64.9
1040	-59.9			

BOX 2

NODE	TEMPERATURE		NODE	TEMPERATURE
1500	-65.2		1510	-90.0
1520	-89.9		1530	-70.7
1540	-65.7			

GR/EP BOX TRUSS DIAGONAL MEMBERS
NODES AND TEMP
(SEE FIGURE 1.7)


```
**************************
*TIME IN ORBIT =4.7840HRS.*
**************************
```

BOX 1

NODE	TEMPERATURE		NODE	TEMPERATURE
1100	-87.8		1110	-83.5
1120	-86.7		1130	-81.3

BOX 2

NODE	TEMPERATURE		NODE	TEMPERATURE
1600	-87.9		1610	-83.8
1620	-84.3		1630	-80.0

CASE 2 RESULTS

Page intentionally left blank

REFLECTOR MEMBRANE
NODES AND TEMP
(SEE FIGURE 1.1)

```
*****************************
*TIME IN ORBIT =3.6764HRS.*
*****************************
```

NODE	TEMPERATURE		NODE	TEMPERATURE
100	79.8		101	78.6
102	77.8		103	78.0
104	75.5		105	73.3
106	78.2		107	75.3
108	72.5		109	80.0
110	77.6		111	75.4
112	80.0		113	77.6
114	75.4		115	78.2
116	75.3		117	72.5
118	78.0		119	75.5
120	73.3		121	79.8
122	78.6		123	77.9

ELECTRODE MEMBRANE
NODES AND TEMP
(SEE FIGURE 1.2)

```
*****************************
*TIME IN ORBIT =3.6764HRS.*
*****************************
```

NODE	TEMPERATURE		NODE	TEMPERATURE
200	82.0		201	79.7
202	78.3		203	79.6
204	75.5		205	72.1
206	79.5		207	74.8
208	70.4		209	81.8
210	77.7		211	74.0
212	81.8		213	77.7
214	74.0		215	79.5
216	74.8		217	70.4
218	79.6		219	75.5
220	72.1		221	82.0
222	79.7		223	78.3

249

DRAWING MEMBRANE
NODES AND TEMP
(SEE FIGURE 1.3)

```
**************************
*TIME IN ORBIT =3.6764HRS.*
**************************
```

NODE	TEMPERATURE		NODE	TEMPERATURE
300	205.4		301	203.2
302	201.6		303	205.8
304	204.1		305	202.8
306	207.0		307	206.1
308	205.3		309	208.3
310	208.3		311	208.1
312	208.3		313	208.3
314	208.1		315	207.0
316	206.1		317	205.3
318	205.8		319	204.1
320	202.8		321	205.4
322	203.2		323	201.6

OUTER SHROUD
NODES AND TEMP
(SEE FIGURE 1.4)

```
**************************
*TIME IN ORBIT =3.6764HRS.*
**************************
```

NODE	TEMPERATURE		NODE	TEMPERATURE
400	107.9		401	78.3
402	13.6		403	14.9
404	15.0		405	13.7
406	78.1		407	108.2

ASTROMAST LONGERONS
NODES AND TEMP
(SEE FIGURE 1.5)

```
***************************
*TIME IN ORBIT =3.6764HRS.*
***************************
```

NODE	TEMPERATURE	NODE	TEMPERATURE
500	-24.1	501	-23.2
502	-29.2	503	-34.5
504	-34.5	505	-34.5
506	-34.5	507	-34.5
508	-34.5	509	-34.5
550	-33.9	551	-33.1
552	-38.8	553	-44.0
554	-44.0	555	-44.0
556	-40.7	557	-26.5
558	-26.5	559	-26.5

REFLECTOR MEMBRANE
NODES AND TEMP
(SEE FIGURE 1.1)

```
***************************
*TIME IN ORBIT =4.1984HRS.*
***************************
```

NODE	TEMPERATURE	NODE	TEMPERATURE
100	99.0	101	102.2
102	103.6	103	94.2
104	93.9	105	92.9
106	89.1	107	84.9
108	81.5	109	87.3
110	81.3	111	77.6
112	87.3	113	81.3
114	77.6	115	89.1
116	84.9	117	81.5
118	94.2	119	93.9
120	92.9	121	99.0
122	102.2	123	103.6

ELECTRODE MEMBRANE
NODES AND TEMP
(SEE FIGURE 1.2)

```
***************************
*TIME IN ORBIT =4.1984HRS.*
***************************
```

NODE	TEMPERATURE	NODE	TEMPERATURE
200	82.6	201	82.7
202	82.2	203	80.0
204	78.3	205	76.3
206	79.3	207	77.1
208	75.0	209	81.6
210	80.7	211	80.4
212	81.6	213	80.7
214	80.4	215	79.3
216	77.1	217	75.0
218	80.0	219	78.3
220	76.3	221	82.6
222	82.7	223	82.2

DRAWING MEMBRANE
NODES AND TEMP
(SEE FIGURE 1.3)

****
TIME IN ORBIT =4.1984HRS.
****

NODE	TEMPERATURE		NODE	TEMPERATURE
300	35.3		301	34.9
302	34.7		303	34.5
304	33.7		305	32.9
306	36.2		307	36.3
308	36.3		309	39.8
310	42.0		311	44.1
312	39.8		313	42.0
314	44.1		315	36.2
316	36.3		317	36.2
318	34.5		319	33.7
320	32.9		321	35.3
322	34.9		323	34.7

OUTER SHROUD
NODES AND TEMP
(SEE FIGURE 1.4)

****
TIME IN ORBIT =4.1984HRS.
****

NODE	TEMPERATURE		NODE	TEMPERATURE
400	8.0		401	7.7
402	115.9		403	197.3
404	197.3		405	115.9
406	7.8		407	8.3

ASTROMAST LONGERONS
NODES AND TEMP
(SEE FIGURE 1.5)

```
**************************
*TIME IN ORBIT =4.1984HRS.*
**************************
```

NODE	TEMPERATURE		NODE	TEMPERATURE
500	25.1		501	26.0
502	19.3		503	13.3
504	13.3		505	13.3
506	13.3		507	13.3
508	13.3		509	13.3
550	45.4		551	46.4
552	39.5		553	33.3
554	33.3		555	33.3
556	33.3		557	33.3
558	33.3		559	33.3

REFLECTOR MEMBRANE
NODES AND TEMP
(SEE FIGURE 1.1)

```
****************************
*TIME IN ORBIT =4.7840HRS.*
****************************
```

NODE	TEMPERATURE	NODE	TEMPERATURE
100	3.2	101	3.2
102	3.3	103	2.6
104	2.3	105	2.0
106	2.7	107	2.4
108	2.1	109	3.3
110	3.1	111	3.2
112	3.3	113	3.1
114	3.2	115	2.7
116	2.4	117	2.1
118	2.6	119	2.3
120	2.0	121	3.2
122	3.2	123	3.3

ELECTRODE MEMBRANE
NODES AND TEMP
(SEE FIGURE 1.2)

```
****************************
*TIME IN ORBIT =4.7840HRS.*
****************************
```

NODE	TEMPERATURE	NODE	TEMPERATURE
200	7.8	201	7.8
202	7.9	203	7.1
204	6.8	205	6.5
206	7.3	207	6.9
208	6.7	209	8.0
210	7.9	211	8.0
212	8.0	213	7.9
214	8.0	215	7.3
216	6.9	217	6.7
218	7.1	219	6.8
220	6.5	221	7.8
222	7.8	223	7.9

DRAWING MEMBRANE
NODES AND TEMP
(SEE FIGURE 1.3)

```
**************************
*TIME IN ORBIT =4.7840HRS.*
**************************
```

NODE	TEMPERATURE		NODE	TEMPERATURE
300	-49.7		301	-51.6
302	-53.2		303	-50.0
304	-51.9		305	-53.7
306	-49.0		307	-50.4
308	-51.4		309	-47.8
310	-48.5		311	-49.1
312	-47.8		313	-48.5
314	-49.1		315	-49.0
316	-50.4		317	-51.4
318	-50.0		319	-51.9
320	-53.6		321	-49.7
322	-51.6		323	-53.2

OUTER SHROUD
NODES AND TEMP
(SEE FIGURE 1.4)

```
**************************
*TIME IN ORBIT =4.7840HRS.*
**************************
```

NODE	TEMPERATURE		NODE	TEMPERATURE
400	-45.2		401	-45.2
402	-35.7		403	-32.4
404	-32.4		405	-35.7
406	-45.4		407	-45.0

ASTROMAST LONGERONS
NODES AND TEMP
(SEE FIGURE 1.5)

```
*************************
*TIME IN ORBIT =4.7840HRS.*
*************************
```

NODE	TEMPERATURE		NODE	TEMPERATURE
500	-85.2		501	-84.5
502	-89.2		503	-93.4
504	-93.4		505	-93.4
506	-93.4		507	-93.4
508	-93.4		509	-93.4
550	-85.2		551	-84.6
552	-89.3		553	-93.5
554	-93.5		555	-93.5
556	-93.5		557	-93.5
558	-93.5		559	-93.5

Page intentionally left blank

CASE 4 RESULTS

Page intentionally left blank

REFLECTOR MEMBRANE
NODES AND TEMP
(SEE FIGURE 1.1)

```
****************************
*TIME IN ORBIT =3.6764HRS.*
****************************
```

NODE	TEMPERATURE		NODE	TEMPERATURE
100	38.6		101	37.6
102	36.7		103	38.6
104	37.6		105	36.6
106	38.6		107	37.6
108	36.6		109	38.6
110	37.7		111	36.7
112	38.6		113	37.7
114	36.7		115	38.6
116	37.6		117	36.6
118	38.6		119	37.6
120	36.6		121	38.6
122	37.6		123	36.7

ELECTRODE MEMBRANE
NODES AND TEMP
(SEE FIGURE 1.2)

```
****************************
*TIME IN ORBIT =3.6764HRS.*
****************************
```

NODE	TEMPERATURE		NODE	TEMPERATURE
200	38.0		201	35.7
202	33.9		203	37.8
204	35.2		205	33.0
206	38.0		207	35.2
208	32.8		209	38.4
210	35.7		211	33.4
212	38.4		213	35.7
214	33.4		215	38.0
216	35.2		217	32.8
218	37.8		219	35.2
220	33.0		221	38.0
222	35.7		223	33.9

DRAWING MEMBRANE
NODES AND TEMP
(SEE FIGURE 1.3)

```
***************************
*TIME IN ORBIT =3.6764HRS.*
***************************
```

NODE	TEMPERATURE	NODE	TEMPERATURE
300	121.3	301	120.0
302	118.9	303	121.3
304	120.1	305	119.0
306	121.4	307	120.3
308	119.2	309	121.5
310	120.4	311	119.4
312	121.5	313	120.4
314	119.4	315	121.4
316	120.3	317	119.2
318	121.3	319	120.1
320	119.0	321	121.3
322	120.0	323	118.9

OUTER SHROUD
NODES AND TEMP
(SEE FIGURE 1.4)

```
***************************
*TIME IN ORBIT =3.6764HRS.*
***************************
```

NODE	TEMPERATURE	NODE	TEMPERATURE
400	-23.1	401	-32.6
402	-43.2	403	-43.4
404	-43.4	405	-43.2
406	-32.2	407	-23.3

ASTROMAST LONGERONS
NODES AND TEMP
(SEE FIGURE 1.5)

```
**************************
*TIME IN ORBIT =3.6764HRS.*
**************************
```

NODE	TEMPERATURE		NODE	TEMPERATURE
500	-15.9		501	-14.7
502	-24.2		503	-34.5
504	-34.5		505	-34.5
506	-34.5		507	-34.5
508	-34.5		509	-34.5
550	-22.1		551	-20.7
552	-31.6		553	-44.0
554	-44.0		555	-44.0
556	-40.7		557	-26.5
558	-26.5		559	-26.5

REFLECTOR MEMBRANE
NODES AND TEMP
(SEE FIGURE 1.1)

```
**************************
*TIME IN ORBIT =4.7840HRS.*
**************************
```

NODE	TEMPERATURE		NODE	TEMPERATURE
100	-30.7		101	-31.4
102	-32.0		103	-30.7
104	-31.3		105	-32.0
106	-30.6		107	-31.3
108	-31.9		109	-30.6
110	-31.2		111	-31.8
112	-30.6		113	-31.2
114	-31.8		115	-30.6
116	-31.3		117	-31.9
118	-30.7		119	-31.3
120	-32.0		121	-30.7
122	-31.4		123	-32.0

ELECTRODE MEMBRANE
NODES AND TEMP
(SEE FIGURE 1.2)

```
**************************
*TIME IN ORBIT =4.7840HRS.*
**************************
```

NODE	TEMPERATURE		NODE	TEMPERATURE
200	-34.0		201	-34.2
202	-34.4		203	-34.1
204	-34.3		205	-34.6
206	-34.2		207	-34.6
208	-34.9		209	-34.3
210	-34.7		211	-35.0
212	-34.3		213	-34.7
214	-35.0		215	-34.2
216	-34.6		217	-34.9
218	-34.1		219	-34.3
220	-34.6		221	-34.0
222	-34.2		223	-34.4

DRAWING MEMBRANE
NODES AND TEMP
(SEE FIGURE 1.3)

```
****************************
*TIME IN ORBIT =4.7840HRS.*
****************************
```

NODE	TEMPERATURE	NODE	TEMPERATURE
300	-185.5	301	-186.6
302	-187.6	303	-185.6
304	-186.7	305	-187.7
306	-185.7	307	-186.7
308	-187.6	309	-185.7
310	-186.7	311	-187.5
312	-185.7	313	-186.7
314	-187.5	315	-185.7
316	-186.7	317	-187.6
318	-185.6	319	-186.7
320	-187.7	321	-185.5
322	-186.6	323	-187.6

OUTER SHROUD
NODES AND TEMP
(SEE FIGURE 1.4)

```
****************************
*TIME IN ORBIT =4.7840HRS.*
****************************
```

NODE	TEMPERATURE	NODE	TEMPERATURE
400	-95.1	401	-95.5
402	-95.7	403	-95.8
404	-95.8	405	-95.7
406	-95.4	407	-95.2

ASTROMAST LONGERONS
NODES AND TEMP
(SEE FIGURE 1.5)

```
***************************
*TIME IN ORBIT =4.7840HRS.*
***************************
```

NODE	TEMPERATURE		NODE	TEMPERATURE
500	-76.5		501	-75.5
502	-83.9		503	-93.4
504	-93.4		505	-93.4
506	-93.4		507	-93.4
508	-93.4		509	-93.4
550	-76.6		551	-75.5
552	-84.0		553	-93.5
554	-93.5		555	-93.5
556	-93.5		557	-93.5
558	-93.5		559	-93.5

APPENDIX D

FIGURE-SENSING TECHNOLOGY

Page intentionally left blank

APPENDIX D

FIGURE-SENSING TECHNOLOGY

1.0 INTRODUCTION

General Research Corporation's initial assessment of figure-sensing tech-
nology focused on identifying interfaces with the control system, evaluating
specific measurement technologies, and assessing the state of development of
key components. The remaining issue is one of integration; how feasible
would it be to implement a specific measurement technology in a spaceborne
system? This issue is best addressed by companies experienced in developing
optical systems. Sections 6.0 and 7.0 give the responses of two companies to
the question of system integration.

The basic conclusion of the initial assessment is that there are three
optical measurement technologies that would be appropriate:

    (1) Rangefinding using modulated lasers;

    (2) Interferometry using two-color or dual-laser techniques;

    (3) Optical triangulation.

The key factors that affect these technologies are sensitivity, data rate,
and sensor positioning. At low-data rates around 1 Hz, millimeter sensitivity
can be achieved by state-of-the-art surveying rangefinders that use 15-MHz
modulation frequency. Extending this technology to higher data rates or more
sensitivity would need custom systems development, but no new development in
optical or electronic components. The optical and electronic components
presently used in military laser radars and in optical communication systems
would be quite appropriate to use in an upgraded laser rangefinder.

For sensitivities better than 100 microns and higher data rates, inter-
ferometry becomes more appropriate. Again, all the components already exist,
and successful laboratory devices have been demonstrated. The basic issues
center around developing compact and stable systems.

Optical triangulation techniques can be fast and sensitive, but they require coordination with some type of distance-measuring device. Still, a fast triangulation sensor could measure a large number of sample points simultaneously, and a slower distance-measuring device could measure only the reference legs. Implementation of such a system depends strongly on the ability to obtain a set of suitable viewing angles.

In an actual system, it might be best to use more than one type of measurement device. This could lead to greater flexibility and reliability. Because all three of the preceding techniques could be implemented with semi-conductor diode lasers, an individual sensor could be quite compact. This would make it feasible to use a large number of sensors that perform data processing in a parallel manner.

2.0 CONTROL SYSTEM'S IMPACT ON FIGURE SENSOR DESIGN

A low-orbit large-membrane mirror will be subject to distortions caused by temperature variations, particularly when the mirror passes from the Earth's shadow to full sunlight. The figure control system must be able to maintain the required surface quality despite temperature variations of 100 K.

There are several levels of control system complexity that can be designed to perform all or part of the figure control task. A brief overview of these levels of complexity is presented in Section 4.7.1. A particular control model, based on an active real-time optical figure sensor, is then used (Sect 3.0) to select the criteria that must be met by the figure sensor. Section 4.0 presents an initial survey of potential figure-sensing technology.

3.0 OPTICAL FIGURE SENSOR CRITERIA

At this time, the most conservative approach is an active control system with an optical real-time figure sensor. Section 4.7.2 discusses the criteria imposed on the figure sensor by this control system.

4.0 SURVEY OF FIGURE SENSOR TECHNOLOGY

The previous sections discussed the system aspects of a figure control system and its constraints on the figure sensor. This section provides an overview of the technology of the measurement system.

The results of a survey of potential figure sensor technology are summarized in Table 4.1. This table lists types of measurement technology and rates them as "reject," "accept," or "possible." The comments column summarizes the findings. Acceptable technologies are temperature and strain sensors and small retroreflectors. The rejected technologies are microwave interferometry, proximity to back surfaces, painted surface patterns, and optical gaging using zoneplates, axicons, or optical fibers. Possibly acceptable technologies include the use of thin lines stretched over the surface, optical triangulation, and laser ranging. It is quite possible that all three technologies could be used to design a complete figure sensor system.

In the next section, the optical ranging, optical triangulation, and combined optical technologies will be analyzed in more detail.

5.0 EVALUATION OF POTENTIAL OPTICAL TECHNOLOGY

The three technologies that passed the initial screening were optical ranging, optical triangulation, and combinations of these systems.

In order to evaluate the current state-of-the-art in these technologies, two steps were followed. The first step was to run a computerized search of the scientific literature. The output from this search was a bibliography, provided at the end of this section. The computerized bibliographic search was reinforced by the use of a General Research Corporation file on figure-sensing literature. The dominant references in this file are from the publications: Applied Optics, Applied Physics, Optical Engineering, and various SPIE Conference Proceedings. The second step was to call manufacturers of critical technological components and obtain specifications on current products and estimates of their adapatability to the figure-sensor problem.

This section first briefly discusses the physical principles underlying four optical ranging techniques and summarizes their applicability to figure sensing. The principles of optical triangulation are also discussed, in particular the techniques underlying close-range photogrammetry.

TABLE 4.1. - INITIAL SURVEY OF POTENTIAL FIGURE SENSOR TECHNOLOGY.

Sensor technology	Evaluation	Comments
Microwave interferometry	Reject	Interferes with radiometer or radar operation. Can have siting and frequency multiplex problems.
Proximity detectors	Reject	Front surface would be measured relative to the back surface, which is subject to large deformations.
Temperature sensors	Accept	Can be located on the back surface and rim.
Strain sensors	Accept	Associate strain sensors with the rim.
Painted surface grid	Reject	Thermal control problems can be caused by the mixed absorptivity and emissivity constants.
Small retroreflectors	Accept	Very small plastic retroreflectors or pieces of Scotchlite[1] tape can be placed on the membrane to permit laser illumination and return to sensor not located at the center of curvature.
Thin lines stretched above surface	Possible	Thin lines attached to the rim might be useful to calibrate sensor angular position. Dielectic properties must not interfere with the operation of the radiometer.

[1] Scotchlite: Registered trademark of Minnesota Mining and Manufacturing Company.

TABLE 4.1. - Continued

Sensor technology	Evaluation	Comments
Optical gaging (zone plates, axicons)	Reject	Problems at long ranges with depth of focus and location of referents.
Optical fiber gaging	Reject	Long (100-m) fibers probably subject to damage and degradation in space environment. Temperature changes may distort measurements. Possible dielectric influence on microwaves.
Optical triangulation Stereoanalysis Electronic photogrammetry Automated theodolites Optical trackers	Possible[a]	Requires that several sensors view each target point on the surface from different angles. There may be possible mounting problems in some directions. Will be discussed in more detail in text.
Laser ranging Surveying rangefinders (pulsed & CW-modulated) 2-color heterodyne interferometry Self-pulsed frequency Stabilized ranger	Possible	Surveying rangefinders now have sufficient sensitivity, but require speeding up the process to handle more than one target per second. Tradeoffs between technologies will be discussed in more detail in the text.

[a] Barnes Engineering has pioneered in optical triangulation technology. We have provided their data in Section 6.0. Barnes believes that triangulation measurements should be an "accepted" technique for shape measuring.

5.1 OPTICAL RANGING

There are four types of optical ranging that could be used as an absolute position sensor for calibration, or as a complete figure sensing system. These four types are pulsed-ranging techniques as presently used in precision surveying; modulated CW ranging techniques, also used in surveying; two-color optical interferometry; and self-pulsed frequency-detection ranging.

5.1.1 Pulsed Laser Rangefinding

In order to operate in full sunlight at a range of 100 to 200 m, a laser rather than an incoherent light source will be required. A pulsed laser can be used with a gated incoherent detector and spectral filters so that the sunlight received during the pulse is an insignificant contributor to the measurement noise compared to the noise generated by the optical detector and electronics. Surveying instruments now in use have ranges up to a kilometer, using diode lasers. This long range is, in large part, made possible by the use of retroreflecting targets and by the small beamwidth of a laser compared to an incoherent source. In space, the performance of a range-finding laser is still better because there is no atmospheric loss or aberration factor. Because terrestrial precision commercial rangefinders can now measure to 3-mm accuracy at a 1-km range, there should be no problem with the required accuracy.

However, the present rangefinders require 7 seconds for the initial measurement and 1 second per measurement to follow the target as it is continuously moved. This data rate must be improved to meet the figure sensor requirements. The basic way to speed the measurement process is to shorten the laser pulse. This can best be seen from the equation for the range accuracy of a measurement in which a series of pulses in averaged:

$$\delta R = \frac{C t_p}{2\sqrt{N}\ (SNR)} \tag{1}$$

where: δR   = measurement accuracy averaged for N pulses

         c   = speed of light in free space

         t_p = pulse duration

         N   = number of pulses

         SNR = power signal-to-noise ratio.

This equation is graphed in Figure 5.1. The parameter is the pulse duration. Commercially avaiable GaAs laser diodes can generate 1-ns pulses. Pulse-train laser systems using Nd-Yag, mode-locked laser devices with a 200-ps pulse length are commercially available as laboratory instruments. There are other laser technologies that can achieve even shorter pulses, but these two systems are the closest to field applications. From Figure 5.1 we see that 200-ps pulse duration would require only two pulses to attain 3-mm accuracy with an SNR of 10. Because the Nd-Yag laser is quite powerful, the actual SNR could be increased, so that 1-mm accuracy is a realistic figure. It may be harder to obtain the accuracy with a GaAs laser unless it is operated at a high-repetition rate.

There are tradeoffs between the diode and Nd-Yag lasers in terms of repetition rate, size, power, and weight. The diode laser can operate at a higher repetition rate, is smaller, draws less power, and weighs less. It also has less output energy, poorer beam quality, and longer pulses. It should be noted that experimental diode lasers have been fabricated with shorter pulses, but these are still laboratory prototypes or restricted technology.

Because both the communications industry and the military are strongly supporting research and development on short-pulse diode lasers, it is quite probable that a 100-ps to 500-ps diode laser would be field-deployable shortly. In this case, the preference would fall to the diode system, at least for applications where compactness, low weight, and low power requirements are important. At present, however, the Nd-Yag laser, operating in a mode-lock pulse-train mode, is closest to attaining measurement accuracy of 1 mm in one

pulse train. The limited repetition rate is a significant problem; thermal effects limit the standard rod laser to only 10 pulse trains per second. There are alternative lasers that would meet the requirement, but they have other problems, especially with triggering. More details on specific systems are given in the references listed in the bibliography.

For a 3-mm measurement accuracy, it should be possible to use available diode laser systems with only minor modifications, provided that the repetition rate can be increased or that the pulse width can be reduced to 200 or 500 ps.
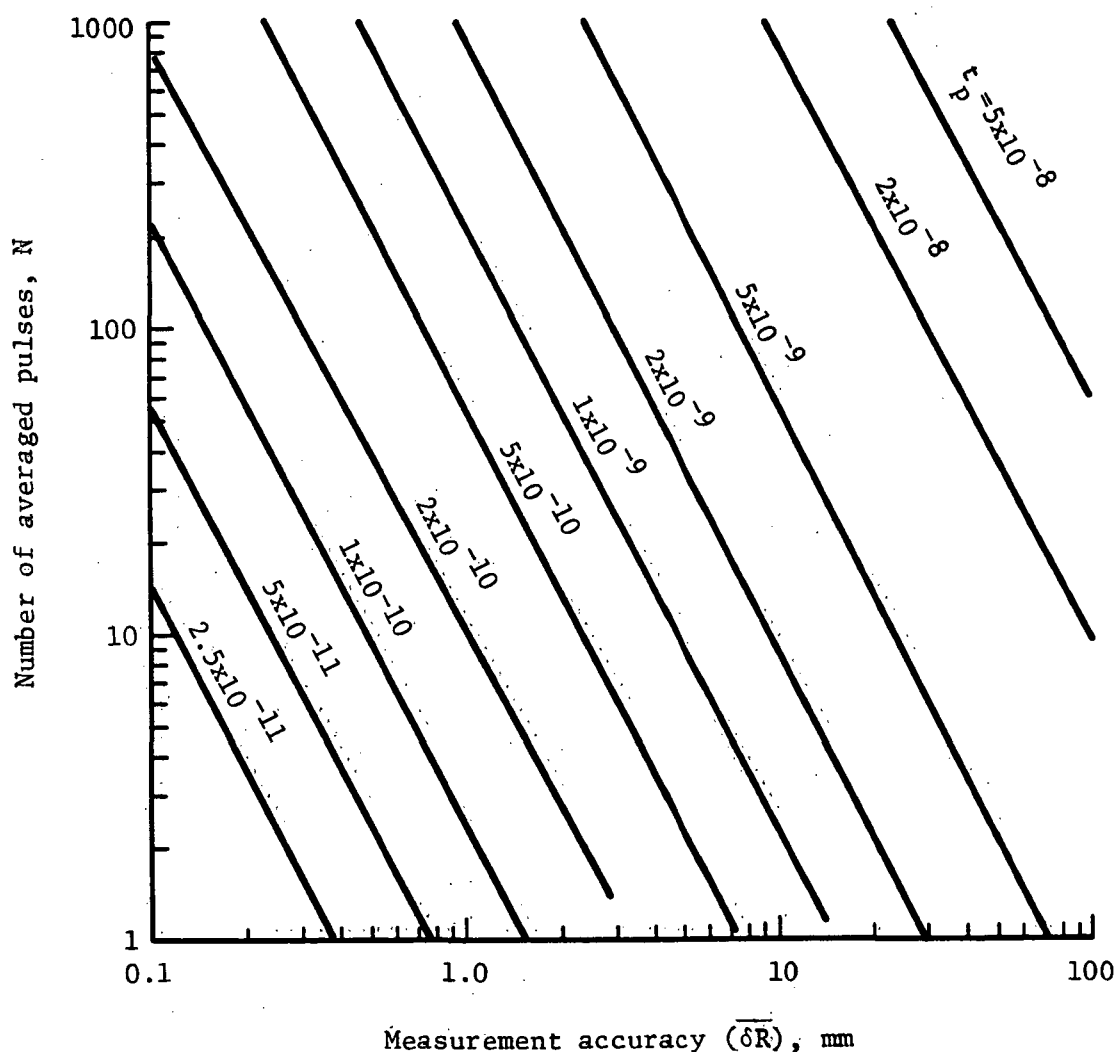
Figure 5.1. - Rangefinder Performance.

There are commercial silicon avalanche detectors that have been developed for measuring mode-locked laser signals. These detectors have rise times less than 50 ps, which is adequate.

It appears that precision rangefinding technology is close to meeting the figure sensor requirements, especially if the accuracy need be no better than 3 or 4 mm.

5.1.2 Modulated CW laser Rangefinding.

In a modulated CW laser rangefinder, the optical carrier is amplitude-modulated and the modulation phase is compared to that of the detected return signal. If the target range exceeds the modulation wavelength, then multiple frequencies of modulation must be used to remove the ambiguity. The measure target range is given by:

$$R = \lambda_m \left[\frac{\Delta\phi}{4\pi} + N_m \right]$$

where: R = measured range

λ_m = modulating wavelength

$\Delta\phi$ = phase difference between the reflected signal and the modulation signal

N_m = number of modulation wavelengths.

Some surveying systems used modulated lasers (fig. 5.2), especially helium-neon, to achieve accuracies comparable to the state-of-the-art in pulsed lasers. It is also possible to used modulated diode lasers in this type of system.

277

Sunlight may be a problem with this system if direct detection is used. Provided that the sun is not exactly behind the laser, and that spectral filters are used, then direct detection with photodetectors would be feasible.

Direct detection is preferable to heterodyne detection, because angular alignment must be extremely stringent for heterodyne detection.

The limiting factor in extending this technology to submillimeter accuracy is likely to be the phase measurement technology. There are commercially available electro-optical modulators that operate around 1 GHz, which is a modulation wavelength of 30 cm. If sufficient phase stability can be maintained with two-color modulation, then this technology could achieve submillimeter accuracy.

5.1.3 Two-Color Heterodyne CO_2 Interferometry

This type of measurement system, shown in Figure 5.3, has been designed for measuring to micron accuracies. It is similar to a modulated CW rangefinder except that a heterodyne scheme is used. Because the wavelength of a CO_2-stabilized laser can be tuned in discrete steps around 10 μm, the "modulation" is provided by running the laser at two nearby frequencies and using the beat frequencies of the detected return signal. Although complex and sensitive, the heterodyne detection is more feasible at the longer optical wavelengths than it is at visible and near-infrared wavelengths (the angular tolerances are proportional to the wavelength). Another advantage of heterodyne detection, besides providing an inherent "modulation" mechanism, is that quantum-limited detection is possible. However, at the measurement ranges of 100 to 200 m, this level of detection is not required. Again, phase stability may prove to be a limiting factor because the signal must maintain phase coherence with the reference beam during the transit time. A stabilized, multicolor CO_2 laser is a complex device and may be inherently nonrobust.

This technology is more applicable to submillimeter measurement accuracies where the rangefinding technologies begin to fail.
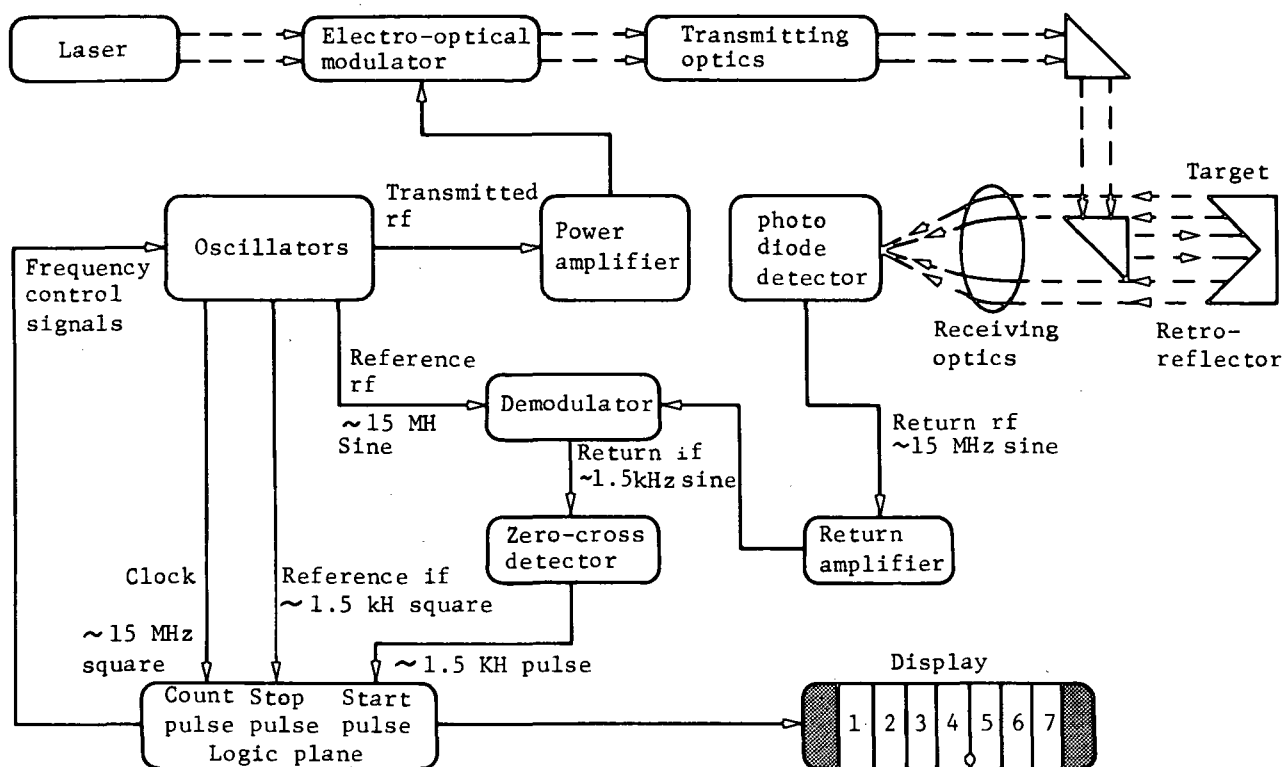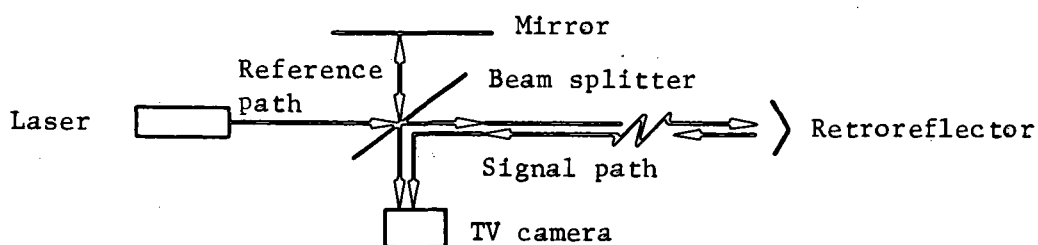
Figure 5.2. - Laser ranging.

Figure 5.3. - Optical interferometry.

5.1.4 Self-Pulsed Frequency Detection Rangefinding

In many ways, this system is similar to a pulsed rangefinder. However, instead of measuring the time of flight of the pulse, which requires highspeed electronics, the returned laser pulse is used simply as a trigger for the laser to send out another pulse. The range accuracy of this system is:

$$R = \frac{c}{2\ PRF} \tag{4}$$

where: R   = range

c   = speed of light

PRF = pulse repetition frequency.

To make 10 measurements per second to millimeter accuracy would require at least a 10-MHz pulse repetition rate. The membrane should be stable during the measurement time or the triggering might be disrupted, possibly spoiling the whole cycle.

The limiting factor in this technology may prove to be the requirement for a high-repetition rate. Although communication-system lasers can meet this condition, they may not have adequate robustness. The technology question for this system should remain open until more research is done.

5.2 Optical Triangulation

For calibration, it will be necessary to have at least one optical ranging system. However, the finite measurement time of the ranging system might not be compatible with the required data rate, if absolute measurements are made on every target. Triangulation may be referenced to the rim structure, provided rim motion is small or can be compensated for during data reduction.

Consequently, optical triangulation measurements are of interest because they can, at least in theory, be made quickly. It will be assumed that all optical triangulation measurements are made from small targets, essentially the same types used for the optical ranging; e.g., Scotchlite tape. Probably it would be feasible to equip each optical triangulation sensor with a small diode laser that would illuminate the target.

Optical triangulation systems determine the spatial coordinates of a target by measuring from three or more angles. Consequently, it is important that measurements can be made from the appropriate angles. This can be a limiting factor if there are restrictions on where the sensors can be located. To some extent, this limitation can be reduced if the triangulation targets maintain a predictable spatial relationship to key calibration targets which can be measured with a ranging sensor. Then, what would otherwise be an underdetermined two-angle measurement could (theoretically) be completed by data processing. Another constraint on triangulation is that the relative locations of all the sensors must be accurately known so that their measurements can be electronically correlated.

The technology of optical triangulation has three mainstream applications: photogrammetry, surveying with optical theodolites, and military angle-only tracking systems. Although new products that use electronic signal processing are rapidly being developed, presently only the military applications have fully electronic systems. They are generally based on optical arrays or vidicons, which have much lower resolution than film. Consequently, it is necessary to compensate for the small resolution by decreasing the field of view. Other ways to compensate are to scan the sensor, to use a reticle pattern, or to arrange the "target" into a special pattern. All these compensation techniques permit the use of interpolation and centroid processing algorithms to effectively "resolve" within a sensor resolution cell or pixel.

5.2.1 Close-Range Photogrammetry

Commercial systems are available that can achieve millimeter accuracy at a range of 100 m (1 part in 10^5). However, these instruments use high-resolution film and manual processing. An advantage of one particular type,

the Geodetic Services system, is that it permits self-calibration algorithms to be incorporated into the measurement. This system might be implemented rather easily with the use of thin lines stretched across the rim.

It would be necessary to incorporate electronic sensor technology into this system. However, by using a narrow field of view of about 0.1 mrad, a high-resolution TV camera would have between 5 and 10 pixels covered by a 1-mm target. This should be sufficient for the required measurement accuracy. If not, then a small dither of the camera scan would permit interpolation. However, the camera must have zoom capability because the target acquisition requirement is for the target to be anywhere within a 1-m circle.

5.2.2 Theodolites

These are surveying triangulation systems. Commercial digital systems are available. However, they are manually operated. One system incorporates a laser diode for distance measurements, as well as angle measurement.

The required accuracy can be met by such systems. However, they must be automated and self-calibration built into the data processing.

5.2.3 Military Angle-Only Trackers

Most of these systems are not highly accurate. It would be possible to incorporate the signal processing and sensor technology of these systems into the more accurate optical systems of the previous section. In that case, millimeter accuracy at 100-m range would probably be achievable.

5.3 COMBINED SYSTEMS

As discussed previously, the angle-only systems are constrained by sensor location and by calibration problems. On the other hand, absolute distance measurements tend to be slower and may require more power. It is desirable to consider combining the two technologies.

282

One way to implement a combined technology would be to subdivide the membrane reflector into regions. Each region could be assigned one absolute sensor and one or more triangulation sensors. The absolute sensor could then be constantly calibrating the angle-only sensors if the membrane distortions were correlated in that region. This approach would also minimize the requirement of large scan angles. However, the dynamic motions of the membrane must be predictable if this approach is to be beneficial.

Another approach is to use a multitude of sensors. Because laser-diode rangers and optical CCD array sensors for angle measurements are small and consume little power, it may be relatively simple to assign hundreds of sensors to the measurement system. Then each sensor could be relatively slow and improve accuracy by averaging. There must be some type of sensor backup if the elements fail, because such a design probably would not be scannable over large angles.

6.0 BARNES TRIANGULATION SYSTEM

Barnes Engineering Company has long been engaged in the production of precision position and angular measurement instruments using electro-optical techniques. In particular, autocollimation instruments have been applied in arc-second measurement of missile-submarine platform alignment and recently in measuring the three-axis attitude of a boom deployed in space from the Magsat satellite. With the availability of charge-coupled device-area arrays and microprocessors, autocollimators have been designed that can monitor a multiplicity of points on such large space structures as antennas and optical systems at high rates and great precision. A preliminary assessment of figure sensing of the large 100-m diameter electrostatic membrane mirror has been made using the Barnes position measuring instrumentation concept and is described in the following discussion.

The Barnes measuring system comprises integral transmit-receive optical heads and microcomputer data processors. In the optical head a light-emitting diode (LED) provides collimated light to illuminate the monitored membrane area. Small corner-cube reflectors, installed at the points of monitoring interest, return LED energy to the sensor and are imaged by the optical system

onto a charge coupled device (CCD) area array. Typically, this array has about 185 000 photo-optical measuring sites (pixels) and can accommodate returned images from as many as 30 reflectors at a time. The electronics sequentially samples each pixel and stores the returned signal data for processing into the required position coordinates for figure determination. For the membrane mirror problem, we are primarily interested in deflections in and out of the "plane" of the mirror. In the position computation process, an algorithm is used that locates each returned corner cube image to better than a tenth of a pixel. This is accomplished by spreading the images over a number of pixels (optical defocusing) and computing the centroid of the pixels containing signal information from each corner cube. Limitations on positional accuracy are therefore not restricted to the granularity of the CCD array resulting from the dimensions of the pixels, their number, and the spacing between them. The system is inherently fast as the pixel signals are clocked out of the CCD array at a frame rate of 30 Hz or greater with the speed of position computation limited primarily by computer speed.

The real-time position measurement of a large number of points can therefore be at least at a 30-Hz rate, with a possibility of much higher rates, if they are required.

Barnes has examined system design requirements for measuring the figure of a 100-m diameter membrane mirror with an accuracy of 3 mm by monitoring 40 points. A sketch of a system configuration that satisfies these requirements is shown as Figure 6.1 and outlined as follows:

(1) Four optical heads of the type described above will be used for sensing corner cubes fastened to the membrane. The sensors will be mounted in pairs on rigid platforms on the rim, at or near the point where the Astromast is attached to the box truss support ring.

(2) The attitude of the two platforms relative to the feed structure will be tracked by separate sensors looking along the Astromast. To handle the larger angular excursions expected of the rim structure, these sensors will have separate transmitters and receivers, which considerably expand their angular measuring range.

(3) The four membrane sensors will have 12 x 48-degree fields of view, which provides overlap, i.e., certain locations can be sensed from both sides by oppositely mounted sensors. This feature should prove valuable for redundancy, position verification, and Sun rejection reasons. Opposing sensors will also provide positional information on the platforms relative to each other.

(4) Because the four optical heads are installed to sense corner cubes on opposite sides of the membrane, their distance from the corner cube reflectors will be from 50 to 100 m. For the selected field of view size and at the 50-m range, 3 mm is equivalent to 0.14 pixels; at the 100-m distance, 3 mm is equivalent to 0.07 pixels. Because the system algorithm has been demonstrated to have a pixel resolution accuracy in excess of these values, accuracy requirements should be met. No problems are foreseen in meeting data rate requirements.

The more difficult membrane sensing problem requiring 0.1-mm accuracy over 300 monitored points with a rate of 100 Hz could also be handled by the same general type of equipment but with greater complexity. The higher accuracy requirement would dictate a sensor design with a field of view 1/30 of the size of the former case. Therefore, the number of sensors would increase by a factor of 30 for the same angular membrane coverage. It might be possible to use a limited number of higher resolution sensors for specific areas of interest with a number of somewhat coarser resolution sensors.

Barnes Engineering Company is now working on an IR&D development of a two axis CCD array position measuring system for laboratory experimental purposes. The system is being assembled with a computer and display terminal and will be available shortly for demonstration to interested parties. It should be possible to simulate many of the membrane mirror parameters and conduct pre-liminary evaluations of the overall technique and the usability of specific corner cubes and other type reflectors.
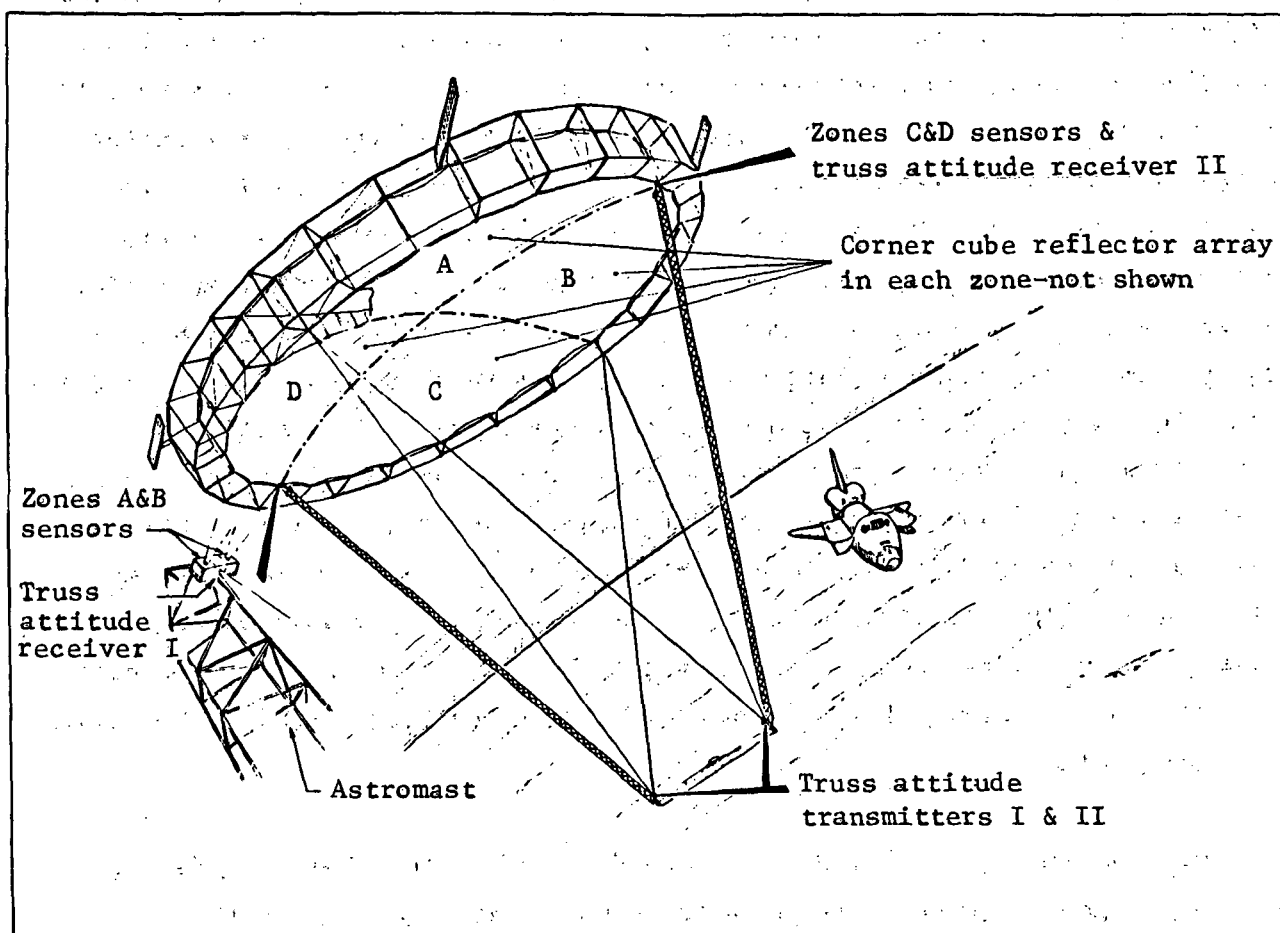
Figure 6.1. - Membrane mirror configuration sensing concept.

7.0 AERODYNE INTERFEROMETRIC SYSTEM

This section discusses the Aerodyne Research Corporation's approach to a figure measurement system. The experimental arrangement is illustrated in Figure 7.1. Attached to the large dish are small, open retroflectors. Each retroreflector is about 1 mm in diameter and weighs less than 1 mg. Thus, for a dish membrane thickness of 0.3 mil, the retroreflector is equivalent to an extra 0.3-mil layer with a 260-mil radius. The following discussion provides details not available in Reference 1.

---

[1] F. Fien, M. Camac, H.J. Caulfield, and S. Ezekiel: "Absolute distance measurement by variable wavelength interferometry," Applied Optics, Vol. 20, p. 400, February 1981.

The heart of the measurement system is a simple Michelson interferometer.
Light beams from two helium-neon lasers, both operating on the 6328 $\overset{o}{A}$ line,
are directed at the interferometer beam-splitter. Some of the light goes to
the reference retroreflector R_o; the other light is directed by a steering
mirror to retroreflectors on the dish. The return beams from the retro-
reflectors are joined by the beam-splitter and directed at two detectors, D1
and D2. Electric signals from the detector go to dc differential amplifiers.
A modulator M, oscillates the reference retroreflector by about one-half a
wavelength, $\lambda/2$. The modulation frequency is several kilocycles. Squarewave
electrical signals go from the modulator to the differential amplifiers; the
polarity of the signals reverse every half-cycle. The output voltage from
each differential amplifier drives a crystal on one of the laser cavity
mirrors that changes the length of the laser cavity. At zero voltage output
from the differential amplifier, the phase between the two arms of the
interferometer is either 0 or 180 degrees; that is, there is either complete
constructive or destructive interference between the beams from the two inter-
ferometer paths.

This method for locking the phase to 0 or 180 degrees has been developed
by several groups (Ref. 2,3). This feedback system can hold the phase to
within several microradians of 0 or 180 degrees. This is over 10 times better
than the requirement for the application discussed in this letter. A beam
chopper, operating at several megacycles, alternates the measurement between
the two lasers. Gating signals from the beam chopper to detectors D1 and D2,
operate D1 when laser 1 is illuminating, and D2 when laser 2 is illuminating.
The reason for the high-frequency chopper is to ensure that measurements from
the two lasers are made essentially simultaneously, thereby eliminating the

[2] G.E. Moss, L.R. Miller, and R.L. Forward: Appl. Opt. 10. p. 2495 (1971).

[3] S. Ezekiel, J.A. Cole, J. Harrison, and G. Sanders, Proc. Soc. Photo-Opt.
Instru. Eng, 157, p. 68 (30-31 Aug. 1978).

effects of any jitter of the interferometer mirrors. A portion of the beams from the two lasers are mixed and directed on detector D3. The differences between the two optical frequencies are in the radio frequency region. Frequency is measured with cycle counters and measurement times must be long enough to obtain sufficient counts. This is the only output of the distance measurement system; the radio frequency is a direct measure of the distance.

This feedback system locks the laser output to produce either 0 or 180 degrees phase between the two interferometer arms. S. Ezekiel (Ref. 3) has shown that the frequency of the system stays stable to several hertz. Thus, with the system shown in Figure 7.1, the rf counter can be accurate to several hertz.
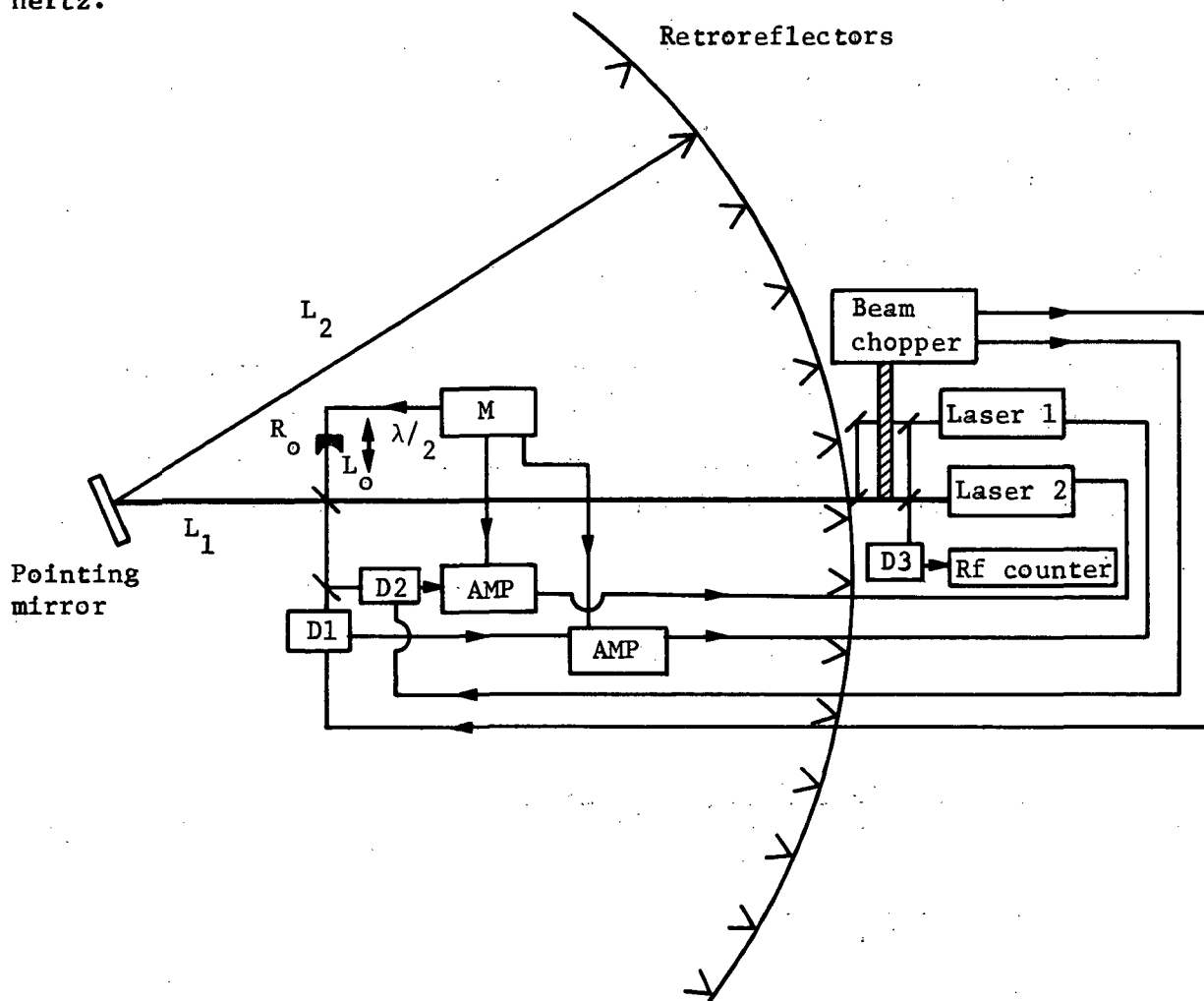
Figure 7.1.- Aerodyne interferometric system arrangement.

Both helium-neon lasers work on the 6328 A. The system selects two wavelengths, λ_1 and λ_2 as shown in Figure 7.2. Figure 7.2 is a plot of the 6328 $\overset{o}{A}$ line intensity as a function of wavelength. Each laser can be tuned to operate at any wavelength within this line, where there is enough gain. λ_1 and λ_2 are selected as follows:

(1) the phase of λ_1 is 0 deg,
    and the phase of λ_2 is 180 deg

(2) both path differences have the same number of
    wavelengths, n.

The interferometer equation becomes:

for λ_1, phase = 0 deg: $\quad 2[(L_1 + L_2) - L_0] = n \qquad \lambda_1 = \dfrac{nc}{f_1}$

for λ_2, phase = 180 deg: $\quad 2[(L_1 + L_2) - L_0] = (n + 1/2)\lambda_2 =$

$$= (n + 1/2)\frac{c}{f_2} \tag{1}$$

L_1 and L_2 are the distances from the beam splitter to the retroreflector on the dish. L_0 is the distance to the reference retroreflector. Interferometers always measure the difference in distance between the two arms. C is the velocity of light and f is the frequency corresponding to the wavelength, λ.

Solving for the frequency difference:

$$(f_2 - f_1) = \frac{(n + 1/2)C}{2[(L_1 + L_2) - L_0]} - \frac{nc}{2[(L_1 + L_2) - L_0]} \tag{2}$$

$$= \frac{C}{4[(L_1 + L_2) - L_0]}$$

Note, that the expression for the difference in frequencies does not contain the number of wavelengths, n. For $(L_1 + L_2 - L_o) = 100$ m, $(f_2 - f_1) = 0.75$ MHz; for $(L_1 + L_2 - L_o) = 10$ m, $(f_2 - f_1) = 7.5$ MHz.

We now treat the accuracy requirements of the system. We want to measure the distance from each retroreflector to the steering mirror, the distance L_2. From Equation (2),

$$L_2 = (L_0 - L_1) + \frac{C}{4(f_2 - f_1)} \tag{3}$$

Thus, if the length $(L_o - L_1)$ remains fixed and known, L_2 is obtained directly from a measurement of $(f_2 - f_1)$.
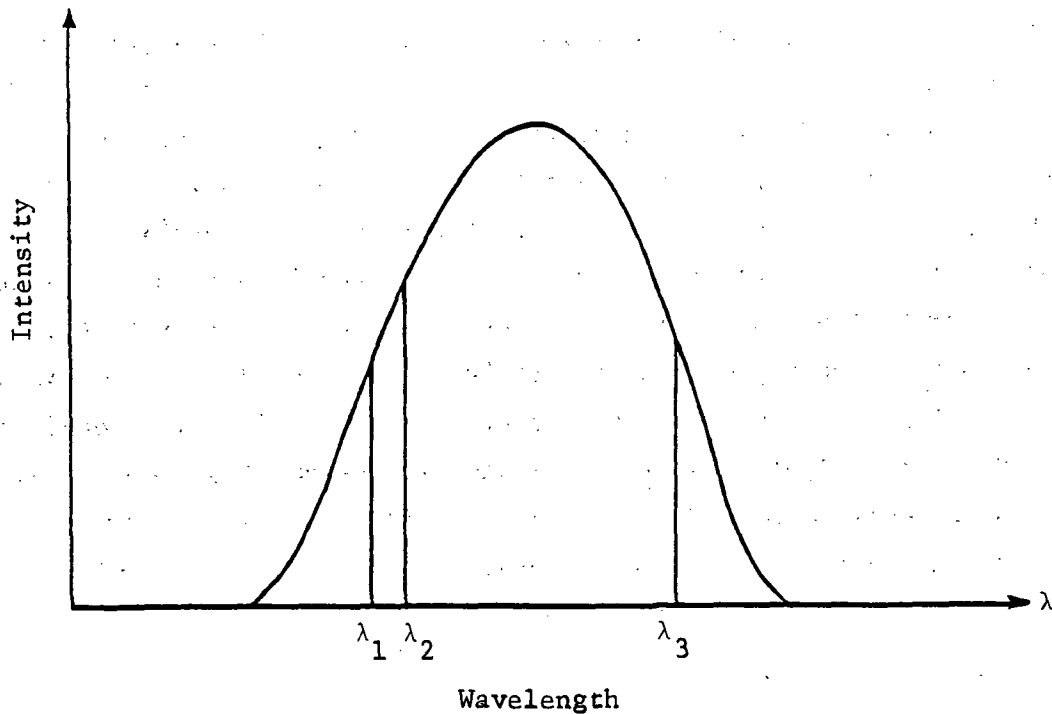
Figure 7.2. - He/Ne laser 6328 $\overset{\circ}{A}$ line.

In practice one cannot obtain exactly a 0 and 180 degrees phase, and small additional phases must be added to Equation (3).

$$2(L_1 + L_2 - L_0) = (n_1 + \phi_1)\frac{c}{f_1}$$

$$2(L_1 + L_2 - L_0) = (n_1 + 1/2 + \phi_2)\frac{c}{f_2}$$
(4)

Solving for the length

$$(L_1 + L_2 - L_0) = \frac{(1/2 + \phi_2 - \phi_1)}{2(f_2 - f_1)}$$
(5)

The fractional error in the length becomes:

$$\frac{\text{Error in } (L_1 + L_2 - L_0)}{(L_1 + L_2 - L_0)} = 2\sqrt{\phi_1^2 + \phi_2^2} + \frac{\text{Error in } (f_2 - f_1)}{(f_2 - f_1)}$$
(6)

A 1-mm accuracy over a 100-m length requires an accuracy of 1 part in 10^5. A 1-mm accuracy over a 10-m length requires an accuracy of 1 part in 10^4. This method for locking of the phase to 0 or 180 degrees is accurate to one part in 3×10^6; thus, our requirement for about 1 part in 10^5 can be easily accomplished. Frequency measurement equipment are cycle counters; counting times must be sufficient so that the round-off errors in the number of counts must be less than the desired error. Thus, for 1 part in 10^5 and 7.5×10^5 hertz, counting must be for at least 0.3 seconds. There are also possible problems with drifts in the laser systems and interferometer components. By rapidly alternating measurements between the two lasers, one avoids errors due to small motion of the interferometer components. 10-m and 100-m measurements to 1-mm accuracy can be obtained in 3 and 300 milliseconds, respectively.

Distances can be obtained more quickly and with more precision by making measurements at three wavelengths, λ_1, λ_2, and λ_3 (fig. 7.2). At λ_3 the laser is set for 0 deg phase between the interferometer arms. The interferometer equation becomes:

$$2(L_1 + L_2 - L_0) = (n_3 + \phi_3)\frac{c}{f_3} \tag{7}$$

where n_3 is the number of wavelengths, and ϕ_3 is a small phase around 0 deg. Combining Equations (4) and (7) one obtains:

$$(L_1 + L_2 - L_0) = \frac{(n_3 - n_1) + (\phi_3 - \phi_1)}{2(f_3 - f_1)} \tag{8}$$

Note that the difference in wavelengths $(n_3 - n_1)$, is an integer. The exact value of the integer is obtained from the relation

$$(n_3 - n_1) = 2\frac{(f_3 - f_1)}{(f_2 - f_1)} \tag{9}$$

Note that we choose λ_1 and λ_3 to be on the opposite sides of the 6328 $\overset{\circ}{A}$ line so that the frequency difference $(f_3 - f_1)$ is about 10^9 Hz. Thus, for mirror distances of 100-m, $(n_3 - n_1)$ becomes approximately 10^4. The fractional error in the length measurement becomes:

$$\frac{\text{Error in } (L_1 + L_2 - L_0)}{(L_1 + L_2 - L_0)} = \frac{\sqrt{\phi_1^2 + \phi_3^2}}{(n_3 - n_1)} + \frac{\text{Error in } (f_3 - f_1)}{(f_3 - f_1)} \tag{10}$$

Note, that an error in the phase is less important because of the factor (n_3-n_1) in the denominator and because the frequency difference (f_3-f_1) is 10^9 Hz. Accuracy of 1 part in 10^5 requires measurements to 10^4-Hz accuracy, corresponding to 100 μs counting times. Thus, with three wavelengths, measurements can be made in several milliseconds to accuracies of much less than 1 mm.

The laser frequency stability and the phase locking capabilities of the system have been demonstrated in References 2 and 3. The most stressing components are helium neon lasers. Other subsystems are simple electronics, passive retroreflectors and other optical components. All the system components have been space qualified in a space measurement system. Aerodyne is prepared to demonstrate the operation of the interferometer system with a single laser and in particular, show its phase locking accuracy and laser frequency stability.

Page intentionally left blank

BIBLIOGRAPHY
(PRIMARY REFERENCES)

Ackermann, F.,: "Experimental Investigation into the Accuracy of Contouring from DTM." Photogramm. Eng. and Remote Sensing, Vol. 44, No. 12, December 1978. (Accuracy; Contouring; Soehnstetten; Electronic Tachometry; Photogrammetric Restitution; Digital Terrain Models)

Agin G.J., Binford T.O.,: "Computer Description of Curved Objects." IEEE Trans. Comput., Vol. C-25, No. 4, April 1976. (Ranging System; Laser; Computer Controlled Optical Deflection Assembly; TV Camera; Three Dimensional Images; Space Curve; Computer Vision; Recognition of Curved Objects)

Allam M.M.,: "DTM Application in Topographic Mapping." Photogramm. Eng. and Remote Sensing, Vol. 44, No. 12, December 1978. (Topographic Mapping; Digital Terrain Models; Electronic Correlator Measurements; Computer System; Water Surfaces; Photogrammetry)

Bartling J.Q.,: "The Use of the Alford and Gold Effect as a Ranging Technique." Proc. IEEE, Vol. 57, No. 7, July 1969.

Bayha W.,: Multi-Function Laser Techniques. U.S. Department of Defense, January 1975.

Bowie J.L., Kuriger W.L.,: "Practical Limitations to the Ranging Accuracy Achievable with a Modulated CW Laser." 21st Annual Southwestern IEEE Conference and Exhibition, 1969.

Carrion W.J.,: "Development of Laser Ranging Systems for Space Application,." Proceedings of the Society of Photo-Optical Instrumentation Engineers, Vol. 134, 13-14 March 1978. (Laser Ranging Systems; Space Application; Tracking)

Chapman, G.D., Green, E.,: "A Noninterferometric Optical Probe. "Rev. Sci. Instrum., Vol. 48, No. 6, June 1977.
(Noninterferometric Optical Probe; Target Movement; External Micrometer Drive; Pulse Length Measurement; Target Surface Characteristics; Target Distortion; Electric Furnace; Light Spots Relative Position; Position Measurement; Target Displacement Measurement; HE-NE Laser; High Temperature Technique; Free Ranging Mode; Null Setting Mode; Steel Member Distortion)

Cooke C.R.,: "Automatic Laser Tracking and Ranging System." Digest of Technical Papers of the 1971 IEE/OSA Conference on Laser Engineering and Applications, 1971.
(Automatic; Laser Tracking System; Laser Ranging System; Retroreflective Targets; Laser Beam Applications)

Cooke C.R.,: "Automatic Laser Tracking and Ranging System," Appl. Opt., Vol. 11, No. 2, February 1972.
(Computer Compatible Data; Manual Initial Acquisition Sequence; Flash Pumped; Q Spoiled; ND-YAG; Optical Dynamic Range 30 DB; Automatic; Laser Tracking and Ranging Systems; Retroreflective Targets; Adjustable Neutral Density Filters; Scintillation)

Dudermel M.M.T., Corno J., Simon J.,: "Photometric Ranging of Wavelengths with the Aid of an Absorption Edge," Optica Acta, (GB), Vol. 17, No. 4, April 1970.

Dundon W., Savitsky E.,: "Receiver for a Neodymium Ranging System." IEEE J. Quantum Electronics, Vol. QE-5, No. 6, June 1969.

Economou G.A., Mackey L.C., Snyder S.A.,: "Precision Long-Range Laser Ranging System." Proceedings of the Society of Photo-Optical Instrumentation Engineers, Vol. 134, 13-14 march 1978.
(Laser Ranging System; Aperture Receiver Telescope)

Erickson E.G., Peynolds P.S.,: Picosecond-Pulse Fieldable Frequency-Doubled ND-YAG laser System for Ultraprecision Ranging. IEPE Optical Society of America Conference on Laser and Electro-optical Systems, December 1976. (Ultraprecision Ranging; Satellite Ranging Applications; Frequency-Doubled ND-YAG Laser; Picosecond Pulse Laser)

Ewanizky T.F., Rohde R.S.,: "Macro-Integrated Optical Technology," U.S. Department of Defense, August 1976.

Fitzmaurice M.W.,: "Ground-Based and Space-Based Laser Ranging Systems. IEEE J. Quantum Electron., Vol. QE-13, No. 9, September 1977. (Laser Ranging Systems; Ground-Based; Space-Based)

Iyer, R.S.,: "Threshold Detection in Pulsed Laser Ranging." Applied Optics, Vol. 15, No. 6, June 1976. (Pulsed Laser Panging; Detection Threshold; Return Pulse Laser Geodetic Satellite)

Jevalian A.V.,: "Optical Aids to Detection and Panging Systems. " Flectron. Prog., Vol. 16, No. 2, Summer 1974. (Laser Beam Applications; Pange Finding; Altimetry; Pointing and Tracking Systems; Laser Radar Systems; Accurate Ranging; Precision; Pulse Doppler Laser System; Cryogenically Cooled Quadrant Detector)

Johnson T.S.,: "Laser Ranging Systems Calibration and Practical Error Sources." Proceedings of the Society of Photo-Optical Instrumentation Engineers, Vol. 134, 13-14 March 1978. (Calibration; Practical Error Sources; Laser Ranging Systems; Pulse Modulation; Coherent Fading; Detection Error; Atmospheric Propagation Error)

Khaytun F.I., Nepogodin I.A.,: "Threshold Relationships in Actively-Scanning Optical Detection and Panging Systems." Optico-Mekh. Prom., (USSP), Translated in Soviet J. Opt. Technol., (USA), Vol. 36, No. 3, May 1969.

297

Landry M.A.,: "G-B-60A Light Detecting and Ranging System (LIDAR)." Sandia Corp., Albuquerque, N.M., Report No. SC-DR-67-115, December 1967.

Leith E.N.,: "Chromatic Aberrations in Pulse-Ranging Systems." 1972 Annual Meeting of the Optical Society of America, Abstracts Only, 17-20 October, 1972. (Chromatic Aberrations; Pulse Ranging; Imaging Systems; Imaging Radars; Phased Array Systems; Image Quality; US Systems)

Leonard S.L.,: K.E. Golden, D.E. Kind, R.C. Ward, "A Novel Laser-Ranging System with 1-cm Resolution." 1973 IEEE/OSA Conference on Laser Engineering and Applications Digest of Technical Papers, 30 May-1 June 1973. (Image Converter Tube; Deflection Plates; Time of Flight; Petroreflector; Corner Cube Arrays; Novel Laser Ranging System; 1 cm)

Mamon, G., Youmans, D.,: "Optical Pulsed Ranging Method for Improving Measurement Accuracy Comment." Applied Optics, Vol. 16, No. 1, January 1977. (Time Interval Measurements; Signal Generation; Optical Pulsed Ranging; Accuracy Improvement; Half Max Detector Mechanization)

Miyake, K.,: "Optical Pulsed Ranging Method for Improving Measurement Accuracy," Applied Optics, Vol. 15, No. 7, July 1976. (Measurement Accuracy; Setting Error; Time Interval Counter; Optimal Pulsed Ranging)

Mocker, H.,: FLIR Rangefinder Research 14316-P. Honeywell, Inc., for U.S. Department of Defense, June 1976.

Muhlberger J.G., Miller E.D.,: (Editors), Proceedings of the Seminar on Optical Tracking Systems, Soc. Photo-Optical Instrumentation Engrs, 18-19 January 1971. (Image Stabilization; Control; Lunar Mapping; Ranging)

Newbery A.R., Mabberley J.C.,: "Ranging, Guidance and Designation", Royal Aircraft Establ., Farnborough, England, Evaluation of the Potential Benefit to the Aeronautical Field from Laser Technology. December 1975. (Ranging; Guidance; Designation; Lasers; Development Trends)

Querzola, B.,: "High Accuracy Distance Measurement by Two-Wavelength Pulsed
Laser Sources." Applied Optics, Vol. 18, No. 1, September, 1975.
(Fractional Accuracies; Ranging; Direct Transit Time Measurements; Error;
Threshold Crossing; Pulse Discrimination; Amplitude Fluctuations; Pulsed Ruby
Laser PTM Emission; High Power Pulsed Telemeters; High Accuracy Distance
Measurement; Two-Wavelength Pulsed Laser Source)

Riegl J.,: "Miniaturized Optical Pulsed-Radar Equipment for Traffic and Film
Applications." Elektronik, (Germany), Vol. 23, No. 2, February 1974.
(Rangefinding; Speed Measurement; Traffic; Optical Pulsed Radar; Semiconductor
Laser Rangefinder; Automatic Focusing, Cameras)

Salwen H.C.,: "Error Analysis of Optical Range Measurement Systems." Proc.
IEEE, Vol. 58, No. 10, October 1970.

Schiel E., Strozyk J.,: Two Micron Rangefinder/Designator Technology. U.S.
Department of Defense, February 1974.

Schiel E.J., Gammarino R.P.,: E. Aras, A. Kleider, "Injection-Laser Terrain
Following System." 1973 IEEE/OSA Conference on Laser Engineering and Applica-
tions Digest of Technical Papers, 1973.
(Repetitively Pulsed Ranging Device; Transmitter; Transistorized Pulse
Generator; Injection Laser Terrain Following System; Light Weight Altimeter;
Sensitive SI Avalanche Photodiodes)

Shimizu M., Ueno Y.,: "Tracking and Ranging Systems Using Semi-Conductor
Lasers and Their Application to Large-Scale Ship's Guiding Apparatus." J.
Soc. Instrum. and Control Eng., (Japan), Vol. 12, No. 8 August 1973.
(Tracking; Ranging Systems; Semi-Conductor Lasers; Large Scale Ship's Guiding
Apparatus; Light Wave Ranging Systems; Angle Measuring Systems)

Shimizu M., Ueno Y.,: "A Tracking Laser-Ranging System." 1973 IEEE/OSA
Conference on Laser Engineering and Applications Digest of Technical Papers,
30 May-1 June 1973.

(Manual Acquisition Procedure; Laser Radar Method; Tracking Laser Ranging System; Docking of Ships; Automatic Link Maintaining; Digital Information of Ship's Position; Distance Measurement; Velocity Measurement)

Snyder S.,: "Mobile Optical Mount System (Laser Ranging). "Electro-Opt. Syst. Des., Vol. 10, No. 10, October 1978.
(Design; Tracking System; Laser Ranging; NASA; Laser Pointing System; Mobile Optical Mount System; Remote Sensing)

Strane R.E.,: "Laser Tracking System--Single-Station Cinetheodolite Ranging and Auto-Tracking." Proceedings of the Society of Photo-Optical Instrumentation Engineers, Vol. 134, 13-14 March 1978.
(Cinetheodolite Ranging; Servo; Laser Tracking System; Auto-Tracking; ND-YAG Laser; Microprocessor)

Suzaki, Y., Tachibana, A.,: "Influence of Photoelectron Fluctuations on Accuracy of Ranging by Pulsed Laser Radar." Flectron. and Commun., Vol. 56, No. 11, November 1973.
(Pulsed Laser Radar; Ranging; Threshold Detection; Standard Deviation; Photomultiplier Output Fluctuation; Satellite Observation Data; Limit Accuracy)

Swinth, K.L., Walker, R.A., Nedrow, N.G.,: High Throughput Dimensional Measurements with Electro-Optics. Battelle Pacific Northwest Labs, for U.S Department of Energy, August 1979.
(ERDA/440300, ERDA/420500, NTISDE)

Ideda T., Terada H.,: "Photogrammetric Application of Moire Fringes Produced with a Parallel Beam of Light, Opt. Eng., Vol. 18, No. 4, July-August 1979.
(Parallel Beam of Light; Contour Fringes; Optical System; Field Lens; Equal Values Contour Intervals; Computer; TV Camera; A/D Converter; Moire Fringes; Biostereometry; Photogrammetry; Human Body Motion)

Trevogo I.S., Vlasenko S.G.,: "About Determining Kinds of Error Functions in Eletro-Optical and Radio-Rangefinder Measurements." Geod. Kartogr. Aerofotos EMKA, (USSR), No. 19, 1974.
(Geodesy; Error Function Determination; Electro-Optical)

Weber P.,: "Adaptation of the Lidar to Aircraft and Missile Rangefinding,"
Rech. Aerosp., (France), No. 1 January-February 1972.
(Optical Radar; Optical Tracking; Lidar; Missile Rangefinding; Space and Time
Coherence; Localization Instrument; Satellites; Aircraft)

Young W.H., Isbell D.M.,: "Production Mapping with Orthophoto Digital Terrain
Models." Photogramm. Eng. and Remote Sensing, Vol. 44, No. 12, December 1978.
(Orthophoto Digital Terrain Models; Topographic Maps; Orthophotography;
Contours; Steroscopic Image; Digital Data; Flood Plain Limits; Photogrammetry)

Yammamoto H., Imazeki H.,: "OPMs Facilitate Laser Photometry." JEE (Japan),
No. 134, Feburary 1978.
(Laser Photometry; Silicon Photodiodes; Thermopiles; Digital Display Systems;
Laser Beam Measurements; Optical Power Meters; Analogue Meters)

Page intentionally left blank

Page intentionally left blank

BIBLIOGRAPHY

(SECONDARY REFERENCES)

Anderson R.H., Huang C.C., and Buholz N.E.,: "Sensing the Position and Vibration of Spacecraft Structures," American Institute of Aerodynamics and Aeronautics, Vol. 4, No. 2, March-April 1981.

Arecchi F.G., Bassan M., Jacobs S.F., and Molesini G.,: "MTF Measurement Via Diffraction Shearing with Optically Superimposed Gratings." Applied Optics, Vol. 18, No. 8, 15 April 1979.

Bennett V.,: "Generation of Pseudo-Fizeau Fringes on Large Objects." Coherent Optics in Mapping, S.P.I.E., March 1974.

Bien F., Camac M., Caulfield H.J., and Ezekiel S.,: "Absolute Distance Measurement by Variable Wavelength Interferometry." Applied Optics, Vol. 20, No. 3, 1 February 1981.

Butters J.N.,: "Application of ESPI to NDT," Optics and Laser Technology, June 1977.

Berdahl M.,: "JPL Self-Pulsed Laser Surface Measurement System Development." Jet Propulsion Laboratory LSST 2nd Annual Technical Review, November 18, 19, 20, 1980.

Brown Duane C.,: Application of Close-Range Photogrammetry to Measurements of Structures in Orbit. Vol. 1, Final Report, Geodetic Services, Incorporated Rept. No. 80-012, September 15, 1980.

Buholz N.E.,: "Selected Five Color Operation of a CO_2 Laser." SPIE, Vol. 228: Active Optical Devices and Applications, 1980.

Chiang F.P. and Bailangadi M.,: "White Light Projection Speckle Method for Generating Deflection Contours." Applied Optics, Vol. 19, No. 15, 1 August 1980.

Cook P.O. and Hamm C.W.,: "Fiber Optic Level Displacement Transducer." Applied Optics, Vol. 18, No. 19, October 1979.

Dreyfus R.W.,: "Versatile Microsecond Movie Camera." Applied Optics, Vol. 19, No. 6, 15 March 1980.

Duguay M.A., Damen T.C., Stone J., Wiesenfeld J.M., and Burrus C.A.,: "Picosecond Pulses from an Optically Pumped Ribbon-Whisker Laser." American Institute of Physics, Applied Physics Letter 37(4), 15 August 1980.

Gillard C.W., Buholz N.E. and Ridder D.W.,: "Absolute Distance Interferometry." SPIE, Vol. 228: Active Optical Devices and Applications, 1980.

Golden K.E., Kind D.E., Leonard S.L., and Ward R.C.,: "Laser Ranging System With 1-cm Resolution," Applied Optics, Vol. 12, No. 7, July 1973.

Hafle R.S. and Cole C.F., Jr.,: "Precise Speed Control through Zero RPM with Special Encoders." Control Engineering, August 1975.

Hewlett-Packard Journal, Vol. 31, September 1980.

Hines R.H. and Hollinshead W.L.,: "An Electro-Optical Distance Measuring Instrument for Surveying," Laser Systems and Electronics, Inc. 1971.

Indebetouw G.,: "Profile Measurement using Projection of Running Fringes." Applied Optics, Vol. 17, No. 18, 15 September 1978.

Johnson C.B., Nevin S., Bebris J., and Abshire J.B.,: "Circular-Scan Streak Tube with Solid-State Readout." Applied Optics, Vol. 19, No. 20, 15 October 1980.

Lokberg O.,: "Electronic Speckle Pattern Interferometry." Physics in Technology, Vol. 11, No. 1, January 1980.

Mak P.S., Mathur V.K., and Lee Chi H.,: "Picosecond Optoelectronic Switching in $C_dS_{0.5}Se_{0.5}$." Optics Communications, Vol. 32, No. 3, March 1980.

Marcatili E.A.J.,: "Optical Subpicosecond Gate." Applied Optics, Vol. 19, No. 9, 1 May 1980.

Margulis W., Sibbett W., Taylor J.R., and Bradley D.J.,: "Reduction of Jitter in Steak-Camera Synchronization with Picosecond Laser Pulses. "Optics Communications, Vol. 32, No. 2, February 1980.

Massie N.A.,: "Real-Time Digital Heterodyne Interferometry: A System." Applied Optics, Vol. 19, No. 1, January 1980.

Massie N.A., Nelson R.D., and Holly S.,: "High-Performance Real-Time Heterodyne Interferometry," Applied Optics, Vol. 18, No. 11, 1 June 1979.

McLellan E.J. and Stotlar S.C.,: "Picosecond Pyroelectrics." Optical Spectra, March 1981.

Nakadate S., Yatagai T., and Saito H.,: "Electronic Speckle Pattern Interferometry Using Digital Image Processing Techniques." Applied Optics, Vol. 19, No. 11, 1 June 1980.

Parker R.J.,: "Surface Topography of Non-Optical Surfaces by Oblique Projection of Fringes from Diffraction Gratings." Optica Acta, Vol. 25, No. 8, 1978 (GB).

Perrin J.C. and Thomas A.,: "Electronic Processing of Moire Fringes: Application to Moire Topography and Comparison with Photogrammetry." Applied Optics, Vol. 18, No. 4, 15 February 1979.

Querzola B.,: "High Accuracy Distance Measurement by Two-Wavelength Pulsed Laser Sources." Applied Optics, Vol. 18, No. 17, 1 September 1979.

Rix H. and Malenge J.F.,: "Detecting Small Variations in Shape." IEEE Trans-
actions on Systems, Man, and Cybernetics, Vol. SMC-10, No. 2, February 1980.

Roblin G.,: "Electronically Generated Limitation of the Sensitivity of
Optical Measurements Using Time Modulation." Optics and Laser Technology,
August 1977.

Rowlands R.E. and Lemens P.O.,: "Moire Strain Analysis in Cryogenic Environ-
ments." Applied Optics, Vol. 18, 15 June 1979.

Schiller N.H., Tsuchiya Y., Inuzuka E., Suzuki Y., Kinoshita K., Kamiya K.,
Iida H., and Alfano R.R.,: "An Ultrafast Streak Camera System: Temporal
Disperser and Analyzer." Optical Spectra, June 1980.

Simon M.C., Simon J.M., and de Zenobi E.L.,: "Testing Optical Surfaces by the
Method of the Caustic Using a Phase-Stripe as Spatial Filter." Applied
Optics, Vol. 18, No. 9, 1 May 1979.

Tang C.L., Levin K.H., Gammel J., and Ballantyne J.M.,: "Dithered-Beam
Metrology." Applied Optics, Vol. 17, No. 24, 15 December 1978.

Rauhala Dr. Urho A.,: Development of Array Algebra Algorithms for Finite
Element Filtering. Final Report, Geodetic Services, Inc., October-November,
1980.

Vaughan H.,: "Seidel Aberrations of an Inflated Membrane." Applied Optics,
Vol. 19, No. 18, 15 September 1980.

Wykes C. and Jones R.,: "Complex Object Geometrics." Europhysics Journal,
June 1978.

1. Report No. NASA CR-3522	2. Government Accession No.	3. Recipient's Catalog No.
4. Title and Subtitle Conceptual Design and Analysis of a Large Antenna Utilizing Electrostatic Membrane Management		5. Report Date May 1982
		6. Performing Organization Code
7. Author(s) A. L. Brook,[a] J. V. Coyner,[b] W. J. Gardner,[b] and D. J. Mihora[c]		8. Performing Organization Report No. MCR-81-1334
		10. Work Unit No.
9 Performing Organization Name and Address Martin Marietta Corporation P. O. Box 179 Denver, Colorado 80201		11. Contract or Grant No. NAS1-16447 Task 1
		13. Type of Report and Period Covered Contractor Report Sept. 1980 - Sept. 1981
12. Sponsoring Agency Name and Address National Aeronautics and Space Administration Washington, D.C. 20546		14. Sponsoring Agency Code

15. Supplementary Notes   Each Task is reported out in a separate volume. This volume is Task I. (a) Program Manager, Martin Marietta Corporation (MMC); · (b) Senior Staff Engineer (MMC); (c) Program Manager, General Research Corporation.
Langley Technical Monitor: U. M. Lovelace

16 Abstract
Radiometer antennas of the 100-m diameter class can be placed into near-Earth orbit with one Shuttle flight. This study explored and developed certain conceptual designs and associated technologies for deployable antennas of this size. The study was divided into three tasks.

The first task was dedicated to the design of an electrostatically suspended and controlled membrane mirror and to the performance of the necessary analysis to develop conceptual designs for the supporting structure. The scope included evaluating three leading structural concepts, selecting two, and proceeding with the design and analysis of the integrated spacecraft including STS cargo bay stowage and development. An antenna performance evaluation was performed as a measure of the quality of the membrane/spacecraft when used as a radiometer in the 1 GHz to 5 GHz region.

The objective of Task II was to provide several related LSS structural dynamic models differing by their stiffness property (and therefore, lowest modal frequencies); then, to take these dynamic models, and develop control systems whose complexity varies inversely with increasing modal frequency regimes.

The objective of Task III was to expand and improve Langley Research Center's (LaRC) interactive computer-aided-design software.

17 Key Words (Suggested by Author(s))	18. Distribution Statement
o Radiometer Antenna Spacecraft o Electrostatically Controlled Membrane Mirror o STS Payload o Deployable Truss	Unclassified - Unlimited Subject Category 18

19 Security Classif. (of this report) Unclassified	20. Security Classif. (of this page) Unclassified	21. No. of Pages 312	22. Price A14

NASA